Strategic Design of Conjugated Polymer Materials for Sensors and Solid-State Lighting

Niamh Willis Fox

A thesis submitted to the University of Dublin, Trinity College
for the degree of Doctor of Philosophy.

Under the supervision of Dr. Rachel C. Evans

School of Chemistry

Trinity College Dublin

November 2015

Declaration

I declare that this thesis has not been submitted as an exercise for a degree at this or any other university and it is entirely my own work, except where otherwise cited, referenced, acknowledged or accredited.

I agree to deposit this thesis in the University's open access institutional repository or allow the library to do so on my behalf, subject to Irish Copyright Legislation and Trinity College Library conditions of use and acknowledgement.

……

Niamh Willis Fox B.A. Mod.

Light (…) gives colour and brilliance to all works of nature and of art, it multiplies the universe by painting it in the eyes of all that breathe.

-Abbé Nollet

The trouble with an open mind, of course, is that people will insist on coming along and trying to put things in it.

-Terry Pratchett

Acknowledgements

I would almost say writing these acknowledgements was the hardest part of writing this thesis (almost but not quite!!), what if I forgot or offended someone!? However, I have to say, it was the easiest thing in the world to realise that first and foremost I want to thank my supervisor Dr. Rachel Evans. As a shy young undergrad I never could have imagined that I would have ended up with a supervisor so supportive of my love of the musical talents of Taylor Swift or one who would subtly instigate a group uniform by buying the same clothes as everyone else. But in all seriousness, I could also never have dreamed I would be lucky enough to have a supervisor as generous with her guidance and support. I have had an amazing four years both personally and professionally and I couldn't have done any of it without you, so truly thank you Rachel.

I was privileged to spend a small portion of my PhD in Boston. They say never meet your heroes but Tim you proved that wrong. Thank you so much for taking me as essentially a blow in from the street and for treating me with the same care and concern you would one of your own students. Also to all the 'Swagerites' that welcomed me with open arms from the very start and made my stay unforgettable; Chris, Myles, Sibo, Yoshi, Greg, Maggie, Joe, Vera and Laura.

I couldn't have done this work left to my own devices; I got endless help from the technical and academic staff. I want to thank John and Manuel for their measurements in the NMR services and particularly to Manuel for help with essentially all of the instruments I set my hands on and for answering my emails even if he was in the pub. Patsy, Helen and Tess thank you for always making me smile, genuinely what would we have done without you. As they saying goes 'there's only one Patsy Green' don't worry girls, Jude and I will teach you the song on our holiday.

To all the members of the Evans group past and present who not only made it a pleasure to come into college everyday but who also put up with all my ridiculous demands like full on costumes for the Keeley cup and other such messing. Special shout out to my lunch buddy Barry, I don't think I've had to clean my tea mug at all in the last two years. It will come as no surprise to anyone that there are two people that I have to single out, Adam and Jude (don't worry Jude he's just going first because he is older). You guys have been right beside me for every moment of this PhD, from the ridiculous (going to pick our stuff up from the Law/Lost Society) to the sublime (suited and booted for the Scholars ball). If I get nothing else from this experience I will have gained two of the best friends the world has to offer, who would totally invite me to their wedding.

I also managed to pick up some other friends along the way. Dee, Ian and Moylan (who immediately took me under her wing), these last few years would have been a much less sociable and entertaining experience without you. I also have to mention my hockey team who attempted (and failed) to get me out running and who almost made 9 am matches on Saturday mornings bearable. Graham and Christian, thanks for all the holidays and staying up until crazy times watching addictive TV shows. Fergus, I have no idea how we managed to get this far without freaking each other out, but to me you will always be more than a 'one act cat'. I also have to mention Emily who had no choice in our friendship in undergrad, I just didn't leave her house. I'm delighted every day to realise the Stockholm syndrome hasn't worn off and she now even voluntarily makes it to my house to supply a cup of tea and some dry humour.

And to my touchstone, Classic Beth, I feel like I don't have to tell you all my deepest thoughts (most of them aren't that deep anyway), you seem to know what they are before I have them. I am never immune to your charm, no one has or can make me laugh and smile so much. It has been wonderful to be part of this friendship that we have been (Met)formin. Last but not least my family, aunts and godparents, thank you for all the love and happy days. Most specially to J, Sheila and Orla (who I never realise how much I miss until she is gone on another amazing adventure). I'm sorry you guys had to put up with the brunt of the bad moods and didn't always get to see the good. Thank you for relentlessly picking me up, dusting me off and setting me in the right direction again. There are no words for how much love and admiration I have for you guys.

Abstract

Conjugated polymers (CPs) have shown extreme promise in a range of applications such as optical sensors and light-emitting devices due to their exceptional optoelectronic properties, low cost and solution processability. CPs are particularly sought after as sensory materials due to their property of amplified quenching, which can facilitate analyte detection at nanomolar concentrations. This work begins by examining the use of a polyfluorene (blue-emitting)-polythiophene (red-emitting) diblock CP with complementary optoelectronic properties attributed to both blocks, which enables fluorimetric and colorimetric detection of biologically important nucleotides. The magnitude of the optical response is sensitive to both nucleotide geometry and charge. The proposed mechanism behind this process involves electron transfer from the nucleobase to the polythiophene block, mediated by the CP triplet state.

Although the vast majority of CP-based sensing schemes involve the detection of electron-poor analytes by electron-rich polymers, there are relatively few examples describing the contrary scenario, electron-rich analyte detection by electron-poor polymers. In Chapter 4, the possibility of increasing the discriminatory action of such electron-poor CP sensor systems through the creation of polyrotaxane species is investigated, whereby macrocycles of differing sizes are exploited to control the effective volume in which the CP and analytes interact. This system may be deposited into the solid-state, whilst retaining its sensing properties to gas phase analytes.

The lifetime of any solid-state CP-based device is limited by the photo- and thermal instability of the CP. Incorporation of CPs into an inorganic host allows modulation of the optical properties and aggregation state of the CP, whilst simultaneously improving the environmental stability. However, due to the chemical incompatibility of the two components, inhibiting phase separation across all length scales can be challenging. In Chapters 5-7, the potential of *di-ureasil* hybrids, comprised of an organic polyether grafted onto a siliceous network *via* urea linkages, as host materials for CPs is investigated. Firstly, blue-emitting polyfluorene-phenylene CPs were physically immobilised into the di-ureasil to form a Class I hybrid. Examination of the optical properties indicated that both the CPs and the di-ureasil host contribute to the photoluminescence properties giving rise to a dramatic enhancement of the photoluminescence quantum yield (PLQY) to ~60%. This is due to effective prevention of CP aggregation by the di-ureasil host and efficient energy transfer between the two components. Subsequent inclusion of the red-emitting CPs, MEH-PPV and P3TMAHT, was carried out in an effort to extend the emission colour from the inherent blue emission of the di-ureasil host across the visible spectrum. The emission colour of these samples was found to be tunable across the blue-white-yellow spectral region due to incomplete Förster resonance energy transfer from the di-ureasil to the CP. Finally, as the properties of such organic-inorganic hybrid materials depend on the interface between the two phases, a polyfluorene was covalently-grafted directly to the siliceous network of a di-ureasil. Energy transfer between the di-ureasil and the CP was observed leading to an improved PLQY when compared to a thin film of the pure CP. On comparison with the physically immobilized samples previously discussed, the magnitude of energy transfer was found to be reduced for the grafted species. This suggests a reduced interaction between the CP and organic component of the di-ureasil, highlighting the ability to further control the interactions between the CP and di-ureasil through careful selection of the incorporation method.

The power of the approach presented in this thesis lies in both its simplicity and versatility. Incorporation within a di-ureasil host has showed improved thermal and photostability for each of the CPs investigated. The electronic coupling between the CPs and the di-ureasil suggests that CP-di-ureasils also offer a wealth of potential applications from composite photovoltaics, to luminescent solar concentrators and optical sensors. While the confinement of the CP within a specific region of an active layer offers the potential to reduce the complexity of multi-layer device architectures and may yield improved device performance.

Table of Contents

Preface

The work described in this thesis was carried out through the support of the Irish Research Council. The majority of this work was undertaken at Trinity College Dublin. The remaining portion was carried out at Massachusetts Institute of Technology *via* support from the Irish Fulbright Commission through the granting of a Fulbright Student Award.

The original work presented here has been published as part of a number of peer-reviewed articles:

Chapter 4: N. Willis-Fox, C. Belger, R. C. Evans, T. M. Swager, Threading the Needle: Fluorescent Poly-*pseudo*-rotaxanes for Size-Exclusion Sensing, *Chem. Mater.*, Submitted.

Chapter 5: N. Willis-Fox, A.-T. Marques, J. Arlt, U. Scherf, L. D. Carlos, H. D. Burrows, R. C. Evans, Synergistic Photoluminescence Enhancement in Conjugated Polymer-Di-ureasil Organic-Inorganic Hybrids, *Chem. Sci*., 2015, **6**, 7227-7237.

Chapter 6: N. Willis-Fox, M. Kraft, J. Arlt, A. Lermoyer, U. Scherf, R. C. Evans, Tunable White-Light Emission from Conjugated Polymer-Di-Ureasil Materials, *Adv. Funct. Mater*., 2015, DOI: adfm201504017.

During the tenure of this studentship a number of other original works were also carried out. These form part of the following separate peer-reviewed articles:

R. C. Evans*, M. Knaapila, N. Willis-Fox, M. Kraft, A. Terry, H. D. Burrows, U. Scherf, Cationic Polythiophene-Surfactant Self-Assembly Complexes: Phase Transitions, Optical Response, and Sensing, *Langmuir*, 2012, **28**, 12348-12356.

I. Meazzini, N. Willis-Fox, C. Blayo, J. Arlt, S. Clément, R. C. Evans, Targeted design leads to tailored photoluminescence from perylene dicarboxdiimide-poly(oxyalkylene)/siloxane hybrids for luminescent solar concentrators, *J. Mater. Chem. C*, 2015, submitted.

Abbreviations

2D – two dimensional

3D – three dimensional

ADC – analogue-to-digital converter

ATP – adenosine triphosphate

ATR – attenuated total reflectance

CB[n] – cucurbit-*n*-uril

CDF – constant function discriminator

CIE – Commission Internationale de l'Éclairage

Conc. – concentrated

COSY – correlation spectroscopy

CP – conjugate polymer

CPE – conjugate polyelectrolyte

CTP – cytidine triphosphate

CV – cyclic voltammograms

D_2O – deuterium oxide

DI – direct insertion

DNA – deoxyribonucleic acid

d-UPTES – di-ureapropyltriethoxysilane

DBSA – dodecylbenzene sulfonic acid

DLS – dynamic light scattering

ds-DNA – double stranded deoxyribonucleic acid

EEM – emission-excitation matrix

EET – exciton energy transfer

EML – emissive layer

ETL – electron transport layer

EtOH – ethanol

FIrpic – iridium bis(4,6-difluorophenyl)pyridinato-N,C^2 picolinate

FTIR – Fourier transform infrared

FRET – Förster resonance energy transfer

FWHM – full width at half maximum

GDP – guanosine diphosphate

GF - grafting

GMP – guanosine monophosphate

GPE – gel-permeation chromatography

GTP – guanosine triphosphate

H_2O – water

HCl – hydrochloric acid

HTL – hole transport layer

IC – internal conversion

ICPTES – 3-isocyanatopropyltriethoxysilane

IRF – instrument response function

ISC – intersystem crossing

ITO – indium tin oxide

IUPAC – International Union of Pure and Applied Chemistry

Jeffamine ED-600 – poly(propylene glycol)-*block*-poly(ethylene glycol)-block-poly(propylene glycol) bis (2-aminopropyl ether)

KBr – potassium bromide

LED – light-emitting diode

MAS – magic angle spinning

MeCN – acetonitrile

MEH-PPV - poly[2-methoxy-5-(2-ethylhexyloxy-1,4-phenylene vinylene)]

MeOD – deuterated methanol

MV^{2+} – methylviologen

NLLS – non-linear least square

NMR – nuclear magnetic resonance

OFET – organic field-effect transistor

OLED – organic light-emitting diode

OPV – organic photovoltaic

P3TMAHT – poly[3-(6-triethylammoniumhexyl)thiophene] bromide

PBS-PFP – poly[9,9-bis(4-sulfonylbutoxyphenyl) fluorene-2,7-diyl-*alt*-1,4-phenylene]

PEO - poly(ethylene oxide)

PF – polyfluorene

PF2/6-NH_2 – 4-aminophenyl end capped poly[9,9-bis(2-ethylhexyl)-fluorene-2,7-diyl]

PF2/6-*b*-P3TMAHT – poly[9,9-bis(2-ethylhexyl)fluorene)-*block*-poly[3-(6-triethylammoniumhexyl)thiophene] bromide

PFO – poly(9,9-di-*n*-octylfluorenyl-2,7-diyl)

PFP-HTMA – poly{9,9-bis[6-(*N*, *N*, *N*-trimethylammonium)hexyl]fluorene-2,7-diyl-*alt*-1,4-phenylene}

PGA – programmable gain amplifier

PL – photoluminescence

PLE – photoluminescence excitation

PLED – polymer light-emitting diode

PLQY – fluorescence quantum yield

PNA – peptide nucleic acid

PPE – poly(phenylene-ethynylene)

PPO – poly(propylene oxide)

PPV – poly(*p*-phenylene vinylene)

PPyV – poly(*p*-pyridyl vinylene)

PT – polythiophene

PVA – poly(vinyl alcohol)

PVK – poly(*N*-vinylcarbazole)

PXRD – powder X-ray diffraction

RNA – ribonucleic acid

r.u. – repeat unit

SANS – small angle neutron scattering

SOS – sodium octyl sulfate

SP – solvent permeation

ss-DNA – single stranded deoxyribonucleic acid

TAC – time-to-amplitude converter

TBAHF - tetrabutylammonium hexafluorophosphate

TCSPC – time-correlated single photon counting

TGA – thermogravimetric analysis

THF – tetrahydrofuran

List of symbols

A – acceptor

α_i – pre-exponential factor

b – average number of small molecules bound to a micelle

C – degree of condensation of the siliceous network

ΔG^o – free energy

ΔH^o – enthalpy

ΔS^o – entropy

d – structural unit distance

D – donor

D_h – hydrodynamic diameter

ε_A – molar absorption coefficient

E – efficiency of energy transfer

E_{00} – zero-zero transition of the fluorophore

$E_{ox}(D)$ – oxidation potential of the donor

$E_{red}(A)$ - reduction potential of the acceptor

f – volume fraction

f_a – fraction of the initial fluorescence accessible to a quencher

F_D – intensity of donor emission spectrum

f_i – fractional contribution of the i^{th} component to the overall fluorescence lifetime

f_{ic} – calculated fit

I – intensity

J_{DA} – spectral overlap

κ – orientation factor

K_a - quenching constant for an accessible fraction of fluorophores

k_B – Boltzmann constant

k_{obs} – rate constant for fluorescence decay in the absence of a quencher

K_m – overall quenching rate constant for micelle quenching model

K_n –quenching rate constant for quenching of PT by nucleotide for micelle quenching model

k_{nr} – non-radiative rate constant

k_q – bimolecular quenching constant

k_{rad} – radiative rate constant

K_s – association constant for static quenching

K_{SV} – Stern-Volmer constant

λ_{em} – emission wavelength

λ_{ex} – excitation wavelength

L – coherence length

M_n – number-average molecular weight

M_W – weight-averaged molecular weight

n – refractive index

p – number of floating parameters

Q – quencher

r – distance between a donor and acceptor

r_{core} – core radius

R_0 – Förster distance

σ_i – standard deviation

s_i – spin angular momentum

S – total spin angular momentum

S_n – the n^{th} singlet excited state

$\%T_i$ – percentage area for the i^{th} peak as determined from fitting of Gaussian curves

$<\tau>$ – average fluorescence lifetime

τ_0 – fluorescence lifetime in the absence of a quencher

τ_i – characteristic lifetime for the i^{th} component of a fluorophore

T_n – the n^{th} triplet excited state

T_n – characteristic signal of Si atoms in different environments within an organosilane

τ_{obs} – observed lifetime

Φ_D – donor emission quantum yield

v – number degrees of freedom

w – peak width

W_d – weight of the dry sample

W_s – weight of the swollen sample

χ^2 – chi squared statistic

x_c – peak centre

x,y – colour coordinates

X, Y, Z – tristimulus values

y_i – measured data value

Chapter One

……

Introduction

1.1 Introduction

In the 1970s the concept of metallic conductivity was first described for organic polymers, earning the Nobel Prize for Shirakawa, MacDiarmid and Heeger in 2000. Conjugated polymers (CPs) contain a π-conjugated backbone that produces a delocalised electronic structure.[1, 2] The linear combination of π-orbitals gives rise to a band structure which allows CPs to be characterised as semiconductors.[3] CPs gained popularity due to their low cost and solution processability, allowing the production of large scale, flexible, light-weight devices. This coupled with the exceptional optoelectronic properties conferred by the CP backbone structure has led to their development in a wide variety of applications such as organic photovoltaic devices (OPVs),[4, 5] optical sensors,[6-8] organic field-effect transistors (OFETs)[9, 10] and light-emitting diodes (LEDs).[11-13] The focus of this thesis is the development of CP-based materials for two of these applications; optical sensing and light-emitting materials. In particular, the first portion of the thesis will focus on the electronic interaction between the CP and analyte to develop new optical sensing platforms in solution. The latter half of the work will examine the incorporation of CPs within a host matrix in an effort to produce more robust, emissive materials for solid-state light-emitting materials. The development of both of these applications is heavily dependent on the fluorescence properties of the CPs in question.

1.2 Optical Properties of Conjugated Polymers

The monomer repeat unit and the extent of conjugation along the polymer backbone determine the magnitude of the energy gap between the valence and conduction bands.[14, 15] The absorption and emission properties of CPs are thus highly dependent on the chemical structure of the monomer unit.[14, 15] This is highlighted in **Fig. 1.1** which shows the blue emission from a solution of a fluorene-containing CP, in contrast to the deep red emission produced by a thiophene-based CP. These two structural motifs are the main constituents for the repeat unit (r.u.) of the majority of the CPs discussed throughout this thesis.

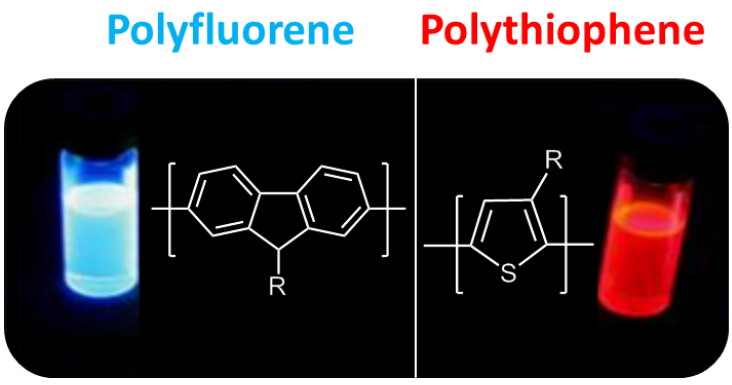

Figure 1.1. The relationship between the emission colour and the chemical structure of the repeat unit for fluorene- and thiophene-containing conjugated polymers.

Historically, the first detailed investigation into the use of photoluminescence (PL) of conjugated polymers for LED devices was reported by the group of Friend in Cambridge. This report detailed the use of a poly(*p*-phenylene vinylene) (PPV) to prepare a device that emitted in the green-yellow spectral region.[1] However, this polymer and many of the early CPs investigated were found to be difficult to process due to extremely high interchain interactions, which resulted in poor solubility. This was overcome through the addition of long hydrocarbon side chains to the polymer backbone, which significantly improved their solubility in organic solvents through the inhibition of interchain interactions.[14, 15] The addition of electron-donating or electron-withdrawing substituents to these side chains may also be used to further modulate the emission properties.[16] The Reynolds group have further utilised the effects of backbone substituents to develop a full colour pallet of polythiophene-based CPs, which contain similar backbone structures but are modified with different bulky substituents.[16-18] The steric effects of these substituents cause differing levels of torsional strain on the backbone, altering the conjugation length of the polymer and enabling tuning of the emission colour across the full visible region (**Fig. 1.2**).

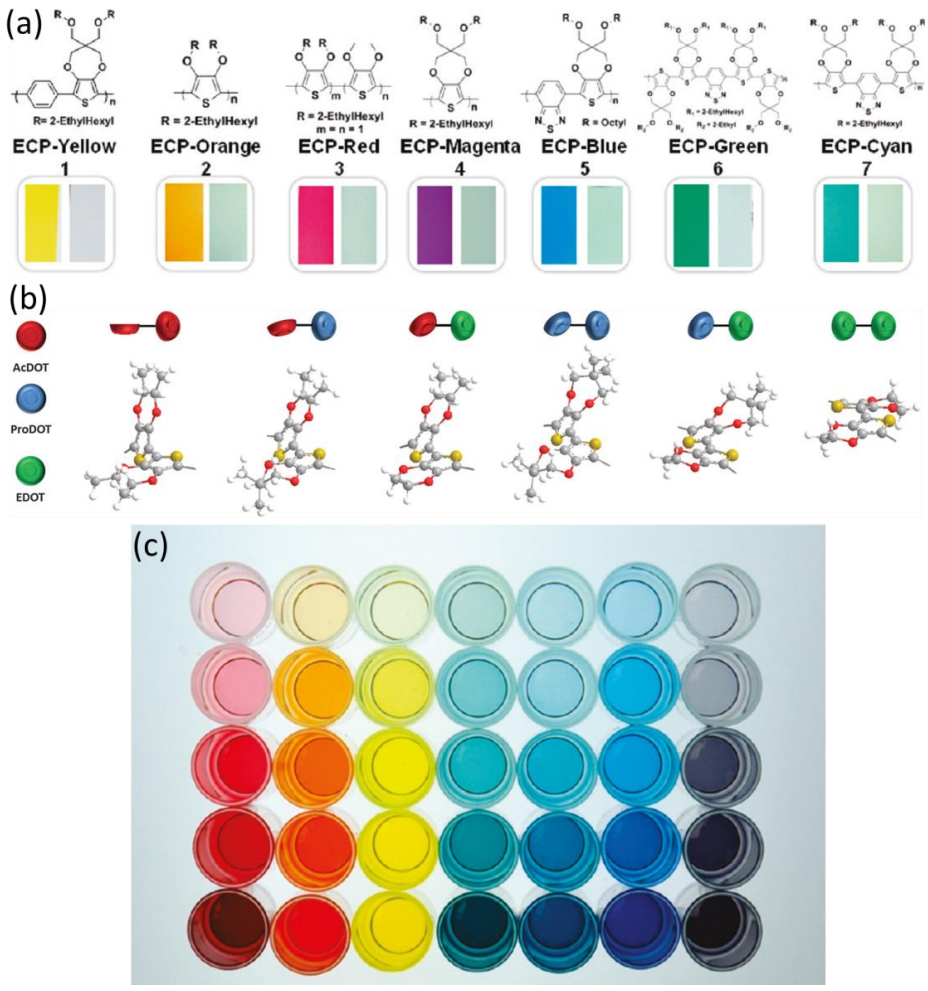

Figure 1.2. (**a**) Repeat unit structures and photographs of spray-cast films of polythiophene based CP with backbone substituents of varying steric bulk.[16] (**b**) Cartoons depicting backbone torsional interactions between neighbouring 3,4-dioxythiophene rings, strain decreases from the left to the right through relaxation of strain in the conjugated backbone.[18] (**c**) Photograph of solutions of the polymers shown in (**a**), illuminated from underneath with concentration increasing from top to bottom.[16]

However, while the addition of hydrocarbon side chains improved the solubility in organic solvents, a drive towards the use of environmentally-friendly processing methods, applications in biological systems and control of the ionic properties of CPs concomitantly led to the development of conjugated polyelectrolytes (CPEs) in the late 1980s.[19] CPEs are conjugated polymers containing a terminal charged unit on their pendant substituents. The ionic nature of CPEs allows them to be soluble in polar solvents such as water. As the charged groups tend to be towards the extremity of the side chain they have little effect on the π-electron system and their optical properties, like their uncharged counterparts, are determined by the structure of the backbone.[20] This was highlighted through a study of five pairs of poly(arylene-ethynylene) CPEs with the same conjugated backbone and oppositely charged side groups.[21] It was found that each pair that shared the same conjugated backbone had virtually the same optical properties, irrespective of the anionic or cationic nature of the CPE. In contrast, changing the arylene repeat units within the CPE backbone caused the absorption maximum to shift from 400 to 550 nm and the PL maximum to range from 440 to 600 nm.

Although the ionic pendent groups of CPEs render them soluble in polar solvents it also creates an inherently amphiphilic structure, as the backbone is hydrophobic and the side groups are hydrophilic in nature. This leads to a tendency to aggregate in aqueous solution or polar organic solvents which may alter their photophysical properties.[20] Aggregation of CPs and CPEs leads to increased interchain interactions giving rise to an increased conjugation length, leading to a red shift in the emission maximum and a decreased photoluminescence quantum yield.[22, 23] The effects of such aggregation has been distinctively demonstrated on investigation of a $-SO_3^-$ containing poly(phenylene-ethynylene) (PPE) (PPE-SO_3). PPE-SO_3 exists as molecularly dissolved chains in methanol and aggregates in water.[24, 25] As the water content of a methanolic solution of PPE-SO_3 is increased the sharp, structured, narrow band in the emission spectrum is replaced by a broad, structureless band that is red-shifted significantly from its position in methanol.[24, 25]

At this point it is pertinent to quickly discuss some polymer nomenclature. Similar to their saturated counterparts, CPs may also be categorised depending on the connectivity and nature of their constituent monomer units.[26] If the polymer chain comprises a single type of repeat unit, it is described as a *homopolymer*. Addition of a second or multiple types of repeat unit allows the polymer to be described as a *copolymer*. Furthermore, the monomeric units may distributed randomly (*random copolymers*), in an alternating arrangement (*alternating copolymer*) or in blocks (*block copolymer*). Each of these structures is represented schematically for two different repeat units in **Fig. 1.3**. These structures may also be extended to incorporate a higher order of monomeric species.

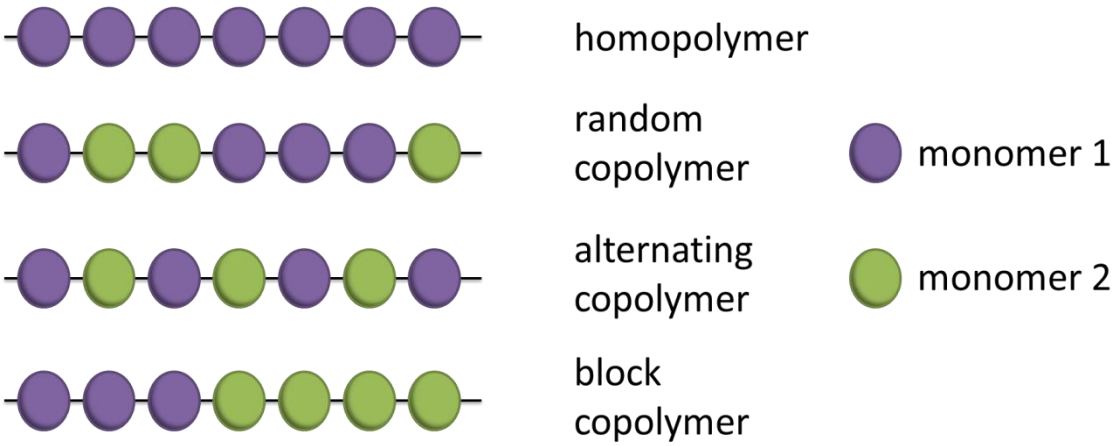

Figure 1.3. Schematic representation of a sample of common polymer structures.

The possibility of forming aggregate structures with well-defined architectures has become possible through the investigation of saturated block copolymers in which each of the blocks possess chemically-distinct characteristics. The morphology of these aggregate structures is dependent on the relative volume fraction of one block with respect to the other.[27] Some of the possible morphologies for block copolymers are shown in **Fig. 1.4** as a function of increasing volume fraction, *f*, of one block with respect to the other.

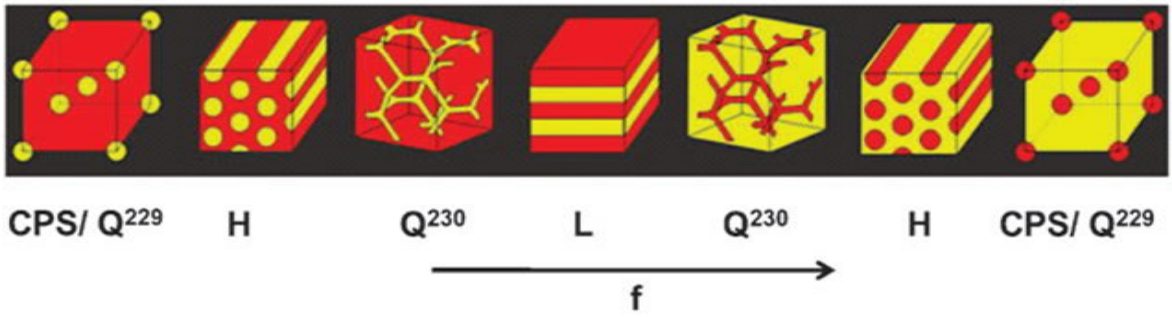

Figure 1.4. Illustrations of the morphologies of a diblock copolymer with increasing volume fraction, *f*, of one block with respect to the other. From left to right, the structures include body centre cubic spheres (CPS/Q^{229}), hexagonal cylinders (H), cubic bicontinuous gyroid (Q^{230}) and lamellar structures (L).[27]

The synthesis of all-conjugated diblock copolymers is reasonably challenging,[28-30] however, their self-assembly into defined nanodomains has led to their particular suitability for use in organic solar cells, driving research in this area.[27] Further control over the morphologies formed by diblock copolymers may be gained through addition of a charged unit to one of the blocks to form a diblock copolyelectrolyte.[29, 30] This has been highlighted by recent work examining the structure-property relationship of polythiophene (PT)-based diblock polyelectrolytes containing one neutral PT block and one cationic PT block.[31] These polymers display solvatochromatic behaviour, with the solution colour changing from dark red/brown in chloroform to dark violet in methanol and water as shown in **Fig. 1.5a**. This shift in optical properties is highlighted in **Fig. 1.5b**, which shows a dramatic red-shift in the absorption and emission maxima accompanied by increasing vibronic structure. This suggests aggregation of the poly(3-hexylthiophene-2,5-diyl)

(P3HT) block in water and methanol due to the fact that water is a non-solvent for the neutral block, and low to moderate solubility of this block is expected for methanol. On investigation of the structure-PL relationship between the two PT blocks using neutron scattering experiments in MeOD-D_2O solvent mixtures, it was found that a core-shell disc structure exists in D_2O, with a core of packed neutral blocks surrounded by a shell comprising the charged blocks which are preferentially solvated. On increasing the MeOD concentration to 50%, the core-shell structure is still retained, however, with improved solvation of both blocks. While in pure MeOD formation of an elongated core-shell cylindrical structure is observed, with a solvated shell and a drier core.

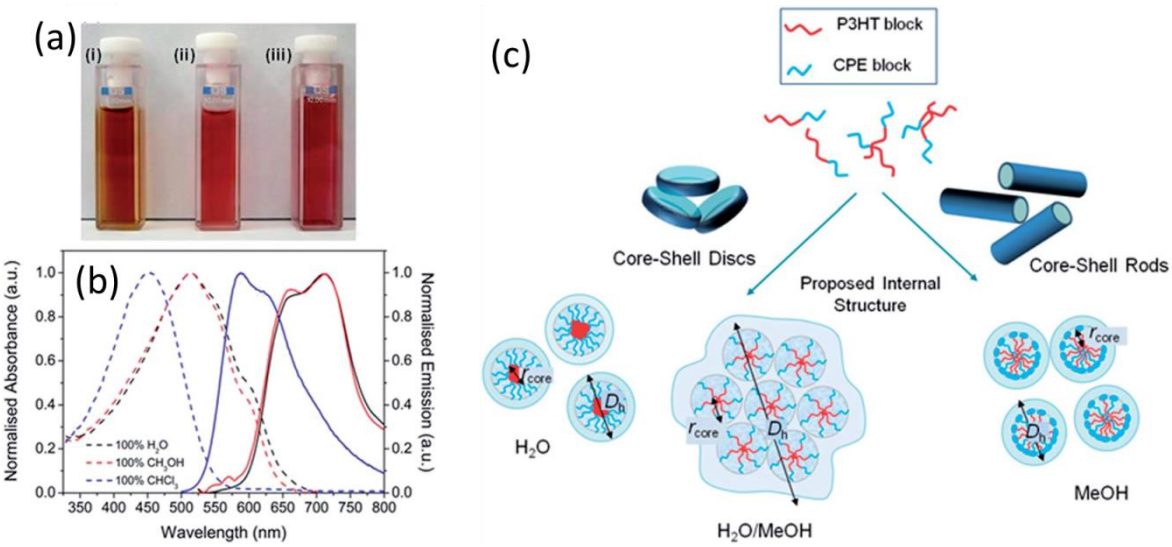

Figure 1.5. (**a**) Cationic polythiophene based CPE in (i) chloroform, (ii) MeOH and (iii) H_2O. (**b**) Corresponding UV/Vis absorption (dashed line) and emission spectra (solid line) of the same polymer in chloroform (blue), MeOH (red) and H_2O (black). (**c**) Schematic representation of the proposed aggregate structure of the diblock CPE in H_2O, MeOH and H_2O-MeOH mixtures. r_{core} is the core radius obtained from fitting of neutron scattering data and D_h is the hydrodynamic diameter measured by dynamic light scattering (DLS). Adapted from ref [31].

The examples discussed here demonstrate the wide variety of methods available to alter the optical properties of CPs in solution. The following section will introduce some of the theoretical background behind photoluminescence in such CPs.

1.3 Photoluminescence of Conjugated Organic Species

1.3.1 Formation of Excited States

Photoluminescence is the emission of light from an electronically excited species. Formation of the excited state may occur upon absorption of a photon. If this photon has the appropriate energy it can cause the promotion of an electron from a bonding (σ, π) to an anti-bonding (σ^*, π^*) orbital. Molecules may also possess electrons in non-bonding orbitals (n orbitals), located on heteroatoms such as nitrogen or oxygen. These electrons may also be promoted into anti-bonding orbitals. The energies of these transitions generally follow the order, $n \rightarrow \pi^* < \pi \rightarrow \pi^* < n \rightarrow \sigma^* < \sigma \rightarrow \pi^* < \sigma \rightarrow \sigma^*$. In small molecules the bonding orbitals involved in the above processes are

localised between pairs of atoms.[32] However, in species with alternating single and double bonds, such as the conjugated polymers discussed throughout this thesis, the idea of localised bonding and antibonding orbitals is not fully adequate. The overlap of the π-orbitals causes the electrons to be delocalised over the whole system. The greater the extent of the conjugated π-system, the lower the energy of the low-lying $\pi \rightarrow \pi^*$ transition, and consequently, the longer the wavelength of the corresponding absorption bands.

1.3.2 Nomenclature of Electronic States

The multiplicity of an electronic state is given by 2S+1, where S is the spin angular momentum ($S=\sum s_i$, with $s_i=\pm½$). If the electron in the excited orbital is paired to the second electron in the ground-state orbital then both are called singlet states (S_n). This is the case as the multiplicity of both states is 1, as S=0. Consequently, return to the ground state *via* a singlet-singlet transition is spin-allowed and occurs rapidly by the emission of a photon. If the electron in the excited orbital has a spin parallel to that of the ground-state electron, then this is called a triplet state (T_n). The multiplicity of this state is 3 as S=½+½=1.[32] According to Hund's Rule, the triplet state has a lower energy than that of the singlet state of the same configuration. The electronic spins and relative energies of the resulting excited states are demonstrated in **Fig. 1.6**.

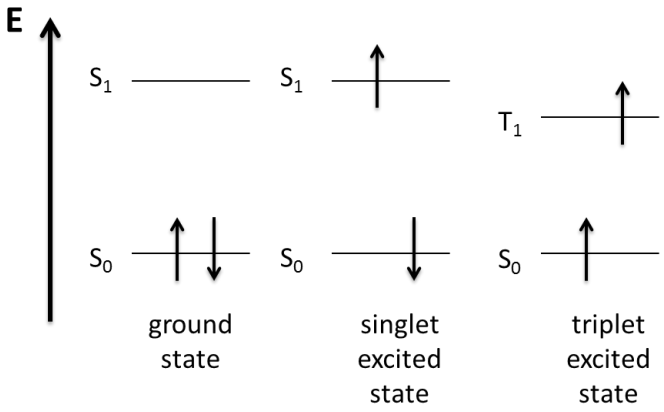

Figure 1.6. Schematic representation of the relative energy levels and the spin of the ground- and excited-state electrons.

1.3.3 Selection Rules

There are two major rules that govern excitation and relaxation of electronic states in polyatomic organic molecules, which describes the probability of transition from one state to another.[32]

(i) Symmetry forbidden transitions: A transition in polyatomic organic species, such as the CPs discussed here, can be forbidden for symmetry reasons which are an extension of the Laporte selection rule for single atoms. This rule states that for species with a centre of inversion only transitions between states of different parity are allowed, *i.e.* where there is a difference in

symmetry between the wavefunctions involved. For single atoms this means that, for example, s → s transitions are forbidden, while s → p transitions are allowed. The symmetry of larger polyatomic species such as CPs, can be related to the symmetry properties of particular point groups.[33] Further discussion on such point groups is beyond the scope of this work. However, it must be noted that these symmetry arguments only hold for completely rigid structures. In practice, molecular vibrations may occur, causing some departure from perfect symmetry. This can distort the molecular structures sufficiently to allow for the occurrence of transitions which would formally be forbidden.

(ii) Spin forbidden transitions: A transition between states of different multiplicities is forbidden as there can be no change in spin angular momentum for transitions between 'pure' states. This means that transitions between singlet and triplet states are formally spin-forbidden.[33] However, it is possible for coupling to occur between the orbital magnetic moment and the spin magnetic moment, which is known as *spin-orbit coupling*. As a result, a wavefunction for a singlet (or triplet) state always contains a small fraction of a triplet (or singlet) wavefunction, allowing for a small but not negligible intensity for a transition between the two states of different multiplicity.

1.3.4 Optical Transitions

The Born-Oppenheimer approximation states that the motions of electrons are much faster than that of the nucleus. The process of absorption takes place on a time scale of ~ 10^{-15} s, while molecular vibrations occur at ~ 10^{-12} - 10^{-14} s. This leads to the Franck-Condon principle, as nuclei are much heavier than electrons, and an electronic transition is most likely to occur without changes in the position of the nuclei, as these transitions occur much faster than the nuclear motion. Thus, an electronic transition is a vertical transition as shown in **Fig. 1.7**. Both the ground and excited states comprise vibrational energy levels. According to the Boltzmann distribution, most of the molecules are in the lowest vibrational level of the ground state. A transition to a specific vibrational level is more likely to occur if there is a more significant overlap between the vibrational wavefunctions (**Fig. 1.7**). The width of any band in the absorption spectrum is a consequence of two effects, homogenous and inhomogeneous broadening. Homogeneous broadening arises due to the existence of the continuous set of vibrational levels within each electronic state. Inhomogeneous broadening results from changes in the structure of the solvent shell surrounding the molecule. The distribution of solute-solvent configurations and the consequent variation in the local electric field lead to a statistical distribution of the energies of the electronic transitions. These broadening effects also apply to emission bands in photoluminescence (PL) spectra. A combination of these two effects can cause the absorption spectra of moderately large and rigid fluorophores in solution to be almost structureless at room temperature.[32]

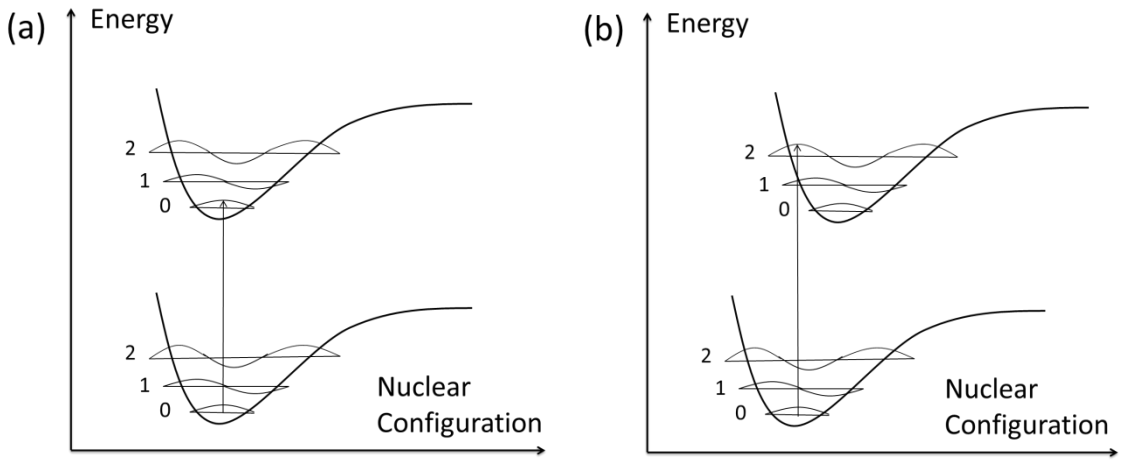

Figure 1.7. Potential energy diagrams showing vertical transitions between states of (**a**) the same nuclear geometry and (**b**) different nuclear geometry.

1.3.5 Deactivation of Excited States

Once in the excited state, the molecule can lose its excess energy through a combination of radiative and non-radiative processes. The transitions and processes occurring on absorption of a photon and the subsequent deactivation pathways of the excited states formed are often illustrated using a Jablonski diagram (**Fig. 1.8**).[34]

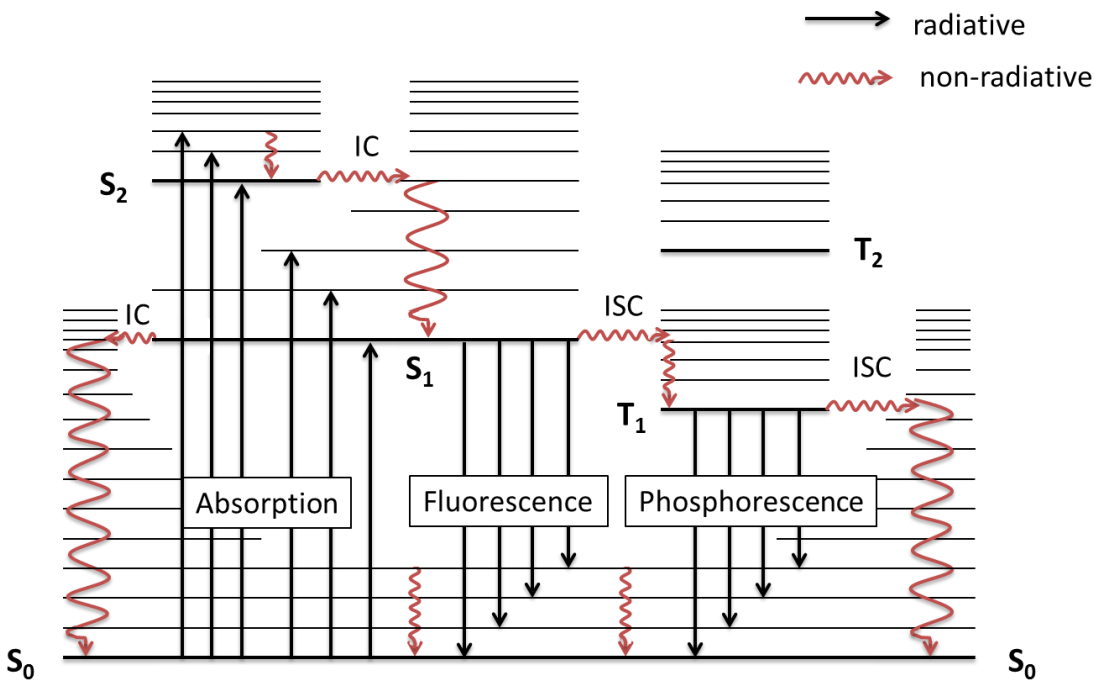

Figure 1.8. Jablonski diagram showing the processes of absorption, fluorescence, phosphorescence, internal conversion (IC) and intersystem crossing (ISC). The radiative transitions are represented by black straight arrows, while non-radiative transitions are represented by red curved arrows.

Internal conversion (IC) is a non-radiative transition between two electronic excited states of the same multiplicity, *e.g.* S_2-S_1. In solution, this process is followed by a vibrational relaxation towards the lowest vibrational level of the final electronic state. Due to such vibrational relaxation, following excitation to higher electronic and vibrational levels, the excess energy is quickly

dissipated; leaving the molecule in the lowest vibrational level of the S_1 excited state. The excess vibrational energy can be transferred to the solvent during collisions of the excited molecules with the surrounding solvent molecules. IC is more efficient between higher excited states as they are closer in energy levels. IC is also possible from S_1 to S_0, however, it is much less efficient than other S_n to S_{n-1} transitions due to the much larger energy gap. Thus, other deactivation pathways are often much more favourable than IC for the S_1 to S_0 transition.

The radiative transition between states of the same multiplicity, *e.g.* $S_1 \rightarrow S_0$ is termed *fluorescence*. The 0-0 transition for absorption and fluorescence is usually the same magnitude. However, the fluorescence spectrum is seen at longer wavelengths (lower energy) due to some energy lost from the excited-state through vibrational relaxation. The fact that emission occurs from the lowest vibrational level of the first excited state is a consequence of Kasha's rule which states that emission spectra are usually independent of the excitation wavelength. Excited state molecules stay in the S_1 state for a certain length of time prior to emission or other forms of deactivation. This gives rise to a characteristic lifetime of the excited state which is usually of the order 10^{-10}-10^{-7} s. The characterisation and measurement of this excited-state lifetime will be discussed further in **Section 2.3.5**. Further deactivation pathways may compete with fluorescence if they occur within the excited-state lifetime.

Relaxation may also occur through *intersystem crossing* (ISC) which is a non-radiative transition between isoenergetic vibronic levels in states of different multiplicity, *e.g.* $S_1 \rightarrow T_1$. Once in the isoenergetic vibronic level of T_1 the molecule relaxes further to the v=0 vibrational level of T_1 though vibrational relaxation. Crossing between states of different multiplicity is forbidden. However, it is possible for coupling to occur; between the orbital magnetic moment and the spin magnetic moment, which is known as *spin-orbit coupling*. If this coupling is large enough intersystem crossing may occur, the probability of intersystem crossing depends on the singlet and triplet states involved. The magnitude of the current and concomitant magnetic field generated by the motion of an electron is dependent on the nuclear charge. As it is this orbital magnetic moment that interacts with the spin magnetic moment, the greater the nuclear charge the greater the spin-orbit coupling. Thus, the rate of such forbidden processes is increased in molecules containing an atom of high atomic number; this is known as the *heavy atom effect*.

The radiative transition from states of different multiplicity, *e.g.* $T_1 \rightarrow S_0$, is a formally forbidden process called *phosphorescence*. As this is a forbidden transition, its radiative rate constant is very low and thus, numerous collisions with solvent molecules favour IC and vibrational relaxation. However, at low temperature or in rigid media, phosphorescence may be observed. Reverse intersystem crossing, $T_1 \rightarrow S_1$, may occur when the energy difference between S_1 and T_1 is small. This results in emission from S_1 but with a much longer decay time constant

compared to normal fluorescence because the molecule stays in the triplet state before emitting from S_1. This is called *thermally activated delayed fluorescence*.

Photoluminescence (PL) is the emission of light following the absorption of a photon and as such encompasses all of the radiative processes discussed here; fluorescence, phosphorescence or thermally activated delayed fluorescence. However, the emission displayed by CPs falls under the classification of fluorescence, hence, the phrases fluorescence and photoluminescence are used interchangeably throughout this thesis.

1.3.6 Excited-State Lifetime

Consider a dilute solution of a fluorescent species *M*, the concentration of which is [*M*]. Following excitation of the fluorophore with an infinitely sharp (δ-function) pulse of light, a certain number of molecules are brought into the excited state S_1. These return to the ground state either radiatively or non-radiatively. Thus, the rate of disappearance of the excited state, M^*, is given by:

$$-\frac{d[M^*]}{dt} = (k_{rad} + k_{nr})[M^*] \quad \textbf{(1.1)}$$

where k_{rad} is the radiative rate constant and k_{nr} is the non-radiative rate constant which is defined as the sum of the rate constants of the non-radiative processes. Letting $[M^*]$ be the time-dependent concentration of the excited-state species and $[M^*]_0$ to be the concentration of excited species at time, $t = 0$ directly after the excitation pulse, integration of **Eqn. 1.1** gives:

$$[M^*] = [M^*]_0 \exp\left(-\frac{t}{\tau_{obs}}\right) \quad \textbf{(1.2)}$$

where τ_{obs} is the lifetime of the excited state S_1, which is given by:

$$\tau_{obs} = \frac{1}{k_{rad} + k_{nr}} \quad \textbf{(1.3)}$$

The photoluminescence quantum yield is the fraction of the number of photons emitted to the number absorbed.[35] As the excited state can be deactivated both radiatively and non-radiatively the emission quantum yield (PLQY), Φ_{PL}, is given by:

$$\Phi_{PL} = \frac{k_{rad}}{k_{rad} + k_{nr}} = \tau_{obs} k_{rad} \quad \textbf{(1.4)}$$

1.3.7 Quenching of Photoluminescence

Any process which decreases the intrinsic photoluminescence intensity of a species is described as quenching. The deactivation pathways discussed in **Section 1.1.1.4** are intrinsic to the excited molecule. However, for the vast majority of quenching processes, a second species, the *quencher*, may also bring about deactivation of this excited state, competing with the intrinsic radiative and non-radiative processes. Thus, the photoluminescence characteristics; emission intensity, excited-state lifetime or emission quantum yield, may be affected as a result of such competition. For such bimolecular processes there are two possible modes of quenching; static and dynamic; the mechanism behind each of these will be discussed in more detail in **Section 3.3.2.1**.

1.3.7.1 Energy Transfer

Fluorescence quenching is an umbrella term used to describe a decrease in fluorescence intensity which can be brought about through a variety of interactions between a donor (*D*) and an acceptor (*A*). One of the possible mechanisms for quenching is energy transfer. Excitation energy may be transferred radiatively or non-radiatively. Radiative energy transfer describes the emission of a photon by *D* which is subsequently absorbed by *A*. This form of transfer does not require electronic coupling between *D* and *A*, but depends on the spectral overlap and the concentration. In contrast, non-radiative transfer processes require both electronic coupling between *D* and *A* and an overlap between the emission spectrum of *D* and the absorption spectrum of *A*.

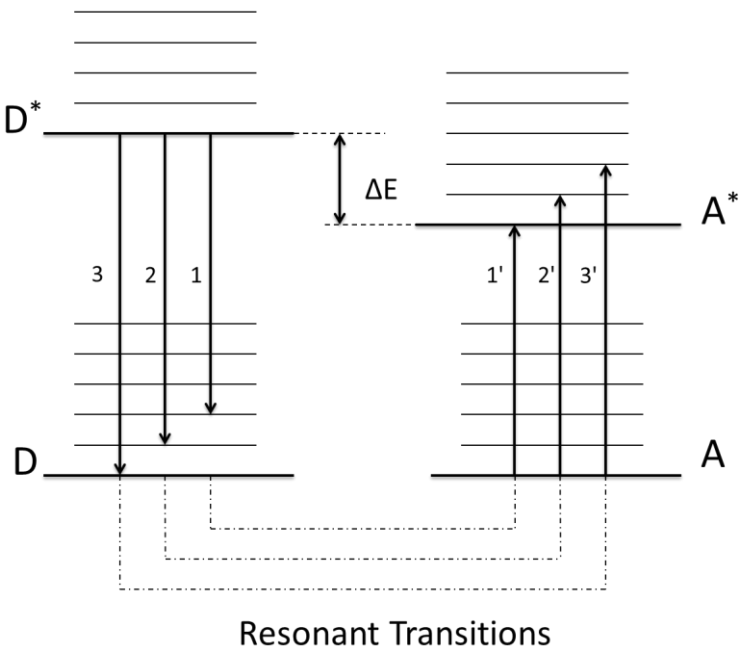

Figure 1.9. Schematic representation of the energy levels and coupled transitions involved in resonance energy transfer.

There are two related mechanisms of non-radiative energy transfer. Förster resonance energy transfer (FRET) is a long range dipole-dipole interaction in which the initially excited

electron on *D* returns to the ground state orbital on *D*, while simultaneously an electron on *A* is promoted to the excited state.[36] FRET may occur when several vibronic transitions in *D* have practically the same energy as the corresponding transitions in *A*. These transitions are coupled and are said to be in resonance (**Fig. 1.9**). As FRET is a Coulombic interaction it operates over a reasonable distance (~100 Å)[36] and does not require direct contact between *D* and *A*. This is in contrast to the different but related mechanism of Dexter energy transfer. This is a short range exchange reaction in which *D* and *A* exchange an electron between either their singlet or triplet state. As it requires overlap of molecular orbitals Dexter exchange requires intimate contact of *D* and *A* and occurs over distances <10 Å.[36] A comparison of the mechanism and requirements for each of these energy exchange processes is shown in **Fig. 1.10**.

(a)

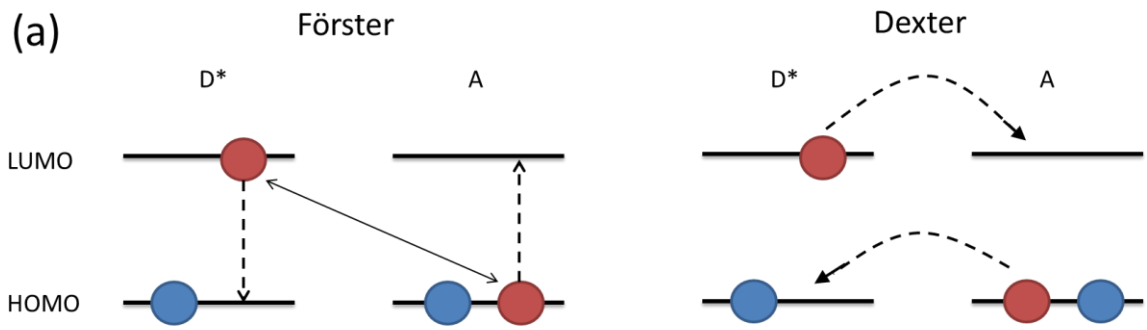

(b)

	Förster	Dexter
Spectral overlap	Yes	Yes
Range	<100 Å	<10 Å
Possible excited states	Singlet	Singlet or triplet
Orbital overlap	No	Yes
Distance dependence	r^{-6}	e^{-r}

Figure 1.10. (**a**) Schematic representation of Förster and Dexter energy transfer. (**b**) Table outlining some of the requirements and properties of each mechanism. *r* is the distance between the *D* and *A*.

Excitation energy transfer involving CPs is preferred by Förster-type mechanism.[37, 38] Based on both classical and quantum mechanical considerations, Förster derived an expression for the rate of energy transfer through long range dipole-dipole interactions:

$$E = \frac{R_0^6}{R_0^6 + r^6} \qquad \textbf{(1.5)}$$

where E is the efficiency of the energy transfer, r is the distance between D and A and R_0 is the Förster distance, the distance at which the energy transfer efficiency is 50%. R_0 may be determined from:

$$R_0^6 = \frac{9000(ln10)\kappa^2 \Phi_D J_{DA}}{128\pi^5 n^4 N_A} \quad (\mathbf{1.6})$$

where Φ_D is the photoluminescence quantum yield of the donor, J_{DA} is the spectral overlap integral, n is the refractive index of the medium and κ is the orientation factor describing the relative orientation of the transition dipoles of the donor and acceptor. For randomly orientated dipoles κ can be taken as 2/3.[36, 37] The spectral overlap integral, J_{DA}, is given by:

$$J_{DA}(\lambda) = \int_0^\infty F_D(\lambda)\varepsilon_A(\lambda)\lambda^4 d\lambda \quad (\mathbf{1.7})$$

where F_D is the intensity of the donor emission spectrum at wavelength λ to $\lambda+\Delta\lambda$, with the total intensity normalised to unity and ε_A is the molar absorption coefficient at wavelength λ.

As FRET is dependent on factors such as spectral overlap and distance between *D* and *A* it is often used as a highly sensitive reporter for distances between fluorophores, particularly in biological systems.[39] The use of FRET as a basis for solution-based sensing systems will be further discussed in **Section 1.6.1**.

1.4 Incorporation of CPs within Host Matrices

Due to the excellent optoelectronic properties and the possibility to cast from solution, CPs were quickly realised as active components for light-emitting diodes[11, 13] and photovoltaic devices.[4, 5] However, the lifetime of any solid-state CP-based device is limited by the photo- and thermal instability of the CP. Encapsulation of CPs within an inorganic host material has been shown to enhance environmental stability[40] and provides an elegant route to indirectly manipulate the conformation and orientation of the polymer within the active layer.[41-43] Device performance depends critically on the morphology of the film in which the polymer is cast.[44] Thus, the ability to control the CP morphology is an important step towards the logical optimisation of CP-based devices.[41]

A variety of incorporation methods and host species have been reported throughout the literature. These include *in situ* polymerisation of monomer units tethered to an inorganic matrix,[45] as well as the incorporation of complete CP species within the channels of preformed nanoporous inorganic structures.[46, 47] Controlled formation of the polyfluorene β-phase has been achieved through cooperative interactions at the phase interface in a three component organic-inorganic system prepared from the CP, a room temperature ionic liquid (RTIL) and silica.[48] The polyfluorene was found to localise in the hydrophobic domains created by π-π stacking between the conjugated portions of the RTIL. Hydrogen bonding between the RTIL and free silanol groups promotes directed orientation of the RTIL species along the silica walls. Similarly, the use of a

polyethylene glycol-based, Pluronics^{TM} surfactant has also been shown to direct the placement of poly[2-methoxy-5-(2'-ethylhexyloxy)-1,4-phenylene vinylene (MEH-PPV) in a titania matrix.[49] The presence of the surfactant was found to cause the formation of a cubic mesostructured titania film. Addition of MEH-PPV prior to gelation of the titania precursor led to incorporation of the CP within the surfactant regions within the mesostructured titania. This controlled placement led to an improved photostability when compared to amorphous mixtures lacking the surfactant structure-directing agent. The effect of the nature of the surfactant on the interaction between the active components was further investigated.[50] The length of the hydrophilic segment of the surfactant was found to influence the interfacial interaction. The long hydrophilic chain and moderately hydrophobic segment of Pluronic F127 promoted enhanced mixing at the CP-titania interface (**Fig. 1.11a**). This is in comparison to mesostructured films prepared using the surfactants Pluronic P123 or Brij58, which contain a more extensive hydrophobic segment. Reduced MEH-PPV-titania interactions are seen for these species, due to preferential association of the hydrophobic MEH-PPV with the hydrophobic alkyl segments of the surfactant species (**Fig. 1.11b**). Higher photovoltaic device efficiencies were observed for the Pluronic F127-based devices due to the enhanced contact between the CP guest species and the titania framework which results in efficient electron transfer at the organic-inorganic interface.

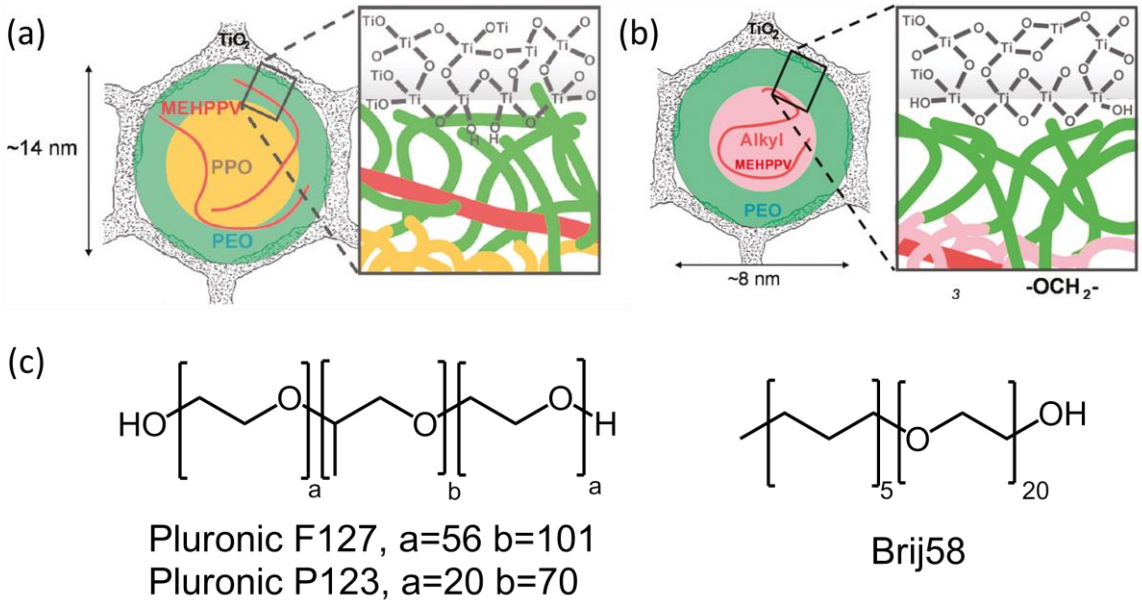

Figure 1.11. (**a**) Schematic representation showing distribution of titania-F127-conjugated polymer species within a single mesochannel: the long polyethylene oxide segments of F127 (green) interact strongly with and are in contact with the titania framework (grey), resulting in close proximity of the MEH-PPV guest species (red) to the titania framework. (**b)** Schematic representation showing distribution of titania-Brij56-conjugated polymer species within a single mesochannel: the short ethylene oxide (green) and alkyl (pink) segments of Brij56 and the MEH-PPV guest species (red) are predominantly excluded from the titania framework (gray).Adapted from ref [50]. (**c**) Structures of surfactants Pluornic F127, Pluronic P123 and Brij58.

Materials such as these, which contain both an organic and an inorganic component, are described as organic-inorganic hybrid materials. One of the most attractive characteristics of

organic-inorganic hybrids is the fact that they possess properties of both the inorganic and organic components.[51] As can be seen from the examples above, the exhibited properties of organic-inorganic hybrids depend on the chemical nature of the components and also on the interaction and interface between the two species.[52] Due to the central role played by this interface, its nature has been used to divide hybrid materials into two different classes.[52-54] *Class I* hybrids are defined as materials in which there are no covalent or iono-covalent bonds between the organic and inorganic species.[52, 54] In these materials the components exchange only weak bonds (van der Waals forces, hydrogen bonding or electrostatic forces).[51, 52, 54] Such materials have recently come to the forefront of research with the development of perovskite-based solar cells,[55, 56] oxygen barrier coatings[57] and drug delivery systems in nanomedicine.[54] In contrast, hybrid materials in which the two phases are totally or partly linked through strong chemical bonds (covalent or iono-covalent bonds) are designated as *Class II* hybrids.[51, 52, 54] Class II materials have provided the backbone for technologies such as white-light emitting materials,[58] sensor platforms[59] and gas capture and storage.[60]

Taking these definitions into account, the vast majority of reports of CP organic-inorganic systems fall into the category of Class I hybrid materials. Although these materials show improved stability of the CP following encapsulation, it has recently been highlighted through incorporation of the two polyfluorene-phenylene CPEs discussed in **Chapter 5** into a purely tetraorthosilicate (TEOS)-based matrix, that the prevention of nanoscale phase separation remains a challenge in Class I hybrids.[61] Thus, we propose the use of a Class II organic-inorganic hybrid host for CPs as such materials should show improved chemical compatibility with the CP dopant compared with a purely inorganic matrix, thereby minimising the risk of phase separation.

1.5 Di-ureasils

The development of organic-inorganic hybrid materials was greatly advanced through the use of soft chemical synthetic methods such as sol-gel processing.[62] This one pot synthesis allows for mild processing conditions ensuring the survival of low weight organic components.[52, 62] This technique is based on the polymerisation of metal alkoxide species $M(OR)_n$.[52] The rich chemistry of silicone has been exploited to synthesise stable, low cost and efficient $M(OR)_n$.-based white light photoluminescent organic-inorganic hybrids lacking metal activator ions.[63] Siloxane based materials also possess attractive optical features such as high laser efficiency and photostability,[64] electroluminescence[64, 65] and nonlinear optical properties.[66] Of particular interest in this thesis are a class of siloxane-based organic-inorganic hybrids called *di-ureasils*. Di-ureasils are composed of poly(ethylene oxide) (PEO)/poly(propylene oxide) (PPO) block copolymer chains chemically grafted to a siliceous network through two urea linkages,[67-69] giving rise to the di-ureasil nomenclature. It is possible to prepare a variety of di-ureasil species through alteration of the organic linker species with syntheses containing block copolymer with molecular weights of 600,

900, 2000, 4000 g mol^{-1} previously reported.[68, 70, 71] Di-ureasils are prepared through hydrolysis and subsequent condensation of a precursor solution designated d-UPTES, the structure of which is shown in **Fig. 1.12** for the 600 g mol^{-1} block copolymer.

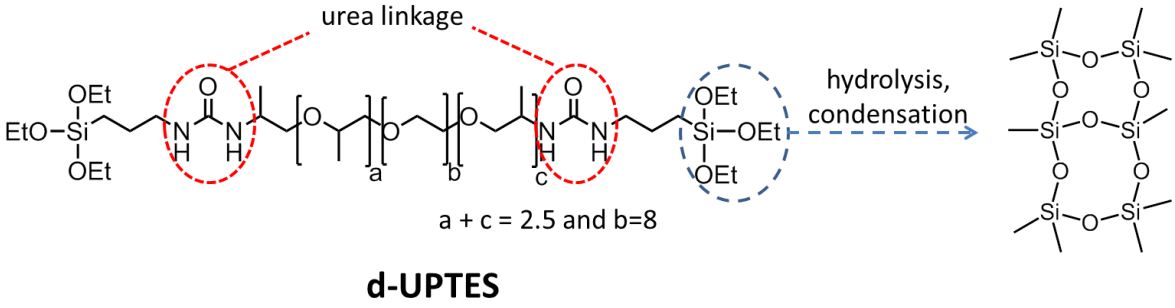

Figure 1.12. Structure of the d-UPTES precursor solution. Red circles highlight the two urea linkages that give rise to the di-ureasil name. The expanded structure on the far right represents the siliceous network formed following hydrolysis and condensation of the Si moieties at either end of the d-UPTES structure.

Undoped di-ureasils are transparent materials with an elastomeric nature imparted by the flexibility of the PEO/PPO chains. Di-ureasils are also inherently photoluminescent, exhibiting an emission band in the purple-blue spectral region, the maximum of which is dependent on excitation wavelength.[68, 72] Due to their desirable optical properties and ease of processability, di-ureasils have been frequently employed as host materials for a range of dopant species. Incorporation of lithium perchlorate ($LiClO_4$) produces materials with high conductivity that is attributed to the flexibility of the host allowing faster movement of the Li^+ ions.[73] Increasing the flexibility by inclusion of further PPO chains within the organic linker causes the conductivity to almost double.[74] These results suggest the utility of di-ureasils as solid polymer electrolytes, which are currently under investigation in the area of Li-ion batteries in attempts to reduce leakage, eliminate the use of volatile organic liquids and increase mechanical flexibility and thermal stability.[73, 74] Furthermore, addition of methacrylic acid modified zirconium clusters within a di-ureasil host is found to modulate the material's refractive index,[75] while simultaneously inducing a red-shift of the excitation wavelength which moves the hybrid hosts intrinsic emission intensity from the UV (365 nm) to the blue (420 nm). An enhancement in the emission quantum yield is also observed, reaching 9.0% for the zirconium doped di-ureasil.[76]

There are also frequent reports of di-ureasils doped with lanthanide ions with the intention of creating materials with interesting optical properties.[77-80] The incorporation of an Eu-β-diketonate complex within a di-ureasil hybrid has been attempted in an effort to enhance its light emission and photostability properties.[78, 81] It was found that on incorporation of this complex into a di-ureasil host, the carbonyl groups of the urea linkages replaced the ethanol species in the coordination sphere of the Eu^{3+} ion observed in solution causing a dramatic enhancement in the quantum efficiency of the complex in the solid state. This is attributed to the removal the OH oscillator from the coordination sphere of the Eu^{3+} ion. Efficient energy transfer from the di-ureasil host to the

Eu^{3+} metal centre was also observed along with increased photostability of the incorporated complex. A similar rearrangement in the lanthanide coordination sphere of a Tb(III)-(acetylacetonate)$_3$ was also observed on inclusion in a di-ureasil host, with the carbonyl of the host replacing the coordinated water molecules within the complex.[79] The temperature dependence of both an Eu-β-diketonate and Tb-β-diketonate complex has recently been developed for use as a self-referencing thermometer with high temperature sensitivity and spatial resolution.[82] The intensity of the green Tb^{3+} luminescence was found to strongly decrease as the temperature increases, while the intensity of the red Eu^{3+} lines begin to increase at precisely the same temperature at which the Tb^{3+} emission decreases. Thus, temperature may be determined by the relative intensities of the Eu^{3+} and Tb^{3+} emission intensities. The inclusion of these complexes within a di-ureasil host shifts the range of operation of the thermometer to room temperature by increasing the activation energy between the triplet state of the host and the excited state of the lanthanide. This makes these materials sufficiently sensitive to be used in the physiological temperature range. Addition of siloxane-based hybrid magnetic nanoclusters allows for the same temperature dependence of the lanthanide complexes (**Fig. 1.13a**) while increasing the sensitivity to 300-350 K (**Fig. 1.13b**).[83]

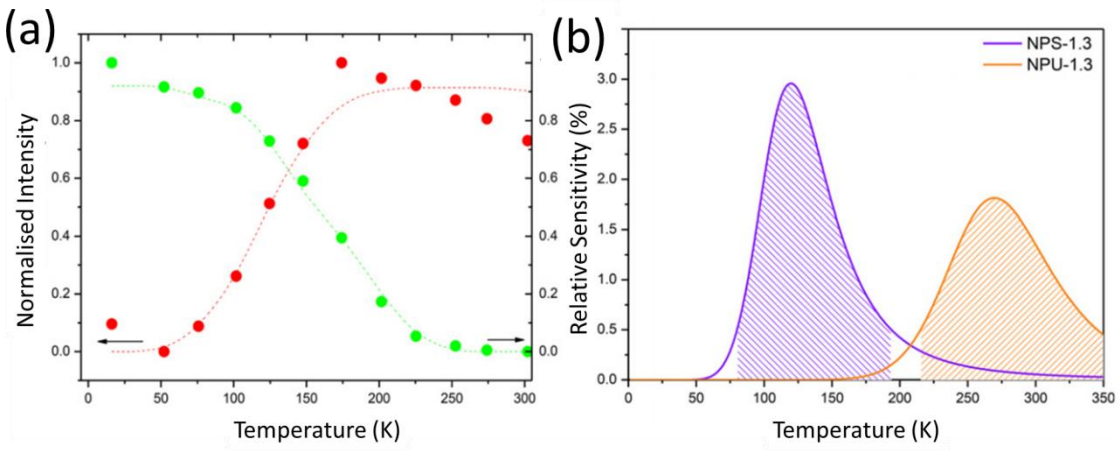

Figure 1.13. (**a**) Integrated intensity of the $^5D_0 \rightarrow {}^7F_2$ (605-635 nm, red circles) and $^5D_4 \rightarrow {}^7F_5$ (535-560 nm, green circles) transitions as a function of temperature for the magnetic nanoclusters co-doped with Eu-β-diketonate and Tb-β-diketonate containing complex discussed in the text. Dashed lines are solely to guide the eye. (**b**) Relative sensitivity computed from experimental data for the pure Eu-β-diketonate and Tb-β-diketonate containing nanoparticles (NPS-1.3) and the di-ureasil coating incorporating the magnetic nanoclusters co-doped with Eu-β-diketonate and Tb-β-diketonate complexes (NPU-1.3) The shadowed areas correspond to the temperatures where the relative sensitivity is greater than 0.5%. Adapted from ref [83].

1.6 Applications

1.6.1 Solution Phase Sensing

As mentioned previously, there are a wide variety of methods available to alter the optical properties of CPs in solution, giving them the ability to translate the presence of an analyte into an

easily measurable optical or electrochemical response. It is no surprise then that this has led to the rational design of a multitude of sensory systems and transduction mechanisms using conjugated polymers. However, by far the largest driving force for use of CPs as sensory materials is their characteristic amplified fluorescence quenching behaviour.

1.6.1.1 Amplified Quenching - 'Molecular Wire Effect'

The idea of amplified quenching, the so-called 'molecular wire effect' associated with CPs, was first described by Zhou and Swager in 1995.[84] The overlap of π-orbitals and subsequent delocalisation along the backbone of CPs gives rise to a semiconducting band structure within the CP, creating a 'molecular wire' capable of transporting excitons (bound electron-hole pairs). The fact that CPs can be thought of a number of recognition sites 'wired in series' gives rise to amplified quenching in CPs when compared to small molecule receptors. If the exciton migration is rapid with respect to the fluorescence lifetime it is free to move along the polymer backbone until it reaches a repeat unit associated with a quencher species.[85] Thus, a single quencher associated to a single repeat unit may dramatically change the total emission. This concept is shown schematically in **Fig. 1.14**, through comparison of the response of a CP and a single molecule quencher. Following exposure of a CP to a quencher, a large fluorescence quenching response would be observed, however, in the case of non-conjugated receptors, exposure to the same analyte concentration would give rise to a small fraction of quenching. Each analyte is confined to its particular molecule and can only affect one binding site. Therefore, emission is still observed from molecules with no quencher association.

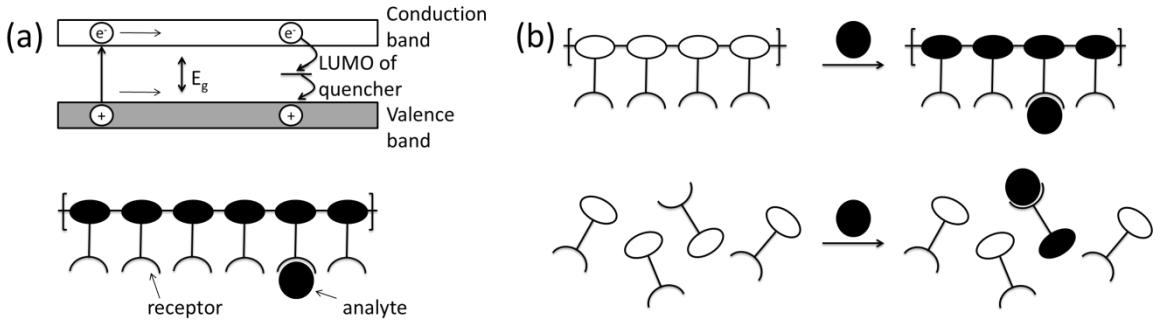

Figure 1.14. (**a**) Schematic band diagram illustrating the mechanism for exciton transport and electron transfer fluorescence quenching of a conjugated polymer upon interaction with an analyte. (**b**) Schematic comparison of a conjugated polymer interacting with a small concentration of quencher giving complete quenching of the polymer chain (top) and individual molecular receptors exposed to the same small concentration of quencher, resulting in partial quenching (bottom). Adapted from [86].

This concept was demonstrated using poly(phenylene-ethynylene) (PPEs) modified with bis(*p*-phenylene)-34-crown-10 groups on each repeat unit.[84, 85] These crown ethers are excellent receptors for methylviologen (MV^{2+}) which is an excellent electron acceptor. When compared to the single receptor model species, the polymers showed considerably larger quenching effects with an increase in the Stern-Volmer constant by a factor of 65, indicating the quenching response is

amplified in the CPs relative to the monomeric model compound. The magnitude of amplification was found to increase with polymer chain length, suggesting that the effect is related to the ability of the exciton to migrate along the polymer chain. However, increasing the chain length above 130 repeat units no longer gives rise to an increase in quenching efficiency which is attributed to the finite excited state lifetime.[87]

Thanks to their solubility in aqueous solution CPEs are prime candidates for biological applications, with CPE-based sensors reported for proteins,[88] enzymes[89] and small molecules.[90] However, the most highly investigated biological sensor system is that for the detection and sequence characterisation of DNA, due to its application in medical diagnostics, identification of genetic mutations, gene delivery monitoring and specific genomic techniques.[91] One of the more elegant schemes for DNA detection has been reported based on FRET between a cationic polyfluorene-phenylene polyelectrolyte and a chromophore attached to a peptide nucleic acid (PNA).[92] A schematic representation of the mechanism of this platform is shown in **Fig. 1.15**. Consider an initial solution that contains the cationic-conjugated polyelectrolyte (CPE, shown in blue) and a PNA strand (shown in red) labelled with a chromophore dye; fluorescein (C*). The optical properties of the CPE and C* were chosen to favour FRET from the CPE (donor) to C* (acceptor). In this initial solution there are no electrostatic interactions between the CPE and the PNA strand, this results in an average CPE-C* distance too large for effective FRET. After addition of single-stranded DNA (ss-DNA) and following an appropriate annealing protocol, two situations are possible. The first of these corresponds to the addition of a ss-DNA strand (shown in S) which is complementary to the PNA strand, thus causing hybridisation with the PNA. Hybridisation with the ss-DNA, gives rise to the addition of multiple negative charges to the C*-containing species. Electrostatic interactions should cause the formation of a complex between the negatively-charged C*-containing species and the positively charged CPE, causing a decrease in the average CPE-C* distance increasing the possibility for FRET. On the other hand, the second possibility is that the ss-DNA strand is not complementary with the C*-bearing PNA and thus hybridisation does not occur. This brings about electrostatic interactions only between the CPE and DNA and dose not reduce the CPE-C* distance to allow for the occurrence of FRET. Hybridisation between the PNA and ss-DNA is therefore measured by FRET efficiency, or the enhanced C* emission, providing a probe for the presence of specific ss-DNA sequences. Excitation of the CPE was shown to give rise to emission from the fluorescein dye >25 times higher than that obtained by directly exciting the dye, allowing detection at concentrations of 10 pM with a standard fluorimeter.

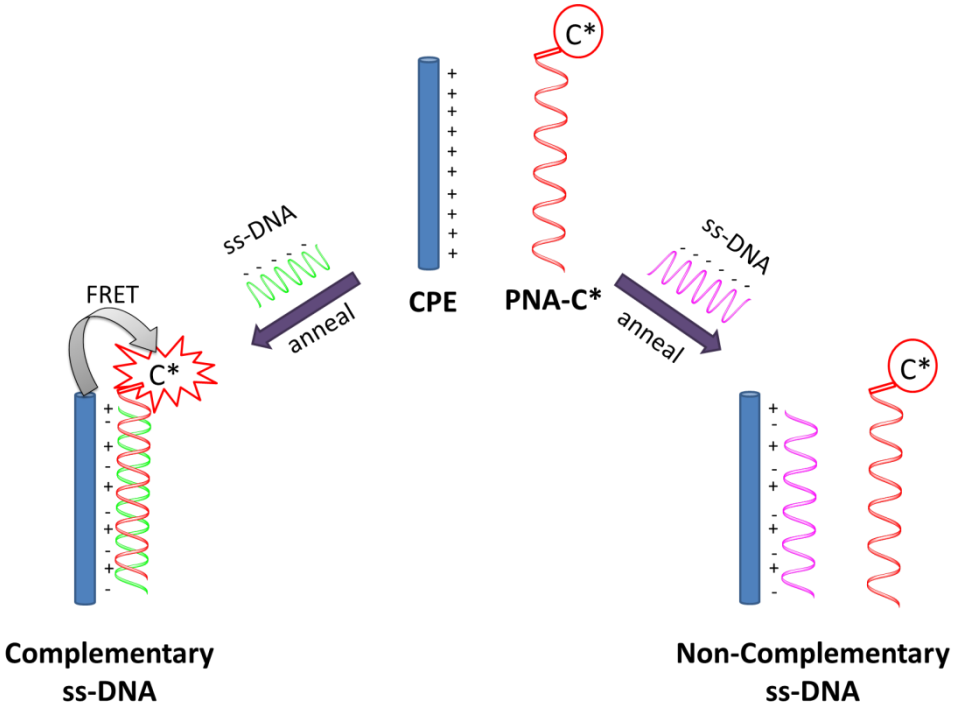

Figure 1.15. Schematic representation for the use of a water-soluble CPE (blue) with a specific PNA-C* (red) optical reporter probe to detect a complementary ss-DNA sequence (green) in comparison to a non-complementary strand (magenta). Adapted from ref [92].

Although PNA is widely used in DNA detection, the synthesis and purification of ss-DNA is far more straightforward. Thus, this scheme has been extended to use ss-DNA-C* as the optical probe over PNA-C*.[93] This modified scheme is based on the idea that the electrostatic interactions between double stranded DNA (ds-DNA) and the CPE would be stronger than that of a ss-DNA. Should a complementary strand be added to a solution of ss-DNA-C*, hybridisation should occur. The higher charge density of the ds-DNA should result in a stronger DNA-CPE electrostatic interaction, relative to any ss-DNA-CPE interactions that may occur if the two ss-DNA strands present are non-complementary. Furthermore, the non-hybridised strand will interfere with the ssDNA-C*/CPE interactions. Substituting a number of the fluorene-phenylene units with a benzothiadiazole derivative has been shown to report accurately on the concentration of ss- and ds-DNA.[94] Increasing the concentration of DNA brings about an increase in CPE aggregation increasing the FRET efficiency between the blue-emitting fluorene-phenylene units to the green-emitting benzothiadiazole units. Measurement of the ratio of the blue emission intensity to the green emission provides a method to accurately determine the concentration of DNA present.

Due to the electron-rich nature of conjugated polymers, there is a wealth of examples of CP/CPE-based sensing systems developed with polymers with a low electron affinity (electron-rich) for the detection of electron-accepting analytes. However, while the number of reports is drastically reduced, it is possible to turn this axiom on its head and produce electron deficient polymers that show a sensory response to electron-rich analytes.[95] This was recently demonstrated following the incorporation of a 3-coordinate boron into the 9-position of a polyfluorene-based

CP.[96] The empty p-orbital on boron has the ability to influence the electronic nature of the polymer, lowering the band gap, while simultaneously maintaining conjugation along the backbone. This causes the optical band gap to decrease by ~0.6 eV when compared to conventional polyfluorenes, while the addition of a vinylene group to the repeat unit causes a further reduction 0.16 eV. This drop in band gap gives rise to a shift in the emission spectrum from that of a typically blue-emitting polyfluorene to two yellow-emitting species, with an emission band in the range 500-700 nm. These polymers showed the ability to detect electron-rich analytes both in solution (fluoride ions) and in the vapour phase (ammonia). Interaction of the polymers with these species caused the disappearance of the emission band at 500-700 nm with the subsequent growth of a band in the region 400-550 nm, mimicking the blue-emission of conventional polyfluorenes. This change in emission colour is highlighted in **Fig. 1.16**. This shift was rationalised by the binding of the electron rich analyte to the vacant p-orbital of the boron atom. This reduces the influence of the p-orbital on the electronic properties of the CP which caused the initial lowering of the band gap. Thus the band gap is once again increased on binding of the electron-rich analyte causing the emission to shift back towards the blue. The optical response is also completely reversible, as following the removal of the ammonia source and exposed to ambient conditions the fluorescence spectrum returned to its original state within 5 min. This suggests that such electron-deficient polymers possess great potential to be used as sensors for electron-rich gases.

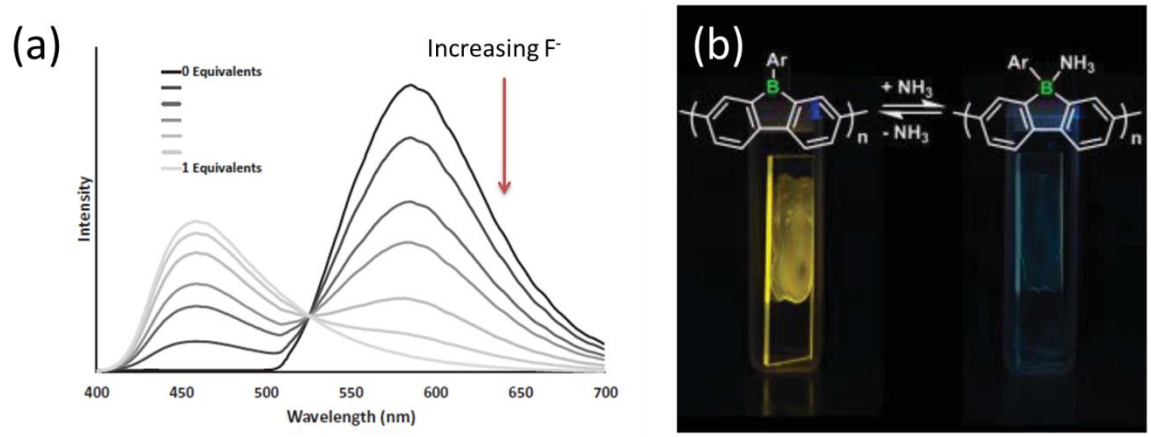

Figure 1.16. (**a**) Fluorescence spectra of boron doped polyfluorene polymer upon titration with Bu_4NF as a source of F^- up to 1 equivalents. (b) Photograph of thin films of the boron doped polyfluorene polymer irradiated with a UV-lamp and exposed to air (left) and NH_3 vapour (right), the structures shown are that of the polymer (left) and the polymer-analyte adduct (right). Adapted from ref [96]

As a result of the prolific history and ever growing number of CP and CPE structures continually being reported, each with variable optoelectronic properties, there is a vast library of CP-based optical sensing platforms throughout the literature designed to selectively report on the presence of specific analytes. The work discussed here is a small fraction of the reported endeavours and were highlighted as representative examples of the varied and interesting sensing mechanisms available. More extensive examples have been covered in recent authoritative reviews.[6, 39, 87, 97]

1.6.2 Light-Emitting Materials

Light-emitting diodes (LEDs) are ubiquitous in our everyday lives, thanks to the work of Akasaki, Amano and Nakamura who demonstrated the first operation of blue-emitting LEDs (for which they won the Nobel Prize in 2014). LED technology has since moved on from the first reported device structure based on inorganic semiconductors to devices based on organic components (OLEDs). OLEDs offer a number of advantages over their predecessors such as superior brightness and colour purity, considerably lower drive voltages along with increased viewing angles.[98] CPs have gained popularity as the active component of OLEDs as they may be processed through solution based techniques such as spin-coating or ink-jet printing, combining advantages such as ease of fabrication and low production cost, particularly for large area devices. This is compared to small molecular organic semiconductors which are usually processed by high vacuum vapour deposition.[99] Thus, the following discussion is focused on conjugated polymer-based devices (PLEDs).

1.6.2.1 Device Structure of PLEDs

PLEDs are based on a multilayer device structure, a typical example of which is shown in **Fig. 1.17**. The initial reports of PLEDs proposed a structure containing simply an emissive layer sandwiched between two electrodes.[1] Modern PLED devices are typically composed of a transparent conducting oxide, indium tin oxide (ITO), coated onto a glass substrate. The electroactive layers are then cast on top of the ITO anode. Finally the device is capped by a low work function metal cathode. Ba, Al or Ca are typically used for this purpose.[100] Following application of an external voltage, under forward bias, electrons are injected to the device from the cathode and holes are injected (electrons extracted) from the anode. These charge carriers migrate through the device under the applied electric field. Electrons and holes recombine in the emissive layer to form singlet and triplet excitons. Subsequent relaxation to the ground state may occur, resulting in the emission of light. For a single layer device it is difficult to balance the injection and transport of the two charge carriers in a single-material matrix.[14] Any imbalance results in a relative increase in drive voltage and the subsequent loss of luminance efficiency. Thus, the incorporation of a hole-transport layer (HTL) and an electron-transport layer (ELT) into the structure, next to the anode and cathode, respectively, has been shown to result in an increase in the device efficiency.[101]

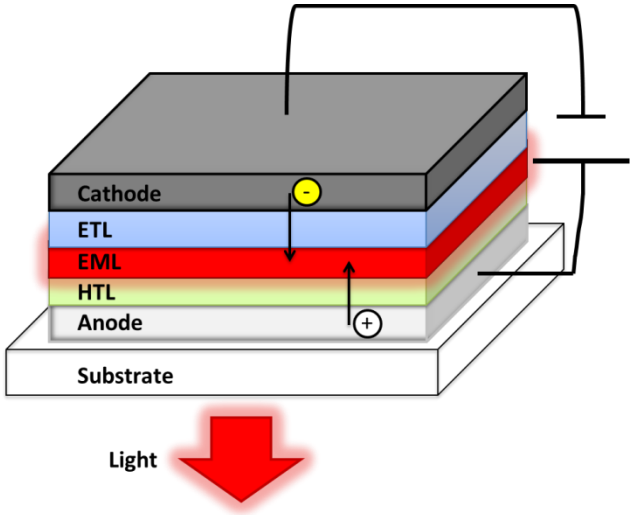

Figure 1.17. Basic PLED structure showing injection of electrons at the cathode into the electron transport layer (ETL) and injection of holes at the anode into the hole transport layer (HTL), electrons and holes may then recombine in the emissive layer (EML) with the subsequent emission of a photon.

As the electronic properties of most CPs are typically hole-dominated and characterised by lower electron mobility, achieving efficient electron injection from the cathode is essential for the optimisation of PLEDs.[102] Thus, introduction of an interlayer with a dipole moment such as that demonstrated using CPEs has been shown to be an effective way to facilitate electron injection even from high work-function metals.[102, 103] The rationale behind the incorporation of each of these extra layers is to modify the energy levels controlling electron and hole transport. However, while optimisation of the composition of each of these layers shows continuing improvement of the device efficiency, it still does not overcome any of the issues that are inherent to the polymer emissive layer itself.

There are two major drawbacks to the use of CP layers within LED devices: (i) the need for multiple layers each of which can damage the previously deposited layer and (ii) the poor stability of the polymers themselves. The very solubility that gives rise to the low-cost, solution processable nature of CP devices can also be a large downfall. The performance of CP-based devices is inherently linked to the morphology of each CP layer.[44, 104] However, upon deposition of a new layer, it is possible that this new layer may cause the previous layer to dissolve owing to the similar solubilities of both layers in the organic solvent.[105] Thus, a number of approaches have been suggested to prevent modification of the morphology of initially cast layers by those deposited subsequently. Some of these include the development of materials which are soluble in orthogonal solvents for each of the subsequent layers.[106] As a method to prevent this, it is possible to render a layer insoluble after processing through means such as ‘hard-baking’ or cross-linking reactions.[105] However, each of these introduces a further level of complexity into the device fabrication process. To circumvent these challenges, PLED devices have been produced by blending either a range of different polymers or a single polymer host with a dopant molecular

dye.[102] However, these systems suffer from intrinsic phase separation[2] and as such, there are increasing reports of CPs in which several chromophores emitting in either the primary or complementary spectral regions are incorporated within a single polymer chain to produce single layer devices.[107] Nonetheless, these polymers present a significant synthetic challenge and do not overcome the inherent instability possessed by CP-based devices.

The second major drawback of the use of CPs in LEDs is the fact that they do not possess high thermal and photochemical stability, severely reducing the operational lifetime of the device. The mechanism by which these polymers undergo degradation involves hydrogen abstraction by a free radical ($r^{\bullet}$), itself formed from the photonic excitation of a chromophoric unit.[108] In the propagation step, the polymer radical ($P^{\bullet}$) reacts with atmospheric oxygen to give a peroxy radical ($PO_2^{\bullet}$) which in turn abstracts another labile hydrogen to yield a hydroperoxide. The latter thermally or photochemically decompose to produce macroalkoxy $PO^{\bullet}$ and hydroxyl radicals.[108] Irradiation in the absence of oxygen reduces any observed photodegradation by a factor of 1000.[109] As such, encapsulation of CPs within an inorganic host material has been shown to enhance environmental stability[40] and also provides an elegant route to indirectly manipulate the conformation and orientation of the polymer within the active layer.[41, 42, 48] Recently the incorporation of a polyfluorene based CP within the interlayer space of inorganic, layered dichalcogenide materials (MoS_2 and SnS_2) has been shown to improve the CP stability which retained its blue emission in ambient conditions for over two years as well as after heating at 100 ^{o}C for 7 h in air and under device-operating conditions.[110] Similar reports have also been described for the same polymer in layered silicate materials.[111] Dovgolevsky *et al*. have shown that the orientation of CPs within a silica matrix can be controlled through the use of surfactant templating.[112] The successful preparation of red-, green- and blue-emitting PLEDs was possible only on formation of the 2D-hexagonal and 3D-cubic phases within the silica and not in the case of the lamellar phase. This is attributed to the insulating nature of silica and the lamellar phase preventing a continuous conducting CP network between the electrodes. In each of these examples the inorganic agent has served primarily to isolate or aggregate the polymer chains and makes no contribution to the functional properties of the material. This represents a missed opportunity, as one of the inherent curiosities of organic-inorganic hybrid materials is the potential of emergent or enhanced properties deriving from the interaction between the two components.

1.7 Aims

This thesis examines the optical properties of a number of conjugated polymers in differing local environments to examine their utility in the development of optical sensing platforms and light-emitting materials.

The first portion of this thesis aims to exploit the optical properties of two different conjugated polymers for the purpose of devising new optical sensing platforms. The first of these

CPs is a polyfluorene-polythiophene based diblock copolyelectrolyte. In **Chapter 3** the observed optical properties of this CP are mapped in the presence of an increasing concentration of a number of biologically-important anions. The mechanism behind the observed response is then discussed in an effort to elucidate the interactions between the CP and the anions. Following on from this the threading of macrocycles of varying dimensions onto a poly(pyridyl vinylene), electron-poor polymer is then investigated in **Chapter 4**. It is believed that the electron-poor nature of this polymer coupled with the pockets of increasing volume created by the threaded macrocycles will allow for size-exclusion based sensing of electron-rich biological species such as indole.

However, as outlined above, the lifetime of any solid-state CP-based device is limited by issues inherent to the nature of the CP. Thus, we believe that incorporation of CPs within a di-ureasil matrix may address some of these issues. Firstly, an organic-inorganic hybrid should show improved chemical compatibility with the CP compared with a purely inorganic matrix, thereby minimising the risk of phase separation. Secondly, the di-ureasil structure presents multiple chemical groups for physical interaction with the CP *via* hydrogen bonding or dipole-dipole interaction. Thirdly, the di-ureasils themselves are intrinsically photoluminescent; as such they should function as active hosts and contribute to the optoelectronic properties of the hybrid material. Finally, as the di-ureasils combine the inherent flexibility of the PEO/PPO component with the thermal and mechanical stability of the organosilica, they are prime candidates as materials for flexible display technologies.

In **Chapter 5** two different methods of incorporation of two polyfluorene-phenyl CPEs into a di-ureasil host are described. The resulting optical properties are demonstrated and the mechanism behind CPE-di-ureasil interaction is discussed. Both CPEs discussed in **Chapter 5** are blue-emitting materials with overlapping spectral properties to that of the di-ureasil host. In **Chapter 6** two red-emitting CPs are incorporated into the di-ureasil in an attempt to extend the emission profile from the blue spectral region further across the visible spectrum. The possibility of energy transfer between the CP and the host will be investigated. **Chapter 7** discusses two unique methods of incorporation of a polyfluorene CP within the di-ureasil structure. As the properties of organic-inorganic hybrids are reported to depend highly the interface between the organic and inorganic component, the first incorporation method yields materials in which CP is not chemically bound to the di-ureasil, while for the second the CP is grafted directly within the siliceous network. Finally, **Chapter 8** looks to summarise some brief conclusions and outlines the future prospects for further studies arising from this work

1.8 References

1. J. H. Burroughes, D. D. C. Bradley, A. R. Brown, R. N. Marks, K. Mackay, R. H. Friend, P. L. Burns and A. B. Holmes, *Nature*, 1990, **347**, 539-541.
2. M. C. Gather, A. Kohnen and K. Meerholz, *Adv. Mater.*, 2011, **23**, 233-248.
3. A. J. Heeger, *Chem. Soc. Rev.*, 2010, **39**, 2354-2371.

4. L. Huo, T. Liu, X. Sun, Y. Cai, A. J. Heeger and Y. Sun, *Adv. Mater.*, 2015, **27**, 2938-2944.
5. J.-S. Wu, S. W. Cheng, Y.-J. Cheng and C.-S. Hsu, *Chem. Soc. Rev.*, 2015, **44**, 1113-1154.
6. H. N. Kim, Z. Guo, W. Zhu, J. Yoon and H. Tian, *Chem. Soc. Rev.*, 2011, **40**, 79-93.
7. S. Rochat and T. M. Swager, *Angew. Chem. Int. Ed.*, 2014, **53**, 9792-9796.
8. C. Wu and D. T. Chiu, *Angew. Chem. Int. Ed.*, 2013, **52**, 3086-3109.
9. C. Liu, J. Jang, Y. Xu, H.-J. Kim, D. Khim, W.-T. Park, Y.-Y. Noh and J.-J. Kim, *Adv. Funct. Mater.*, 2015, **25**, 758-767.
10. B. Nketia-Yawson, H. S. Lee, D. Seo, Y. Yoon, W. T. Park, K. Kwak, H. J. Son, B. Kim and Y. Y. Noh, *Adv. Mater.*, 2015, **27**, 3045-3052.
11. C. Duan, K. Zhang, X. Guan, C. Zhong, H. Xie, F. Huang, J. Chen, J. Peng and Y. Cao, *Chem. Sci.*, 2013, **4**, 1298-1307.
12. L. Ying, C. L. Ho, H. Wu, Y. Cao and W. Y. Wong, *Adv. Mater.*, 2014, **26**, 2459-2473.
13. P. Zalar, Z. B. Henson, G. C. Welch, G. C. Bazan and T. Q. Nguyen, *Angew. Chem. Int. Ed.* 2012, **51**, 7495-7498.
14. M. T. Bernius, M. Inbasekaran, J. O'Brien and W. Wu, *Advanced materials*, 2000, **12**, 1737-1750.
15. A. J. Heeger, *Angew. Chem. Int. Ed.*, 2001, **40**, 2591-2611.
16. A. L. Dyer, E. J. Thompson and J. R. Reynolds, *ACS Appl Mater. Interfaces*, 2011, **3**, 1787-1795.
17. C. M. Amb, A. L. Dyer and J. R. Reynolds, *Chem. Mater.*, 2011, **23**, 397-415.
18. J. A. Kerszulis, K. E. Johnson, M. Kuepfert, D. Khoshabo, A. L. Dyerac and J. R. Reynolds, *J. Mater. Chem. C*, 2015, **3**, 3211-3218.
19. A. O. Patil, Y. Ikenoue, F. Wudl and A. J. Heeger, *J. Am. Chem. Soc.*, 1987, **109**, 1858-1859.
20. H. Jiang, P. Taranekar, J. R. Reynolds and K. S. Schanze, *Angew. Chem. Int. Ed.*, 2009, **48**, 4300-4316.
21. X. Zhao, M. R. Pinto, L. M. Hardison, J. Mwaura, J. Muller, H. Jiang, D. Witker, V. D. Kleiman, J. R. Reynolds and K. S. Schanze, *Macromoleules*, 2006, **39**, 6355-6366.
22. T. Q. Nguyen, I. B. Martini, J. Liu and B. J. Schwartz, *J. Phys. Chem. B*, 2000, **104**, 237-255.
23. Z. Xu, H. Tsai, H. Wang and M. Cotlet, *J. Phys. Chem. B*, 2010, **114**, 11746-11752.
24. C. Tan, E. Atas, J. G. Muller, M. R. Pinto, V. D. Kleiman and K. S. Schanze, *J. Am. Chem. Soc.*, 2004, **126**, 13685-13694.
25. C. Tan, M. R. Pinto and K. S. Schanze, *Chem. Commun.*, 2002, 446-447.
26. M. P. Stevens, in *Polymer Chemistry An Introduction*, Oxford University Press, 1999, pp. 16-25.
27. M. C. Orilall and U. Wiesner, *Chem. Soc. Rev.*, 2011, **40**, 520-525.
28. A. Gutacker, N. Koenen, U. Scherf, S. Adamczyk, J. Pina, S. M. Fonseca, A. J. Valente, R. C. Evans, J. S. de Melo, H. D. Burrows and M. Knaapila, *Polymer*, 2010, **51**, 1898-1903.
29. M. Knaapila, R. C. Evans, A. Gutacker, V. M. Garamus, M. Torkkeli, S. Adamczyk, M. Forster, U. Scherf and H. D. Burrows, *Langmuir*, 2010, **26**, 5056–5066.
30. U. Scherf, A. Gutacker and N. Koenen, *Acc. Chem. Res.*, 2008, **41**, 1086-1097.
31. A. Thomas, J. E. Houston, N. Van den Brande, J. De Winter, M. Chevrier, R. K. Heenan, A. E. Terry, S. Richeter, A. Mehdi, B. Van Mele, P. Dubois, R. Lazzaroni, P. Gerbaux, R. C. Evans and S. Clément, *Polym. Chem.*, 2014, **5**, 3352-3362.
32. B. Valeur, in *Molecular Fluorescence: Principles and Applications*, Wiley-VCH, 2001, pp. 20-33.
33. P. Douglas, H. D. Burrows and R. C. Evans, in *Applied Photochemistry*, Springer, 2013, p. 56.
34. B. Valeur, in *Molecular Fluorescence: Principles and Applications*, Wiley-VCH, 2001, pp. 34-70.
35. J. R. lakowicz, in *Principles of Fluorescence Spectroscopy*, Springer, 2006, pp. 331-351.
36. B. Valeur, in *Molecular Fluorescence: Principles and Applications*, Wiley-VCH, 2001, pp. 72-123.
37. H. Y. Byun, I. J. Chung, H. K. Shim and C. Y. Kim, *Macromoleules*, 2004, **37**, 6945-6953.
38. F. Kong, Y. M. Sun and R. K. Yuan, *Nanotechnology*, 2007, **18**, 265707.

39. X. Feng, L. Liu, S. Wang and D. Zhu, *Chem. Soc. Rev.*, 2010, **39**, 2411–2419.
40. M. Alvaro, A. Corma, B. Ferrer, M. S. Galletero, H. Garcia and E. Peris, *Chem. Mater.*, 2004, **16**, 2142-2147.
41. R. C. Evans, *J. Mater. Chem. C*, 2013, **1**, 4190.
42. T. Q. Nguyen, J. Wu, V. Doan, B. J. Schwartz and S. H. Tolbert, *Science*, 2000, **288**, 652-656.
43. J. Wu, A. F. Gross and S. H. Tolbert, *J. Phys. Chem. B*, 1999, **103**, 2374-2384.
44. B. H. Hamadani, S. Jung, P. M. Haney, L. J. Richter and N. B. Zhitenev, *Nano lett.*, 2010, **10**, 1611-1617.
45. N. K. Minar, P. Docampo, D. Fattakhova-Rohlfing and T. Bein, *ACS Appl. Mater.Interfaces*, 2015, **7**, 10356-10364.
46. K. M. Coakley, B. S. Srinivasan, J. M. Ziebarth, C. Goh, Y. Liu and M. D. McGhee, *Adv. Funct. Mater.*, 2005, **15**, 1927-1932.
47. Y. Zhang, C. Wang, L. Rothberg and M.-K. Ng, *J. Mater. Chem.*, 2006, **16**, 3721-3725.
48. R. C. Evans and P. C. Marr, *Chem. Commun.*, 2012, **48**, 3742-3744.
49. S. Neyshtadt, M. Kalina and G. L. Frey, *Adv. Mater.*, 2008, **20**, 2541-2546.
50. S. Neyshtadt, J. P. Jahnke, R. J. Messinger, A. Rawal, T. Segal Peretz, D. Huppert, B. F. Chmelka and G. L. Frey, *J. Am. Chem. Soc.*, 2011, **133**, 10119-10133.
51. C. Sanchez, B. Julián, P. Belleville and M. Popall, *J Mater Chem*, 2005, **15**, 3559–3592.
52. C. Sanchez, F. Ribot and B. Lebeau, *J. Mater. Chem.*, 1999, **9**, 35-44.
53. P. Judeinstein and C. Sanchez, *J. Mater. Chem.*, 1996, **9**, 511-525.
54. C. Sanchez, P. Belleville, M. Popall and L. Nicole, *Chem. Soc. Rev.*, 2011, **40**, 696–753.
55. J. Berry, T. Buonassisi, D. A. Egger, G. Hodes, L. Kronik, Y.-L. Loo, I. Lubomirsky, S. R. Marder, Y. Mastai, J. S. Miller, D. B. Mitzi, Y. Paz, A. M. Rappe, I. Riess, B. Rybtchinski, O. Stafsudd, V. Stevanovic, M. F. Toney, D. Zitoun, A. Kahn, D. Ginley and D. Cahen, *Adv. Mater.*, 2015, **27**, 5102-5112.
56. T. Y. Yang, G. Gergori, N. Pellet, M. Gratzel and J. Maier, *Angew. Chem. Int. Ed.*, 2015, **54**, 7905-7910.
57. J. M. Fuentes-Alventosa, L. Introzzi, N. Santo, G. Cerri, A. Brundu and S. Farris, *RSC Adv.*, 2013, **3**, 25086–25096.
58. A. Layek, P. C. Stanish, V. Chirmanov and P. V. Radovanovic, *Chem. Mater.*, 2015, **27**, 1021-1030.
59. D. Wencel, M. Barczak, P. Borowski and C. McDonagh, *J. Mater. Chem.*, 2012, **22**, 11720–11729.
60. P. Silvia, S. M. F. Vilela, J. P. C. Tome and F. A. A. Paz, *Chem. Soc. Rev.*, 2015, **44**, 6774-6803.
61. R. C. Evans, A. G. Macedo, S. Pradhan, U. Scherf, L. D. Carlos and H. D. Burrows, *Adv. Mater.*, 2010, **22**, 3032-3037.
62. C. Sanchez, B. Lebeau, F. Chaput and J.-P. Boilot, *Adv. Mater.*, 2003, **15**, 1969-1994.
63. W. H. Green, *Science*, 1997, **276**, 1826-1828.
64. C. Sanchez and B. Lebeau, *MRS Bull.*, 2001, **26**, 377-387.
65. T. Dantes de Morais, F. Chaput, K. Lahlil and J.-P. Boilot, *Adv. Materials*, 1999, **11**, 107-112.
66. P. Innocenzi and B. Lebeau, *J. Mater. Chem.*, 2005, **15**, 3821-3831.
67. V. d. Z. Bermudez, L. D. Carlos and L. Alcácer, *Chem. Mater.*, 1999, **11**, 569-580.
68. L. D. Carlos, V. d. Z. Bermudez, R. S. A. Ferreira, L. Marques and M. Assunção, *Chem. Mater.*, 1999, **11**, 581-588.
69. L. D. Carlos, R. S. A. Ferreira, V. d. Z. Bermudez and S. J. L. Ribeiro, *Adv. Funct. Mater.*, 2001, **11**, 111-115.
70. B. Orel, *Solid State Ion.*, 2003, **165**, 235-246.
71. E. Stathatos, P. Lianos, B. Orel, A. Surca and R. Jese, *Langmuir*, 2003, **19**, 7587-7591.
72. L. D. Carlos, R. S. A. Ferreira, R. N. Pereira, M. Assunção and V. d. Z. Bermudez, *J. Phys. Chem. B*, 2004, **108**, 14924-14932.
73. D. Saikia, H.-Y. Wu, Y.-C. Pan, C.-C. Liao, C.-F. Chen, G. T. K. Fey and H.-M. Kao, *Electrochim. Acta*, 2009, **54**, 7156–7166.
74. D. Saikia, Y.-H. Chen, Y.-C. Pan, J. Fang, L.-D. Tsai, G. T. K. Fey and H.-M. Kao, *J. Mater. Chem.*, 2011, **21**, 10542-10551.

75. D. C. Oliveira, A. G. Macedo, N. J. O. Silva, C. Molina, R. S. A. Ferreira, P. S. André, K. Dahmouche, V. d. Z. Bermudez, Y. Messaddeq, S. J. L. Ribeiro and L. D. Carlos, *Chem. Mater.*, 2008, **20**, 3696–3705.
76. R. A. S. Ferreira, D. C. Oliveira, L. Q. Maia, C. M. S. Vicente, P. S. André, V. Z. Bermudez, S. J. L. Ribeiro and L. D. Carlos, *Opt. Mater.*, 2010, **32**, 1587-1591.
77. L. Fu, R. A. S. Ferreira, N. J. O. Silva, A. J. Fernandes, P. Ribeiro-Claro, I. S. Gonçalves, V. d. Z. Bermudez and L. D. Carlos, *J. Mater. Chem.*, 2005, **15**, 3117-3125.
78. P. P. Lima, F. A. Almeida Paz, R. A. S. Ferreira, V. de Zea Bermudez and L. D. Carlos, *Chem. Mater.*, 2009, **21**, 5099-5111.
79. P. P. Lima, R. A. S. Ferreira, S. A. Júnior, O. L. Malta and L. D. Carlos, *J. Photochem. Photobiol. A.*, 2009, **201**, 214-221.
80. M. E. Mesquita, S. S. Nobre, M. Fernandes, R. A. S. Ferreira, S. C. G. Santos, M. O. Rodrigues, L. D. Carlos and V. de Zea Bermudez, *J. Photochem. Photobiol. A.*, 2009, **205**, 156-160.
81. P. P. Lima, S. A. Junior, O. L. Malta, L. D. Carlos, R. A. Sá Ferreira, R. Pavithran and M. L. P. Reddy, *Euro. J. Inorg. Chem.*, 2006, **2006**, 3923-3929.
82. C. D. Brites, P. P. Lima, N. J. Silva, A. Millan, V. S. Amaral, F. Palacio and L. D. Carlos, *Adv. Mater.*, 2010, **22**, 4499-4504.
83. C. D. S. Brites, P. P. Lima, N. J. O. Silva, A. Millán, V. S. Amaral, F. Palacio and L. D. Carlos, *J. Lumin.*, 2013, **133**, 230-232.
84. Q. Zhou and T. M. Swagger, *J. Am. Chem. Soc.*, 1995, **117**, 7017-7018.
85. Q. Zhou and T. M. Swager, *J. Am. Chem. Soc.*, 1995, **117**, 12593-12602.
86. T. M. Swager, *Acc. Chem. Res.*, 1998, **31**, 201-207.
87. S. Rochat and T. M. Swager, *ACS Appl. Mater. Interfaces*, 2013, **5**, 4488−4502.
88. J. Wang and B. Liu, *Chem. Commun.*, 2009, **17**, 2284–2286.
89. Y. Liu, K. Ogawa and K. S. Schanze, *Anal. Chem.*, 2008, **80**, 150-158.
90. Y. Wang and B. Liu, *Macromol. Rapid Commun.*, 2009, **30**, 498-503.
91. K. V. Balakin, V. A. Korshun, I. I. Mikhalev, G. V. Maleev, A. D. Malakhov, I. A. Prokhorenko and Y. A. Berlin, *Biosens. Bioelectron.*, 1998, **13**, 771-778.
92. B. S. Gaylord, A. J. Heeger and G. C. Bazan, *Proc. Natl. Acad. Sci.*, 2002, **99**, 10954-10957.
93. B. S. Gaylord, A. J. Heeger and G. C. Bazan, *J. Am. Chem. Soc.*, 2003, **125**, 896-900.
94. J. W. Hong, W. L. Hemme, G. E. Keller, M. T. Rinke and G. C. Bazan, *Adv. Mater.*, 2006, **18**, 878-882.
95. Y. C. Kim, J. E. Whitten and T. M. Swager, *J. Am. Chem. Soc.*, 2005, **127**, 12122-12130.
96. I. A. Adams and P. A. Rupar, *Macromol. Rapid Commun.*, 2015, **36**, 1336−1340.
97. Y. Salinas, R. Martinez-Manez, M. D. Marcos, F. Sancenon, A. M. Costero, M. Parra and S. Gil, *Chem. Soc. Rev.*, 2012, **41**, 1261-1296.
98. J. G. C. Veinot and T. J. Marks, *Acc. Chem. Res.*, 2005, **38**, 632-643.
99. F. Huang, H. Wu and Y. Cao, *Chem. Soc. Rev.*, 2010, **39**, 2500-2521.
100. M. Kuik, G. J. Wetzelaer, H. T. Nicolai, N. I. Craciun, D. M. De Leeuw and P. W. Blom, *Adv. Mater.*, 2014, **26**, 512-531.
101. L. S. Hung and C. H. Chen, *Sci. Eng. R.*, 2002, **39**, 143-222.
102. H. Wu, L. Ying, W. Yang and Y. Cao, *Chem. Soc. Rev.*, 2009, **38**, 3391-3400.
103. C. V. Hoven, A. Garcia, G. C. Bazan and T.-Q. Nguyen, *Adv. Mater.*, 2008, **20**, 3793-3810.
104. G. Li, V. Shrotriya, J. Huang, Y. Yao, T. Moriarty, K. Emery and Y. Yang, *Nat. Mater.*, 2005, **4**, 864-868.
105. R. Trattnig, L. Pevzner, M. Jäger, R. Schlesinger, M. V. Nardi, G. Ligorio, C. Christodoulou, N. Koch, M. Baumgarten, K. Müllen and E. J. W. List, *Adv. Funct. Mater.*, 2013, **23**, 4897-4905.
106. C. Duan, K. Zhang, C. Zhong, F. Huang and Y. Cao, *Chem. Soc. Rev.*, 2013, **42**, 9071-9104.
107. E. Ravindran, S. J. Ananthakrishnan, E. Varathan, V. Subramanian and N. Somanathan, *J. Mater. Chem. C*, 2015, **3**, 4359-4371.
108. S. C. G. Santos, A. Tournebize, D. Begue, H. Peisert, T. Chasse, J.-L. Gardette, S. Therias, A. Rivaton and R. C. Hiorns, *RSC Adv.*, 2014, **4**, 54919–54923.

109. A. Rivaton, A. Tournebize, J. Gaume, P.-O. Bussiere, J.-L. Gardette and S. Therias, *Polym. Int.*, 2014, **63**, 1335–1345.
110. E. Aharon, A. Albo, M. Kalina and G. L. Frey, *Adv. Funct. Mater.*, 2006, **16**, 980-986.
111. J. H. Park, Y. T. Lim, O. O. Park, J. K. Kim, J.-W. Yu and Y. C. Kim, *Adv. Funct. Mater.*, 2004, **14**, 377-382.
112. E. Dovgolevsky, S. Kirmayer, E. Lakin, Y. Yang, C. J. Brinker and G. L. Frey, *J. Mater. Chem.*, 2008, **18**, 423-436.

Chapter Two

Experimental

2.1 Materials

2.1.1 Chemicals

Poly(propylene glycol)-block-poly(ethylene glycol)-block-poly(propylene glycol) *bis* (2-aminopropyl ether) (Jeffamine ED-600), 3-isocyanatopropyltriethoxysilane (ICPTES), ethanol (HPLC grade), hydrochloric acid (37% Puriss), toluene (reagent grade), methanol (analytical grade), potassium bromide (FTIR grade), acetonitrile (HPLC grade), 1,4-dioxane (HPLC grade), potassium chloride (≥99%), tetrabutylammonium hexafluorophosphate (TBAHF) (98%), guanosine triphosphate sodium salt hydrate (≥95%), guanosine diphosphate sodium salt hydrate (≥96%), guanosine monophosphate sodium salt hydrate (≥99%), cytidine triphosphate disodium salt (≥95%) and adenosine triphosphate disodium salt (≥99%) were purchased from Sigma Aldrich and used as received. Tetrahydrofuran (THF) (99.9%) and deuterated THF (99.5 atom% D) were obtained from Fischer Scientific and used as received. Cucurbit-*n*-urils (99+%) were purchased from Strem Chemicals Inc. and used without further purification. Deuterated formic acid was purchased from Cambridge Isotope Laboratories, Inc. and used as received. Water was passed through a Milli-Q purifier before use (resistivity >18 MΩ cm^{-1})

2.1.2 Polymers

Poly[9,9-bis(2-ethylhexyl)fluorene]-*b*-poly[3-(6-triethylammoniumhexyl)thiophene] bromide (**PF2/6-*b*-P3TMAHT**) with a number-averaged molecular weight, M_n, of 28,250 g mol^{-1} (~679 g mol^{-1} (r.u.)), poly[3-(6-triethylammoniumhexyl)thiophene] bromide (**P3TMAHT**), with an M_n of 17,000 g mol^{-1} (~304 g mol^{-1} (r.u.)), poly[9,9-bis(4-sulfonylbutoxyphenyl)fluorene-2,7-diyl-*alt*-1,4-phenylene] (**PBS-PFP**) and poly{9,9-bis[6-(*N*,*N*,*N*-trimethylammonium)hexyl]fluorene-2,7-diyl-*alt*-1,4-phenylene} (**PFP-HTMA**) both with an M_n of 6500 g mol^{-1}(~740 g mol^{-1} (r.u.) for **PBS-PFP** and ~776 g mol^{-1} (r.u.) for **PFP-HTMA**) were a kind gift from Prof. Ullrich Scherf, Bergische Universität Wuppertal, Germany. The M_n were measured by gel permeation chromatography for the uncharged polymer precursors with bromo containing side chains. Direct molecular weight measurement of the charged polymers is not possible due to strong interaction of the conjugated polyelectrolyte with the column.

Poly(*p*-pyridyl vinylene), (**PPyV**) (~103 g mol^{-1} (r.u.)) was a kind gift from Prof. Tim Swager, Massachusetts Institute of Technology (MIT), USA. The M_n, for this polymer was unable to be measured due to the lack of polymer solubility in appropriate GPC solvents but is estimated to be ~8,000-11,000 g mol^{-1} based on the synthesis and characterisation of similar polymers.

4-aminophenyl end-capped poly[9,9-bis(2-ethylhexyl)fluorene-2,7-diyl] (**PF2/6-NH_2**), with an M_n of 16,900 g mol^{-1}(~388 g mol^{-1} (r.u.)) was a kind gift from Prof. Hugh D. Burrows, Universidade de Coimbra, Portugal, and Prof. Ullrich Scherf, Bergische Universität Wuppertal, Germany.

Poly[2-methoxy-5-(2-ethylhexyloxy-1,4-phenylene vinylene)] (**MEH-PPV**), with a weight-averaged molecular weight, M_W of >100,000 g mol^{-1}(~260 g mol^{-1} (r.u.)) was purchased from American Dye Source Inc. and was used as received.

Due to their polydisperse nature, the solution-phase concentrations of the CPs are discussed throughout this thesis in terms of CP repeat unit (r.u.), which is consistent with the conventions used in the literature.

2.2 Instrumentation

2.2.1 Fourier Transform Infrared Spectroscopy (FTIR)

FTIR spectra were measured on a Perkin-Elmer Spectrum 100 FTIR spectrometer at room temperature. FTIR spectra were collected over a range of 4000-650 cm^{-1} by averaging 64 scans at a resolution of 4 cm^{-1}. Solution phase samples were measured using a universal attenuated total reflectance (ATR) sampling accessory. Solid-state samples (~5 mg) were finely ground and mixed with potassium bromide (~175 mg) and pressed into pellets.

2.2.2 Powder X-Ray Diffraction (PXRD)

PXRD patterns were measured on a Siemens D500 diffractometer using Cu K_α radiation (λ = 1.54056 Å). All samples were measured using a [100] silicon substrate to minimise for background scatter. Samples were prepared by lightly grinding the crystalline material, which was then lightly sprinkled onto a thin layer of petroleum jelly on the substrate. All diffraction patterns were measured at room temperature in the 2θ range 2-70° using a 0.02° step size and 14.7 s counting rate.

2.2.3 Solid-State Nuclear Magnetic Resonance (ss-NMR)

Solid-state NMR was measured at the EPSRC National Solid-State NMR Service at Durham University by Dr. David Apperley. Solid-state ^{29}Si and ^{13}C cross polarised (CP) and directly polarised (DP) nuclear magnetic resonance (NMR) spectroscopy were performed at ambient temperature on a Varian VNMRS 400 instrument operating at 79.4435 MHz for ^{29}Si and 100.56 MHz for ^{13}C. Spectra were recorded against an external tetramethyl silane (TMS) standard with magic angle spinning (MAS) at a spinning rate of 4300-5000 Hz. The ^{13}C CP spectra were obtained as single contact experiments with a contact time of 5 ms and recycled delay of 1.0 s (700 repetitions).

2.2.4 Solution Phase Nuclear Magnetic Resonance (NMR)

Solution phase NMR spectroscopy was performed in TCD on a Bruker DPX 400 NMR machine. ^{1}H and ^{13}C spectra were obtained at an operating frequency of 400 and 151 MHz, respectively, and were measured by either Dr. John O'Brien or Dr. Manuel Ruether. Samples were

dissolved in a suitable deuterated solvent identified during sample preparation. Chemical shifts are reported in parts per million (ppm).

Solution phase NMR spectroscopy was performed in MIT on a Bruker Avance-400 NMR spectrometer at an operating frequency of 400 MHz for ^{1}H spectra. Samples were measured with the assistance of Dr. Christian Berger. Samples were dissolved in a 50/50 *v/v* mixture of D_2O/d_2-formic acid. Chemical shifts are reported in parts per million (ppm).

2.2.5 Thermogravimetric Analysis (TGA)

TGA was performed using a Perkin Elmer Pyris 1 TGA thermogravimetric analyser in the range 30-900 °C in an air atmosphere using *ca*. 2-5 mg sample, at a heating rate of 10 °C min^{-1} in a ceramic crucible. The instrument was calibrated to In and Ni standards in an air atmosphere.

2.2.6 UV-Vis Absorption (UV/Vis) and Steady-State Photoluminescence (PL) Spectroscopy

All solution phase optical characterisation techniques were carried out in a 10 mm pathlength quartz cell. Solution phase UV-Vis absorption spectra were recorded at room temperature using either a Shimadzu UV2401 PC UV-Vis scanning spectrometer with slit width of 1 nm or a Varian Cary 50 spectrometer with a slit width of 2 nm. Both solution and solid-state steady-state PL spectroscopy were performed on a Fluorolog-3 spectrophotometer (Horiba Jobin Yvon), using the front-face configuration for solid-state samples. Emission and excitation spectra were corrected for the wavelength response of the system and the intensity of the lamp profile over the excitation range, respectively, using correction factors supplied by the manufacturer. The emission and excitation slit width were varied depending on the nature of the sample being investigated.

2.2.7 Photoluminescence Quantum Yield (PLQY)

PLQYs were measured using an F-3018 integrating sphere accessory attached to the Fluorolog-3 described above. The values reported are the mean of three repeat measurements. The method is accurate to within ±5%.[1] Corrections to the measured PLQYs to correct for self-absorption were carried out as described in **Section 2.3.3.**

2.2.8 Picosecond Time-Correlated Single Photon Counting (ps-TCSPC)

Fluorescence decays were measured using the picosecond time-correlated single photon counting (ps-TCSPC) method at the Collaborative Optical Spectroscopy, Micromanipulation and Imaging Centre (COSMIC), University of Edinburgh, U.K. The excitation source was the second harmonic of the pulse-picked output of a Ti-Sapphire femtosecond laser system (Coherent, 10 W Verdi and Mira Ti-Sapphire), consisting of pulses of ~200 fs at 4.75 MHz repetition rate. Fluorescence decays were measured using an Edinburgh Instruments spectrometer equipped with

TCC900 photon counting electronics. The instrument response of the system was ~50 ps full width at half maximum (FWHM). Depending on the requirements of the sample, fluorescence decays curves were analysed using a standard iterative reconvolution method, assuming a multiexponential decay function, or tail fitting. Reconvolution and data fitting for the tail fits was performed as individual fits to each decay using DAS6 software (HORIBA). Reconvolution and fitting of the remaining fluorescence decays were carried out either as individual fits or as part of a global analysis, as specified, using Globals WE® software package.[2] The quality of fit was judged on the basis of the reduced chi-square statistic, χ^2, and the randomness of residuals. The fitting of the fluorescence decays is discussed further in **Section 2.3.5**.

2.2.9 Nanosecond Flash Photolysis

All samples were degassed for 45 min prior to measurement. Flash photolysis experiments were performed with an Edinburgh Instruments (model LP920) flash photolysis spectrometer. The samples were excited by the second harmonic (355 nm) of a Nd:YAG laser (Spectra Physics). Transient transmittance changes were recorded using a xenon arc lamp (450 W) as a probe working in pulsed mode and at right angles to the excitation beam. A photomultiplier R928 was used for signal detection. Transient spectra were obtained by monitoring the optical density change at 10 nm intervals over the 380-860 nm range, averaging at least 10 decays at each wavelength. Kinetic analysis was performed using the provided Edinburgh Instruments software, L900.

2.2.10 Confocal Microscopy

Confocal microscopy was performed using a Carl Zeiss LSM 700 confocal laser scanning system on an Axio Observer.Z1 inverted microscope stand with an excitation wavelength of 405 nm or 488 nm.

2.2.11 Isothermal Calorimetery (ITC)

ITC experiments were carried out by Dr. Amir Khan, Trinity College Dublin, and performed using a MicroCal VP-ITC instrument (MicroCal Inc., Northampton, MA) interfaced with a computer equipped with VP-2000 viewer instrument control software. ITC data were analysed with Origin 7.0 software. In ITC experiments 2 μl of a 500 μM guanosine triphosphate (GTP) solution was injected every 180 s for a total of 15 injections into a solution of **P3TMAHT** in the calorimeter cell at 30 μM. The observed heat for each injection (peak) was measured by area integration of the power peak with respect to time. ITC data were fitted according to a standard model that assumes a single set of equivalent binding sites.

2.2.12 Electrochemical Measurements

All electrochemical experiments were undertaken in a standard three-electrode cell. The working and counter electrodes were Pt wires, while an Ag/AgCl electrode was employed as the

reference electrode. Cyclic voltammograms were measured on 1 mM solutions in H_2O by using potassium chloride (KCl, 0.1 M) as the supporting electrolyte. The electrochemical measurements were performed using a high performance digital potentiostat (CH model 1760 D Bi-potentiostat system monitored using CH1760D electrochemical workstation beta software). All solutions were degassed for 15 min before the analysis to eliminate any dissolved oxygen present in the electrolyte.

2.2.13 Spectroelectrochemical Measurements

Spectroelectrochemical measurements were carried out using the experimental set-up described above with a platinum mesh electrode as the working electrode. Prior to measurements, samples were diluted to obtain a solution of Abs ~0.3. UV/Vis *in-situ* electrochemical measurements were performed using an ALS SEC2000 UV/Vis miniature spectrophotometer with the Visual Spectra 2.1 software. The light sources were a tungsten-halogen lamp (SEC2000-TH) and a deuterium and tungsten lamp (SEC2000-DH) for the visible and UV/Vis regions, respectively.

2.3 Data Fitting

2.3.1 Non-Linear Least Square (NLLS) Fits

Each of the fitting procedures used throughout this thesis utilise the method of NLLS analysis. A least squares analysis requires a model that is believed to describe the observed data.[3] The aim of least squares analysis is to test whether the chosen model is consistent with the data and to determine the parameter values for the model that provide the best match between the measured data, y_i, and the calculated fit, f_{ic}, using assumed initial parameter values. This is achieved by minimising the goodness-of-fit parameter, χ^2, which is described by:

$$\chi^2 = \sum_{i=1}^{n} \left[\frac{y_i - f_{ic}}{\sigma_i}\right]^2 \qquad \textbf{(2.1)}$$

where σ_i is the standard deviation and n is the number of data points. If the deviation of the experimental data from the theoretical model is proportional to the value of the data it can be said[4]:

$$\sigma_i^2 = y_i$$

$$\chi^2 = \sum_{i=1}^{n} \frac{(y_i - f_{ic})^2}{y_i} \qquad \textbf{(2.2)}$$

Thus, the value of χ^2 is the sum of the squared deviations between the measured data, y_i, and the value expected from the model, f_{ic}, each divided by the measured data. The fit is then run in an iterative manner until the smallest sum of the squares is found.[3, 4] Depending on the results and parameters produced by the previous fit, an iterative process involves incremental changes in the fitting parameters for each subsequent fit to find the minimum value of χ^2.

2.3.2 Gaussian Peak Fitting

2.3.2.1 Fitting of ss-NMR Spectra

To calculate the degree of condensation of the siliceous network in the di-ureasil samples, single Gaussian curves were fitted to each of the T_n signals observed in the ss-NMR, using data analysis program OriginPro 8.5. A T_n signal is characteristic of Si atoms in different environments within the organosilane, representing an alkyltrialkoxysilane containing varying numbers of silicon-oxygen-silicon bridges, *i.e.* T_1 = R′Si(OSi)-$(OR)_2$, T_2 = R′Si$(OSi)_2$(OR) and T_3 = R′Si$(OSi)_3$. The form of the Gaussian peak is given by:

$$y = y_0 + \frac{A}{w\sqrt{\frac{\pi}{2}}} e^{-2\frac{(x-x_c)^2}{w^2}} \quad \textbf{(2.3)}$$

where y_0 is the off-set from the baseline y, w is the width of the peak, x_c is the centre of the peak and A is the area of the peak. Using the area of each peak provided by the fitting, the degree of condensation of the siliceous network, C, was calculated from[5]:

$$C = {}^{1}/_{3}\,(\%T_1 + 2\%T_2 + 3\%T_3) \quad \textbf{(2.4)}$$

where $\%T_n$ is the percentage contribution of the area of T_n peak to the total area.

2.3.2.2 Fitting of FTIR Spectra

To examine the contributions from hydrogen bonding interactions associated with C=O stretching, the amide I bands (1610-1779 cm^{-1}) of the FTIR spectra were deconvoluted. This was carried out by fitting multiple Gaussian bands to the specific region using the data analysis program OriginPro 8.5. The form of the peak is shown in **Eqn. 2.3**. The quality of all Gaussian fits were assessed qualitatively by comparing the cumulative fit peak (produced by summing the intensity of each of the fit peaks at a given x value) to the raw data. The quality of the fit was ensured quantitatively by confirming that the coefficient of determination, the R^2 value, for each of the fits was above 0.999.

2.3.3 PLQY Self-Absorbance Correction

The measurement of PLQY of solid-state or thin film samples is more challenging than the corresponding solution measurements due to the fact that in the solid-state the PL is emitted anisotropically.[6-8] This arises due to the distribution of the chromophores and corresponding emission dipole moments.[7] The use of an integrating accessory has been popularised in an attempt to overcome this challenge.[7,8] A schematic of the integrating sphere experimental set-up compared to the conventional front-face set-up used for solid-state luminescence is shown in **Fig. 2.1**.

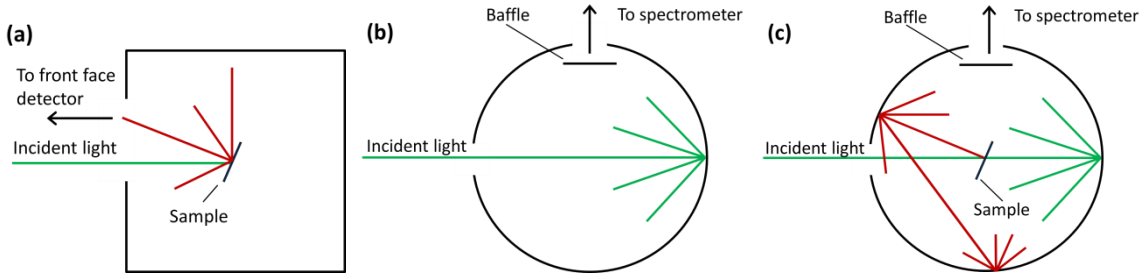

Figure 2.1. Schematic representation of the experimental set-up for (**a**) conventional front-face emission measurements of solid-state samples, and (**b**) the empty integrating sphere and (**c**) the integrating sphere containing a sample to be measured.

Illumination with monochromatic light at a selected wavelength is directed into the integrating sphere through a small entrance hole. The incident light strikes either the sample or the highly reflective Spectralon coating of the sphere, at which point it is emitted/reflected back into the sphere. A coated baffle prevents light from the excitation source being reflected directly to the detector. The geometry and reflective coating of the sphere ensures that emission in any direction from the sample is reflected around the sphere and eventually to the detector port.

For films with high refractive index and optically thick samples such as the di-ureasils measured in this thesis, waveguiding and reabsorption of the emitted photons may lead to further errors in the measured PLQY. Thus, PLQY measurements were performed using an integrating sphere, following the procedure reported by de Mello *et al.*[7] and following this the measurements were corrected for self-absorption following the method put forward by Ahn *et al.*[6] This approach takes into account the initial anisotropy of the emission and also any absorption and re-emission processes that occur to establish the true PLQY. Reabsorption and distortion of the measured spectrum can only occur in a region in which there is overlap between the absorption and emission spectra. Therefore, it is assumed that at the red-edge of the emission spectrum no spectral reshaping occurs. Thus, the shape in this region of spectrum measured in the integrating sphere matches the shape of the red edge of the true spectrum, $F(\lambda)$ (obtained by measuring the photoluminescence for a sample whose spectrum is not distorted by self–absorption). Hence, the long wavelength emission is described by:

$$F'(\lambda) = \frac{F(\lambda)}{1 - a(PLQY)} = \alpha F(\lambda) \qquad \textbf{(2.5)}$$

where $F(\lambda)$ is the photoluminescence spectrum in photons per wavelength, normalised to $\int_0^\infty F(\lambda)d\lambda = 1$ and a is the probability of self-absorption of an emitted photon. The factor α represents an empirical factor that scales the true spectrum, $F(\lambda)$, to an enhanced spectrum $F'(\lambda)$ whose red-edge is matched to that of the observed photoluminescence spectrum $F_{obs}(\lambda)$.

The probability of self-absorption of an emitted photon, a, is determined from:

$$\frac{\int_0^\infty F_{obs}(\lambda)d\lambda}{\int_0^\infty F'(\lambda)d\lambda} = 1 - a \tag{2.6}$$

which provides the expression for the true photoluminescence quantum yield (PLQY):

$$PLQY = \frac{PLQY_{obs}}{1 - a + a(PLQY_{obs})} \tag{2.7}$$

In an ideal situation, the true photoluminescence spectrum, *F(λ)*, should be obtained by measuring a dilute solution of the lumophore ensuring that self-absorption does not occur. However, in CP doped di-ureasil systems, both the CP and the di-ureasil are photoluminescent and thus, no solution state equivalent exists. To overcome this, the true spectrum for each series is taken to be that of the lowest wt% sample measured in the front-face configuration (not in the integrating sphere) as in theory this sample should present minimal reabsorption.

This assumption was tested by comparison of the solution phase spectrum of the polymers with the lowest wt% sample measured in the front-face configuration; see **Fig. 2.2** for DI-PBS-2.0 as an illustrative example.

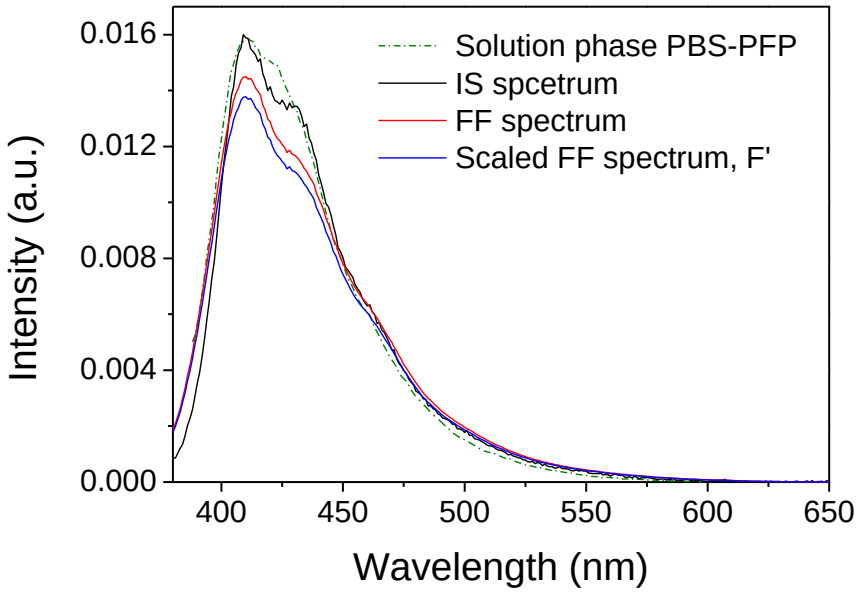

Figure 2.2. Area-normalised solution phase emission spectrum for PBS-PFP in 25:75% *v/v* 1,4-dioxane/water (green dash line), the area normalised integrating sphere (IS) photoluminescence spectrum ($F_{obs}(\lambda)$) (black line), the area-normalised front-face (FF) photoluminescence spectrum ($F(\lambda)$) (red line) and the scaled unattenuated photoluminescence spectrum (F′(λ)) for DI-PBS-2.0. The scale factor, *α*, is adjusted so that $F'(\lambda)$ matches $F_{obs}(\lambda)$ at λ_{em} = 500 nm and longer.

2.3.4 Commission Internationale de l'Éclairage (CIE) Chromaticity Diagrams

The human eye contains three types of colour sensitive cones in the retina which are responsible for the perception of colour. The sensitivity of each of these types of cones is specific to each individual, but the general sensitivity is represented in **Fig. 2.3**:

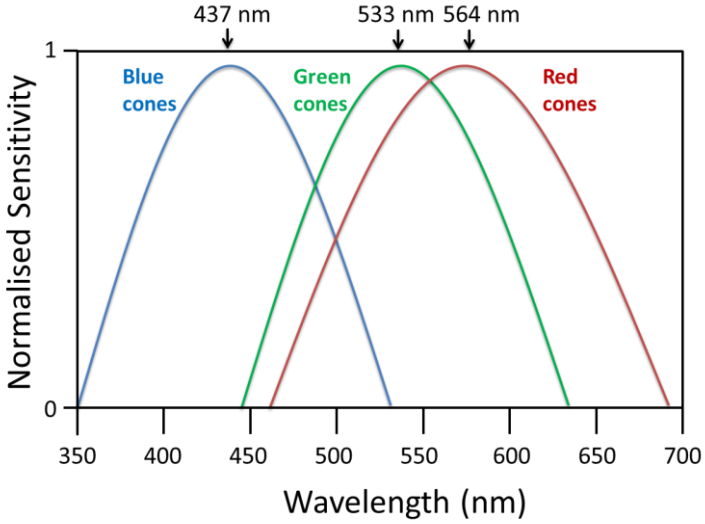

Figure 2.3. Normalised spectral response of the cones in the human eye adapted from ref [9].

The CIE chromaticity diagram is a tool to numerically describe how the human eye will experience incident light represented by a given spectrum.[10] The CIE chromaticity diagram is a colour space defined by three colour matching functions, $\bar{x}_\lambda$, $\bar{y}_\lambda$ and $\bar{z}_\lambda$, which simulate the sensitivity of the cones in the human eye.[11] Colour matching functions act as weighting functions to determine the tristimulus values, X, Y, Z , according to the following equations[11]:

$$X = \sum_{\lambda=380}^{700} \bar{x}_\lambda . I(\lambda)\Delta\lambda$$
$$Y = \sum_{\lambda=380}^{700} \bar{y}_\lambda . I(\lambda)\Delta\lambda \qquad \textbf{(2.8)}$$
$$Z = \sum_{\lambda=380}^{700} \bar{z}_\lambda . I(\lambda)\Delta\lambda$$

where I is the intensity at wavelength λ. These tristimulus values, defined by the CIE 1931 colour space, are akin to primary colours in an additive colour system.[12] These values also take into account the perceived brightness of a spectrum, with the Y value representing the luminosity of a perceived colour.[11]

The chromaticity of a colour is described by two derived parameters, x and y, which are functions of the tristimulus values and are also known as colour coordinates.[13]

$$x = \frac{X}{X+Y+Z}$$
$$y = \frac{Y}{X+Y+Z} \quad \textbf{(2.9)}$$

These *x*,*y* coordinates are plotted onto a two-dimensional chromaticity diagram (**Fig. 2.4**) that contains all the possible chromaticities perceived by the average human eye, the gamut of human vision. Pure white light is defined as having the coordinates (0.33, 0.33).[13, 14] The horse-shoe shaped border of this plot is called the spectral locus and corresponds to monochromatic light in the range 380-770 nm.

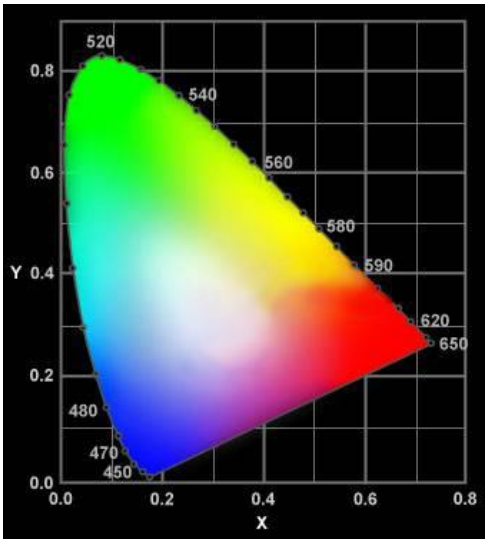

Figure 2.4. CIE-(1931) chromaticity diagram representing the gamut of human vision.

The *XYZ* tristimulus values and *xy* colour coordinates for each spectrum investigated were calculated from corrected emission spectra at 5 nm intervals as described above.

2.3.5 Fluorescence Lifetime Decay Fitting

2.3.5.1 Fluorescence Lifetime Theory

In the measurement of the fluorescence lifetime of a fluorophore, the ideal experimental set-up involves the excitation of the fluorophore with an infinitely sharp (δ-function) pulse of light. This promotes n_0 fluorophores to the excited state. This initial excited-state population decays with the rate[15]:

$$\frac{dn(t)}{dt} = (k_{rad} + k_{nr})n(t) \quad \textbf{(2.10)}$$

where *n(t)* is the number of fluorophores in the excited state at time *t* after excitation, k_{rad} is the emissive rate and k_{nr} is the non-radiative rate. Emission is a spontaneous, random event and as such each fluorophore in the excited state has equal probability of emitting in a given period of time. This results in an exponential decay of the excited state population:

$$n(t) = n_0 \exp(-t/\tau) \quad \textbf{(2.11)}$$

where τ is the characteristic lifetime of the excited state. This equation is given in terms of number of fluorophores in the excited state, *n(t)*. However, in reality fluorescence intensity, *I*, is measured which is proportional to *n(t)*. Thus it is possible to rewrite this equation as:

$$I(t) = I_0 \exp(-t/\tau) \quad \textbf{(2.12)}$$

where I_0 is the fluorescence intensity at time 0. The characteristic lifetime, τ, is the inverse of the total decay rate, $\tau = (k_{rad} + k_{nr})^{-1}$. The fluorescence lifetime can be determined by calculating the slope of a plot of log *I(t) vs. t*, or *via* the more standard practice of fitting the data to an assumed decay model.

The above expression (**Eqn. 2.12**) describes the decay of a single component system displaying a single decay time. However, both the conjugated polymers and di-ureasil samples measured in this thesis possess complex multi-exponential decays. This requires a multi-exponential decay model:

$$I(t) = \sum_i \alpha_i \exp(-t/\tau_i) \quad \textbf{(2.13)}$$

where α_i and τ_i are the pre-exponential factor and characteristic lifetime for the i^{th} component, respectively. In this model the intensity is assumed to decay as the sum of individual single exponential decays. When examining a single fluorophore displaying a complex decay it is generally safe to assume that the fluorophore has the same radiative decay rate in each environment. Thus, in this case α_i represents the fraction of the molecules in each environment at t=0.[16]

The fractional contribution f_i of each decay component to the steady-state intensity can be calculated from:

$$f_i = \frac{\alpha_i \tau_i}{\sum \alpha_i \tau_i} \quad \textbf{(2.14)}$$

Similarly by knowing α_i and τ_i, it is possible to calculate the intensity average lifetime, $\langle\tau\rangle$, which is given by:

$$\langle\tau\rangle = \frac{\sum \alpha_i \tau_i^2}{\sum \alpha_i \tau_i} \quad \textbf{(2.15)}$$

The fluorescence lifetime decays described in this thesis were measured *via* time-correlated single photon counting (TCSPC) using the experimental set up described in **Section 2.2.8**.

2.3.5.2 General Principles of Time-Correlated Single Photon Counting (TCSPC)

During TCSPC measurements, the sample is excited by a laser pulse; see **Fig. 2.5** for schematic representation of the experimental set-up. The conditions are such that less than one emitted photon is detected per excitation pulse. This is due to the fact that if more than one photon is detected per excitation, then the results are biased towards shorter times.[17] The initial laser pulse passes through a beam splitter, with one portion passing on to excite the sample while the second is passed through a photodetector to a constant function discriminator (CFD). This accurately measures the arrival time of the pulse. The signal from this CFD is passed on to a time-to-amplitude converter (TAC) as the 'start' signal. The TAC generates a voltage ramp on arrival of the 'start' signal. This is a voltage that increases linearly with time on the nanoscale, and is achieved by charging a capacitor during the time interval between pulses. Typically, the capacitor is charged from 0 to 10 V over a specific time range. Emission of a single photon from the sample excited state is detected on a second channel. The time of this signal is again accurately measured on passing through a photodetector to a second CFD. This sends a 'stop' signal to the TAC, which stops the charging of the capacitor. Thus, if the chosen time range is 20 ns and a stop pulse is recorded after 10 ns then the charging of the TAC stops at 5 V. The TAC now contains a stored voltage proportional to the time delay between the excitation and emission pulses. The voltage is then amplified by a programmable gain amplifier (PGA) and passed on to the analogue-to-digital converter (ADC) which converts the signal into a numerical value. Finally to minimise false readings the signal is restricted to a set range of voltages. If the signal does not lie within this range then it is suppressed by a window discriminator (WD). The voltages within the correct range that are converted to a digital value are stored as a single event with the measured time delay. This process is repeated for a set number of times or until a single time channel has reported a set number of events.

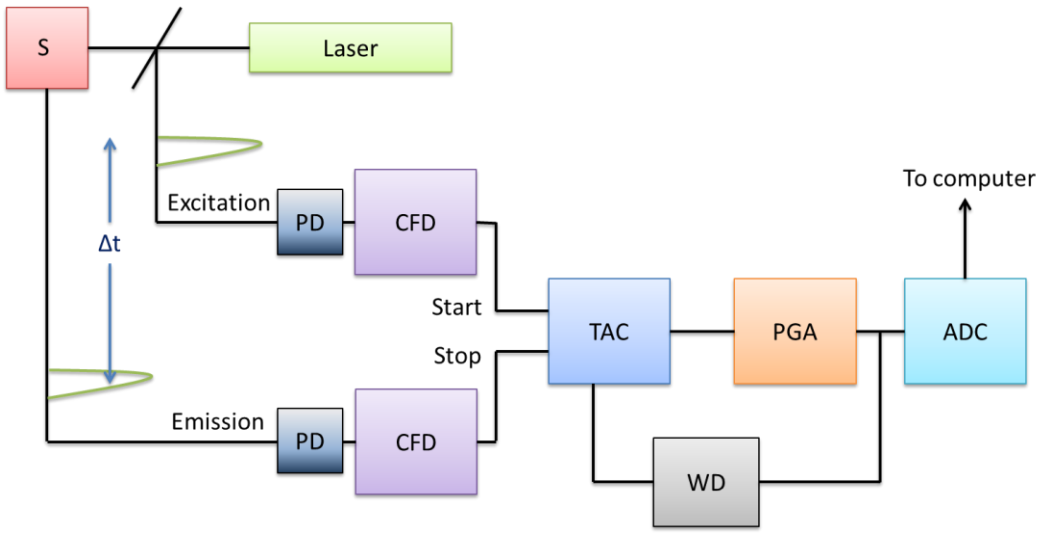

Figure 2.5. Schematic of the components and operation of TCSPC; S – sample, PD – photodetector, CFD - constant function discriminator, TAC - time-to-amplitude converter, WD - window discriminator, PGA - programmable gain amplifier and ADC - analogue-to-digital converter.

The instrument response function (IRF) is the response of the instrument to a zero lifetime sample.[17] It represents the shortest time profile that can be measured by the instrument. The instrument response function depends on the shape of the excitation pulse and how this pulse is detected by the instrument.[15] In reality it is impossible to excite the sample with an infinitely sharp (δ-function) excitation pulse or to have a δ-function for the instrument response. This causes the measured data to be a convolution of the sample response and the lamp function.[17] It is possible to visualise the lamp response to be a series of δ-functions with different amplitudes. Each of these δ-functions prompts a response from the sample, the intensity of which is proportional to the amplitude of the δ-function (**Fig. 2.6**). The measured decay is the sum of all these sample responses that begin at different times with different amplitudes.

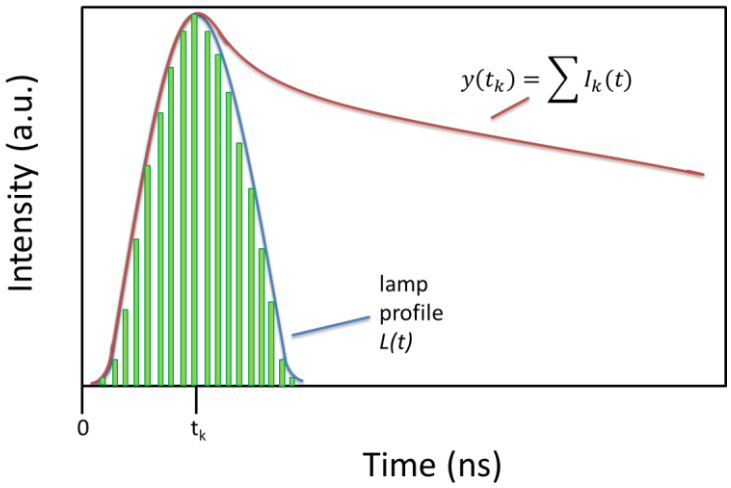

Figure 2.6. Convolution of a sample response, *I(t)*, with a lamp profile, *L(t)*, to yield the measured data, *y(t)*.

2.3.5.3 Reconvolution Fits

As mentioned above, in reality the excitation pulse is not an infinitely short δ-function and thus the sample does not only decay starting directly after the pulse. Thus, the theoretical sample decay (**Eqn. 2.14**) must be reconvoluted with the instrumental response function (IRF) (which includes the width of the excitation pulse and possible electronic responses of the instrument) in the form:

$$I'(t) = \int_0^t E(t')I(t-t')dt' \qquad \textbf{(2.16)}$$

where *E(t)* is the excitation pulse and *I(t)* is the theoretical decay model (12). This expression states that the experimentally measured intensity at time *t* is given by the sum of the intensities expected for all δ-function excitation pulses that occur until time *t*, if the excitation pulse is imagined to be comprised as a series of δ-functions with different amplitudes. This model is then fitted to the measured decay through the method of NLLS analysis, described in **Section 2.3.3**.

Thus, during the fitting process α_i and τ_i are varied until χ^2 is at a minimum. This occurs when the data, y_i, and fitted point, f_{ic}, are most closely matched. α_i and τ_i are changed after each iteration to minimise χ^2. As χ^2 is dependent on the number of data points, the value of χ^2 will be larger for larger data sets. For this reason the reduced χ^2 value is used when evaluating TCSPC fits. The reduced χ^2 is given by[7]:

$$\chi_r^2 = \frac{\chi^2}{n-p} = \frac{\chi^2}{v} \quad \textbf{(2.17)}$$

where n is the number of data points, p is the number of floating parameters and v is the number of degrees of freedom. Typically, for TCSPC the number of data points far surpasses the number of parameters such that n-p is equal to n. If only random errors contribute to the fit, then the reduced χ^2 is expected to be close to 1. If the model does not fit the data then the reduced χ^2 is expected to be much greater than unity. Thus, the quality of the fits obtained was judged based by the value of the reduced χ^2 and also on the randomness of the residuals, which are the vertical deviation of the measured data points from the fitted curve. Non-random behaviour in the residuals plot suggests a poor fit or a hidden variable.

2.3.5.4 Tail Fits

Tail fits are also carried out using NLLS to reduce the value of χ^2. The difference when compared to the reconvolution method is that for tail fitting the sample curve is not convoluted with the IRF prior to fitting. Tail fitting is only applicable in the region where there is no further sample excitation, *i.e.* only after the excitation pulse has disappeared (**Fig. 2.7**). The IRF is not directly required during fitting, and thus does not strictly need to be recorded. Tail fits can only yield information on the decays that are dominant within the range being fit, as highlighted in **Fig. 2.7**. Lifetime parameters in the shorter region cannot be discriminated using this method; for this data it is more appropriate to use the reconvolution method.

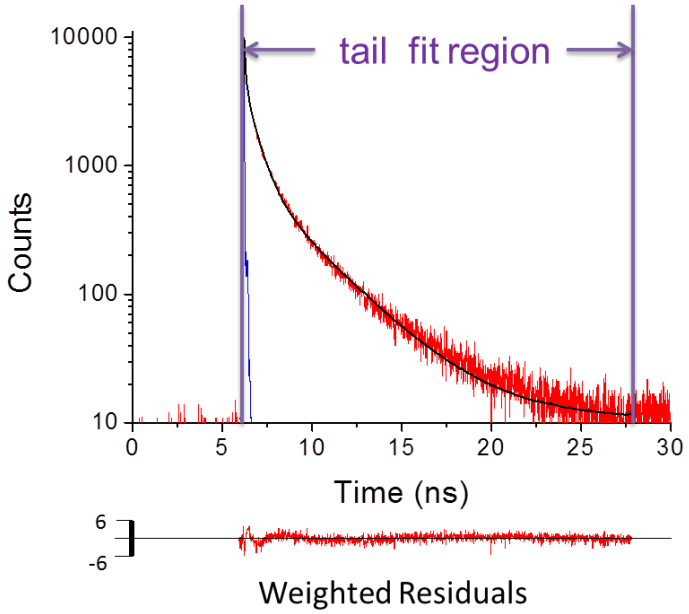

Figure 2.7. PL emission decay curves (solid red line) (λ_{ex}= 365 nm and λ_{em}= 420 nm), and fit (solid black line) for P3T-6.6 showing the tail fit region as a representative example. The instrument response function (solid blue line) is also shown.

2.4 References

1. L. Porres, A. Holland, L. O. Pålsson, A. P. Monkman, C. Kemp and A. Beeby, *J. Fluoresc.*, 2006, **16**, 267-272.
2. E. Gratton, J. Beechem, Globals WE (software), Laboratory for Fluorescence Dynamics, University of California, Irvine, CA 2004.
3. J. R. Lakowicz, in *Principles of Fluorescence Spectroscopy*, Springer, 2006, pp. 130-131.
4. M. Ledvij, *The Industrial Physicist, American Institute of Physics*, 2003, 24-27.
5. P. P. Lima, R. A. S. Ferreira, S. A. Junior, O. L. Malta and L. D. Carlos, *J. Photochem. Photobiol. A*, 2009, **201**, 214-221.
6. T.-S. Ahn, R. O. Al-Kaysi, A. M. Muller, K. M. Wentz and J. C. Bardeen, *Rev. Sci. Instrumen.*, 2007, **78**, 086105.
7. J. S. de Mello, F. H. Whittman and R. H. Friend, *Adv. Mater.*, 1997, **9**, 230-232.
8. L. O. Pålsson and A. P. Monkman, *Adv. Mater.*, 2002, **14**, 757-758.
9. J. E. Dowling, *The Retina: An Approachable Part of the Brain*, Harvard University Press, 1987.
10. M. Xu, L. Wang, D. Jia and F. Le, *J. lumin.*, 2015, **158**, 125-129.
11. R. C. Evans and P. Douglas, *Anal. Chem.*, 2006, **78**, 5645-5652.
12. S. Westland, in *Handbook of Visual Display Technology*, eds. J. Chen, W. Cranton and M. Fihn, Springer, 2012, pp. 139-146.
13. R. W. Hunt, *Measuring colour*, Fountain Press, 1998.
14. R. C. Evans, L. D. Carlos, P. Douglas and J. Rocha, *J. Mater. Chem.*, 2008, **18**, 1100-1107.
15. J. R. Lakowicz, in *Principles of Fluorescence Spectroscopy*, Springer, 2006, pp. 99-100.
16. J. R. Lakowicz, in *Principles of Fluorescence Spectroscopy*, Springer, 2006, pp. 142.
17. J. R. Lakowicz, in *Principles of Fluorescence Spectroscopy*, Springer, 2006, pp. 103-106.

Chapter Three

……

Come to Your Senses: Selective Detection of Biologically Important Anions Using the Di-block Conjugated Copolymer PF2/6-*b*-P3TMAHT

3.1 Introduction

The chemically-distinct nature of the constituent segments of block copolymers provides a unique platform for self-assembly into structures organised on the nanometre scale. This approach has been increasingly exploited for the design of bulk heterojunction solar cells and energy storage materials.[1-3] The differing properties in each block may also introduce complementary optical properties, for example through the addition of multiple emitting species such as a blue-emitting polyfluorene (PF) block or a red-emitting polythiophene (PT) block.[4] Further control over the self-assembly of block copolymers can be achieved through the addition of charged pendant groups to one of the polymer blocks, thus creating a conjugated polyelectrolyte (CPE).[5, 6] This additionally affects the solubility of the block copolymer, as the CPE block may be preferentially soluble in polar, environmentally friendly solvents such as water.

The optical properties of CP(E)s are highly dependent on their conformation and aggregation state. Thus, changes to the molecular structure, and concomitant changes in the emission properties, of conjugated block copolymers in solution can be controlled through manipulation of the polarity of the solvent system. This has been demonstrated for a PF-PT polymer, **PF2/6-*b*-P3TMAHT** (**Fig. 3.1**) containing a charged side chain on the PT block and neutral side chains on the PF block, in methanol and water[7] and THF-water mixtures.[5, 8] THF is a non-selective solvent for both the PF and PT blocks, while water is selective for the PT block. In THF the characteristic spectra are observed for both blocks suggesting that they are not in close enough proximity to undergo efficient energy transfer.[8] However, addition of water to form a 50/50 THF-water mixture brings about the formation of more disordered aggregates. In contrast, in pure water the PF blocks are essentially non-solvated and located in the interior of the aggregates minimising solvent interactions.

Previous work has shown that the cationic PT block, **P3TMAHT**, of the above polymer can undergo electrostatic interaction with oppositely charged species such as halide ions[9] and oppositely charged surfactants.[8, 10] These reports highlight the change in the conformation and PL properties of the PT upon complexation. The ionic nature of the CPE causes it to be soluble in water, a highly desirable property for materials to be used as biological sensors. The fact that electrostatic binding brings about the subsequent change in the polymer structure and optical properties has allowed for the development of ratiometric fluorescence based sensors for both halide ions[9] and double and single stranded DNA.[9, 11] The ratiometric nature of these sensing platforms is imparted due to the fact that interaction between the charged analytes and the charged pendent groups of the PT block leads to quenching of thiophene photoluminescence while the PL of the non-complexed PF block remains unquenched. Measuring the difference in the PL intensities for these components provides a quantitative ratiometric method for sensing. Electrostatic interactions appear to play a role in the quenching of the PT block, suggesting that

this diblock copolymer may potentially be developed as a sensory material for a range of negatively charged species.

3.1.1 Aims

In this chapter, the optical response of the diblock copolymer **PF2/6-*b*-P3TMAHT** (**Fig. 3.1**) with a number of biologically-important anions will be investigated in an attempt to develop a sensory platform. The biological anions chosen are the nucleotides guanosine triphosphate (**GTP**), guanosine diphosphate (**GDP**), guanosine monophosphate (**GMP**), adenosine triphosphate (**ATP**) and cytidine triphosphate (**CTP**) (**Fig. 3.2**). These anions will be split into two different series. The first covers the three guanosine species with different numbers of phosphate groups to investigate the effect of charge on any observed response. The second set of anions are those with the same number of phosphates, but two have a purine base (**GTP** and **ATP**) while the final anion contains a pyrimidine base (**CTP**), in an attempt to investigate the effect of the nature of the nucleobase on any observed PL response. These anions were chosen as they play an important role in biological processes ranging from RNA synthesis[12] to energy metabolism.[13] The optical properties of the CPE will be examined as a function of increasing anion concentration. Steady-state photoluminescence, time-resolved emission studies and transient absorption studies will be used to probe any interaction between the CPE and anions. Isothermal calorimetry and spectroelectrochemical studies will be used to examine the binding and redox process occurring between the two species, respectively.

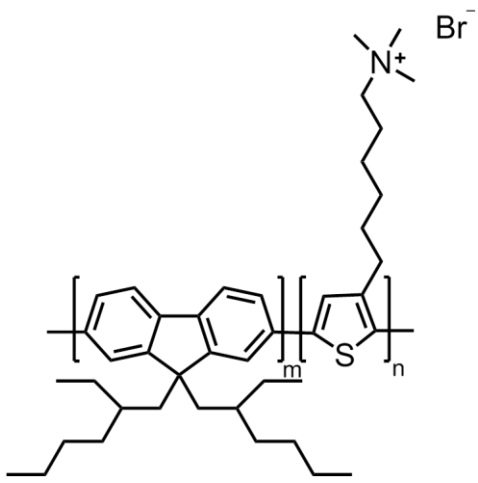

Figure 3.1. Chemical structure of the diblock copolymer poly[9,9-bis(2-ethylhexyl)fluorene)-*b*-poly[3-(6-triethylammoniumhexyl)thiophene] bromide (**PF2/6-*b*-P3TMAHT**).

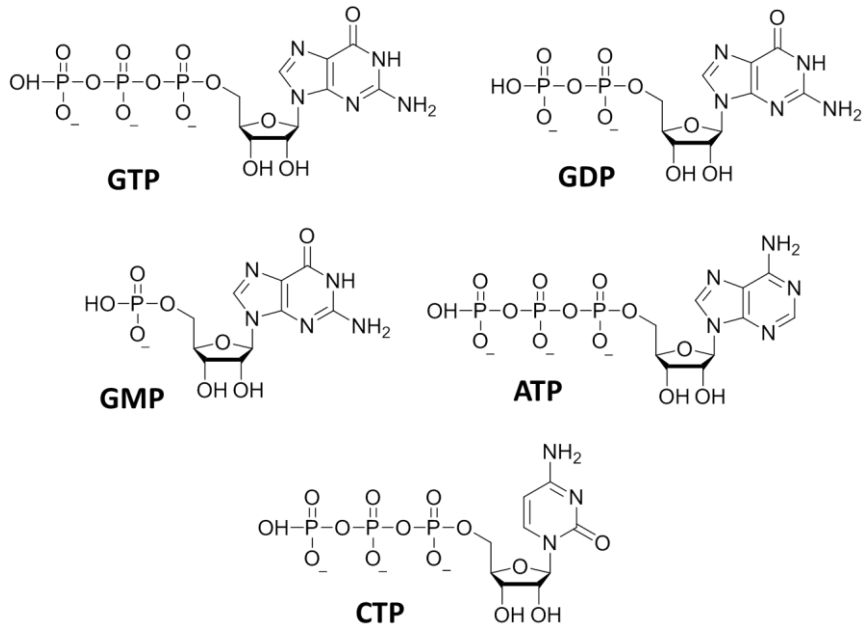

Figure 3.2. Chemical structure and charges on each of the anions investigated under physiological conditions.[14, 15]

3.2 Experimental

3.2.1 Polymer

Poly[9,9-bis(2-ethylhexyl)fluorene)-*b*-poly[3-(6-triethylammoniumhexyl)thiophene] bromide (**PF2/6-*b*-P3TMAHT**) with a number-averaged molecular weight, M_n, of 28,250 g mol^{-1} (~679 g mol^{-1} (r.u.)) was synthesised by Dr. Andrea Gutacker as previously reported.[5, 16]

3.3 Results and Discussion

A schematic representation of the possible mechanisms of fluorescence quenching in **PF2/6-*b*-P3TMAHT** by the range of biologically important anions examined during this work is shown in **Fig. 3.3**. Each of the mechanisms exhibited in this figure will be discussed in the following section as a function of increasing anion concentration.

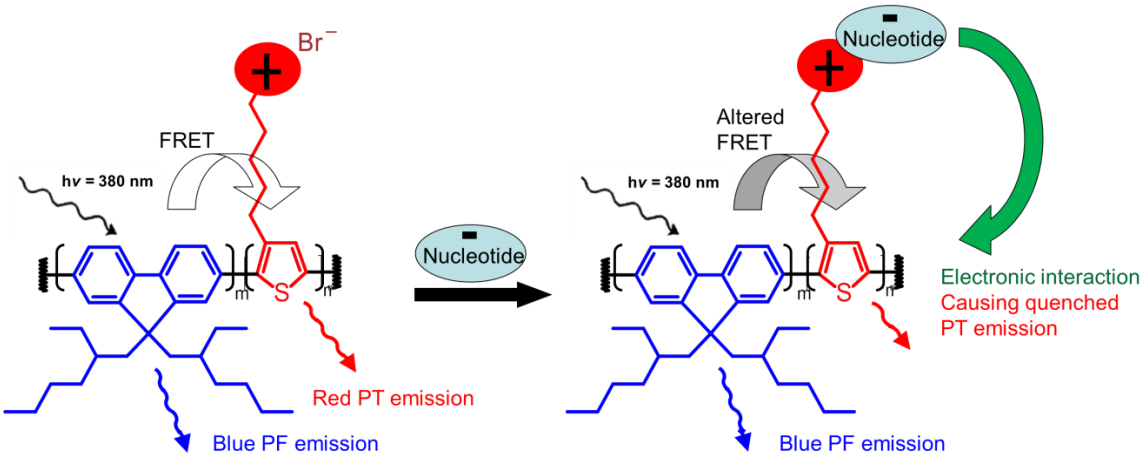

Figure 3.3. Schematic representation of the possible mechanism of fluorescence quenching of **PF2/6-*b*-P3TMAHT** by the nucleotides under investigation.

3.3.1 Optical Properties on Addition of Nucleotides to PF2/6-*b*-P3TMAHT in Solution

3.3.1.1 Steady-State Spectroscopy Studies

The UV/Vis absorption spectrum of **PF2/6-*b*-P3TMAHT** in aqueous solution shows two distinct bands (**Fig. 3.4a**). The band with a maximum at 370 nm is attributed to the PF block of the polymer, while the second at 460 nm is ascribed to absorption of the PT block.[5] On direct excitation of the PF block (λ_{ex} = 380 nm) two bands are observed in the PL spectrum, attributed to the PF and PT blocks, respectively (**Fig. 3.4b**). The emission maximum for the PF block lies at 420 nm and the PT block is observed at 630 nm. The observation of emission from the PT block following selective excitation of the PF block is attributed to Förster resonance energy transfer (FRET) from the PF to the PT block.[8] This is confirmed by the observation of a second band (associated with the PF block) in the PL excitation spectrum while monitoring at the PT emission maximum (see Appendix, **Fig. A.3.1**).

Addition of the nucleotides investigated in this study to an aqueous solution of **PF2/6-*b*-P3TMAHT** induces a response in both the UV/Vis absorption and PL spectra, the nature and magnitude of which are dependent on the anion in question. The specific response seen on addition of **GTP** is shown in **Fig. 3.4**, as a representative example for the guanosine containing series. In general, a decrease in absorbance and a red-shift in the absorbance maximum of the PT block is observed, while the PF block is essentially unaffected. The magnitude of the shift in the PT absorption band is dependent on the number of phosphate groups on the anion following the trend **GTP**>**GDP**>**GMP**, as highlighted in **Fig. 3.4c**. The fact that the PF absorbance is unaffected suggests a unique binding interaction occurs between the nucleotides and the positively charged PT units. Moreover, a red-shift such as that seen for the PT block might indicate an increase in polymer aggregation upon binding. The corresponding PL spectra show little to no effect on the PF block, while quenching of the emission from the PT block occurs, the magnitude of which decreases as the number of phosphate groups on the anion decreases. This is highlighted in **Fig. 3.4d** which shows the relative final emission intensity of the PT block compared to the initial emission intensity for addition of a large excess of **GTP**, **GDP** and **GMP**.

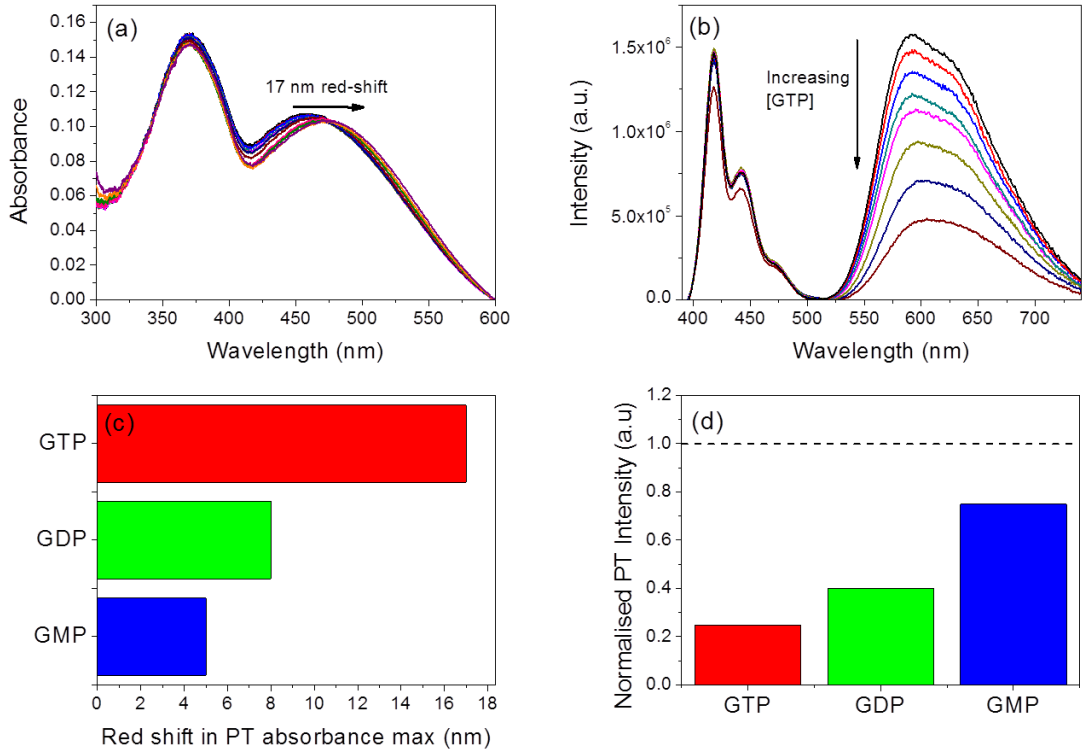

Figure 3.4. (**a**) UV/Vis absorption and (**b**) PL spectra (λ_{ex} = 380 nm) for **PF2/6-*b*-P3TMAHT** (9.8 μM (r.u.)) in aqueous solution in the presence of increasing concentration of **GTP** (0 – 38 μM). (**c**) Magnitude of the shift in PT absorption maximum and (**d**) intensity of the PT emission on addition of an excess of **GTP**, **GDP** and **GMP** normalised relative to the initial PT emission intensity. The black dash line serves only to guide the eye, indicating the relative intensity of the initial PT emission.

On comparison of different nucleotides containing an equal number of phosphate groups and different nucleobases (**GTP**, **ATP** and **CTP**), similar results, matching those shown in **Fig. 3.4a** and **b**, were obtained for anions containing a purine base (**GTP** and **ATP**). In contrast **CTP**, which contains a pyrimidine base, showed a different optical response. **Fig. 3.5a** and **b** show the UV/Vis and PL responses of **PF2/6-*b*-P3TMAHT** on addition of **CTP**. A reduced red-shift in the absorption maximum of the PT block (**Fig. 3.5c**), and also a large decrease in the relative absorbance is observed. However, the nature of the nucleobase did not seem to have such a drastic effect on the quenching of the PL of PT block, as the emission spectra with all three anions show similar quenching behaviour. The magnitude of quenching observed for **GTP** and **ATP** are almost identical, while **CTP** shows a slightly reduced degree of quenching. This is highlighted in **Fig. 3.5d** which shows relative final emission intensity of the PT block compared to the initial emission intensity for addition an excess of **GTP**, **ATP** and **CTP**, respectively.

The shift in the absorption band of the PT block for both the guanosine and the triphosphate series suggests an interaction between the PT block and the nucleotides. This is most likely mediated by electrostatic interaction between the positively-charged pendant groups of the PT block and the varying number of negatively-charged phosphate groups on each of the nucleotides.

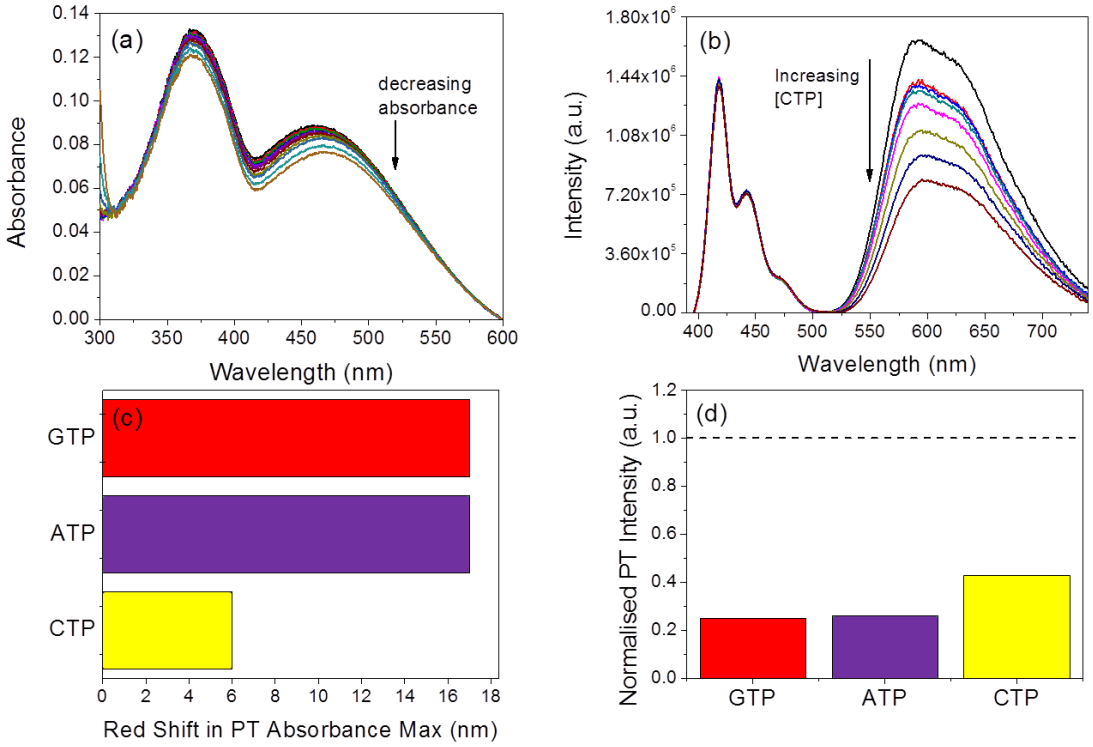

Figure 3.5. (**a**) UV/Vis absorption and (**b**) PL spectra (λ_{ex} = 380 nm) for **PF2/6-*b*-P3TMAHT** (9.8 μM (r.u.)) in aqueous solution in the presence of increasing concentration of **CTP** (0 – 38 μM). (**c**) Magnitude of the shift in PT absorption maximum and (**d**) intensity of the PT emission on addition of an excess of **GTP**, **ATP** and **CTP** normalised relative to the initial PT emission intensity. The black dash line serves only to guide the eye, indicating the relative intensity of the initial PT emission.

Previous work in the Evans group has examined the effect of smaller anions (K_2CO_3, Na_2CO_3, Na_2SO_3, KCl, KI and NaI) on the quenching of the PT block of **PF2/6-*b*-P3TMAHT** in aqueous solution. Each of these anions caused quenching of the PT emission albeit to a significantly reduced extent than the nucleotides mentioned above. The largest quenching response was seen in the case of the iodide ion, most likely due to the heavy atom effect. Commonly, studies on biological species, such as the nucleotides described here, are carried out in buffer solution to simulate biological conditions containing competitive small anions. The above titrations, when carried out in buffer solution also showed a dramatic quenching of the PT emission, as can be seen for titration with **GTP** in Tris buffer (100 mM, pH = 7.4) in **Fig. 3.6**. There is a notably more dramatic response in the buffer solution when compared to Millipore water. However, as the presence of small anions such as those present in the buffer affects the response of **PF2/6-*b*-P3TMAHT**, further studies into the interactions between the CP and the nucleotides were carried out in pure Millipore water in an effort to examine the mechanism of purely the nucleotide-**PF2/6-*b*-P3TMAHT** interactions.

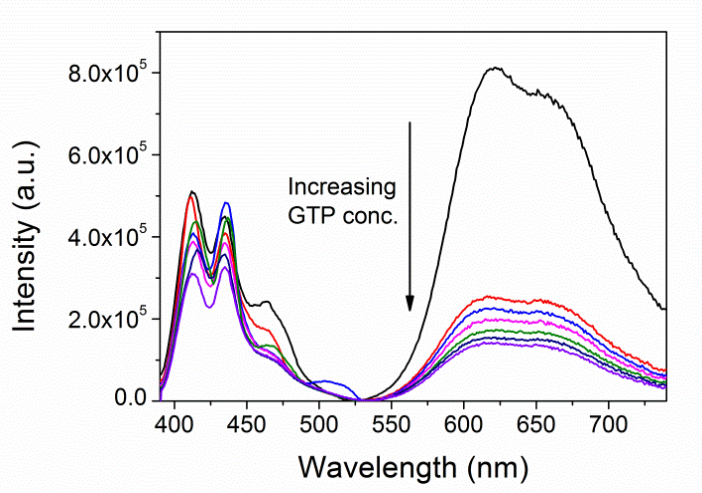

Figure 3.6. PL spectra (λ_{ex} = 380 nm) for **PF2/6-*b*-P3TMAHT** (9.8 μM (r.u.)) in Tris buffer solution (100 mM, pH = 7.4) in the presence of increasing concentration of **GTP** (0 – 38 μM).

3.3.1.2 CIE (1931) Colour Coordinates

The quenching of the PT emission can be further quantified using Commission Internationale d'Éclairage (CIE) 1931 *xy* chromaticity diagrams. The CIE (1931) colour coordinates were determined as outlined in **Section 2.3.4**. The chromaticity diagram for the addition of **GTP** to **PF2/6-*b*-P3TMAHT** is shown in **Fig. 3.7a**. The *xy* coordinates for pure **PF2/6-*b*-P3TMAHT** in solution are (0.54, 0.32) in the red spectral region. The quenching of the PT emission caused by the addition of **GTP** causes these coordinates to shift towards the blue spectral region (0.41, 0.21). As the magnitude of the observed quenching is dependent on the charge and nature of the anion under investigation, so too is the relative shift in the chromaticity coordinates, as can been seen on comparing the chromaticity diagram for quenching with the guanosine series; **GTP** (**Fig. 3.7a**), **GDP** (**Fig. 3.7b**) and **GMP** (**Fig. 3.7c**).

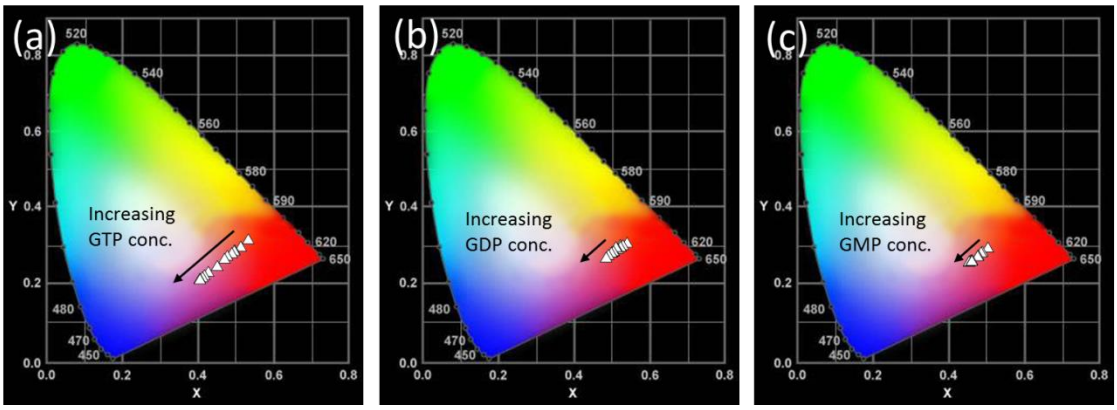

Figure 3.7. CIE *x,y* chromaticity diagrams for quenching of **PF2/6-*b*-P3TMAHT** (9.8 μM (r.u.), λ_{ex} = 380 nm) by (**a**) **GTP** (**b**) **GDP** and (**c**) **GMP** (0 – 38 μM).

3.3.2 Mechanism of Quenching

For a complex system such as that under investigation there are many possible modes of quenching. As the excitation of the PT block occurs *via* FRET from the PF block, it is possible that

the presence of the nucleotides causes a change to the CP structure in solution similar to that seen on complexation with oppositely charged surfactants.[5] Such a change in aggregated structure may affect the FRET efficiency between the two blocks. It is also conceivable that some form of energy transfer occurs between the anions and **PF2/6-*b*-P3TMAHT** *via* excited state energy transfer or electron transfer. Each of these possibilities will be discussed below along with the specific mode of quenching.

3.3.2.1 Static *vs*. Dynamic Quenching Modes

The quenching of a fluorophore in solution can occur *via* two possible modes; static or dynamic quenching. Both modes require contact between the fluorophore and the quencher. During dynamic quenching, the quencher, *Q*, must diffuse to the fluorophore, *F*, within the fluorophore's excited-state lifetime. On contact, the fluorophore returns to the ground state, without emission of a photon, *i.e.* a new non-radiative pathway is introduced. Whereas, in the case of static quenching, a non-fluorescent complex is formed between the fluorophore and the quencher upon contact.[17] A schematic representation of the two different quenching modes is given in **Fig. 3.8**.

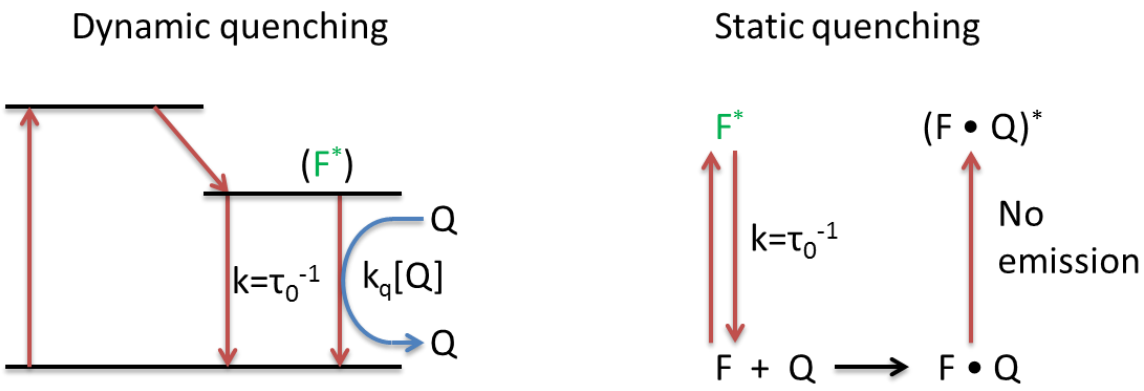

Figure 3.8. Schematic representation of the processes involved in dynamic and static quenching where F is the ground-state fluorophore, F* is the fluorophore in the excited state, Q is the quencher, *k* is the rate constant for deactivation of the excited state and k_q is the bimolecular quenching rate constant.

Dynamic quenching of the PL of a fluorophore can be described by the Stern-Volmer equation:

$$\frac{I_0}{I} = 1 + k_q\tau_0[Q] = 1 + K_{SV}[Q] \qquad (3.1)$$

where I_0 is the PL intensity of the fluorophore in the absence of the quencher, I is the PL intensity in the presence of the quencher, $[Q]$ is the quencher concentration, k_q is the bimolecular quenching constant and τ_0 is the lifetime of the fluorophore in the absence of the quencher. The Stern-Volmer constant, K_{SV}, is given by $K_{SV} = k_q\tau_0$.

This relationship can be derived for dynamic quenching by considering the fluorescence intensities in the absence and presence of a quencher.[18] The PL intensity for a fluorophore is proportional to its concentration in the excited state, [*I**]. The differential equation describing [*I**] in the absence of a quencher is given by **Eqn. 3.2**, as under continuous illumination a constant population of excited fluorophore is established and therefore d[*I**]/dt=0.

$$\frac{d[I^*]}{dt} = f(t) - k_{obs}[I^*]_o = 0 \tag{3.2}$$

where *f(t)* is the constant excitation function and k_{obs} is the rate constant for the decay of the fluorophore in the absence of the quencher. Thus, $k_{obs} = \tau_0^{-1}$, where τ_0 is the lifetime of the fluorophore in the absence of the quencher. The fluorophores excited state decays at a rate which is the sum of its radiative (k_{rad}) and non-radiative (k_{nr}) decay rates, *i.e.* $k_{obs} = k_{rad} + k_{nr}$. In the presence of a quencher there is the additional decay rate, $k_q[Q]$, and so the differential equation is given by:

$$\frac{d[I^*]}{dt} = f(t) - (k_{obs} + k_q[Q])[I^*] = 0 \tag{3.3}$$

Division of **Eqn. 3.2** by **Eqn. 3.3** gives **Eqn. 3.4**, which is the Stern-Volmer relationship. This gives rise to a linear dependence when I_0/I is plotted against [Q].

$$\frac{I_0}{I} = \frac{k_{obs} + k_q[Q]}{k_{obs}} = 1 + k_q\tau_0[Q] \tag{3.4}$$

As dynamic quenching is a rate process that depopulates the excited state, the lifetimes in the absence, τ_0, and presence of a quencher, τ, are given by:

$$\tau_0 = {k_{obs}}^{-1} \tag{3.5}$$

$$\tau = \left(k_{obs} + k_q[Q]\right)^{-1} \tag{3.6}$$

Consequently,

$$\frac{\tau_0}{\tau} = 1 + k_q\tau_0[Q] \tag{3.7}$$

This highlights the fact that for dynamic quenching there is a simultaneous decrease in fluorescence intensity and lifetime. The change to the fluorescence lifetime occurs because quenching is an additional rate process that depopulates the excited state.

During static quenching a non-fluorescent complex is formed between the fluorophore and quencher. When this complex absorbs light it returns to the ground state without emitting a photon. Thus, the dependence of the emission intensity upon quencher concentration can be derived by considering the occurrence of complex formation. The association constant for this process, K_s, is given by[18]:

$$K_s = \frac{[F-Q]}{[F][Q]} \quad \textbf{(3.8)}$$

where [F] is the concentration of the un-complexed fluorophore, [Q] is the quencher concentration and [F-Q] is the concentration of the complex. As the complex is non-fluorescent, the fraction of the fluorescence that remains (F/F_0) is determined by the fraction of the total fluorophores that are not complexed. The total concentration of fluorophore $[F]_0$ is given by:

$$[F]_0 = [F] + [F-Q] \quad \textbf{(3.9)}$$

substituting this into **Eqn. 3.8** gives:

$$K_s = \frac{[F]_0 - [F]}{[F][Q]} = \frac{[F]_0}{[F][Q]} - \frac{1}{[Q]} \quad \textbf{(3.10)}$$

As stated previously, the fluorescence intensities are proportional to concentration so the intensities can be substituted in and **Eqn. 3.10** becomes:

$$\frac{I_0}{I} = 1 + K_s[Q] \quad \textbf{(3.11)}$$

This equation also shows a linear dependence of F_0/F on [Q]. However, in the case of static quenching there is no effect on the fluorescence lifetime. Static quenching causes a fraction of the fluorophores to become non-fluorescent, and thus they are not observed. Fluorescence is only observed from the un-complexed fluorophores, which is not altered by any new decay pathway and thus there is no change to the lifetime. Therefore, in the case of static quenching $\tau_0/\tau = 1$, while in contrast for dynamic quenching, $F_0/F = \tau_0/\tau$.

Previous experiments carried out by the Evans group have shown that the excited-state lifetime of **PF2/6-*b*-P3TMAHT** is unaffected on addition of the nucleotides investigated, suggesting that quenching occurs predominantly by a static quenching mode. This is reasonable considering the electrostatic interaction between the positively charged PT blocks and the negatively charged nucleotides. Stern-Volmer plots derived from the steady-state emission intensity data on addition of the guanosine series (**Section 3.3.2**) are shown as a representative example in **Fig. 3.9**. Each of the Stern-Volmer plots exhibit a steep linear portion that plateaus at

the charge equivalence point. The Stern-Volmer constants for a linear fit to the initial steep portion of the plot up to charge equivalence are shown in **Table 3.1**. The magnitude of these K_S constants and the unaffected lifetime values upon nucleotide addition indicate that quenching proceeds through a static quenching mode. There is a slight difference between the K_s constants on direct excitation of PT block compared to population *via* energy transfer from the PF block, suggesting that a change in the FRET efficiency may also occur on nucleotide binding, this will be discussed further in **Section 3.3.2.3**. However, the deviation from linearity at concentrations above the charge equivalence point may suggest that simple static quenching does not fully describe the quenching behaviour observed.

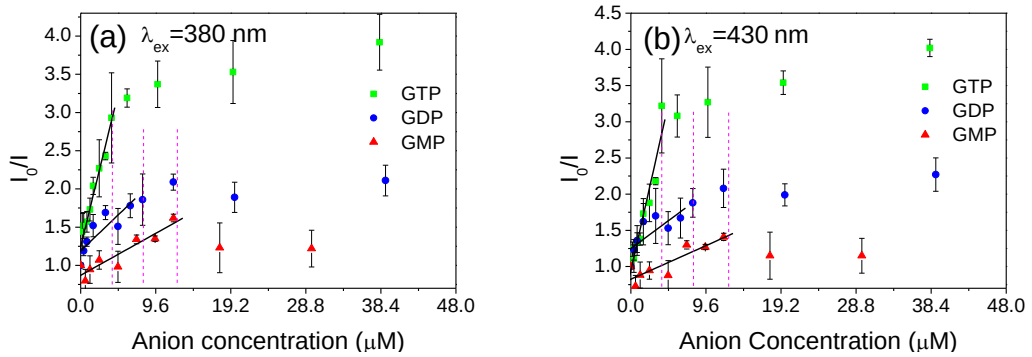

Figure 3.9. Stern-Volmer plots for quenching of PT emission of PF2/6-P3TAHT (9.8 μM (r.u.)) on excitation of (**a**) PF block (λ_{ex} = 380 nm) and (**b**) direct excitation of the PT block (λ_{ex} = 430 nm). The pink dash lines represent the charge equivalence point for the titration with each of the nucleotides (**GTP** - 40 μM, **GDP** - 80 μM, **GMP** – 120 μM)

Table 3.1. Stern-Volmer constants, K_{SV}, for the quenching of the PT block when **PF2/6-*b*-P3TMAHT** is excited into the PF block (λ_{ex} = 380 nm) and when **PF2/6-*b*-P3TMAHT** is excited directly into the PT block (λ_{ex} = 430 nm).

Anion	**K_{SV} (λ_{ex} = 380 nm) (M^{-1})**	**K_{SV} (λ_{ex} = 430 nm) (M^{-1})**
GTP	$1.2 \times 10^5 \pm 3 \times 10^4$	$1.1 \times 10^5 \pm 3 \times 10^4$
GDP	$9.8 \times 10^4 \pm 2 \times 10^4$	$8.0 \times 10^4 \pm 3 \times 10^3$
GMP	$5.2 \times 10^4 \pm 9 \times 10^3$	$4.8 \times 10^4 \pm 2 \times 10^3$
ATP	$1.4 \times 10^5 \pm 2 \times 10^4$	$2.5 \times 10^5 \pm 3 \times 10^4$
CTP	$1.2 \times 10^5 \pm 2 \times 10^4$	$1.0 \times 10^5 \pm 4 \times 10^4$

A deviation from linear behaviour in the Stern-Volmer plot can indicate the involvement of multiple processes in the quenching mechanism. An upward curvature in the Stern-Volmer plots is indicative of combined dynamic and static quenching processes. The fraction of fluorescence is

governed by the product of the fraction of fluorophores that are not complexed and the fraction not quenched by collisional encounters. The modified Stern-Volmer relationship becomes second order in [Q] giving rise to the upward curvature.[19] Whereas a downward curvature in the Stern-Volmer plot, as seen in **Fig. 3.9**, has previously been attributed to a number of different scenarios. One suggestion involves a fraction of the fluorophore population being inaccessible to the quencher species[20] while an alternative sees the quenching of fluorophore emission in ionic micelles being induced by counter-ions within the Stern layer.[21] Each of these possibilities will be discussed in further detail in **Section 3.3.2.1.1**.

3.3.2.1.1 Modelling of Stern-Volmer Plots

Previous studies on the solvent-driven aggregation of **PF2/6-*b*-P3TMAHT** have shown that in water the polymer takes on structures in which the hydrophobic PF block is predominantly contained in the aggregate core.[7] However, this does not preclude the presence of some PT species within this core. Thus, the quenching data were fit to a model which describes a system in which a portion of the fluorophores are buried and therefore inaccessible to the quencher.[20] This leads to two separate populations of fluorophore, one of which is accessible (*a*) to quencher molecules and the other being inaccessible or buried (*b*). The total fluorescence in the absence of quencher (I_0) is given by:

$$I_0 = I_{0a} + I_{0b} \tag{3.12}$$

where the subscript '0' refers to the fluorescence intensity in the absence of quencher. As the intensity of the available fraction, I_{0a}, decreases according to the Stern-Volmer relationship, the buried fraction, I_{0b}, is not quenched and the resulting observed intensity is given by:

$$I = \frac{I_{0a}}{1 + K_a[Q]} + I_{0b} \tag{3.13}$$

where K_a is the quenching constant of the accessible fraction. Subtracting **Eqn. 3.13** from **Eqn. 3.12** gives:

$$\Delta I = I_0 - I = I_{oa} + I_{ob} - \frac{I_{0a}}{1 + K_a[Q]} - I_{0b}$$

$$= I_{0a}\left(1 - \frac{1}{1 + K_a[Q]}\right)$$

$$= I_{oa}\left(\frac{K_a[Q]}{1 + K_a[Q]}\right) \tag{3.14}$$

Dividing **Eqn. 3.13** by **Eqn. 3.14** gives:

$$\frac{I_0}{\Delta I} = \frac{I_{oa} + I_{ob}}{I_{oa}\left(K_a[Q] \Big/ 1 + K_a[Q]\right)}$$

$$= \frac{I_{oa} + I_{ob}}{I_{oa}}\left(\frac{1 + K_a[Q]}{K_a[Q]}\right)$$

$$= \frac{1}{f_a K_a[Q]} + \frac{1}{f_a} \quad \textbf{(3.15)}$$

where f_a is the fraction of the initial fluorescence that is accessible to the quencher and is given by:

$$f_a = \frac{I_{0a}}{I_{0a} + I_{0b}} \quad \textbf{(3.16)}$$

Thus, a plot of $I_0/\Delta I$ *vs*. $1/[Q]$ should yield a straight line with an intercept of $1/f_a$ and a slope of $1/f_a K_a$.

On plotting $I_0/\Delta I$ *vs*. $1/[Q]$ for the quenching with each anion, the resulting data were found to not be completely linear, as can be seen for **GTP** in **Fig. 3.10**. As seen in the earlier/ simpler quenching models, a steep linear portion was noted in these plots, followed by a deviation towards the *x*-axis. The fits to this buried fluorophore model gives K_a constants in the range 4×10^5-3×10^6 M^{-1} and an accessible fraction of fluorophores that decreases with the number of phosphate groups on the anion (**Table 3.2**). These K_a constants are similar in magnitude to the K_s values obtained through Stern-Volmer analysis. However, lack of linearity in these plots indicates that a population of completely inaccessible fluorophores is not the cause of the deviation from the original Stern-Volmer model for static quenching.

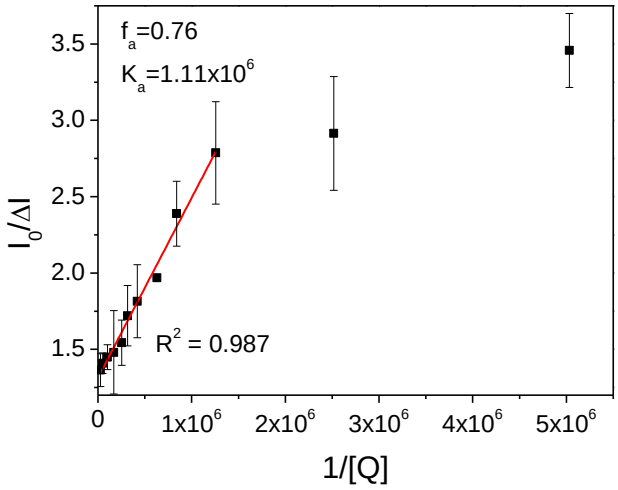

Figure 3.10. Linear fit to buried fluorophore model of modified Stern-Volmer plot (λ_{ex} = 380 nm) for fluorescence quenching of **PF2/6-*b*-P3TMAHT** (9.8 μM (r.u.)) by **GTP** (0 - 38 μM).

Table 3.2. Stern-Volmer constants, K_a, and fraction of buried fluorophores, f_a, derived from fitting to the buried fluorophore model for the quenching of the PT block of **PF2/6-b-P3TMAHT** (λ_{ex} = 380 nm).

Anion	f_a	K_a (λ_{ex} = 380 nm) (M^{-1})
GTP	0.76 ± 0.01	$1.11 \times 10^6 \pm 5 \times 10^4$
GDP	0.49 ± 0.03	$1.05 \times 10^6 \pm 9 \times 10^4$
GMP	0.37 ± 0.03	$2.68 \times 10^6 \pm 1 \times 10^4$
ATP	0.70 ± 0.04	$4.15 \times 10^5 \pm 5 \times 10^4$
CTP	0.57 ± 0.09	$4.23 \times 10^5 \pm 9 \times 10^4$

As mentioned previously, **PF2/6-*b*-P3TMAHT** has been shown to take on an aggregate structure with a PF-rich core and a PT-rich outer surface when in water.[7] This is similar to ionic micelles in solution. Recently a model describing quenching in ionic micelles induced by counter-ions within the Stern layer has been found to accurately describe the quenching of **PF2/6-*b*-P3TMAHT** by smaller halide ions, which follow the order I^- >Br^- >Cl^-.[9] This model takes into account diffusion of a quencher held in the Stern layer into an ionic micelle allowing it to also interact with the inside of the micelle.[21] This is in contrast to the buried fluorophore model in which the buried population is completely inaccessible to the quencher. This ionic micelle model can be understood by considering the relationship between quencher concentration and total concentration. Through consideration of the occurrence of multi equilibria, the average number of small molecules bound to a micelle, *b*, has been shown to be related to the total concentration of that species in solution by[21]:

$$b = \frac{nK_n[Q]}{1 + K_n[Q]} \quad \textbf{(3.17)}$$

where *n* is the number of vacant sites and K_n is the association constant between the CPE 'micelle' and the nucleotide quencher. As quenching for this model is only affected by species in the Stern layer, the effective quencher concentration becomes equivalent to the number of bound species, *b*. Expressing the effective concentration in this manner ensures that no assumptions are made about the size of structure of the micelle surface. At a given quencher concentration and micelle size the rate constant for decay, k_m, is given by:

$$k_m = k_{obs} + k_q b \quad \textbf{(3.18)}$$

where k_q is the quenching rate constant of the polythiophene block by the bound nucleotides. Combining **Eqn. 3.17** and **Eqn. 3.18** gives:

$$k_m = k_{obs} + \frac{k_q n K_n[Q]}{1 + K_n[Q]} \quad \textbf{(3.19)}$$

Substituting **Eqn. 3.19** into **Eqn. 3.3** and dividing this new expression into **Eqn. 3.2** gives rise to the following model:

$$\frac{I_0}{I} = 1 + \frac{\tau_0 k_q n K_n[Q]}{1 + K_n[Q]} = 1 + \frac{K_{sv} n K_n[Q]}{1 + K_n[Q]} \quad \textbf{(3.20)}$$

The quenching data were plotted as (I_0/I)-1 *vs.* [Q] and fitted to the model in **Eqn. 3.20**. This led to good fits to the quenching data for the nucleotides, see **Fig. 3.11** for **GTP** as a representative example (see Appendix **Fig. A.3.2** for the other systems). The K_{SV} values (**Table 3.3**) are all in the range of that reported for **PF2/6-*b*-P3TMAHT** when quenched by NaCl.[9] The good fits to the data and the agreement with literature for quenching by NaCl indicates that the quenching is adequately described by this multi-equilibrium model in which the quenching is controlled by the nucleotides held in the Stern layer of a charged **PF2/6-*b*-P3TMAHT** aggregate that acts like an ionic micelle, most likely with the PT blocks on the aggregate surface for the most part. The association constants extracted from fitting to this model are similar to those observed when fitting to the initial linear portion of the Stern-Volmer plots (**Table 3.2**).

Quenching clearly decreases with the number of phosphate groups on the anion as the order of the K_{SV} values follows the order **GTP**>**GDP**>**GMP**. While quenching for the purine based anions is higher than that for the pyrimidine-based **CTP**. If the observed quenching was simply brought about by an electrostatic interaction between the phosphate groups of the nucleotides and the positively charged PT block, then each of the triphosphate series should show similar binding constants. This however is not the case, indicating a more complex mechanism.

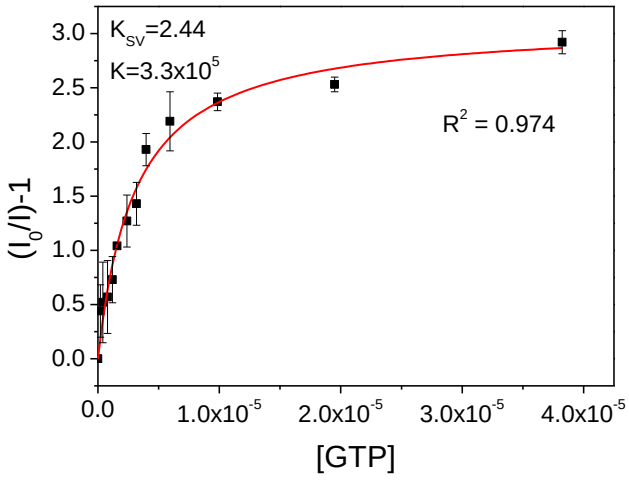

Figure 3.11. Fit to a multi-equilibrium model of modified Stern-Volmer plot (λ_{ex} = 380 nm) for fluorescence quenching of **PF2/6-*b*-P3TMAHT** (9.8 μM (r.u.)) by **GTP** (0 - 38 μM).

Table 3.3. Stern-Volmer constants, K_{SV}, and association constants, K_n, derived from fitting to the ionic micelle model for the quenching of the PT block of **PF2/6-*b*-P3TMAHT** (λ_{ex} = 380 nm).

Anion	K_{SV} (M^{-1})	K_n (M^{-1})
GTP	2.4 ± 0.1	$3.3\times10^5 \pm 5\times10^4$
GDP	1.8 ± 0.1	$2.5\times10^5 \pm 8\times10^4$
GMP	0.5 ± 0.1	$1.3\times10^5 \pm 9\times10^4$
ATP	2.0 ± 0.2	$1.3\times10^5 \pm 3\times10^4$
CTP	1.4 ± 0.2	$2.4\times10^5 \pm 9\times10^4$

3.3.2.2 Isothermal Titration Calorimetry (ITC) Studies

As the PL data indicate that quenching occurs due to electrostatically-bound nucleotides within the Stern layer of the ionic polymer aggregate structure, the binding between **PF2/6-*b*-P3TMAHT** and **GTP** was examined using isothermal calorimetry (**Fig. 3.12**). ITC has become an increasingly popular tool to study the binding of conjugated polyelectrolytes with oppositely charged species, in particular surfactants.[22-24] Isothermal titrations allow direct observation of the binding enthalpy (ΔH^0) and derivation of entropy and K_a (association constant) from curve fitting and the free energy relationship, $\Delta G^0=\Delta H^0-T\Delta S^0= -RTlnK_a$.[25] This plot represents heat evolved *vs.* molar ratio for injecting **GTP** into a **PF2/6-*b*-P3TMAHT** solution which has been corrected for the contribution of the heat of dilution of the polymer and normalised by the amount of added **GTP**. The resulting thermodynamic parameters were calculated assuming a single set of equivalent binding sites and are displayed in **Table 3.4**. For each injection, the heat released or absorbed, q, is given by[26]:

$$q = V\Delta H\Delta[L_B] \quad \textbf{(3.21)}$$

where $\Delta[L_B]$ is the change in the bound nucleotide concentration, ΔH is the change in enthalpy and V is the volume of the reaction. The total cumulative heat released or absorbed, Q, is directly proportional to the total amount of the bound ligand[26]:

$$Q = V\Delta H\sum \Delta[L_B] = V\Delta H[L_B] \quad \textbf{(3.22)}$$

where $[L_B]$ is the concentration of bound nucleotide. For a system exhibiting a single set of equivalent, independent binding sites the concentration of bound nucleotide is given by[26]:

$$[L_B] = [M]\frac{nK_a[L]}{1+K_a[L]} \quad \textbf{(3.23)}$$

where $[M]$ is the concentration of CP macromolecule capable of binding the nucleotide, K_a is the CP-nucleotide association constant, n is the number of binding sites and $[L]$ is the concentration of

the free nucleotide. Thus, by substituting **Eqn. 3.23** into **Eqn. 3.22** the cumulative heat released can be expressed as:

$$Q = V[M]\sum \frac{n\Delta H K_a[L]}{1 + K_a[L]} \quad \textbf{(3.24)}$$

which can be related to the total ligand concentration by way of the mass conservation expression $[L_T]=[L_B]+[L]$, where $[L_T]$ is the total nucleotide concentration. Fitting to the calorimetric data provides values for n, K_a and ΔH.

Table 3.4. Thermodynamic parameters of the interaction between **GTP** and **PF2/6-*b*-P3TMAHT**.

Anion	Number of binding sites, n	Binding constant, K_a (M^{-1})	ΔH^0 (kJ mol^{-1})	T (K)	ΔS^0 (kJ mol^{-1} K^{-1})	ΔG^0 (kJ mol^{-1})
GTP	0.152 ±0.009	$1.2\times10^6\pm5\times10^5$	-10.3±0.9	293	0.082±0.002	-34.3±0.9

When examining protein association reactions it has previously been found that a negative ΔH^0 and positive ΔS^0 value is indicative of ionic or charge neutralisation processes.[27] The negative ΔH^0 and positive ΔS^0 value obtained here indicated that the binding of **GTP** to **PF2/6-*b*-P3TMAHT** is both enthalpically and entropically favourable.[25] It is known that the binding of surfactants with oppositely charged conjugated polyelectrolytes shows an initial endothermic binding when the polymer backbone is hydrophilic and an exothermic binding when the polymer backbone is hydrophobic.[22] An initial exothermic binding is shown for **PF2/6-*b*-P3TMAHT** in **Fig. 3.12a**. This is attributed to cooperative binding[23, 28] between the oppositely charged nucleotides and the PT block of **PF2/6-*b*-P3TMAHT**. A transition between exothermic and endothermic behaviour, as is seen here, has been observed previously upon increasing the charge density of the polymer backbone.[29]

The slight discrepancy between the binding constant obtained from the ITC data compared to that observed on fitting the Stern-Volmer plots is most likely due to the fact that the **PF2/6-*b*-P3TMAHT** aggregate structures may not act identically to ionic micelles in the solvent system described here. However, the comparable values of the binding constants suggest that this model is a more than reasonable approximation.

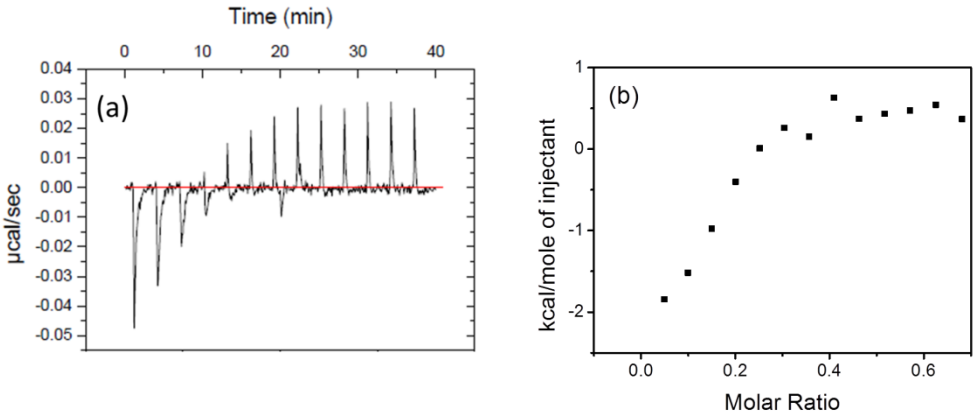

Figure 3.12. (**a**) Thermogram and (**b**) differential enthalpy curve for the titration of **GTP** (0- 30 mM) into **PF2/6-*b*-P3TMAHT** (60 mM) at 20 °C.

3.3.2.3 Change in FRET Efficiency

Direct excitation of the PF absorption band (λ_{ex} = 380 nm), results in emission from both the PF and PT blocks of **PF2/6-*b*-P3TMAHT**. This has previously been attributed to Förster resonance energy transfer (FRET) from the PF block (donor, *D*) into the PT block (acceptor, *A*) due to the appearance of a band attributed to PF excitation in the excitation spectrum of **PF2/6-*b*-P3TMAHT** at the monitoring wavelength of PT emission (λ_{ex} = 380 nm), see Appendix, **Fig. A.3.1**. FRET is based on long-range dipole-dipole interactions,[30, 31] which requires a strong overlap between donor emission and the acceptor absorption spectra.[30] As shown in **Fig. 3.13** this criterion is met by the PF and PT blocks of **PF2/6-*b*-P3TMAHT**.

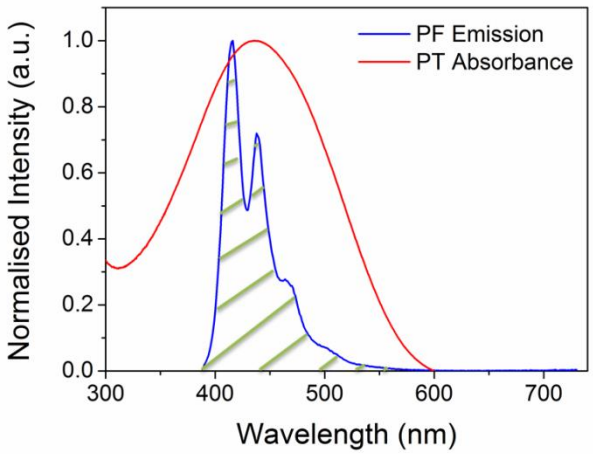

Figure 3.13. Spectral overlap between the emission spectrum of **PF2/6** (blue line, λ_{ex} = 370 nm in THF) and UV/Vis absorption spectrum of **P3TMAHT** (red line, λ_{ex} = 430 nm in aqueous solution). The green shaded region highlights the spectral overlap.

The spectral overlap integral, J_{DA}, was quantified as 1.47×10^{-14} M^{-1} cm^3 for the PF-PT pair using **Eqn. 1.7**. Following this the Förster distance, R_0, was calculated to be 2.9 nm using **Eqn. 1.6**.

Due to the fact that these materials are in the solution phase, κ was taken to be 2/3, which is appropriate for dynamic random averaging of the donor and acceptor.[30] The R_0 value is extremely similar to those reported for both polyfluorene and polythiophene based systems, ($R_0 \approx 2.6 \sim 3.0$ nm).[32]

The FRET efficiency is highly dependent on the centre to centre distance between *D* and *A*,[33] as described in **Eqn. 1.5**. Thus, any alterations to the distance between *D* and *A* will affect the efficiency of energy transfer. The PL titrations and Stern-Volmer plots indicate a static quenching mode influenced by electrostatic binding between the PF block and the nucleotides. The ground-state complex formed may cause a reorganisation of the polymer aggregate structure on binding. It is possible that this reorganisation may change the PF-PT distance, thereby affecting the FRET efficiency between the two blocks.

The structures of both **PF2/6-*b*-P3TMAHT** and the PT block alone, **P3TMAHT**, in solution have been shown to be to be highly dependent on the solvent system in use and on interaction with oppositely charged surfactants.[5, 7, 8, 10] The addition of the negatively charged surfactant sodium octyl sulphate (SOS) to **P3TMAHT** causes the spherical polymer particles to change shape to cylindrical or sheet-like aggregates depending on the SOS concentration.[10] Small-angle neutron scattering (SANS) measurements will be used in the future to quantify the structure of **PF2/6-*b*-P3TMAHT** in solution on addition of the nucleotides discussed here.

3.3.2.4 (Spectro)electrochemistry

Although a change in the CP aggregate structure in solution is possible on addition of the nucleotides, the fact that the PF emission is relatively unaffected suggests that it is certainly not a major component of the observed quenching. Another possible mechanism is electron transfer involving the PT block of the diblock CP. To examine this possibility, spectroelectrochemical measurements were carried out. Spectroelectrochemistry measures a change in the absorption of a species on changing the redox potential or *vice versa*. The cyclic voltammograms (CV) for **PF2/6-*b*-P3TMAHT** and **P3TMAHT** alone are shown in **Fig. 3.14**. **P3TMAHT** contains a reversible redox couple at 1.03/0.92 V and an irreversible band at -0.01 V, while **PF2/6-*b*-P3TMAHT** exhibits a similar oxidation peak at 0.88 V and a reduction peak at -0.33 V. Each of these spectra match those previously reported for similar polymers.[34-36]

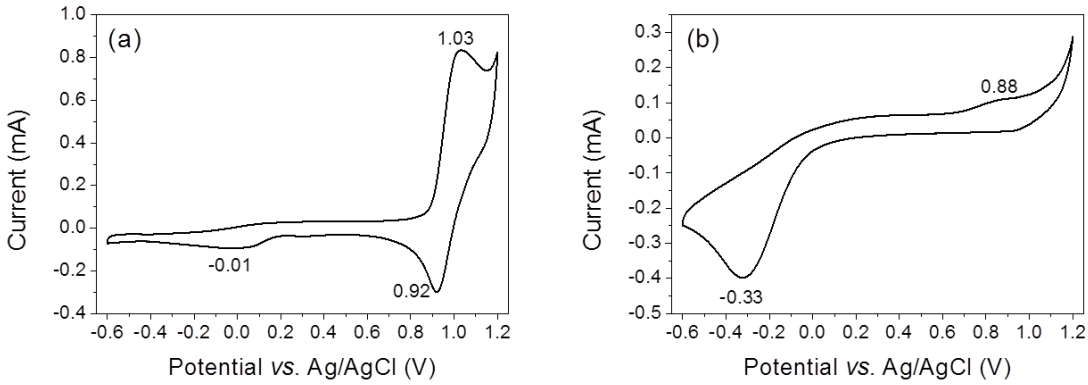

Figure 3.14. Cyclic voltammogram for (**a**) **P3TMAHT** in H_2O and (**b**) **PF2/6-*b*-P3TMAHT** in THF/H_2O 20/80 *v/v* at 50 mV s^{-1} using Pt as the working and counter electrode, Ag/AgCl as reference electrode and KCl (0.1 M) as the supporting electrolyte.

To examine the change in polymer absorption on oxidation or reduction the UV/Vis spectrum was measured at set intervals of 30 s as the potential of the cell was held at a certain potential. For these experiments **P3TMAHT** was used as a simple model system rather than the diblock copolymer. As can be seen in **Fig. 3.15**, when **P3TMAHT** is held at its oxidation potential (1.03 V, determined from the CV experiments shown in **Fig. 3.14a**) the absorption band at 430 nm, attributed to the **P3TMAHT** backbone, reduces in intensity and a second band appears with a peak maximum at 330 nm. An isosbestic point occurs at 365 nm indicating the presence of two species in solution. When **P3TMAHT** is held at its reduction potential (-0.01 V), the intensity of the band at 430 nm reduces but retains its shape and no second band appears. The growth of the second band at 330 nm is most likely due to the oxidised **P3TMAHT** species, with the loss of electrons from the polythiophene backbone causing the drastic shift in optical properties. On titration with the nucleobases under investigation there is no dramatic blue shift in the PT absorption band (**Fig. 3.4a** and **3.5a**) indicating that the nucleotides are not causing the PT to be oxidised. However, the reduction in intensity of the band at 430 nm (without the subsequent growth of another band) (**Fig. 3.15a**) matches the behaviour of the absorbance band of the PT block on addition of the nucleotides (**Fig. 3.4a** and **3.5a**) suggesting the possibility that the polymer is reduced following interaction with the nucleotides investigated.

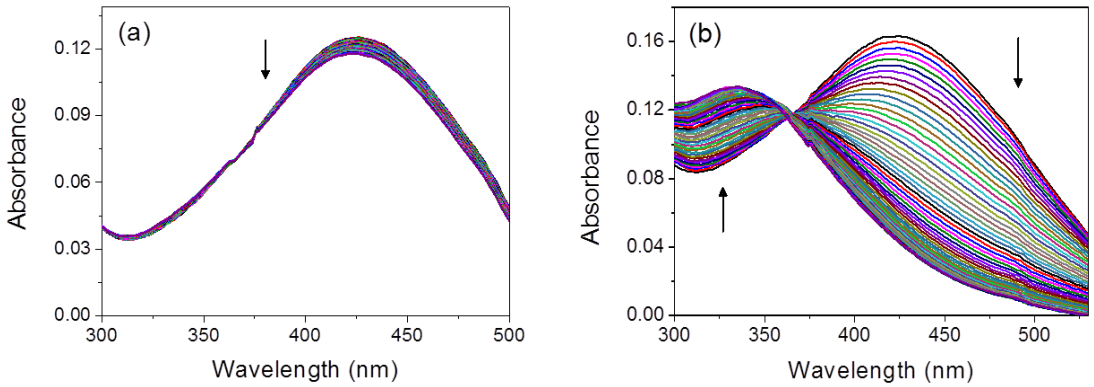

Figure 3.15. (**a**) UV/Vis spectroelectrochemical results of **P3TMAHT** in MeOH held at -0.01 V *vs*. Ag/AgCl (**b**) UV/Vis spectroelectrochemical results of **P3TMAHT** in MeOH held at +1.03 V *vs*. Ag/AgCl.

The possibility of photo-induced electron transfer between **P3TMAHT** and the nucleotides was investigated using the Rehm-Weller equation[35, 38]:

$$\Delta G^0 = E_{ox}(D) - E_{red}(A) - E_{00} + C \qquad \textbf{(3.25)}$$

where $E_{ox}(D)$ is the oxidation potential of the donor species, E_{red} (A) is the reduction potential of the acceptor species, E_{00} is the zero-zero transition of the CPE and C is a solvent term that can be ignored in polar solvents.[39, 40] The CVs of the nucleotides in water could only be measured between -0.6 and 1.2 V due to the electrochemical window of water, outside of which oxygen and hydrogen evolution occur. Each of these spectra contained a number of bands attributed to the redox activity of the OH groups of the varying number of phosphates on each nucleotide (see Appendix, **Fig. A.3.3**). The oxidation potentials of the nucleobases (the heterocyclic components in the nucleotides) have previously been reported in organic solvents to be above the electrochemical window stated above.[38] Due to the fact that the highly polar nucleotides are not soluble in organic solvents and that nucleobases are the most redox active components of the nucleotides the previously reported redox potentials of the nucleobases were taken as a reasonable estimation of the redox potentials of the nucleotides under investigation. These potentials are outlined in **Table 3.5.**

Table 3.5. Electrochemcial potentials for guanosine, adenosine and cytidine (reduction potentials obtained from [38] and oxidation potentials obtained from [41]).

Nucleobase	E_{ox} **(V)**	E_{red} **(V)**
Guanosine	-2.56	1.49
Adenosine	-2.32	1.62
Cytidine	-2.15	1.8

The free energy change for each of the anions was estimated using the Rehm-Weller equation for both the situation where the polymer acts as the electron donor and the electron acceptor, the results of which are shown in **Table 3.6**. E_{00} was calculated from the overlap of the absorption and emission spectrum of **P3TMAHT** and found to be 2.29 eV.

Table 3.6. Table of free energy change (ΔG^0) for electron transfer calculated using the Rehm-Weller equation with **P3TMAHT** as the electron acceptor or electron donor.

Nucleobase	Donor (eV)	Acceptor (eV)
Guanosine	1.25	-0.37
Adenosine	1.01	-0.24
Cytidine	0.84	-0.06

As can be seen from **Table 3.6** the scenario where **P3TMAHT** accepts an electron from **GTP** has a negative ΔG^0, suggesting it will occur spontaneously. In contrast if **P3TMAHT** acts as the electron donor, the process has a positive ΔG^0, suggesting that it does not occur. This is an unusual situation as in the majority of cases, polythiophenes act as an electron donor, most notably in P3HT in the electron transport layer in organic solar cells.[42, 43] However, the nucleobases are reasonably strong reducing agents and the order of quenching for the nucleotides follows the oxidation potential of their respective nucleobases guanosine>adenosine>cytidine. This situation is not completely unprecedented as electron transfer to polythiophene is suggested in an imidazolium modified polythiophene-CdSe quantum dot system.[35] Moreover, electron transfer from DNA to naphthalimide-viologen dyads has been shown to occur affecting the triplet state of the naphthalimide-viologen complex.[41, 44]

3.3.2.5 Transient Absorption Studies

Spectroelectrochemical measurements indicate the occurrence of electron transfer from the nucleobase to the PT block. As such nanosecond (ns)-flash photolysis experiments were carried out as this technique can be used to show the presence of such oxidised nucleobase species. Flash photolysis is a 'pump/probe' technique in which the absorption characteristics of a species in its excited state are studied. To create this excited state the ground state species of the sample must first undergo absorption. To generate a sufficiently high concentration of excited state species a powerful excitation source is required. A ns-laser is used to excite the sample while a continuous steady-state light source is used to monitor the absorbance of the sample solution. This technique produces a difference spectrum (ΔOD) which compares the transmittance through the sample before and after creation of the excited state. Thus, in this spectrum any absorbance from the

ground state species is observed as a bleaching (negative Δ*OD* values), while absorbance from the excited state will appear as a positive band. Measuring the transmittance through the sample at varying times following formation of the excited state allows information on the kinetics of the excited state decay to be extracted along with the energies of states involved.

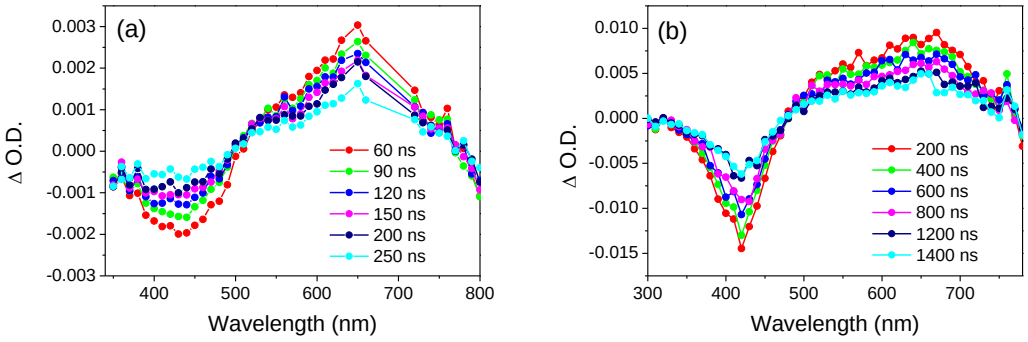

Figure 3.16. Nanosecond (ns) singlet-triplet difference spectra of (**a**) **PF2/6-*b*-P3TMAHT** and (**b**) **P3TMAHT** in aqueous solution (λ_{ex} = 355 nm). The solution was degassed for 20 min prior to measurement.

The transient absorption spectra of both **PF2/6-*b*-P3TMAHT** and **P3TMAHT** in aqueous solution are shown in **Fig. 3.16**. The spectrum of **PF2/6-*b*-P3TMAHT** shows depletion of ground-state (S_1) absorbance at 430 nm and the appearance of a band at 650 nm assigned to the first excited T_1 state. The **P3TMAHT** spectrum shows ground state bleaching at 420 nm and T_1 absorbance at 670 nm. These results are in good agreement with the results previously reported for **PF2/6-*b*-P3TMAHT** and similar alternating fluorene-thiophene copolymers.[7, 45] Investigation of alternating fluorene-thiophene copolymers have indicated that the energies of singlet depletion and triplet absorption on the copolymer are essentially those of the thiophene block,[7, 45] as polyfluorene triplet states occur at >700 nm.[46] The difference between the homopolymer and the copolymer arises due to the influence of the polyfluorene component, with the most likely scenario for triplet formation in the copolymer involving energy migration from the S_1 state to the polythiophene on excitation of the polyfluorene followed by intersystem crossing on the polythiophene block.[7, 45] This is suggested to be due to the high efficiency of triplet state formation of polythiophenes, polymers which is most likely due to spin-orbit coupling caused by the moderate heavy atom effect induced by the sulfur heteroatom.[7] However, on addition of the nucleotide species no observable change in the transient absorption spectra was measured. Although this may indicate that no oxidised species is formed, it is also possible that the appearance of this new species is masked by the presence of the CP spectrum.

It is also possible to measure the intensity as a function of time at a specific wavelength. This allows the lifetime of the excited triplet state to be determined. The triplet state lifetime (τ_t) was determined for **P3TMAHT** and **PF2/6-*b*-P3TMAHT** as a function of **GTP** concentration; and is tabulated in **Table 3.7**. The results show the lifetime of the triplet state decreases on addition of

all the anions suggesting that the triplet is partially affected by the CP-nucleobase interaction, however, further ns-flash photolysis experiments are required.

Table 3.7. Triplet lifetime (τ_t) (λ_{em} = 355 nm) for **P3TMAHT** and **PF2/6-*b*-P3TMAHT** in the absence and presence of **GTP**. Numbers in brackets show the concentration of nucleotide added represented in terms of charge ratio between the charge on the nucleotide and polymer repeat units.

Sample	k_t (s^{-1})	τ_t (µs)
P3TMAHT (0.16 mM (r.u.))	$7.1\times10^4 \pm 9.6\times10^3$	14 ± 1.1
P3TMAHT + GTP (0.08 mM)	$1.3\times10^5 \pm 8.7\times10^4$	7.6 ± 0.4
PF2/6-*b*-P3TMAHT (32 µM (r.u.))	$1.2\times10^5 \pm 2.5\times10^4$	8.1 ± 1.1
PF2/6-*b*-P3TMAHT + GTP (6.4 µM)	$1.3\times10^5 \pm 1.7\times10^4$	7.6 ± 0.9

3.4 Conclusions

The optical response of the diblock copolymer **PF2/6-*b*-P3TMAHT** was successfully mapped on addition of a range of biologically important anions; **GTP**, **GDP**, **GMP**, **ATP** and **CTP**. Addition of these nucleotides causes a red-shift in the absorption band attributed to the PT block, leaving the PF band unaffected. Similarly in the PL spectra, addition of the nucleotides in question leaves the PF emission unchanged, while giving rise to quenching of the PT emission, the magnitude of which is dependent on the charge and nature of the anion. The order of quenching appeared to follow **GTP**>**GDP**>**GMP** for the guanosine series with differing numbers of phosphates and **GTP**≈**ATP**>**CTP** on comparison of nucleotides with different nucleobase cores but an identical number of phosphate groups. This PL response was further quantified using CIE colour coordinates which show a shift from the red spectral region towards the blue on addition of the nucleotide, the magnitude of which decreases with the number of phosphate groups. These results highlight both the sensitivity and selectivity of the optical response of **PF2/6-*b*-P3TMAHT** to various nucleotides, characteristics which are vital for the development of any type of sensing platform.

On examination of the mechanism behind the observed quenching it was found to be a complex interplay of different processes. Initially Stern-Volmer plots of the quenching data along with lifetime measurements carried out previously in the Evans group indicated that the quenching occurred through a static mode. However, deviations from linearity at higher concentrations in the Stern-Volmer plots suggested that the standard static quenching model did not completely describe the processes occurring. As **PF2/6-*b*-P3TMAHT** has previously been shown to form aggregates with a PF-rich core in water, the possibility that a portion of the PT blocks were ‘buried’ within this core and therefore inaccessible to the quencher was examined. Once again, a deviation from

linearity indicated that this model did not accurately describe the quenching process. A similar situation was then considered in which the quenching was modelled using a multi-equilibrium model which represents quenching in ionic micelles induced by counter-ions within the Stern layer. This model led to good fits to the entire range of quenching data. The structure of **P3TMAHT** aggregates has previously been shown to be dramatically altered by the presence of oppositely charged surfactants. Thus, any change in the **PF2/6-*b*-P3TMAHT** aggregate structure brought about by the presences of the nucleotides investigated here will be probed in the future using small-angle neutron scattering. Spectroelectrochemistry was used to examine the possibility of electron transfer between the nucleobase and the polymer. These experiments suggested the occurrence of electron transfer from the nucleobase to the PT block of the polymer. These results are contrary to literature discussing PTs used in solar cell technology in which the PT acts at and electron donor rather than an electron acceptor. Thus, to further examine the formation of the nucleobase oxidised species ns-flash photolysis was carried out on the **P3TMAHT** block alone and on addition of **GTP**. A signal for the guanine radical was not observed during these experiments, possibly due to the fact that it was masked by the polymer spectrum. However, a decrease in the triplet lifetime of the polymer was noted on addition of GTP, suggesting that the triplet state is somehow affected by the CP-nucleobase interaction.

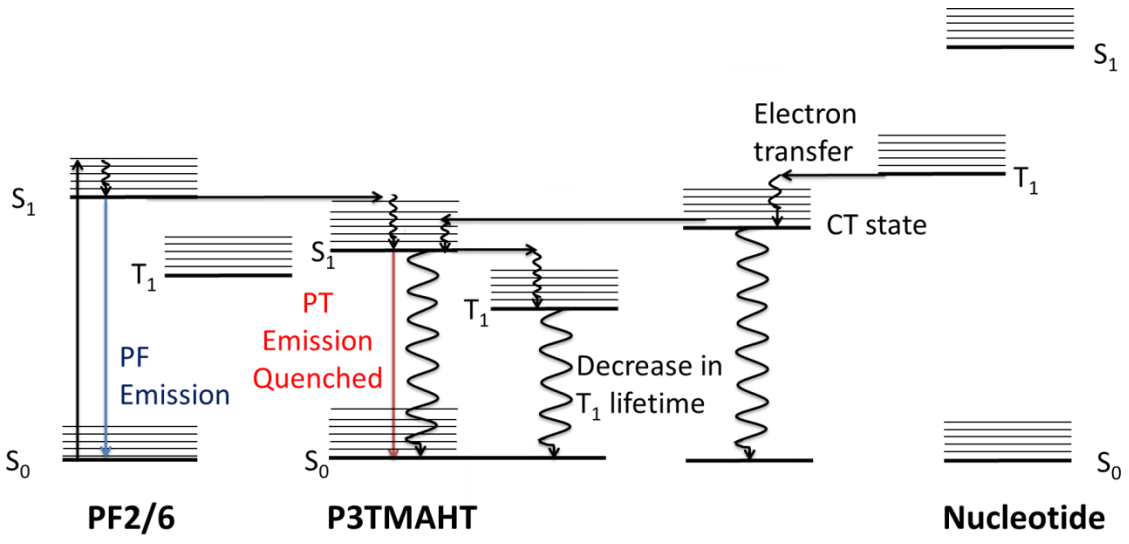

Figure 3.17. Schematic representation of the proposed mechanism of fluorescence quenching of **PF2/6-*b*-P3TMAHT** by the nucleotides under investigation, showing electron transfer from the nucleotide to the singlet of the PT block *via* a charge transfer (CT) state.

Taking the above results into account, the proposed mechanism involves electrostatic binding of the nucleotide to the PT block of **PF2/6-*b*-P3TMAHT** *via* the phosphate groups. Following this a non-fluorescent species is formed through electron transfer from the nucleobase to the singlet of PT block which is mediated by a possible charge transfer state (**Fig. 3.17**). The order of quenching for the triphosphate series follows the oxidation potentials of the nucleobases while the order of quenching for the guanosine series (**GTP**>**GDP**>**GMP**) is rationalised by the fact that

an increased number of phosphate groups should lead to stronger interactions with the charged PT block bringing the nucleotide and polymer into closer contact. The sensitivity and selectivity of the observed optical response and subsequent proposed mechanism on addition of the nucleotides **GTP**, **GDP**, **GMP**, **ATP** and **CTP** to **PF2/6-*b*-P3TMAHT** highlights its potential as a sensory platform.

3.5 References

1. P. Bujak, I. Kulszewicz-Bajer, M. Zagorska, V. Maurel, I. Wielgus and A. Pron, *Chem. Soc. Rev.*, 2013, **42**, 8895-8999.
2. H.-Y. Hsueh, C.-T. Yao and R.-M. Ho, *Chem . Soc. Rev.*, 2015, **44**, 1974-2018.
3. M. C. Orilall and U. Wiesner, *Chem . Soc. Rev.*, 2011, **40**, 520-535.
4. G. Tu, H. Li, M. Forster, R. Heiderhoff, L. J. Balk, R. Sigel and U. Scherf, *Small*, 2007, **3**, 1001–1006.
5. A. Gutacker, S. Adamczyk, A. Helfer, L. E. Garner, R. C. Evans, S. M. Fonseca, M. Knaapila, G. C. Bazan, H. D. Burrows and U. Scherf, *J. Mater. Chem.*, 2010, **20**, 1423-1430.
6. U. Scherf, A. Gutacker and N. Koenen, *Acc. Chem. Res.*, 2008, **41**, 1086-1097.
7. A. Gutacker, N. Koenen, U. Scherf, S. Adamczyk, J. Pina, S. M. Fonseca, A. J. M. Valente, R. C. Evans, J. S. de Melo, H. D. Burrows and M. Knaapila, *Polymer*, 2010, **51**, 1898-1903.
8. M. Knaapila, R. C. Evans, A. Gutacker, V. M. Garamus, M. Torkkeli, S. Adamczyk, M. Forster, U. Scherf and H. D. Burrows, *Langmuir*, 2010, **26**, 5056-5066.
9. S. M. Fonseca, R. P. Galvao, H. D. Burrows, A. Gutacker, U. Scherf and G. C. Bazan, *Macromol. Rapid Commun.*, 2013, **34**, 717-722.
10. R. C. Evans, M. Knaapila, N. Willis-Fox, M. Kraft, A. Terry, H. D. Burrows and U. Scherf, *Langmuir*, 2012, **28**, 12348−12356.
11. M. Knaapila, T. Costa, V. M. Garamus, M. Kraft, M. Drechsler, U. Scherf and H. D. Burrows, *J. Phys. Chem. B*, 2015, **119**, 3231-3241.
12. J. M. Berg, J. L. Tymocko and L. Stryer, in *Biochemistry*, W. H. Freeman and Company, 2012, pp. 114-116.
13. J. M. Berg, J. L. Tymocko and L. Stryer, in *Biochemistry*, W. H. Freeman and Company, 2012, pp. 446 - 449.
14. H. Dugas, *Bioorganic Chemistry: A Chemical Approach to Enzyme Action*, Springer, 1981.
15. D. S. Wishart, D. Tzur, C. Knox, R. Eisner, A. C. Guo, N. Young, D. Cheng, K. Jewell, D. Arndt, S. Sawhney, C. Fung, L. Nikolai, M. Lewis, M.-A. Coutouly, I. Forsythe, P. Tang, S. Shrivastava, K. Jeroncic, P. Stothard, G. Amegbey, D. Block, D. D. Hau, J. Wagner, J. Miniaci, M. Clements, M. Gebremedhin, N. Guo, Y. Zhang, G. E. Duggan, G. D. MacInnis, A. M. Weljie, R. Dowlatabadi, F. Bamforth, D. Clive, R. Greiner, L. Li, T. Marrie, B. D. Sykes, H. D. Vogel and L. Querengesser, *Nucleic. Acids Res.*, 2007, **35**, D521−D526.
16. U. Scherf, S. Adamczyk, A. Gutacker and N. Koenen, *Macromol. Rapid Commun.*, 2009, **30**, 1059-1065.
17. J. R. Lakowicz, in *Principles of Fluorescence Spectroscopy*, Springer, 2006, p. 277.
18. J. R. Lakowicz, in *Principles of Fluorescence Spectroscopy*, Springer, 2006, pp. 278-282.
19. J. R. Lakowicz, in *Principles of Fluorescence Spectroscopy*, Springer, 2006, p. 283.
20. J. R. Lakowicz, in *Principles of fluorescence Spectroscopy*, Springer, 2006, p. 289.
21. H. D. Burrows, S. o. J. Formosinho, M. F. J. R. Paiva and E. J. Rasburn, *J. Chem. Soc., Faraday Trans. 2*, 1980, **76**, 685-692.
22. I. E. Franco, P. Lorchat, J. P. Lamps, M. Schmutz, A. Schroder, J. M. Catala, J. Combet and F. Schosseler, *Langmuir*, 2012, **28**, 4815-4828.
23. Y. Lapitsky, M. Parikh and E. W. Kaler, *J. Phys. Chem. B*, 2007, **111**, 8379-8387.
24. X. Wang, Y. Li, J. Li, J. Wang, J. Wang, Z. Guo and H. Yan, *J. Phys. Chem. B*, 2005, **109**, 10807-10812.

25. P. S. Nagle, S. J. Quinn, J. M. Kelly, D. H. O'Donovan, A. R. Khan, F. Rodriguez, B. Nguyen, W. D. Wilson and I. Rozas, *Org. Biomol. chem.*, 2010, **8**, 5558–5567.
26. E. Freire, O. L. Mayorga and M. Straume, *Anal. Chem.*, 1990, **62**, 950-959.
27. P. D. Ross and S. Subramanian, *Biochemistry*, 1981, **20**, 3096-3102.
28. C. Wang and K. C. Tam, *Langmuir*, 2002, **18**, 6484-6490.
29. C. Wang and K. C. Tam, *J. Phys. Chem. B*, 2004, **108**, 8976-8982.
30. H. Y. Byun, I. J. Chung, H. K. Shim and C. Y. Kim, *Macromolecules*, 2004, **37**, 6945-6953.
31. F. Kong, Y. M. Sun and R. K. Yuan, *Nanotechnology*, 2007, **18**, 265707.
32. K. F. Karlsson, P. Asberg, K. P. R. Nilsson and O. Inganas, *Chem. Mater.*, 2005, **17**, 4202-4211.
33. K. S. Adarsh, M. K. Singh, M. A. Shivkumar, M. K. Rabinal, B. N. Jagatap, B. G. Mulimani, M. I. Savadatti and S. R. Inamdar, *J. Lumin.*, 2015, **160**, 216-222.
34. M. Dobbelin, R. Tena-Zaera, R. Marcilla, J. Iturri, S. Moya, J. A. Pomposo and D. Mecerreyes, *Adv. Funct. Mater.*, 2009, **19**, 3326–3333.
35. R. van Beek, A. P. Zoombelt, L. W. Jenneskens, C. A. van Walree, C. de Mello Donega, D. Veldman and R. A. Janssen, *Chem. Eur. J.*, 2006, **12**, 8075-8083.
36. Y. Zhang, S. Tu, K. Mitsudo, H. Tanaka, S. Suematsu, K. Machida, D. Horii, S. Ishimoto and K. Tamamitsu, *Tet. Lett.*, 2009, **50**, 6057-6059.
37. B. Zhao, D. Liu, L. Peng, H. Li, P. Shen, N. Xiang, Y. Liu and S. Tan, *Euro. Poly. J.*, 2009, **45**, 2079-2086.
38. C. A. M. Seidel, A. Schulz and M. H. M. Sauer, *J. Phys. Chem.*, 1996, **100**, 5541-5553.
39. T. Heinlein, J.-P. Knemeyer, O. Piestert and M. Sauer, *J. Phys. Chem. B*, 2003, **107**, 7957-7964.
40. M. Torimura, S. Kurata, K. Yamada, T. Yokomaku, Y. Kamagata, T. Kanagawa and R. Kurane, *Anal. Sci.*, 2001, **17**, 155-160.
41. J. E. Rogers, S. J. Weiss and L. A. Kelly, *J. Am. Chem. Soc.*, 2000, **122**, 427-436.
42. M. T. Dang, L. Hirsch, G. Wantz and J. D. Wuest, *Chem. Rev.*, 2013, **113**, 3734−3765.
43. A. Li, J. Amonoo, B. Huang, P. K. Goldberg, A. J. McNeil and P. F. Green, *Adv. Funct. Mater.*, 2014, **24**, 5594-5602.
44. J. E. Rogers, T. P. Le and L. A. Kelly, *Photochem. Photobiol.*, 2001, **73**, 223-229.
45. S. M. Fonseca, J. Pina, L. G. Arnaut, J. S. de Melo, H. D. Burrows, N. Chattopadhyay, L. Alcácer, A. Charas, J. Morgado, A. P. Monkman, U. Asawapirom, U. Scherf, R. Edge and S. Navaratnam, *J. Phys. Chem. B*, 2006, **110**, 8278-8283.
46. A. P. Monkman, C. Rothe, S. King and F. Dias, *Adv. Polym. Sci.*, 2008, **212**, 187-225.

Chapter Four

……

Threading the Needle: Enhanced Fluorescence and Size-Exclusion based Sensing from Poly-*pseudo*-rotaxanes based on Cucurbit[*n*]urils and Poly(pyridyl vinylene)

4.1 Introduction

As discussed in **Chapter 3**, CPs offer great potential as fluorescence sensor materials for biologically important species. The majority of PL sensor platforms focus on electron-donating polymers for the detection of electron-accepting analytes,[1-6] while the inverse situation, the development of n-type semiconducting polymers, is reasonably limited.[7-12] However, even the scarce number of reports of these CPs have shown their potential in a variety of applications, ranging from polymer solar cells[13] to organic light-emitting diodes.[10] The development of such n-type CPs has been demonstrated by doping of p-type semiconductors with highly electron-withdrawing species such as fluorine substituents[14, 15] or through the introduction of electron-deficient heterocyclic aromatics into the conjugated polymer backbone.[7, 8] Recently, a number of these CPs have shown a great tendency to selectively detect electron-rich analytes. Poly(pyridinium phenylene)s containing pentiptycene units have been shown to selectively sense the presence of the biologically important species, indole, through a mechanism of electron-transfer quenching of the photoluminescence.[11] A range of similar cationic conjugated cationic polymers without the pentiptycene unit have also been prepared through anion exchange reactions.[12] These CPs demonstrate the ability to distinguish between industrially relevant amine vapours below or close to their permissible exposure limits. The specificity of this system is conferred by the differing solubility and optoelectronic properties that arise from the anions utilised.

Rotaxane systems have also been demonstrated as effective sensing platforms for a wide range of charged guest species as guest binding brings on a dynamic response, most often read out as a change in the optical properties of the system.[16, 17] Rotaxanes are defined by IUPAC as '*molecules in which a ring encloses another, rod-like molecule having end groups too large to pass through the ring opening, and thus holds the rod-like molecule in position without covalent bonding*'.[18] If the bulky stopper groups are not present and the ring could possibly slip off the axle, the system is dubbed a *pseudo*-rotaxane.[19] Polyrotaxanes, in which a number of cyclic units are threaded onto a linear chain, have also been demonstrated as effective sensing devices[20] and find particular use in biotechnology due to their low cytotoxicity.[19] A combination of the molecular recognition bestowed by the host-guest interactions of polyrotaxanes and the amplified response generated in conjugated polymers has previously been demonstrated to produce highly selective sensing schemes for Cu^{+} ions.[21, 22]

This work aims to develop polyrotaxane systems based on a single n-type CP threaded with macrocycles of varying proportions to realise a sensor for electron-rich analytes. The macrocycles chosen for this work are a series of highly symmetrical molecules known as cucurbit[*n*]urils. Cucurbit[*n*]urils were chosen due to their excellent solubility in the solvent systems required for the polypyridyl based CP used, with cucurbit[7]uril showing a solubility of

700 mM in 50/50 *v/v* formic acid/H_2O.[23] Cucurbit[*n*]urils comprise varying numbers of glycoluril units giving rise to two partially negatively charged carbonyl portals encapsulating a hydrophobic cavity.[24] They exhibit selective binding of neutral and positively charged guest species,[23, 24] indicating their potential to bind the positively charged repeat units of the CP used here. Furthermore, the volume and binding properties of the cucurbit[*n*]uril pocket have been shown to discriminate between a range of aliphatic and aromatic species.[25-27] The amplified response of the conjugated polymer, combined with the highly discriminating binding ability of cucurbit[*n*]urils, highlight the potential of this simple system as a dual-mode sensory platform based on the principles of both fluorescence quenching and size-exclusion.

4.1.1 Aims

In this chapter, the formation of poly-*pseudo*-rotaxanes through the threading of neutral macrocycles, cucurbit[*n*]urils (**CB[n]**s), of varying size onto the backbone of the positively charged form of the polymer **PPyV** (**Fig. 4.1**) will be examined. The protonation of **PPyV** in acidic solution to prepare the cationic CP will be discussed (**Fig. 4.1**). NMR and PL spectroscopy will be used to verify the threading of the positively charged CP backbone by the cucurbit[*n*]uril species. The development of this **PPyV-CB[n]** system as a solution-phase, size-exclusion based PL sensor for electron-rich analytes is considered. Preliminary work towards the creation of true polyrotaxanes is also investigated.

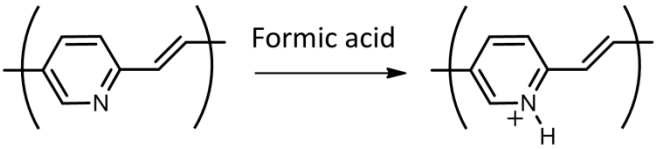

PPyV

Figure 4.1. Chemical structure of **PPyV** in the solid-state and the cationic protonated form when dissolved in concentrated acid (pH = 1.18).

4.2 Experimental

4.2.1 Polymer

Poly(pyridyl vinylene) (**PPyV**), (103 g mol^{-1} (r.u.)) was synthesised as previously reported[28-30] in the group of Prof. Tim Swager. The number averaged molecular weight, M_n, for this polymer was unable to be measured due to the lack of polymer solubility in appropriate GPC solvents, but is estimated to be ~8,000-11,000 g mol^{-1} based on the synthesis and characterisation of similar polymers.[29, 30]

4.2.2 Cucurbit[*n*]urils

Due to the increasing number of methylene-bridged glycoluril repeat units, the portal size and cavity dimensions increase for each subsequent **CB[n]**, while the overall height of the

macrocycles remain the same. These dimensions are outlined in **Fig. 4.2** and **Table 4.1**. Cucurbit[*n*]urils are designated as **CB[n]** where n stands for the number of glycoluril repeat units.

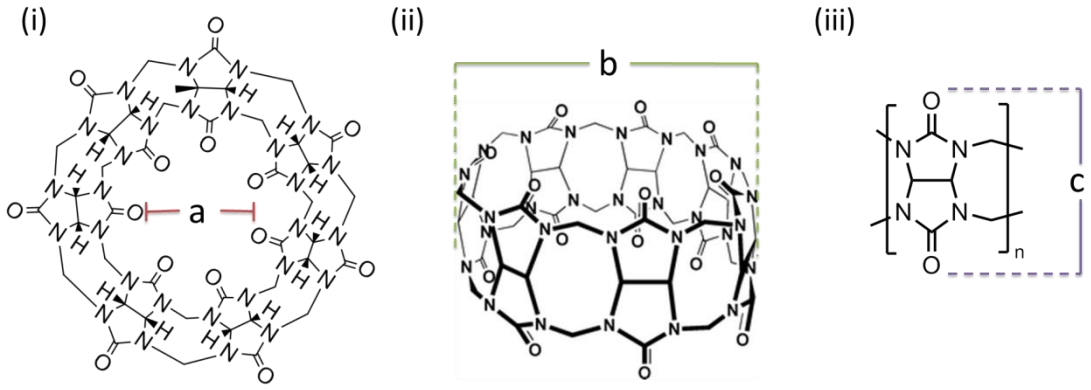

Figure 4.2. (**i**) The flattened structure of a **CB[7]** molecule showing the portal diameter, a, (**ii**) the 3D structure of a **CB[7]**[17] molecule showing the outside width of the **cucurbit[7]uril**, b, and (**iii**) the structure of the methylene bridged glycoluril repeat units, showing the height, c, of the **CB[n]** molecules.

Table 4.1. Physical properties and dimensions of **CB[n]** series.

	M_w (g mol^{-1})	a (Å)	b (Å)	c (Å)	V (Å^3)
CB[5]	830	2.4	4.4	9.1	82
CB[6]	996	3.9	5.8	9.1	164
CB[7]	1163	5.4	7.3	9.1	279
CB[8]	1329	6.9	8.8	9.1	479

4.2.3 Titrations

As discussed in **Chapter 2**, the concentrations of CPs are conventionally discussed in terms of the concentration of the CP repeat units in solution. It is possible that many **CB[n]** species thread onto a single CP backbone, each one interacting with a different r.u. Hence, the concentrations discussed throughout this chapter are discussed in terms of the concentration of CP r.u. to the concentration of entire **CB[n]** macrocycles. Thus, a ratio of 20 **PPyV** r.u: 1 **CB[n]** macrocycle indicates that there is one **CB[n]** macrocycle in the solution for every 20 repeat units of **PPyV**.

4.3 Results and Discussion

4.3.1 Protonation of PPyV in Formic Acid

The optical properties of **PPyV** are dominated by its solubility, which is extremely low in the majority of common solvent systems. Thus, initial studies with this CP were carried out in

concentrated formic acid. The optical properties for **PPyV** in formic acid are shown in **Fig. 4.3a**, and match those previously reported.[28] The UV/Vis absorption and PL excitation spectra exhibit a broad band centred at 403 nm, while the emission band is centred at 480 nm. The molar absorption coefficient for **PPyV** was measured to be 6,901 M^{-1} cm^{-1} in formic acid (**Fig. 4.3b**).

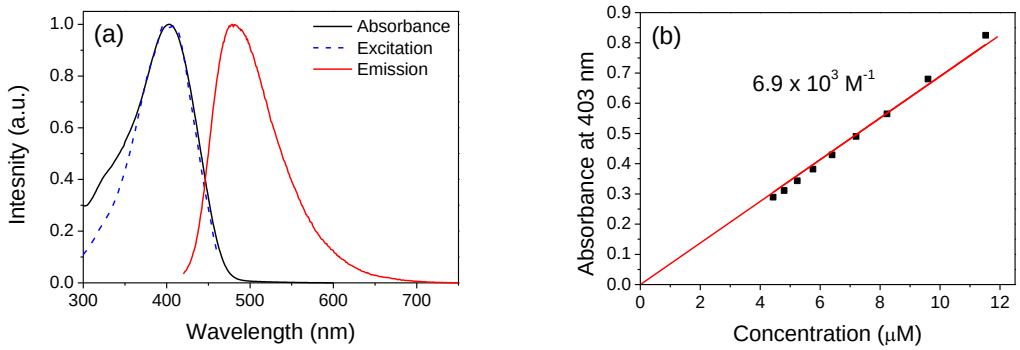

Figure 4.3. (**a**) UV/Vis absorption (black line), PL (λ_{ex} = 403 nm, red line) and PL excitation (λ_{em} = 480 nm, blue line) spectra for **PPyV** in formic acid. (**b**) Plot of absorbance at 403 nm of **PPyV** in formic acid *vs.* concentration, showing a linear relationship yielding a molar absorption coefficient of 6,901 M^{-1} cm^{-1}.

PPyV is also surprisingly soluble in the neutral species, *m*-cresol (3-methylphenol). It is believed that when dissolved in concentrated acid the pyridyl N-atom of the CP backbone becomes protonated (**Fig 4.1**). To examine this protonation, **PPyV** was dissolved in *m*-cresol and the pH of the solution was progressively lowered through addition of dodecylbenzene sulfonic acid (DBSA). The emission spectrum of **PPyV**, in *m*-cresol, has a maximum at 460 nm (**Fig. 4.4a**). Both the UV/Vis absorption and emission maxima are red shifted with increasing DBSA concentration, towards the maximum seen for the CP in concentrated acid (480 nm) (**Fig. 4.4b**), indicating the protonation of the pyridyl moieties in the CP.

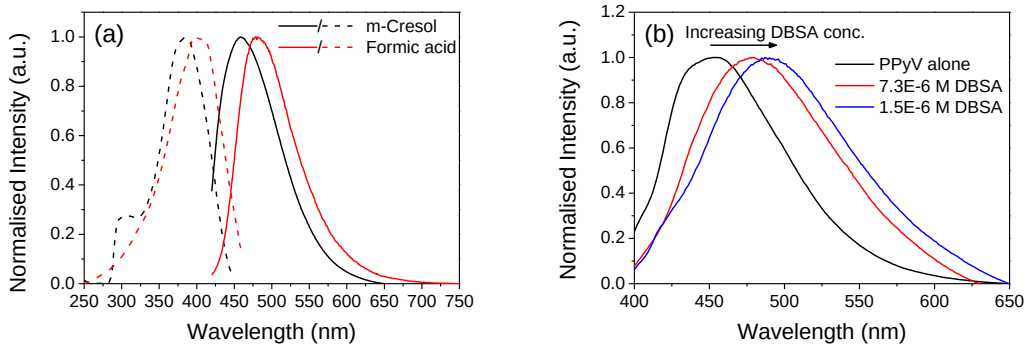

Figure 4.4. (**a**) PL and PL excitation spectra for **PPyV** in *m*-cresol (black lines, λ_{ex}= 385 nm λ_{em}= 460 nm) and formic acid (red lines, λ_{ex}= 403 nm λ_{em}= 480 nm). Emission and excitation spectra are shown as solid and dashed lines, respectively. (**b**) PL spectra (λ_{ex}= 385 nm) of **PPyV** in *m*-cresol as a function of increasing DBSA concentration.

4.3.2 Binding of Cucurbit[*n*]urils with PPyV

The formation of poly-*pseudo*-rotaxanes was achieved through self-assembly using non-covalent interactions as outlined in the cartoon in **Fig. 4.5**. The **CB[n]**s bind guest species largely through a combination of hydrophobic and dipole-dipole interactions.[23, 24] The strength of these

interactions along with the size of the individual cucurbit[*n*]urils is expected to control the extent of threading onto the **PPyV** backbone.

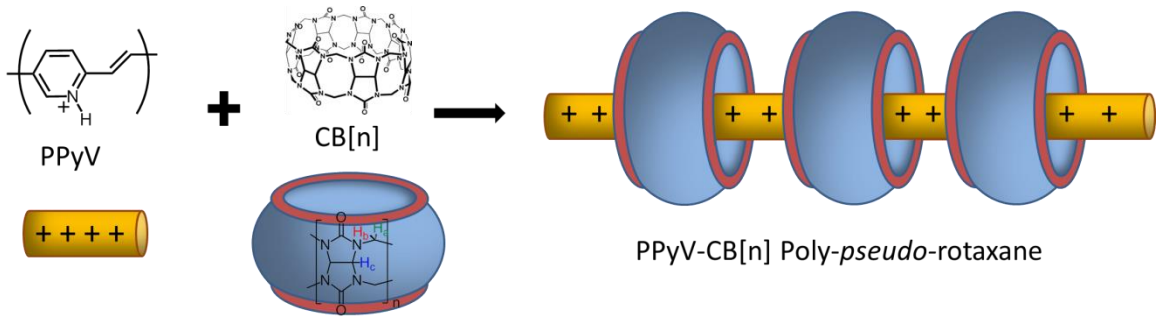

Figure 4.5. Schematic representation of poly-*pseudo*-rotaxane formation *via* binding of positively charged repeat units of **PPyV** by a host cucurbit[*n*]uril macrocycle.

4.3.3 Solution Phase ^{1}H NMR

In order to examine the physical threading of the **CB[n]** species onto the **PPyV** backbone, solution phase ^{1}H NMR studies were carried out in D_2O/d_2-formic acid (50/50 *v/v*). The ^{1}H NMR spectrum of **PPyV** shows a number of signals in the region 6.2 to 7.8 ppm (**Fig.4.6**). These signals are not extremely well resolved due to the polydispersity and high molecular weight of **PPyV**.[31] The signals at 6.3 and 6.6 ppm are assigned to the vinyl protons H_6 and H_5, respectively, while the signals at 7.3, 7.6 and 7.7 ppm are assigned to the aromatic protons of the pyridyl repeat unit, H_3, H_4 and H_2, respectively. The signal for the protonated nitrogen species is expected further downfield (>8 ppm) however as these experiments were carried out in deuterated solvents no such signal is expected.

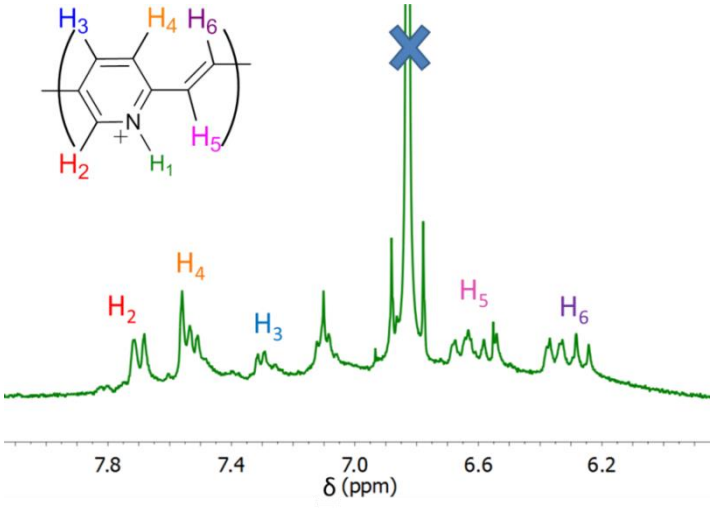

Figure 4.6 ^{1}H NMR spectrum of **PPyV** in 50/50 *v/v* D_2O/d_2-formic acid at 298 K

The ^{1}H NMR spectra of the **CB[n]** molecules show three distinct signals (shown in **Fig. 4.7** for **CB[7]** as a representative example). While the signals are much sharper than that for **PPyV** they are still a little broad owing to the repeat units that make up the **CB[n]** macrocycle. The signals are assigned in **Fig. 4.7** according to literature reports.[32-34]

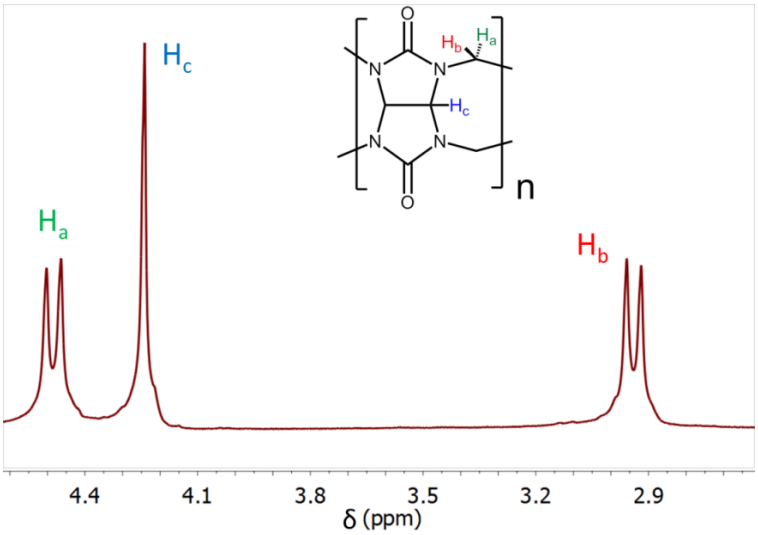

Figure 4.7 ^{1}H NMR spectrum for **CB[7]** in 50/50 *v/v* D_2O/d_2-formic acid at 298 K.

In general, encapsulation of a guest molecule within a **CB[n]** cavity causes an upfield shift of the guest protons. Protons located at the portal of the **CB[n]** undergo a downfield shift as they experience a deshielding effect due to the carbonyl groups surrounding the cavity opening.[23, 24] The ^{1}H NMR spectrum of **PPyV** was measured as a function **CB[n]** concentration. On increasing the **CB[7]** concentration, a broadening and an upfield shift is observed for the **PPyV** protons (**Fig. 4.8a**), indicating threading of the **PPyV** by **CB[7]**. However, in the **CB[7]** region, all three of the proton signals are shifted upfield for low concentrations. At a ratio of 20 P**PyV** r.u. to 1 **CB[7]**, a signal appears at 4.20 ppm with a shoulder at 4.25 (**Fig. 4.8b**), attributed to H_c for bound and unbound **CB[7]**, for the peak and shoulder, respectively. Also at this concentration the signal at 2.90 ppm becomes unresolvable as a doublet due to the close proximity of the signals attributed to H_b for both bound and unbound **CB[7]**. As the concentration of **CB[7]** is increased, the contributions from the signals of the unbound **CB[7]** also increase and swamp the signal of the bound **CB[7]**. This indicates that the binding of **CB[7]** with **PPyV** does not scale linearly with **CB[7]** concentration and saturation occurs at reasonably low concentrations (between 20:1 and 10:1 **PPyV** r.u. to **CB[n]**).

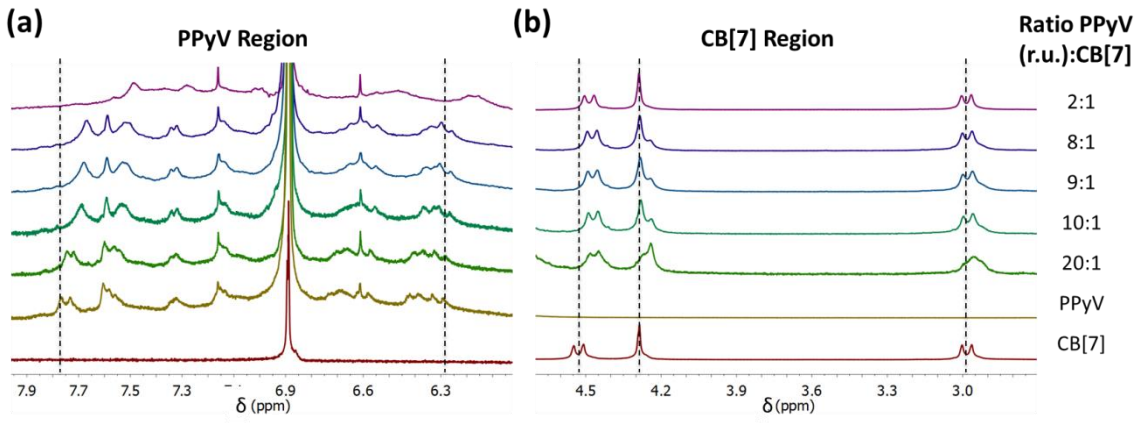

Figure 4.8 ^{1}H NMR spectra for **PPyV** with increasing concentration **CB[7]** in 50/50 *v/v* D_2O/d_2-formic acid at 298 K.

Fig. 4.9 shows the ^{1}H NMR spectra on addition of **CB[5]** to **PPyV** as a function of increasing **CB[5]** concentration. No signal broadening or upfield shift is exhibited by the **PPyV** proton signals (**Fig. 4.9a**), indicating that **CB[5]** does not thread the CP backbone. However, addition of **CB[5]** to the polymer solution does cause a shift in the **CB[n]** region of the spectrum. At the lowest concentration examined, 10:1 **PPyV** r.u.:**CB[5]**, the singlet attributed to H_c is shifted downfield while the doublet attributed H_a is shifted upfield causing the two signals to merge into one broad peak. While the lack of broadening and an upfield shift in the **PPyV** region indicates that the CP is not threaded by **CB[5]**, the shift in the CB region suggests that there is some form of interaction between the two species. Owing to the tendency of **CB[5]** to bind small positively charged species[17] it is possible that **CB[5]** binds the proton attached to the pyridyl N–atom of the CP backbone. More concrete evidence for this would be suggested by a downfield shift in a signal associated with this nitrogen bound proton, however, this signal was not discernible at any concentration.

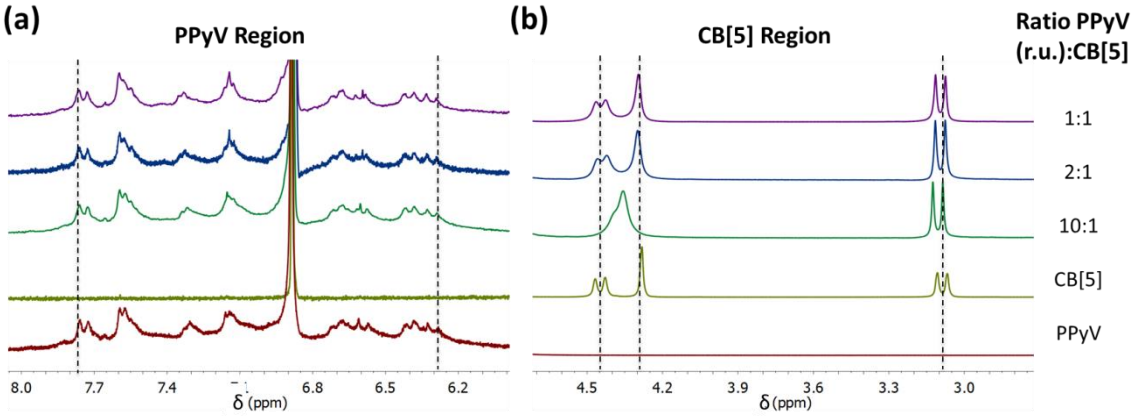

Figure 4.9 ^{1}H NMR spectra for **PPyV** with increasing concentration **CB[5]** in 50/50 *v/v* D_2O/d_2-formic acid at 298 K.

Fig. 4.10 shows the ^{1}H NMR spectra of **PPyV** on addition of **CB[6]**. As expected there is an upfield shift in the **PPyV** region of the spectrum (**Fig. 4.10a**), supporting the threading of **CB[6]** onto the CP backbone. However, the extent of the shift is less that that seen for **CB[7]** (**Fig. 4.8**) potentially suggesting reduced interaction between **PPyV** and **CB[6]**. The CB region of the spectrum also exhibits an upfield shift in the doublet associated with H_a, as was observed for **CB[7]**. Similarly for a concentration of 10:1 **PPyV** r.u.:**CB[6]**, a small signal appears upfield of the signal for H_c, indicating the presence of bound **CB[6]** which is swamped by the increasing signal for unbound **CB[6]** as the concentration is increased. The difference observed in this region for **CB[6]** is the appearance of a very small signal slightly downfield of the doublet associated with H_b, potentially suggesting a different mechanism of association with **CB[6]**. Márques *et al*. have previously suggested a 'flip-flop' mechanism for the incorporation of amine residues into the **CB[6]** cavity, whereby the rate-determining step involving the formation of an inclusion complex requires significant distortion of the **CB[6]** portal, rendering this pathway slower.[35]

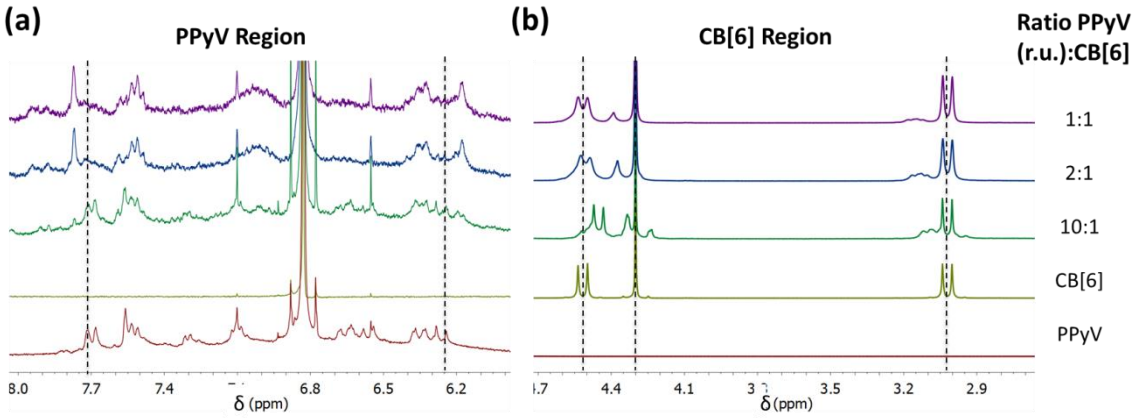

Figure 4.10. ^{1}H NMR spectra for **PPyV** with increasing concentration of **CB[6]** in 50/50 *v/v* D_2O/d_2-formic acid at 298 K.

CB[8] showed poor solubility at the concentrations needed to carry out ^{1}H NMR experiments, which caused the samples to be very dilute. The NMR spectra for pure **PPyV**, pure **CB[8]** and a mixture of **PPyV** and **CB[8]** at a ratio of 30:1 **PPyV** r.u.:**CB[8]** are shown in **Fig. 4.11**. The dilute nature of the mixed sample makes it difficult to resolve the spectra completely, particularly in the CB region, however, the expected broadening and upfield shift is suggested in the **PPyV** domain, hinting at threading of **CB[8]** onto the backbone of **PPyV**.

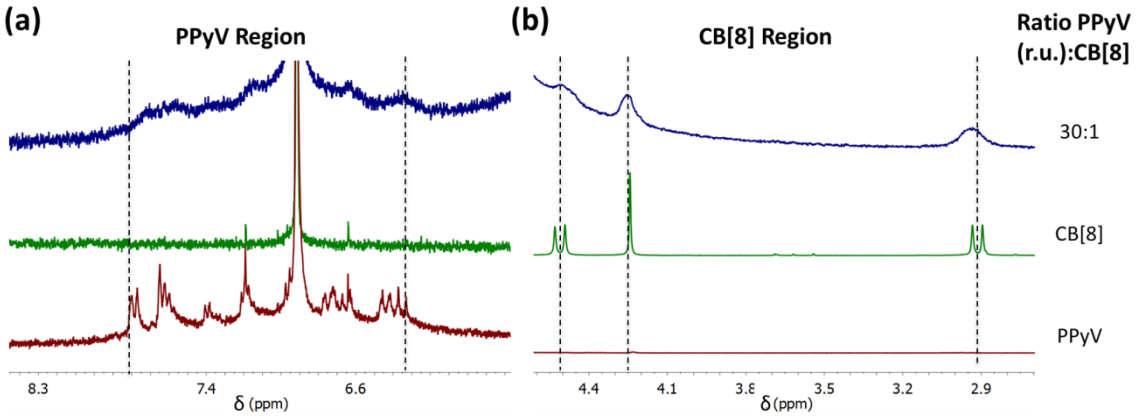

Figure 4.11. ^{1}H NMR spectra for **PPyV** with increasing concentration **CB[8]** in 50/50 *v/v* D_2O/d_2-formic acid at 298 K.

4.3.4 Photoluminescence Studies

While initial PL studies of **PPyV** were carried out in concentrated formic acid, the **CB[n]** series are soluble in a 50/50 *v/v* formic acid/H_2O mixture. Thus, the optical properties of **PPyV** in formic acid were measured as a function of increasing water concentration (**Fig. 4.12**). As the fraction of water is increased, the intensity of both the emission and excitation spectra decreases. This is accompanied by a red shift in the emission maximum with increasing water content, indicating increasing aggregation of the CP.[36]

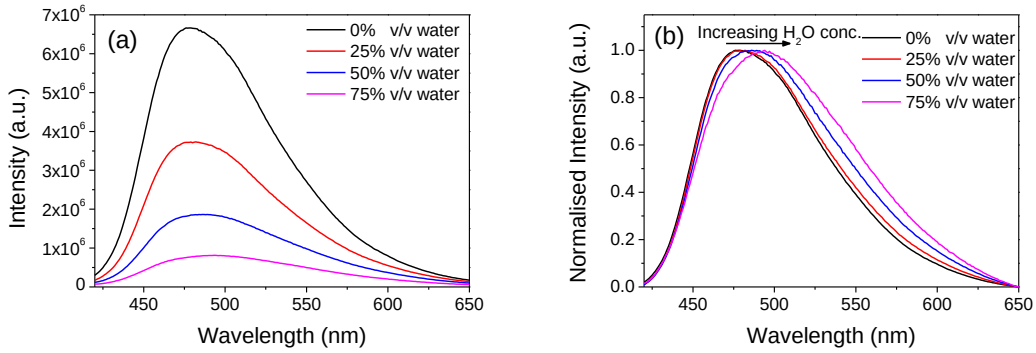

Figure 4.12. (**a**) PL spectra of **PPyV** in formic acid (6.4 × 10^{-6} M (r.u.)) as a function of increasing H_2O concentration (λ_{ex} = 403 nm) (**b**) Normalised PL spectra of **PPyV** in formic acid as a function of increasing H_2O concentration (λ_{ex} = 403 nm), highlighting red shift in emission maximum.

However, addition of the **CB[n]**s to **PPyV** causes a dramatic response in the PL spectra, the magnitude of which is dependent on the size of the cucurbit[*n*]uril ring, as shown in **Fig. 4.13**.

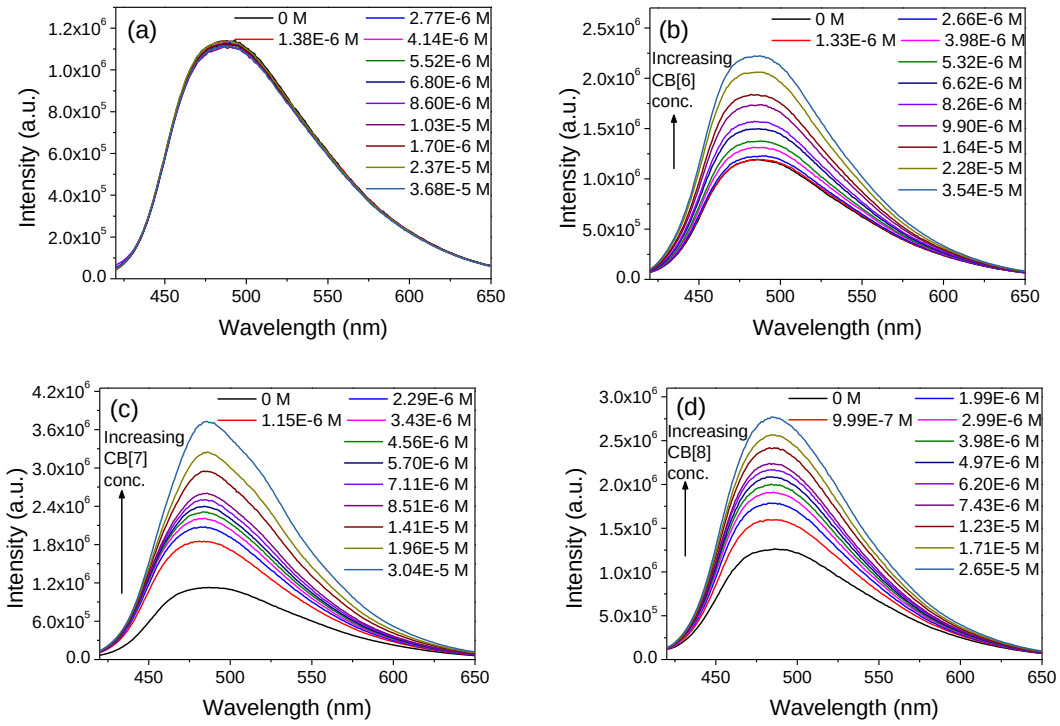

Figure 4.13. PL spectra (λ_{ex} = 403 nm) of **PPyV** in 50/50 *v/v* formic acid/H_2O (6.4 × 10^{-6} M (r.u.)) upon increasing concentration of (**a**) **CB[5]** (**b**) **CB[6]** (**c**) **CB[7]** and (**d**) **CB[8]**.

Titration of **CB[5]** into **PPyV** gives rise to little or no change to the PL emission or excitation spectra. While addition of **CB[6]** causes an increase in the PL intensity, which at a concentration of 26:1 **PPyV** r.u.:**CB[6]**, rises to ~1.75 times that of the pure **PPyV**. Addition of **CB[8]** also causes a PL enhancement, with the emission intensity rising to just over twice that of pure **PPyV**. Finally, introduction of **CB[7]** causes the most dramatic PL enhancement, with the emission intensity reaching nearly 3 and a half times its original value by a concentration of 30:1 **PPyV** r.u.:**CB[7]**. This variation in the magnitude of the observed PL enhancement is shown in

Fig. 4.14, which shows the emission intensity of **PPyV**, as a function of increasing **CB[n]** concentration, normalised to the intensity of the initial solution.

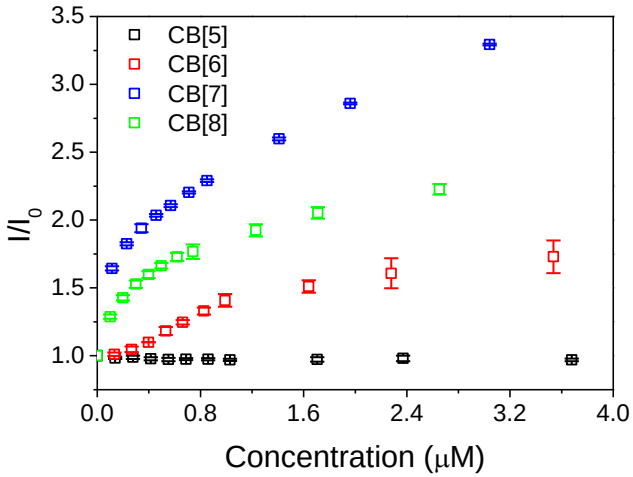

Figure 4.14. PL intensity of **PPyV** on increasing **CB[n]** concentration (**CB[5]** (black squares), **CB[6]** (red squares), **CB[7]** (blue squares) and **CB[8]** (green squares)) normalised to initial intensity of pure **PPyV** in formic acid/H_2O 50/50 *v/v*.

Previously, the enhancement of the PL signal observed on binding of a guest species within a **CB[n]** host has been attributed to increasing the guest solubility and changing the polarity of the microenvironment.[37-39] Titration of **CB[5]** into **PPyV** gives rise to little or no change to the PL spectrum. This further confirms the evidence from the ^{1}H NMR studies, which indicates that **CB[5]** does not thread the **PPyV** backbone. The fact that **CB[5]** does not thread onto the **PPyV** backbone was expected as the dimensions of the cavity cause it to be unable to bind anything larger than a proton or a very small, positively-charged ion such as an ammonium moiety at its portal.[23] The diameter of pyridine, the major component of **PPyV** is reported to be 4.92 Å parallel to the C_{2v} axis and 5.12 Å perpendicular to this axis in the plane of the molecule.[40] It is clear that the portal diameter of **CB[5]** (2.4 Å) is too small to thread onto the aromatic backbone of **PPyV** and thus it cannot influence the microenvironment of the chromophoric segments of the **PPyV** polymer chain to bring about the increase in PL intensity observed for the three larger **CB[n]**s.

The dimensions of the **CB[n]** portal and cavity not only control the ability of the **CB[n]** to thread onto the **PPyV** backbone, but also have an influence on the magnitude of the concomitant PL enhancement observed which follows the order **CB[6]** < **CB[8]** < **CB[7]**. It is also observed in **Fig. 4.14** that there is a sigmoidal shape to the enhancement seen for **CB[6]** which is not observed for **CB[7]** or **CB[8]** suggesting possibly a slightly different mechanism for **CB[6]** threading. **CB[6]** has previously been reported to bind linear hydrocarbons[26] and smaller aromatic molecules.[41] While **CB[7]** and **CB[8]** have both been shown to easily encapsulate aromatic molecules[42] with the larger portal of **CB[8]** capable of binding two aromatic molecules.[23] The binding of any of these species relies heavily on dipole-dipole interactions between the guest species and the carbonyl groups that decorate each of the cavity openings and through hydrophobic interactions.[24] Based on

these observations we propose a 'Goldilocks-like' situation in terms of the enhancement seen in the PL spectrum of **PPyV**. The portal diameter of **CB[6]** (3.9 Å) is a little too small and requires extra time to thread onto the **PPyV** backbone. The portal diameter of **CB[8]** is 6.9 Å, which is a little too big, thus it threads **PPyV** easily but is too large to form and maintain effective dipole-dipole interactions with the **PPyV** and so can easily dethread, while in **CB[7]** for which the portal diameter 5.4 Å, is just the right size to thread **PPyV** and has strong enough interactions with the CP to remain threaded. This is similar behaviour to that found for the binding of an oxazine dye within the cavity of **CB[7]** and **CB[8]**, wherein **CB[7]** was shown to undergo a stronger binding to the oxazine dye than the **CB[8]** host due to the compatible portal diameter of **CB[7]**.[42] The difference in the PL enhancement for each of the **CB[n]**s is visible to the naked eye, as demonstrated in **Fig. 4.15**, which shows a photograph of solutions of **PPyV** under UV-illumination with the same concentration of different **CB[n]** rings.

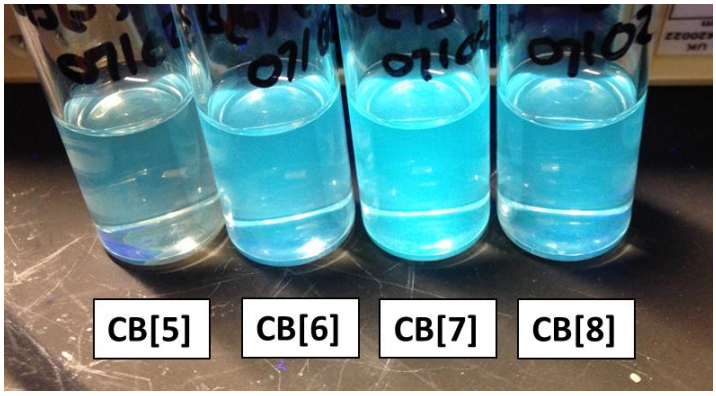

Figure 4.15. Photograph of **PPyV** with **CB[5]**, **CB[6]**, **CB[7]** and **CB[8]** (30:1 **PPyV** r.u.:**CB[n]**) in 50/50 *v/v* formic acid/H_2O under UV-illumination (λ_{ex} = 365 nm).

The sigmoidal shape seen in the plot of intensity *vs.* concentration (**Fig. 4.14**) upon addition of **CB[6]** to **PPyV** suggests that there may be a time dependence associated with the observed PL enhancement. A fixed ratio of **CB[n]** rings to **PPyV** (r.u.) for **CB[6]**, **CB[7]** and **CB[8]** (25 **CB[n]** rings to 1 **PPyV** r.u.) were added to different solutions of **PPyV** and the PL intensity was monitored over 4 h. Due to the length of time required to run an emission spectrum, it was not possible to record the intensity over the first 30 s after **CB[n]** addition. However, it can be seen from **Fig. 4.16** that for **CB[7]** and **CB[8]** the PL enhancement occurs within the first 30 s following **CB[n]** addition and remains constant thereafter. As expected from the steady-state PL, the enhancement observed for **CB[7]** is greater than for **CB[8]**. The scenario is different for **CB[6]**, which shows a gradual growth in the PL intensity over the first 30 min which reaches a maximum and plateaus by 2 h. This is consistent with the idea that **CB[6]**, the portal diameter for which is 3.9 Å, is too small to easily thread onto the CP backbone and requires more time to thread the **PPyV** backbone. This is not unusual as with larger guest species that match or are larger than the **CB[6]** portal, significant deformation of the macrocycle must first occur which has led to slower incorporation of target molecules.[35, 43]

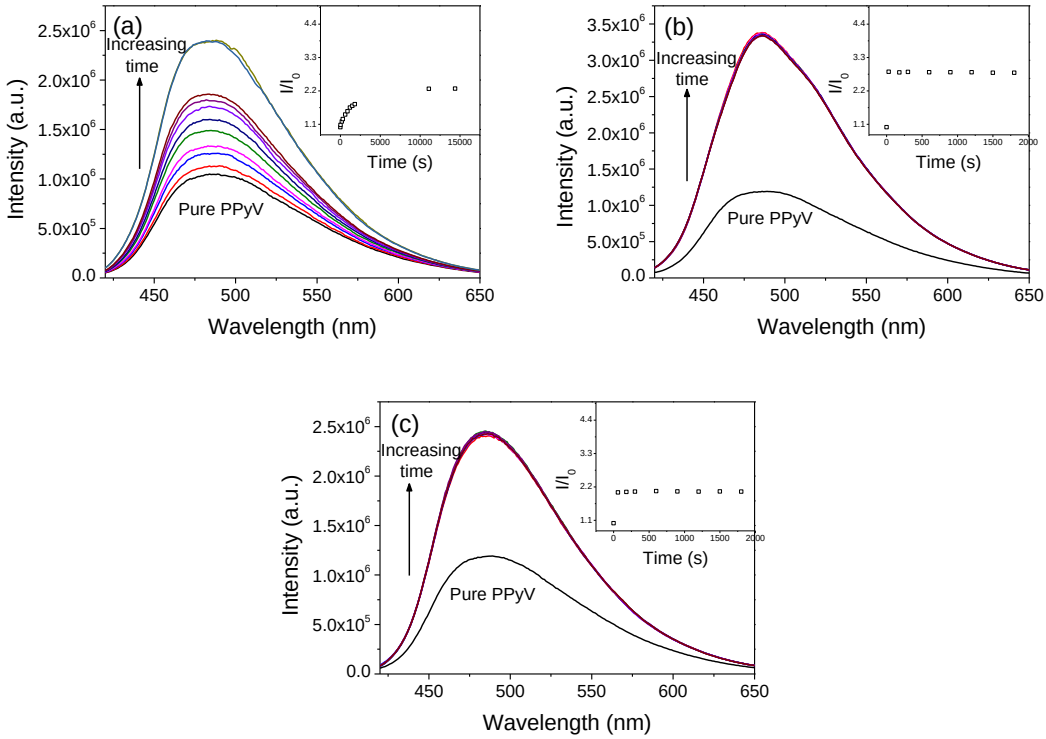

Figure 4.16. PL spectra of **PPyV** in formic acid/H_2O 50/50 *v/v* as a function of increasing time after addition (0-4 h) of (**a**) **CB[6]** (**b**) **CB[7]** and (**c**) **CB[8]** each with an inset showing the PL intensity as a function of time for the solution normalised to initial intensity of the pure **PPyV** in 50/50 *v/v* formic acid/H_2O.

4.3.5 Size-Exclusion Sensing

4.3.5.1 Quenching of PPyV by Electron-Rich Analytes

Previously, the high excited-state electron affinity of similar cationic, high ionisation potential, conjugated polymers has been exploited to develop PL-based sensor materials for biologically important electron-rich analytes.[9, 11] Thus, the PL response of **PPyV** was investigated in the presence of indole (**Fig. 4.17**), which was chosen due to its biological significance as the aromatic portion of the essential amino acid tryptophan. The change of fluorescence intensity of **PPyV** with indole and a typical Stern-Volmer plot are shown in **Fig. 4.17a**. The Stern-Volmer quenching constant (K_{SV}) was determined to be 2830 M^{-1}. The magnitude of this value indicates a static quenching process, however, time-resolved studies are required for further confirmation.

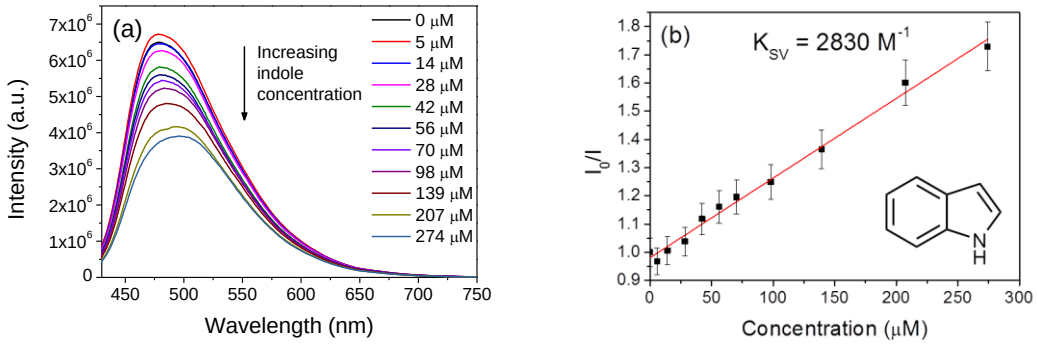

Figure 4.17. (**a**) PL spectra of **PPyV** in formic acid as a function of increasing indole concentration and (**b**) Stern-Volmer plot for titration of indole into **PPyV**. The inset shows the chemical structure of indole.

4.3.5.2 Quenching of PPyV-CB[n] by Indole

Size exclusion is a technique often used in polymer chemistry to determine the molecular weight of synthesised molecules,[44, 45] and in biological sciences to isolate a particular species of interest.[46, 47] Size-exclusion chromatography relies on the basis that different analytes have the ability to penetrate into different volumes of a stationary phase (with a fixed volume of free space) depending on the analyte size or hydrodynamic volume. This work aims to develop a similar system of size-exclusion based sensing. However, in this case the volume into which the analyte may penetrate will be varied by taking advantage of the varying volume of the different **CB[n]** cavities. To examine this mode of sensing, a specific ratio of **CB[n]** (25 **CB[n]** rings to 1 **PPyV** r.u.) was added to **PPyV** to create the initial PL enhancement described in **Section 4.3.2.4.2.** The resulting solution was then titrated with indole. The addition of indole to the **PPyV-CB[7]** solution gives rise to a reasonably low level of quenching (**Fig. 4.18a**), which leads to a K_{SV} of 714 M^{-1} ± 80 M^{-1} (**Fig. 4.18b**). While, the addition of indole to **PPyV-CB[8]** (**Fig. 4.18c**) gives rise to a higher Stern-Volmer constant, K_{SV} of 864 M^{-1} ± 30 M^{-1} (**Fig. 4.18d**). The large difference in K_{SV} for the **CB[n]** containing systems when compared to that of the pure polymer potentially suggests a different quenching mechanism. Two of the possibilities to rationalise the quenching of **PPyV-CB[n]** are that the quenching is either governed by the extent of **CB[n]** threading on the **PPyV** backbone, which blocks the interaction between indole and the CP, or that the quenching is controlled by the varying ability of the **CB[n]**s to incorporate both **PPyV** and indole bringing them in close enough contact to effectively interact and bring about the observed quenching response.

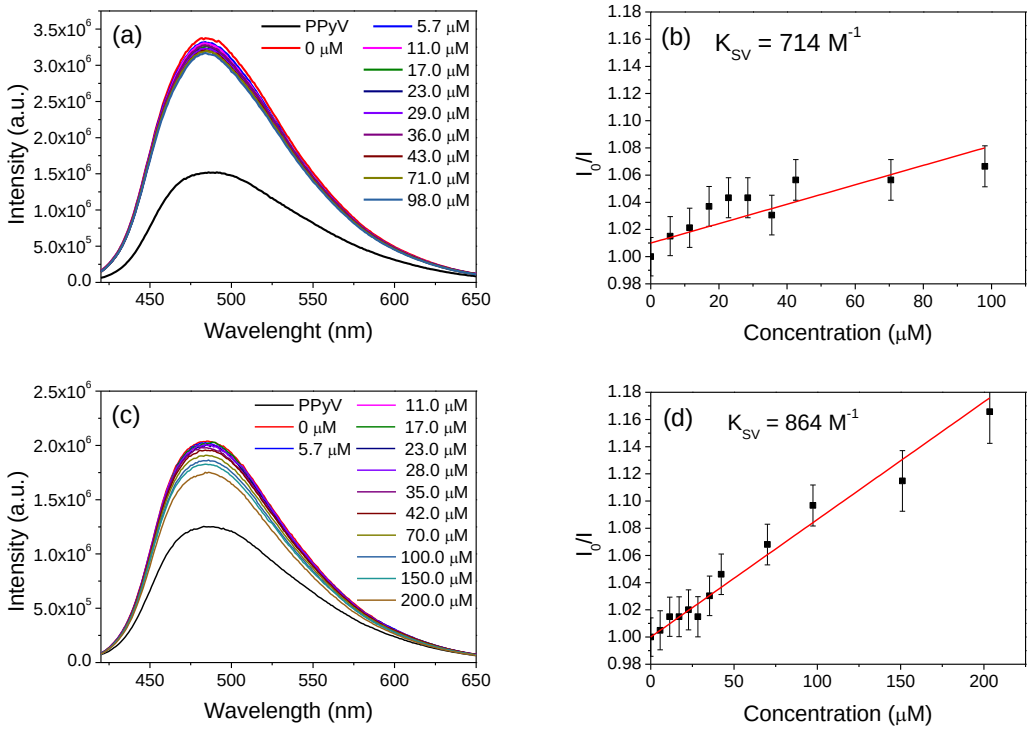

Figure 4.18. (**a**) PL spectra of **PPyV** in 50/50 *v/v* formic acid/H_2O with **CB[7]** as a function of increasing indole concentration and (**b**) Stern-Volmer plot for the titration of **PPyV-CB[7]** with indole. (**c**) PL spectra of **PPyV** in 50/50 *v/v* formic acid/H_2O with **CB[8]** as a function of increasing indole concentration and (**d**) Stern-Volmer plot for the titration of **PPyV-CB[8]** with indole.

It must be noted that in this discussion, the magnitude of the PL enhancement on addition of the **CB[n]** is taken to be at least indicative of the extent of **CB[n]** threading on the **PPyV** backbone, rather than an outright quantitative measurement of the threading. However, this suggests that the extent of threading onto the backbone follows the trend **CB[7]**>**CB[8]**>**CB[6]**>>>**CB[5]**. If the size of the **CB[n]** cavity is the factor controlling the observed response then the magnitude of quenching for **PPyV-CB[8]** with indole is expected to be greater than for **PPyV-CB[7]**, as is the case observed in **Fig. 4.18**. However, this situation is also expected to arise if the extent of threading onto the **PPyV** backbone is the factor controlling the quenching, as there is a greater quantity of the **PPyV** backbone exposed following addition of **CB[8]**, leaving it free to interact with indole. The cavity size of **CB[6]** is such that it can sparingly include the CP backbone and thus, can certainly not incorporate a second species such as indole. Thus, in an effort to further distinguish between the proposed quenching mechanism, PL response of **PPyV-CB[6]** was examined on addition of indole (**Fig. 4.19**). The quenching of **PPyV-CB[6]** was found to be less than that of **PPyV-CB[7]** (K_{SV} of 529 M^{-1} ± 100 M^{-1}), indicating that cavity size is in fact the parameter determining the magnitude of observed quenching. If the extent of threading onto the CP backbone was the major factor involved then the quenching of **PPyV-CB[6]** should be greater than both **PPyV-CB[7]** and **PPyV-CB[8]** as it displays the smallest amount of threading onto the CP backbone of the three systems. The idea that **CB[n]** cavity size can determine the interaction between indole and the **PPyV** is consistent with the number of aromatic

species each **CB[n]** species can bind. **CB[8]** shows ample ability to comfortably bind two aromatic species, particularly if they possess complimentary electrostatic profiles[23] as with protonated **PPyV** and indole, while **CB[7]** also shows the ability bind aromatic species.[24] **CB[6]** on the other hand is slow to bind a single aromatic species as seen in **Section 4.3.4** and for the most part tends to bind aliphatic amines.[23] Thus, **CB[6]** is certainly too small to bind both the **PPyV** backbone and indole as it is an additional aromatic species, leading to the reduced quenching response exhibited.

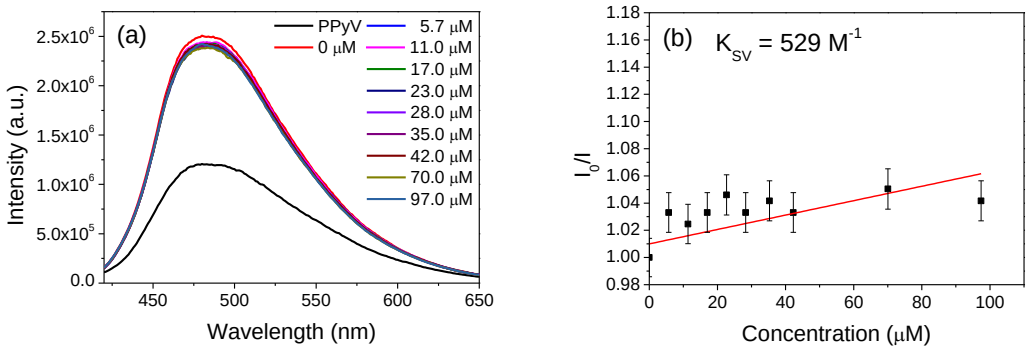

Figure 4.19. (**a**) PL spectra of **PPyV** in 50/50 *v/v* formic acid/H_2O with **CB[6]** as a function of increasing indole concentration and (**b**) Stern-Volmer plot for the titration of **PPyV-CB[6]** with indole.

4.3.5.3 Quenching of PPyV-CB[n] by Methyl Pyrrole

To further examine the role of cavity size on the quenching behaviour of the **PPyV-CB[n]** system, the PL response was measured on titration with *n*-methyl pyrrole, the structure of which is shown in **Fig. 4.20b**. This analyte was chosen due to its smaller size on comparison with indole and its electron-rich nature suggesting an ability to quench the PL of **PPyV**. The K_{SV} for titration of *n*-methyl pyrrole into pure **PPyV** was found to be 31,448 M^{-1}. A smaller yet similar quenching constant was observed for *n*-methyl pyrrole on titration with **PPyV-CB[7]** and **PPyV-CB[8]** as shown in **Fig. 4.20**. This result is consistent with the idea that the quenching of the **PPyV-CB[n]** system is governed by the volume available within the **CB[n]** following threading onto the **PPyV** backbone. The smaller size of *n*-methyl pyrrole allows it easier access into the cavities of both **CB[7]** and **CB[8]** to bring about the observed quenching. Further titration with **CB[6]** would be an interesting indication on the effect of cavity size. As **CB[6]** is not expected to bind more than one aromatic species, the K_{SV} would be expected to be reasonably small as *n*-methyl pyrrole should not be able to enter into the **CB[6]** cavity. Larger K_{SV} constants are observed for titration of indole and *n*-methyl pyrrole with pure **PPyV** when compared to the **PPyV-CB[n]** systems. However, these **PPyV-CB[n]** systems show the added advantage of size-exclusion sensing imparted by the varying volume of the **CB[n]** cavity.

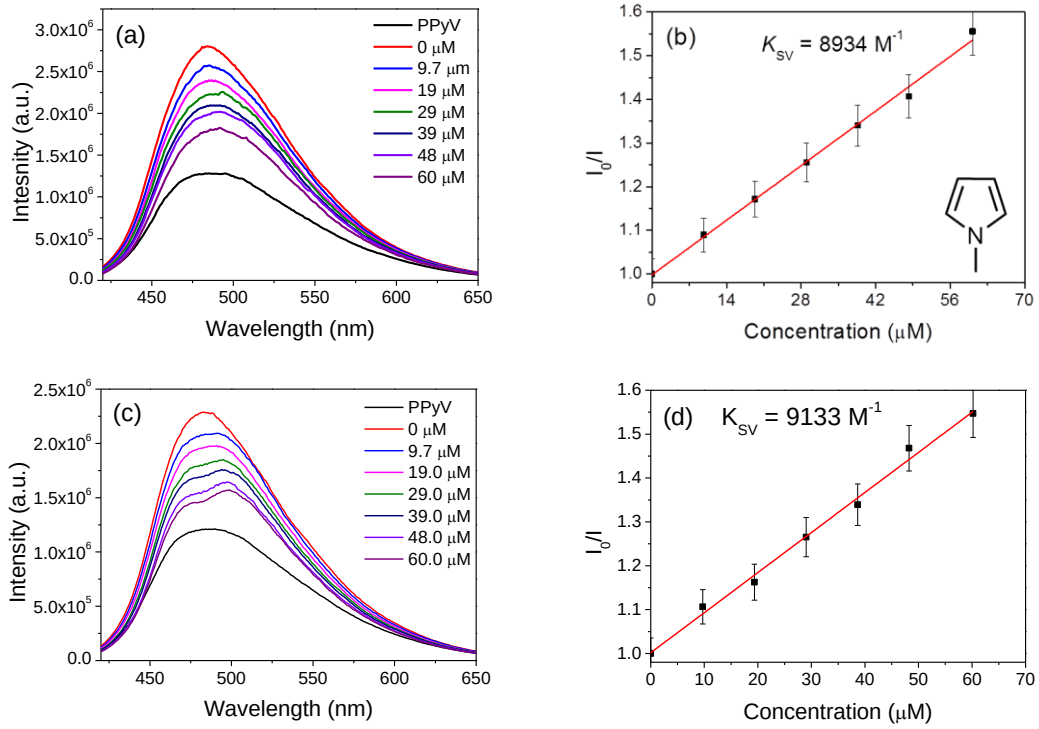

Figure 4.20. (**a**) PL spectra of **PPyV** in 50/50 *v/v* formic acid/H_2O with **CB[7]** as a function of increasing *n*-methyl pyrrole concentration and (**b**) Stern-Volmer plot for the titration of **PPyV-CB[7]** with *n*-methyl pyrrole, insert shows the chemical structure of *n*-methyl pyrrole. (**c**) PL spectra of **PPyV** in 50/50 *v/v* formic acid/H_2O with **CB[8]** as a function of increasing *n*-methyl pyrrole concentration and (**d**) Stern-Volmer plot for the titration of **PPyV-CB[7]** with *n*-methyl pyrrole.

4.3.6 Chemical Anchoring of CB[n] onto PPyV Backbone

Each of the **PPyV-CB[n]** systems discussed above fall into the category of *pseudo*-rotaxanes due to the fact that the **CB[n]** rings are not physically anchored onto the **PPyV** backbone. Preliminary efforts were made to move from *pseudo*-rotaxane systems to conventional true rotaxane systems.

4.3.6.1 Deposition of Thin Films

The first attempt to physically lock the **CB[n]** rings onto the CP backbone was through deposition of thin films onto glass slides. Although this is does not create true polyrotaxanes, as by definition that requires the addition of bulky stopper groups, transfer to the solid-state holds each species in a fixed position, with a similar result to the stopper species which prevent dethreading. The dramatic PL enhancement observed on addition of **CB[n]** remained on deposition, as shown in **Fig. 4.21**. The PL maximum of the deposited thin film of **PPyV** from 50/50 *v/v* formic acid/H_2O ($\lambda_{em\ max}$ = 580 nm) is considerably red-shifted compared to the solution spectrum ($\lambda_{em\ max}$ = 485 nm).The magnitude of this shift matches that previously reported for deposition of thin films of similar cationic conjugated polymers.[12] The red-shift in the PL maximum of CPs is attributed to increased aggregation in the solid-state.[36] The PL maximum of the thin film of **PPyV-CB[7]**, shown in **Fig. 4.21c**, is blue shifted ($\lambda_{em\ max}$ = 545 nm) when compared to the **PPyV** film alone. This suggests that the threading of **CB[7]** causes reduced aggregation of **PPyV** in the solid-state.

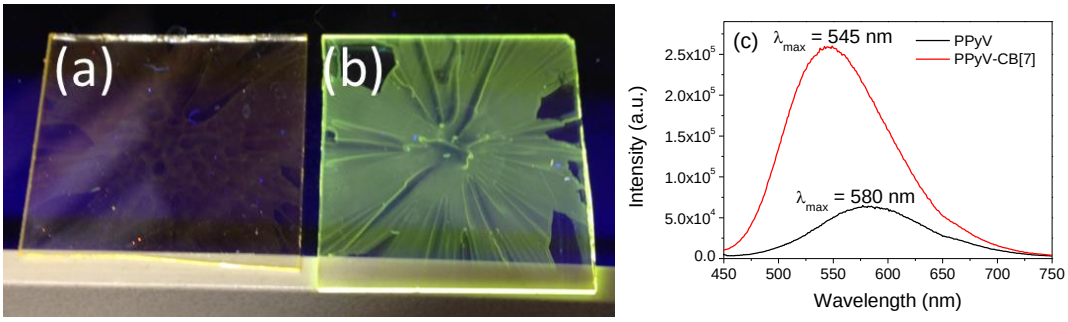

Figure 4.21. Photograph of thin films of (**a**) **PPyV** and (**b**) **PPyV-CB[7]** on glass under UV-illumination (λ_{ex} = 365 nm) and (**c**) PL spectra for the slides shown in (**a**) and (**b**).

These thin films are also capable of sensing indole in the gaseous phase. After exposing a thin film of **PPyV-CB[7]** (25 **CB[n]** rings to 1 **PPyV** r.u.) to the vapour from a solution of indole (1 mg ml^{-1} in 50/50 *v/v* formic acid/H_2O) for 5 min, the PL intensity dropped to ~50% of the initial film intensity. This initial intensity was recovered 25 min after the removal of the indole vapour (**Fig. 4.22**). This is a promising indication of the potential for these **PPyV-CB[n]** systems to be used as reversible sensors for gaseous electron-rich analytes. Further investigation of the kinetics and magnitude of quenching on exposure to a range of such analytes is required.

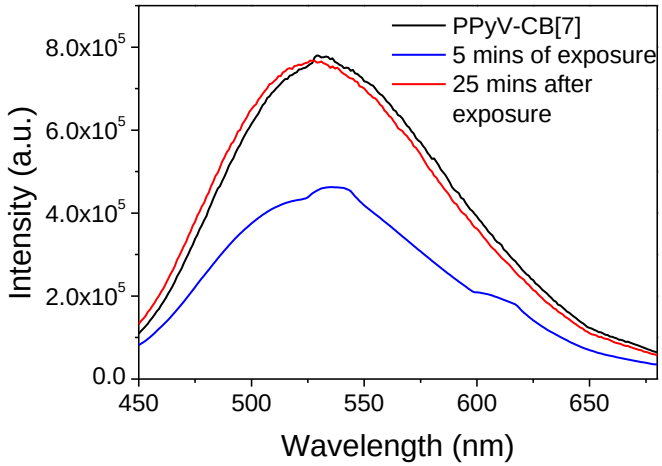

Figure 4.22. PL spectra of a thin film of **PPyV-CB[7]** (25 **CB[n]** rings to 1 **PPyV** r.u.) at t = 0 min, after 5 min of exposure to indole vapour and 25 min after removal of indole source and recovery in ambient conditions.

4.3.6.2 Addition of Stoppering Groups across Vinylene Bond

The second attempt at anchoring the **CB[n]** rings onto the **PPyV** backbone was to add physical stoppers to the CP backbone once the **CB[n]** rings were in place through nucleophilic attack of the double bonds, as shown in **Scheme 4.1**. To prepare the nucleophilic solution required, sodium hydroxide was added to a solution of 4-*tert*-butylbenzenethiol, causing the thiol to be deprotonated. Addition of this solution to that of the **CB[n]-PPyV** solution causes the thiol to attack the vinyl group of **PPyV**. Following this, protonation at carbon reduces the vinyl group, breaking the conjugation of the **PPyV** backbone and adding bulky stopper groups.

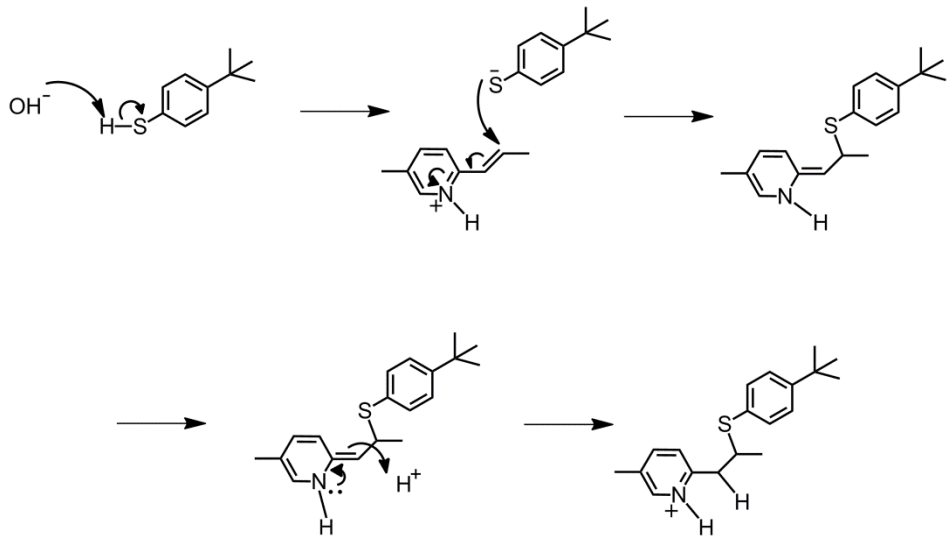

Scheme 4.1. The nucleophilic addition of 4-*tert*-butylbenzenethiol to the vinyl group of **PPyV** creating physical stoppers for **PPyV-CB[n]** rotaxanes. Brackets donating multiple repeat units and the structure of the **CB[n]** species are omitted for clarity.

The poor solubility of the thiol/base solution in the formic acid/H_2O mixture used for the **PPyV-CB[n]** species made it impossible to get NMR data to confirm the occurrence of the above reaction stoppering the rotaxanes. However, some indication of its occurrence was observed in the PL properties of the resulting solution. The emission from the CP is directly related to the conjugation of its backbone. Addition of the stopper groups across the vinyl portion of **PPyV** causes a break in the conjugation of the CP backbone. Thus, a change in the CP emission is expected. This change was observed qualitatively on comparison of four different solutions the compositions of which are described below (**Table 4.2**).

Table 4.2. Composition of solutions prepared for chemical anchoring of 4-*tert*-butylbenzene thiol to **PPyV**.

Solution	PPyV	CB[6]	Thiol	Base
A	×	-	-	-
B	×	×	-	-
C	×	×	×	×
D	×	-	×	×

On comparison of solution A and solution B under UV-illumination (λ_{ex} = 365 nm), the expected enhancement of the PL intensity on introduction of **CB[n]** is observed (**Fig. 4.23**). Following this on comparison of solution A and solution D a reduction of the PL intensity is noted. This is believed to be caused by a dramatic break in the conjugation of the **PPyV** backbone on introduction of the thiol/base solution. Finally, comparison with solution C shows a greater PL intensity than solution D. This suggests that the break-up of the CP conjugation does not occur to the same extent in solution C, most likely due to the presence of **CB[6]** both blocking some of the vinyl groups from nucleophilic addition and also driving the previously observed PL enhancement.

The addition of at least some thiol groups to the **PPyV** in solution C is indicated by the fact that its PL intensity is not as great as solution B, suggesting that breaking of the CP conjugation is occurring to some limited extent. Investigation of further base/stopper combinations with greater solubility in the formic acid/H_2O solution used is required for a quantitative confirmation of the formation of polyrotaxanes.

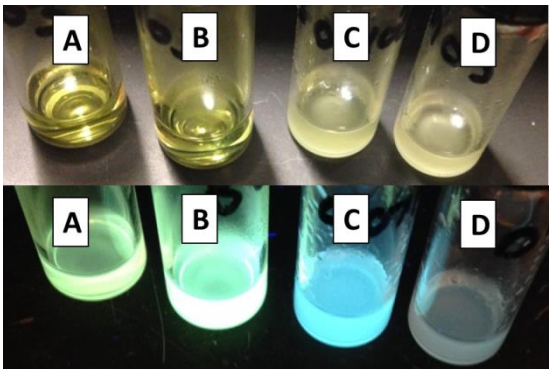

Figure 4.23. Photograph of solutions A-D outlined in **Table 4.2** (top) in daylight and (bottom) under UV-illumination (λ_{ex} = 365 nm).

4.4 Conclusions

The preparation of poly-*pseudo*-rotaxanes through threading of cucurbit[*n*]urils onto the backbone of **PPyV** has been demonstrated. The neutral form of the CP was found to be extremely insoluble in common solvent systems. However, dissolution in concentrated acid causes the protonation of the nitrogen moiety producing the much more soluble cationic conjugated polymer. Threading of the **PPyV** backbone was confirmed *via* ^{1}H NMR studies. An upfield shift of the proton signals of the CP on increasing concentration of **CB[6]** and **CB[7]** indicates incorporation of the CP backbone within the **CB[n]** cavity. At low **CB[n]** concentration, signals attributed to bound **CB[n]** appear in the NMR spectra. These signals are swamped by peaks attributed to unbound **CB[n]** as the concentration increases, indicating saturation and no further threading of the CP backbone at reasonably low concentrations of **CB[n]** *i.e.* <10 **PPyV** r.u. to **CB[n]**. The proton signals of **PPyV** show no shift on increasing concentration of **CB[5]**, demonstrating that **CB[5]** does not thread the **PPyV** backbone.

Examination of the optical properties of the **PPyV-CB[n]** systems demonstrated an enhancement of the PL intensity which is dependent on the cavity size of the **CB[n]**. The observed enhancement is attributed to both break-up of polymer aggregates through improved solubility and a change in the polarity of the microenvironment of the **PPyV** r.u. encapsulated within the **CB[n]** cavity. The magnitude of the observed enhancement follows the order **CB[7]**>**CB[8]**>**CB[6]**. This indicates a 'Goldilocks' like situation; **CB[6]** is a little too small to easily fit but will thread the backbone to some extent, **CB[8]** is a little too big, it threads easily but is too large to effectively interact with the CP backbone and de-threads again, while **CB[7]** is just the right size to thread

onto the **PPyV** backbone and to have sufficient dipole-dipole interactions to be held in place. No PL enhancement is exhibited by the **PPyV-CB[5]** system as **CB[5]** is too small to thread onto the CP backbone. The size of the **CB[n]** cavity was further exploited to develop a sensing system for electron-rich analytes based on the principles of size exclusion. The PL of **PPyV** alone was found to be quenched by the biologically-important species, indole. Following investigation of the quenching of **PPyV-CB[n]** species on interaction with indole the magnitude of quenching was found to be dependent on **CB[n]** cavity size. The greatest K_{SV} was exhibited by **PPyV-CB[8]** which has free volume within the cavity to incorporate both **PPyV** and the indole analyte. A reduced K_{SV} is observed for **PPyV-CB[7]** due to the fact that **CB[7]** has a smaller free volume and this it is more difficult to incorporate two aromatic species; **PPyV** and indole. Finally, extremely low levels of quenching are displayed by **PPyV-CB[6]** as **CB[6]** is slow to thread even the **PPyV** backbone alone and thus cannot also interact with indole. The varying dimensions of the CB[n] cavity allows the addition of size-exclusion based sensing to the **PPyV-CB[n]** species on top of the already impressive quenching displayed by the pure **PPyV** systems.

Finally, initial attempts to physically anchor the **CB[n]** species onto the **PPyV** backbone to prepare polyrotaxanes were discussed. Deposited thin films of **PPyV-CB[7]** retained the PL enhancement noted in solution. Exposure of these films to indole vapour brought about reversible quenching with the original PL intensity being recovered after 25 min exposure to ambient conditions. Due to poor solubility, chemical stoppering of **CB[n]** onto the CP backbone could not be quantitatively confirmed. However, visual examination of the PL intensities on addition of bulky stopper groups suggest that further optimisation of the stoppering system should lead to successful polyrotaxanes. The simple combination of **PPyV** and **CB[n]** species to produce poly-*pseudo*-rotaxanes allows the coupling of the electronic interactions of the CP-analyte with the size selectivity of the **CB[n]**-analyte interactions with the potential to produce a highly discriminatory sensing platform.

4.5 References

1. X. Feng, L. Liu, S. Wang and D. Zhu, *Chem. Soc. Rev.*, 2010, **39**, 2411-2419.
2. S. Hussain, A. H. Malik, M. A. Afroz and P. K. Iyer, *Chem. Commun.*, 2015, **51**, 7207-7210.
3. H. N. Kim, Z. Guo, W. Zhu, J. Yoon and H. Tian, *Chem. Soc. Rev.*, 2011, **40**, 79-93.
4. S. Rochat and T. M. Swager, *ACS Appl. Mater. Interfaces*, 2013, **5**, 4488-4502.
5. Y. Salinas, R. Martinez-Manez, M. D. Marcos, F. Sancenon, A. M. Costero, M. Parra and S. Gil, *Chem. Soc. Rev.*, 2012, **41**, 1261-1296.
6. T. M. Swager, *Acc. Chem. Res.*, 1998, **31**, 201-207.
7. A. Babel and S. A. Jenekhe, *J. Am. Chem. Soc.*, 2003, **125**, 13656-13657.
8. D. Izuhara and T. M. Swager, *J. Am. Chem. Soc.*, 2009, **131**, 17724-17725.
9. Y. Kim, J. E. Whitten and T. M. Swager, *J. Am. Chem. Soc.*, 2005, **127**, 12122-12130.
10. A. P. Kulkarni, C. J. Tonzola, A. Babel and S. A. Jenekhe, *Chem. Mater.*, 2004, **16**, 4556-4573.
11. S. Rochat and T. M. Swager, *J. Am. Chem. Soc.*, 2013, **135**, 17703-17706.
12. S. Rochat and T. M. Swager, *Angew. Chem. Int. Ed.*, 2014, **53**, 9792-9796.

13. L. Hu, F. Wu, C. Li, A. Hu, X. Hu, Y. Zhang, L. Chen and Y. Chen, *Macromolecules*, 2015, **48**, 5578-5586.
14. I. A. Adams and P. A. Rupar, *Macromol. Rapid Commun.*, 2015, **36**, 1336-1340.
15. Y. Takeda, T. L. Andrew, J. M. Lobez, A. J. Mork and T. M. Swager, *Angew. Chem. Int. Ed.*, 2012, **51**, 9042-9046.
16. P. A. Gale and C. Caltagirone, *Chem. Soc. Rev.*, 2015, **44**, 4212-4227.
17. M. J. Langton and P. D. Beer, *Acc. Chem. Res.*, 2014, **47**, 1935-1949.
18. G. P. Moss, P. A. S. Smith and D. Tavernier, *Pure & Appl. Chem.*, 1995, **67**, 1307-1375.
19. S. F. van Dongen, S. Cantekin, J. A. Elemans, A. E. Rowan and R. J. Nolte, *Chem. Soc. Rev.*, 2014, **43**, 99-122.
20. M. Arunachalam and H. W. Gibson, *Prog. Poly. Sci.*, 2014, **39**, 1043-1073.
21. S. S. Zhu, P. J. Carroll and T. M. Swager, *J. Am. Chem. Soc.*, 1996, **118**, 8713-8714.
22. S. S. Zhu and T. M. Swager, *J. Am. Chem. Soc*, 1997, **119**, 12568-12577.
23. J. Lagona, P. Mukhopadhyay, S. Chakrabarti and L. Isaacs, *Angew. Chem. Int. Ed.*, 2005, **44**, 4844-4870.
24. E. Masson, X. Ling, R. Joseph, L. Kyeremeh-Mensah and X. Lu, *RSC Adv.*, 2012, **2**, 1213-1247.
25. F. Biedermann and W. M. Nau, *Angew. Chem. Int. Ed.*, 2014, **53**, 5694-5699.
26. M. Florea and W. M. Nau, *Angew. Chem. Int. Ed.*, 2011, **50**, 9338-9342.
27. W. Jiang, Q. Wang, I. Linder, F. Klautzsch and C. A. Schalley, *Chem. Eur. J.*, 2011, **17**, 2344-2348.
28. J. W. Blatchford, T. L. Gustafson, A. J. Epstein, D. A. Vanden Bout, J. Kerimo, D. A. Higgins, P. F. Barbara, D.-K. Fu, T. M. Swager and A. G. MacDiarmid, *Phys. Rev. B*, 1996, **54**, R3684.
29. M. J. Marsella, D.-K. Fu and T. M. Swager, *Adv. Mater.*, 1995, **7**, 145-147.
30. J. Tian, C. C. Wu, M. E. Thompson, J. C. Sturm, R. A. Register, M. J. Marsella and T. M. Swager, *Adv. Mater.*, 1995, **7**, 395-398.
31. J. U. Izunobi and C. L. Higginbotham, *J. Chem. Educ.*, 2011, **88**, 1098–1104.
32. M. El Haouaj, M. Luhmer, Y. H. Ko, K. Kim and K. Bartik, *J. Chem. Soc., Perkin Trans. 2*, 2001, 804-807.
33. M. E. Haouaj, Y. Ho Ko, M. Luhmer, K. Kim and K. Bartik, *J. Chem. Soc., Perkin Trans. 2*, 2001, 2104-2107.
34. L. Zhu, H. Yan, X. J. Wang and Y. Zhao, *J. Org. Chem.*, 2012, **77**, 10168-10175.
35. C. Marquez and W. M. Nau, *Angew. Chem. Int. Ed.*, 2001, **40**, 3155-3160.
36. H. D. Burrows, S. M. Fonseca, C. L. Silva, A. A. C. C. Pais, M. J. Tapia, S. Pradhan and U. Scherf, *Phys. Chem. Chem. Phys.*, 2008, **10**, 4420–4428.
37. I. Ghosh, A. Mukhopadhyay, A. L. Koner, S. Samanta, W. M. Nau and J. N. Moorthy, *Phys. Chem. Chem. Phys.*, 2014, **16**, 16436-16445.
38. M. Megyesi, L. Biczok and I. Jablonkai, *J. Phys. Chem. C*, 2008, **112**, 3410-3416.
39. Z. Miskolczy, L. Biczok, M. Megyesi and I. Jablonkai, *J. Phys. Chem. B*, 2009, **113**, 1645–1651.
40. R. H. Herber and Y. Maeda, *Inorg. Chem.*, 1981, **20**, 1409-1415.
41. D. Tuncel, O. Ozsar, H. B. Tiftik and B. Salih, *Chem. Commun.*, 2007, 1369-1371.
42. M. Sayed, M. Sundararajan, J. Mohanty, A. C. Bhasikuttan and H. Pal, *J. Phys. Chem. B*, 2015, **119**, 3046-3057.
43. C. Marquez, R. R. Hudgins and W. M. Nau, *J. Am. Chem. Soc.*, 2004, **126**, 5806-5816.
44. M. Knaapila, L. Almasy, V. M. Garamus, C. Pearson, S. Pradhan, M. C. Petty, U. Scherf, H. D. Burrows and A. P. Monkman, *J. Phys. Chem. B*, 2006, **110**, 10248-10257.
45. A. T. Marques, H. D. Burrows, J. S. S. de Melo, A. J. M. Valente, L. L. G. Justino, U. Scherf, E. Fron, S. Rocha, J. Hofkens, E. W. Snedden and A. P. Monkman, *J. Phys. Chem. B*, 2012, **116**, 7548−7559.
46. A. Berthaud, J. Manzi, J. Pérez and S. Mangenot, *J. Am. Chem. Soc.*, 2012, **134**, 10080−10088.
47. J. T. Petty, O. O. Sergev, D. A. Nicholson, P. M. Goodwin, B. Giri and M. D. R., *Anal. Chem.*, 2013, **85**, 9868−9876.

Chapter Five

……

Out of the Blue: Unexpected Enhancement of the Optical Properties of Polyfluorene CPEs within a Di-ureasil Host

5.1 Introduction

Water-soluble polyfluorene-based conjugated polyelectrolytes (CPEs) are of extreme interest in the area of blue light-emitting devices.[1, 2] However, these rigid-rod CPEs have a tendency to aggregate in solution, which leads to low solubility and a marked decrease in the photoluminescence quantum yield.[3, 4] CP-based devices typically consist of multi-layer architectures, the performance of which is intrinsically linked to the nanoscale morphology and interfacial contact between the active layers.[5, 6] While these devices can be prepared through low cost solution processing, control over layer morphology can still be challenging to achieve.

In an effort to overcome this issue, CPs have been incorporated into a range of inorganic host matrices, providing organic-inorganic-composite materials.[7-11] This has provided an elegant route to manipulate both the conformation and orientation of the CP,[9-11] as well as improving the environmental stability.[7, 8] The directed mesostructural ordering of CPs within a silica matrix *via* addition of surface-active agents has been shown to control device electroluminescence by influencing the continuous conducting pathway created by the CP network.[8] Furthermore, a range of self-assembly processes can also be exploited to modulate the morphology of CPs at the organic-inorganic phase interface.[12] However, in these examples the inorganic matrix primarily serves to localise the CP and does not make a contribution to the functional properties of the organic-inorganic material. This is a somewhat missed opportunity, since one of the main attractions of organic-inorganic hybrid materials is the potential for enhanced, tunable properties of each species depending on the ratio and interaction between each component present.[13-15]

In an attempt to include an 'active' host material, this work focusses on the incorporation of CPEs into an organic-inorganic host known as a *di-ureasil*. Di-ureasils are composed of poly(ethylene oxide) (PEO)/poly(propylene oxide) (PPO) block copolymer chains chemically grafted to a siliceous network through two urea linkages[16, 17], giving rise to the di-ureasil nomenclature. Undoped di-ureasils are transparent, elastomeric materials that are prepared *via* mild sol-gel processes that reduce the possibility of damage to the organic component.[13, 18] Di-ureasils were chosen as the host material for a number of reasons. The presence of the organic PEO/PPO domains should provide improved compatibility with the organic CPE, compared with the purely inorganic matrices described above. The di-ureasil structure intrinsically possesses a variety of functional groups that may interact with the CPE through hydrogen bonding or dipole-dipole interactions. Di-ureasils are also inherently photoluminescent, exhibiting an emission band in the purple-blue spectral region, the maximum of which is dependent on excitation wavelength.[16, 19] They have been frequently employed as host materials for a range of dopant species ranging from lanthanide complexes[18] to quantum dots,[20] for applications such as light-emitting materials[21] and luminescent solar concentrators.[22] The combination of the flexible nature of the PEO/PPO domains

with the thermal and mechanical stability of the organosilica, suggests that these materials are excellent candidates as materials for flexible display technologies.

5.1.1 Aims

In this chapter, the incorporation of two water-soluble, blue-emitting, polyfluorene-phenylene conjugated polyelectrolytes, **PBS-PFP** and **HTMA-PFP** (**Fig. 5.1**), within a di-ureasil host matrix will be examined. Two distinct incorporation methods are discussed. The synthesis, structural characterisation and optical properties of these CPE-di-ureasils will be investigated as a function of CPE concentration. Steady-state photoluminescence and time-resolved emission studies will be used to determine the contribution from each of the components to the optical properties and to rationalise the mechanism behind the observed CPE-di-ureasil interaction.

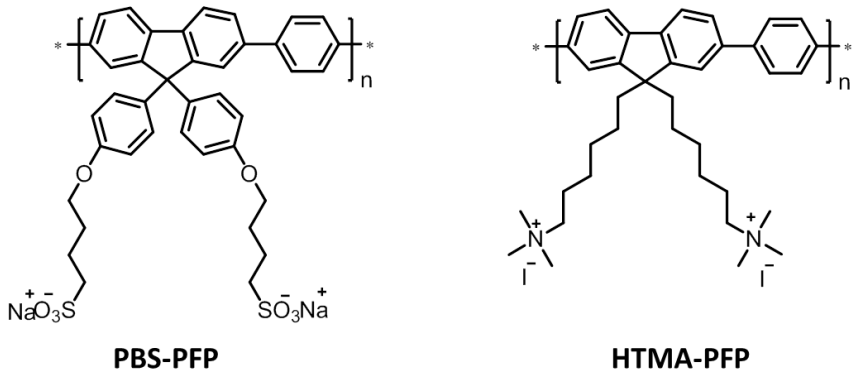

Figure 5.1. Chemical structures of the CPEs investigated.

5.2 Experimental

5.2.1 Polymers

Poly[9,9-bis(4-sulfonylbutoxyphenyl) fluorene-2,7-diyl-*alt*-1,4-phenylene] (**PBS-PFP**) and poly{9,9-bis[6-(*N*, *N*, *N*-trimethylammonium)hexyl]fluorene-2,7-diyl-*alt*-1,4-phenylene} (**PFP-HTMA**), both with an M_n = 6,500 g mol^{-1} determined by gel permeation chromatography (~740 g mol^{-1} repeat units (r.u.) for **PBS-PFP** and ~776 g mol^{-1} (r.u.) for **PFP-HTMA**), were synthesised by Dr. Ana-Teresa Marques as previously reported.[1, 23, 24] Both CPEs contain an identical polyfluorene-phenylene backbone and differ only in the charged side chains that they possess. **PBS-PFP** contains two anionic sulfate groups per r.u., and **HTMA-PFP** contains two cationic ammonium groups per r.u.

5.2.2 Synthesis of CPE-Di-ureasils

CPE-di-ureasils were prepared *via* two different methods identified as *Direct Insertion* (*DI*) and *Solvent Permeation* (*SP*).[25] Both methods involve the preparation of a di-ureapropyltriethoxysilane (d-UPTES) precursor solution, which has been described in detail elsewhere.[16, 17] In brief, Jeffamine ED-600 (1 ml, 1.75 mmol) was dissolved in THF (5 ml), to

which 3-isocyanatopropyltriethoxysilane (ICPTES) (0.9 ml, 3.0 mmol) was added under stirring. This mixture was refluxed at 70 ˚C for 24 h to prepare the d-UPTES precursor solution. The undoped di-ureasil is obtained by addition of ethanol (0.409 ml, 7 mmol), HCl (0.5 M, 0.040 ml) and H_2O (0.095 ml, 5.3 mmol) to the d-UPTES solution, which triggers the acid-catalysed sol-gel reaction. This corresponds to a ratio of 1 ICPTES: 2.3 EtOH: 1.8 H_2O: 0.006 HCl molar equivalents. The solution was stirred for 5 min before being poured into a polypropylene mould which was then covered with Parafilm. After 24 h, the Parafilm was pierced to encourage slow evaporation of the solvent. The samples were then placed in the oven at 40 ˚C for 48 h to complete the drying process which produced free-standing, transparent monoliths.

Table 5.1. Composition of CPE-di-ureasils prepared in this study. [CPE] is the concentration of the stock CPE solution (in mM (r.u.)), that is either added to the d-UPTES intermediate (*DI* method) or in which the di-ureasil is immersed (*SP* method).

Preparation Method	Polymer	Sample	[CPE] (mM (r.u.))	CPE wt%
Direct Insertion (DI)	PBS-PFP	DI-PBS-0.0	0	0
		DI-PBS-1.0	0.2	1×10^{-3}
		DI-PBS-2.0	0.4	2×10^{-3}
		DI-PBS-4.0	0.8	4×10^{-3}
		DI-PBS-8.0	1.6	8×10^{-3}
Direct Insertion (DI)	HTMA-PFP	DI-HTMA-0.0	0	0
		DI-HTMA-1.0	0.2	1×10^{-3}
		DI-HTMA-2.0	0.4	2×10^{-3}
		DI-HTMA-4.0	0.8	4×10^{-3}
		DI-HTMA-8.0	1.6	8×10^{-3}
Solvent Permeation (SP)	PBS-PFP	SP-PBS-0.0	0	0
		SP-PBS-0.7	0.01	0.7×10^{-3}
		SP-PBS-2.0	0.03	2.0×10^{-3}
		SP-PBS-3.4	0.05	3.4×10^{-3}
		SP-PBS-7.0	0.1	7.0×10^{-3}

In the *DI* method, a fixed volume of CPE solution was added to the d-UPTES precursor described above, prior to the addition of the gelation agents. The volume of the CPE solution was varied to produce CPE-di-ureasils with the doped wt% described in **Table 5.1**. The samples for the *DI* method are denoted **DI-PBS-x** and **DI-HTMA-x** for **PBS-PFP** and **HTAM-PFP**, respectively, where x represents the concentration (in 10^{-3} wt%) of the CPE within the di-ureasil. In the *SP* method, preformed blank di-ureasils were placed in a CPE solution of fixed volume (4 ml) and known concentration, upon which the hybrid swells taking up the CPE solution in which it is immersed. The concentrations of stock CPE solution used are outlined in **Table 5.1**. Following immersion for 300 min, the samples were removed and allowed to dry for 24 h, after which the samples contracted back to their initial size and form. The samples for the *SP* method are denoted

SP-PBS-x where x represents the concentration (in 10^{-3} wt%) of the CPE within the di-ureasil. Although it is possible to prepare **SP-HTMA** species, the results obtained are comparable to the **SP-PBS-x** samples, indicating that the nature of the ionic side chain has little influence on this method of synthesis. Thus, the discussion in this work focuses on the **SP-PBS-x** series.

5.3 Results and Discussion

A schematic representation of the two incorporation methods used to prepare CPE-di-ureasils is shown in **Fig. 5.2**. The *DI* method involves the condensation of the d-UPTES solution around the CPE which is *in situ*. Due to the intimate mixing of the CPE and the precursor solution the CPE is expected to be distributed homogeneously throughout the final sample obtained. During the *SP* method however, a preformed di-ureasil is immersed into the CPE solution upon which it swells taking on both the solvent and the CPE. Thus the samples created *via* this method are expected to contain a concentration gradient with the majority of the CPE being incorporated at the sample surface.

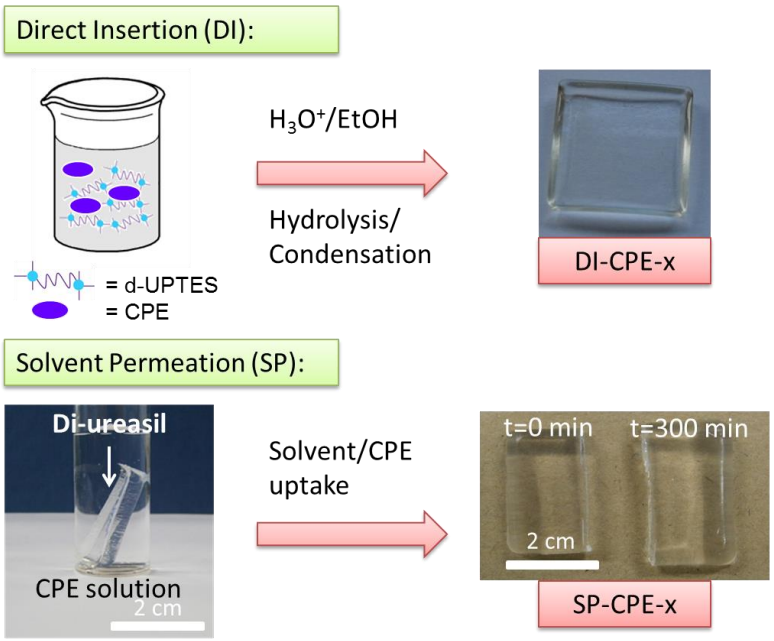

Figure 5.2. Schematic representation of the two synthetic methods used to prepare CPE-di-ureasil composites.

5.3.1 Preparation of d-UPTES Precursor Solution

The mechanism for the reaction between ED-600 and ICPTES to form the precursor solution, d-UPTES, is shown in **Scheme 5.1**. This reaction was followed by FTIR spectroscopy through the disappearance of the band at 2270 cm^{-1} (**Fig. 5.3**), which is characteristic of the isocyanate group of ICPTES.[15] The formation of amide bonds in the urea linkages is also indicated by the appearance of a broad band at 3356 cm^{-1} ascribed to a hydrogen bonded N-H moiety, along

with the appearance of two medium intensity bands at 1632 and 1561 cm^{-1} attributed to C=O stretch and N-H bending.[17]

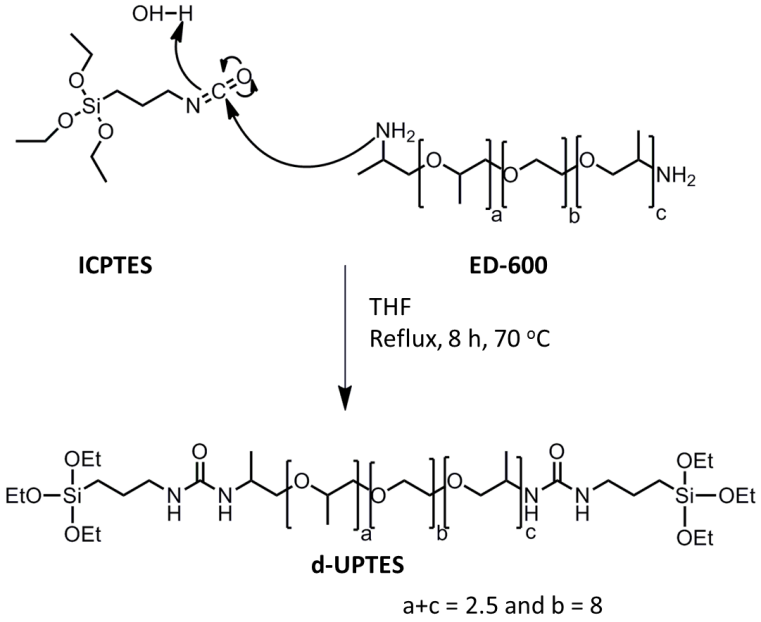

Scheme 5.1. The nucleophilic attack of ICPTES by ED-600, forming the urea linkages of the precursor solution, d-UPTES.

The spectral changes in the FTIR spectrum observed upon formation of d-UPTES are shown in **Fig. 5.3**, along with assignments of the main bands in the spectra of ED-600, ICPTES and d-UPTES.

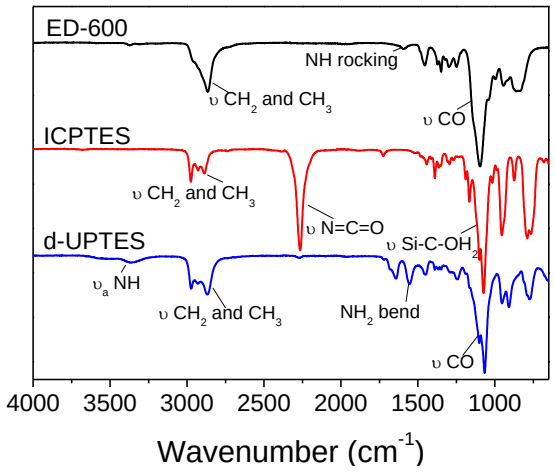

Figure 5.3. FTIR spectra of the starting materials ED-600 (black line) and ICPTES (red line) and the di-ureasil precursor solution, d-UPTES (blue line).

5.3.2 Hydrolysis and Condensation of d-UPTES

The undoped di-ureasil is prepared *via* a sol-gel reaction through the acid-catalysed hydrolysis and condensation of the d-UPTES precursor solution. The first step in this reaction involves hydrolysis of the ethoxy groups as shown in **Scheme 5.2**. Under the acidic conditions used in this work, HCl protonates the oxygen of the Si-OR group. This leads to the formation of a

pentacoordiante intermediate through interaction with the water present. This occurs as protonation of the Si-OR species causes electron density to be withdrawn from the central Si atom making it more electrophilic and thus more susceptible to attack by water. Protonation of the alkoxy species makes it a better leaving group and allows the nucleophilic substitution of the OR groups by OH.[26]

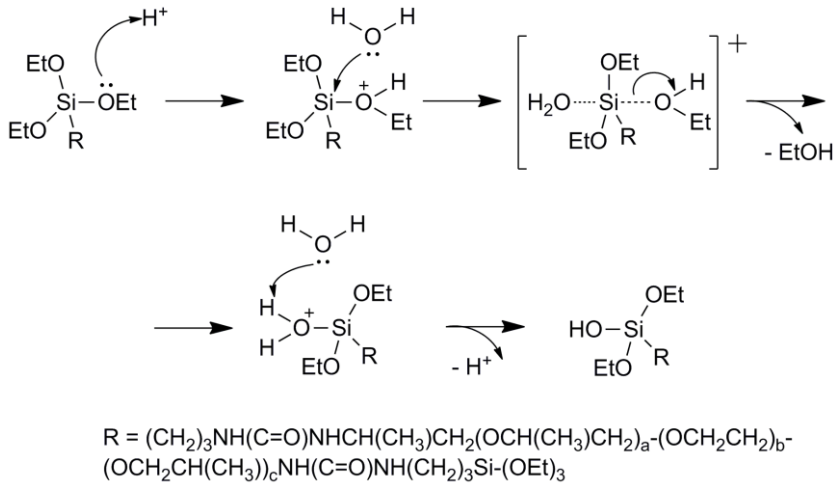

Scheme 5.2. Mechanism of the acid-catalysed hydrolysis of the alkoxy silane groups of d-UPTES.

A number of the newly formed Si-OH groups undergo condensation to form the siliceous network, the mechanism for which is similar to hydrolysis as shown in **Scheme 5.3**. The oxygen of the Si-OH species is protonated by the acid catalyst. Again, this causes the withdrawal of electron density from the central Si atom, leaving it susceptible to nucleophilic attack. This time, however, the nucleophile is another Si-OH species. This again leads to the formation of a pentacoordinate intermediate species. Water is released as a good leaving group and now bridging oxygen atoms are deprotonated by the solvent, giving rise to condensation product containing a Si-O-Si bridge.[26]

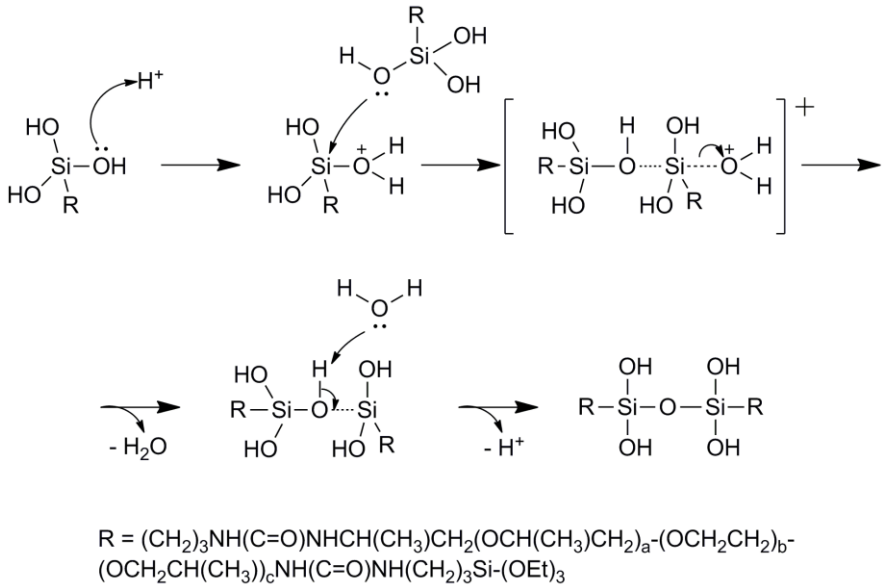

Scheme 5.3. Mechanism of the acid-catalysed condensation reaction of d-UPTES.

5.3.3 Incorporation and Localisation of the CPE within the Di-ureasil

5.3.3.1 Swelling Studies

The uptake of the CPE stock solution by the di-ureasil samples for the *SP* method was investigated through swelling studies. The di-ureasil samples, which had been swollen in CPE stock solution, were removed at controlled time intervals and excess solution was removed by dabbing on filter paper. Once clear of excess solution, the samples were weighed and the percentage solution uptake was calculated by comparison with the weight of the dry di-ureasil sample prior to immersion from:

$$\%\ uptake = \frac{(W_s - W_d)}{W_d} \times 100 \qquad \textbf{(5.1)}$$

where W_s is the weight of the swollen sample and W_d is the weight of the original dry sample.

Fig. 5.4a shows the % uptake for different batches of di-ureasil samples immersed in 1,4 dioxane/H_2O (25:75% *v/v*) containing no CPE. The % uptake is identical for each batch suggesting a highly reproducible synthetic method. The % uptake slows at longer immersion times (>1000 min) and plateaus at ~180%, which corresponds to the solvent equilibrium point.[27] Comparable trends have previously been reported for related di-ureasil samples prepared from the longer diamine, Jeffamine ED-2000, in ethylene carbonate/propylene carbonate mixtures.[28] Despite the fact that longer immersion times lead to higher percentage uptake, these samples exhibit a greater tendency to crack upon drying. This is due to a reduction in the degree of cross-linking in the swollen state.[29, 30] Thus, the immersion time was limited to 5 h, which corresponds to a percentage uptake of ~70%, to limit the effects of cracking while also ensuring sufficient uptake.

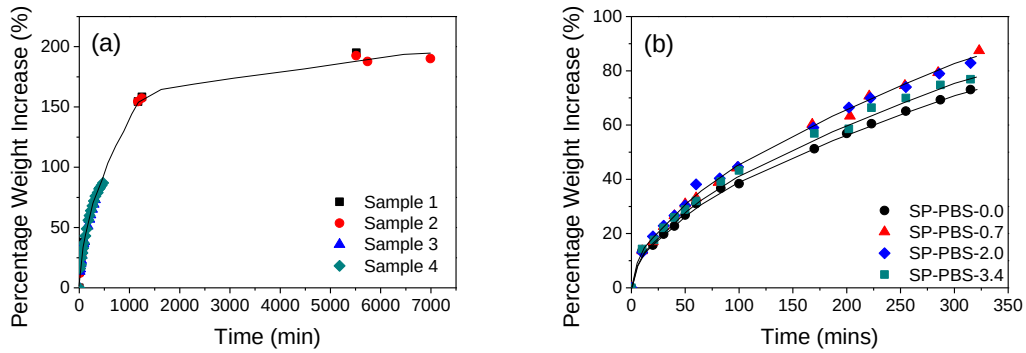

Figure 5.4. (**a**) % Uptake for di-ureasil samples as a function of immersion time for the *SP* method in 1,4 dioxane/H_2O (25:75% *v/v*); sample 1 - black squares, sample 2 - red circles, sample 3 – blue triangles, sample 4 - green diamonds. (**b**) % Uptake for di-ureasil samples as a function of immersion time in **PBS-PFP** solution (1,4-dioxane/H_2O 25:75% *v/v*); **SP-PBS-0.0** – black diamonds, **SP-PBS-0.7** - red triangles, **SP-PBS-2.0** - blue diamonds, **SP-PBS-3.4** – green squares. The solid lines serve only to guide the eye.

Fig. 5.4b shows the % uptake for di-ureasil samples immersed in 1,4-dioxane/H_2O (25:75% *v/v*) containing different concentrations of **PBS-PFP**. The % uptake is greater for

immersion in the CPE stock solution when compared to the pure solvent. However, this increase is not strongly dependent on the concentration of the CPE stock, within the concentration range examined.

5.3.3.2 Confocal Microscopy

Confocal microscopy was used to investigate the influence of the preparation method on the localisation of the CPE within the di-ureasil. **Fig. 5.5a** and **b** show confocal microscopy images (λ_{ex} = 405 nm) taken at 20 and 4 μm below the surface of **DI-PBS-1.0** and **SP-PBS-0.7**, respectively, showing clear emission from the CPE incorporated within the di-ureasil. The distribution of the CPE within the di-ureasil was examined by taking confocal microscopy images at varying distances from the surface of the CPE-di-ureasil sample. It can be seen from the intensity depth profile in **Fig. 5.5c** that the *DI* method results in the homogeneous distribution of the CPE throughout the di-ureasil. However, for samples prepared *via* the *SP* method, see **Fig. 5.5d** for **SP-PBS-0.7** as a representative example, a dense layer of CPE of ~12-14 μm in thickness is observed at the sample surface. This is consistent with the two synthetic processes. For the *DI* method the di-ureasil network condenses around the CPE which is *in situ*. However, for the *SP* method the CPE is incorporated *via* diffusion into the swollen di-ureasil. For this method, the permeation distance is determined by the immersion time, the solubility parameters of the di-ureasil, CPE and solvent, and the degree of cross-linking of the di-ureasil network. Thus, for the CPE concentration range and immersion time used in this work, the CPE is unable to permeate further than this ~12-14 μm layer.

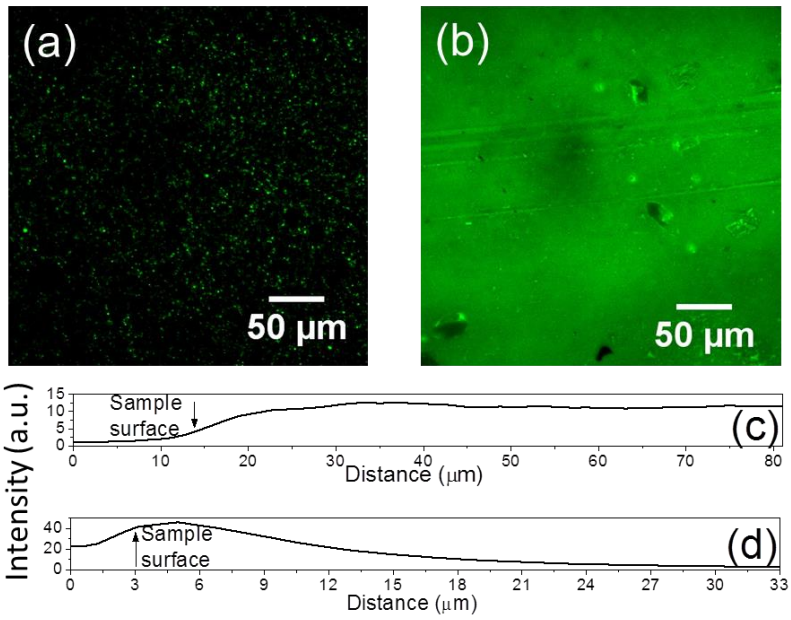

Figure 5.5. Confocal microscopy images (λ_{ex} = 405 nm) from 20 and 4 μm beyond the surface of (**a**) **DI-PBS-1.0** and (**b**) **SP-PBS-0.7**, respectively. Depth profiles of the average fluorescence intensity for a lateral cross-section (λ_{ex} = 405 nm) of (**c**) **DI-PBS-1.0**, showing fluorescence throughout the sample depth investigated, 68 μm and (**d**) **SP-PBS-0.7** showing fluorescence from a 12 -14 μm surface layer, sample depth investigated, 32 μm.

5.3.3.3 CPE Release Studies

To investigate the retention of the CPEs once incorporated within the di-ureasil *via* both methods, CPE-di-ureasil samples were immersed in the appropriate solvent system (1,4-dioxane/H_2O (25:75% *v/v*) for the **PBS-PBP** and MeCN/H_2O (25/75% *v/v*) for the **HTMA-PFP**). Following immersion for up to 24 h, no detectable CPE photoluminescence was observed from the immersion solution (**Fig 5.6**, see **Fig. A.5.1** for **DI-HTMA-4.0** and **SP-PBS-3.4**). This suggests that the CPE is well retained within the di-ureasil on incorporation *via* both synthetic methods.

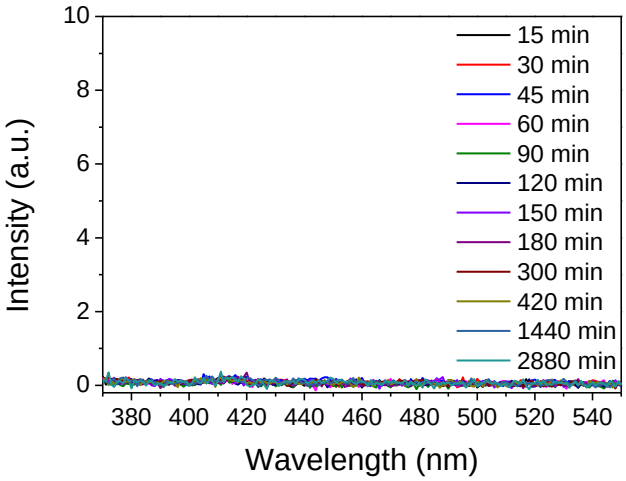

Figure 5.6. Photoluminescence spectra of the immersion solutions following sample removal after different immersion times for **DI-PBS-4.0** in 1,4-dioxane/H_2O (25:75% *v/v*) (λ_{ex} = 360 nm).

5.3.4 Physical Characterisation

5.3.4.1 Powder X-Ray Diffraction

PXRD experiments were carried out to examine the bulk structural features of the CPE-di-ureasils. All of the CPE-di-ureasil samples display XRD patterns that match those previously reported for di-ureasils,[13, 18, 19, 31] containing a main peak at 22.5˚ with a shoulder at 16.6˚ 2θ (**Fig. 5.7**).

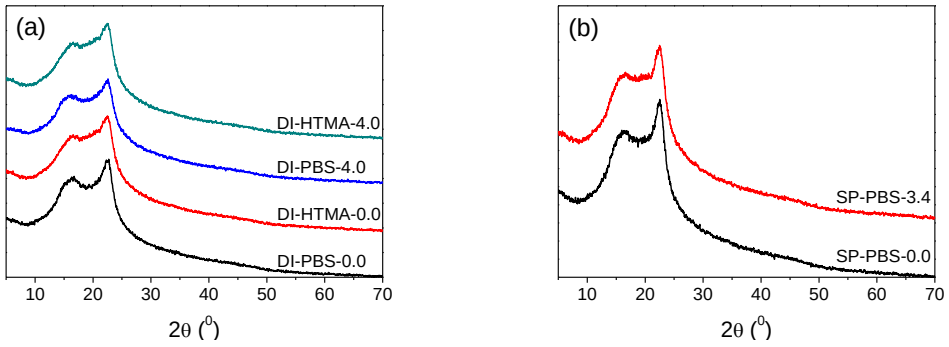

Figure 5.7. Powder X-ray diffractograms for (**a**) **DI-PBS-0.0**, **DI-HTMA-0.0**, **DI-PBS-4.0** and **DI-HTMA-4.0** and (**b**) **SP-PBS-0.0** and **SP-PBS-3.4** in the range 2θ = 5-70˚.

The main peak is associated with the presence of ordering within the siliceous domains.[18, 31] From this, the structural unit distance, *d*, was calculated to be 4.0 ± 0.1 Å (from Bragg's Law). The shoulder at 16.6° 2θ has previously been reported for similar di-ureasil samples prepared through carboxylic acid solvolysis and is attributed to in-plane ordering of additional intra-siloxane domains.[31] The coherence length, *L*, over which the structural unit survives, was estimated to be 21 ± 2 Å (from the Scherrer equation[32]). This is comparable to the diameter of siliceous domains reported for self-assembled alkyl-siloxane hybrids.[33] The position and shape of the peaks in the XRD patterns are independent of incorporation method or CPE charge or concentration. This suggests that no significant structural changes to the di-ureasil network are induced by either method of CPE incorporation.

5.3.4.2 Solid-State NMR

To further examine the structural features of the CPE-di-ureasil samples, solid-state NMR studies were carried out at room temperature. All ^{29}Si MAS-NMR spectra possess three broad signals characteristic of T_1, T_2 and T_3 units (**Fig. 5.8**). These are labelled according to the conventional T_n notation, where *n* (*n* = 1, 2, 2) is the number of Si-bridging oxygen atoms, *i.e.* T_1 = R′Si(OSi)-$(OR)_2$, T_2 = R′Si$(OSi)_2$-(OR) and T_3 = R′Si$(OSi)_3$. The T_2, ~ -58 ppm, and the T_3, ~ -66 ppm, are the dominant signals with a minor contribution from T_1, ~ -49 ppm. The absence of a T_0 signal confirms that no unreacted precursor remains.[13, 18, 31]

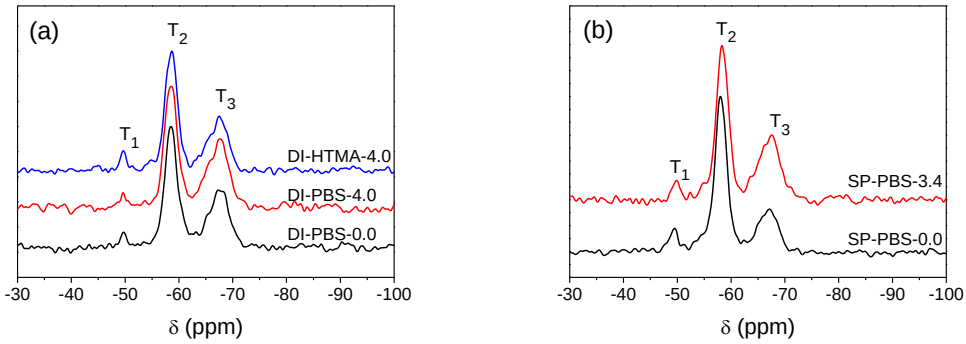

Figure 5.8. ^{29}Si solid-state MAS NMR spectra for (**a**) **DI-PBS-0.0**, **DI-PBS-4.0** and **DI-HTMA-4.0** and (**b**) **SP-PBS-0.0** and **SP-PBS-3.4**.

The degree of condensation of the siliceous network, *C*, was calculated from:

$$C\ (\%) = 1/3\ (\%T_1 + 2\%T_2 + 3\%T_3) \qquad \textbf{(5.2)}$$

where $\%T_i$ is the percentage area for the i^{th} peak as determined from fitting of Gaussian bands to each of the peaks observed in the NMR (see **Section 2.3.2.1**). The degree of condensation was found to be between 73-81%, see **Table 5.2**, which is in agreement with di-ureasils doped with lanthanide ions.[18] The degree of condensation does not seem to be affected by either the method of incorporation, the charge on the CPE or its concentration, corroborating the PXRD results.

Table 5.2. ^{29}Si MAS-NMR chemical shifts (ppm *vs.* TMS), population of different T_n species (%), T_n species ratios, and degree of condensation, *C* (%) of CPE-di-ureasils.

Sample	T_1 (%)	T_2 (%)	T_3 (%)	T_1: T_2: T_3	*C* (%)[a]
SP-PBS-0	-49.8 (7.5)	-58.4 (63.6)	-66.8 (28.8)	1: 8.5: 3.8	73.76
SP-PBS-3.4	-49.4 (4.4)	-58.1 (55.1)	-66.8 (40.5)	1: 12.5: 9.2	78.68
DI- PBS-0	-49.7 (3.4)	-58.6 (55.0)	-67.4 (41.6)	1: 16.2: 12.2	79.41
DI- PBS-4.0	-49.7 (3.0)	-58.5 (51.7)	-67.2 (45.3)	1: 17.2: 15.1	80.75
DI- HTMA-4.0	-49.6 (5.2)	-58.7 (55.3)	-67.4 (39.4)	1: 10.6: 7.6	78.07

[a] $C = 1/3(\%T_1+2\%T_2+3\%T_3)$[18]

Fig. 5.9 shows the ^{13}C CP-MAS NMR for the CPE-di-ureasil samples each of which matches those previously reported for di-ureasils of this type.[31] Assignments of the main peaks can be found in **Table 5.3**. Once again, no significant changes in the peaks are observed on comparison of the charge or concentration of the CPE or the preparation method, further confirming the integrity of the di-ureasil network is maintained upon CPE incorporation.

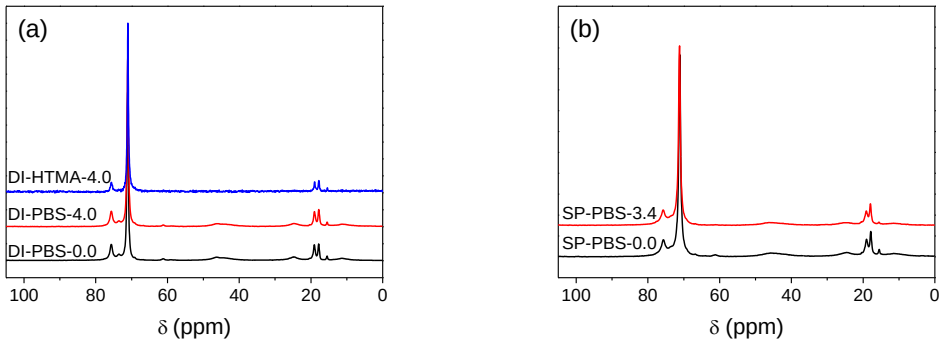

Figure 5.9. ^{13}C solid-state CP/MAS NMR spectra for (**a**) **DI-PBS-0.0**, **DI-PBS-4.0** and **DI-HTMA-4.0** and (**b**) **SP-PBS-0.0** and **SP-PBS-3.4**.

Table 5.3. ^{13}C solid-state CP-MAS NMR chemical shifts (ppm *vs.* TMS) of CP-di-ureasils.

Signal assignment	DI-PBS-0.0	DI-PBS-4.0	DI-HTMA-4.0	SP-PBS-0.0	SP-PBS-3.4
-OCH	75.7	75.6	75.6	75.7	75.7
-(OCH_2CH_2)	71.1	71.1	71.1	71.1	71.1
-NCH_2 in $N(CH_2)_3Si$	46.3	45.9	45.6	46.2	46.3
-'CH_2 in $N(CH_2)_3Si$	24.8	24.6	24.5	24.5	25.3
-CH_3 in – $OCH_2CH(CH_3)$	19.0	18.9	19.0	18.9	19.1
-CH_3 in – $(CH_3CH_2O)_3Si$	17.8	17.7	17.6	17.7	17.9
-CH_2Si in – $N(CH_2)_3Si$	11.4	11.2	11.0	11.4	11.4

5.3.4.3 Fourier Transform Infrared Spectroscopy

FTIR spectra for all CPE-di-ureasil samples prepared *via* both methods show similar spectra to those previously reported for di-ureasils (**Fig. 5.10**).[17] However, subtle differences in the extent of hydrogen bonding and changes to the coordination environment of the urea groups can be examined by probing the Amide I region of the FTIR spectrum.[13, 18] The Amide I region is a complex vibration providing information about the specificity and degree of hydrogen bonding interactions associated with C=O stretching frequencies in different local environments.[17] Gaussian deconvolution of the Amide I region was carried out in the region 1610-1770 cm^{-1}, as described in **Section 2.3.2.2**. Deconvolution of this band reveals three components centred at 1708 (Peak 1), 1663 (Peak 2) and 1635 cm^{-1} (Peak 3) (**Fig. 5.11**).

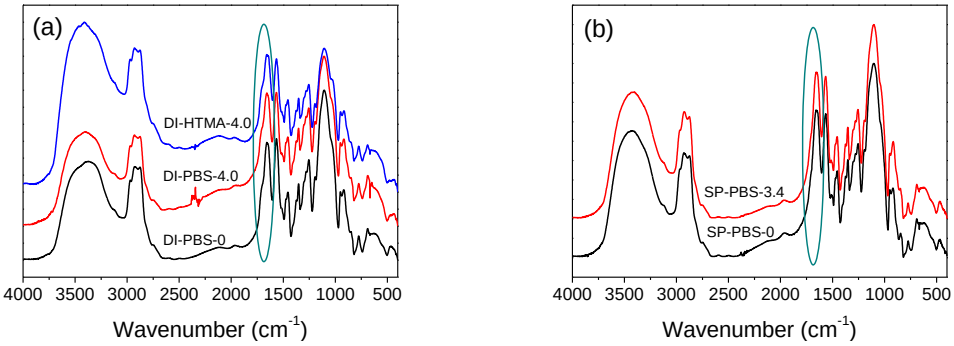

Figure 5.10. FTIR spectra for CPE-di-ureasil samples prepared *via* (**a**) the *DI* method and (**b**) the *SP* method, (4000-450 cm^{-1}, at a resolution of 4 cm^{-1}). The Amide I regions are highlighted by dark cyan circles.

Peaks 1 and 2 are attributed to $\nu_{C=O}$ stretches involved in disordered hydrogen-bonded poly(ethylene oxide) (POE)-urea associations of increasing strength.[13, 17, 18] While Peak 3 is assigned to self-organised, hydrogen-bonded urea-urea interactions.[13, 17, 18] The absence of a band at 1750 cm^{-1} confirms that all urea groups are involved in varying degrees of hydrogen-bonding.[17, 18] When examining the *DI* samples, the Amide I band of the CPE-di-ureasils is only moderately affected by the charge and concentration of the CPE added most notably at the highest concentration (4×10^{-3} wt%), see **Table 5.4**. A slight decrease in the contribution of Peak 3 is observed for **DI-PBS-4.0** when compared to **DI-HTMA-4.0**, suggesting the formation of a less ordered di-ureasil network upon incorporation of the anionic **PBS-PFP**. However, significant differences are observed in the contribution from the three bands on comparison of the two preparation methods. The *SP* samples also contain three peaks; however, their relative contributions differ considerably. For the *SP* samples there is a decrease in Peak 1 accompanied by a concomitant increase in the relative contribution of Peak 2 (10%). This suggests that the incorporation of the CPEs *via* the *DI* method disrupts and reorganises the disordered hydrogen-bonding in the POE-urea associations. This is consistent with the swelling process undergone by the di-ureasil during this preparation method.

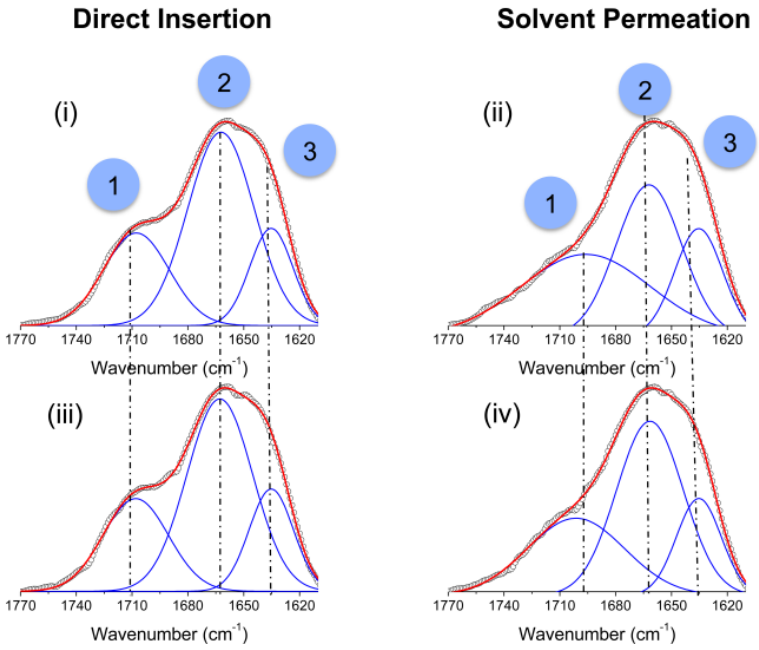

Figure. 5.11. Results of curve-fitting preformed in the 'Amide I' region of the samples prepared *via* both the *Direct Insertion* and *Solvent Permeation* methods: (**i**) **DI-PBS-0.0**, (**ii**) **SP-PBS-0.0**, (**iii**) **DI-PBS-4.0** and (**iv**) **SP-PBS-3.4**. The numbers identify the peaks described in the text.

Table 5.4. Results of Gaussian curve fitting of the 'Amide I' band of CPE-di-ureasils prepared *via DI* and *SP* methods, showing peak position, area and % contribution for each component resolved.

Sample	**Peak (cm^{-1})**	**Area (% of total area)**	**Peak (cm^{-1})**	**Area (% of total area)**	**Peak (cm^{-1})**	**Area (% of total area)**
DI-PBS-0.0	1708	19.95 (26.3%)	1662	42.24 (55.6%)	1635	16.85 (18.1%)
DI-PBS-1.0	1708	19.90 (26.0%)	1663	41.72 (54.6%)	1635	15.92 (19.4%)
DI-PBS-2.0	1708	22.31 (28.8%)	1663	42.35 (54.7%)	1635	14.65 (16.5%)
DI-PBS-4.0	1707	21.19 (28.0%)	1662	40.74 (53.8%)	1635	14.29 (18.3%)
DI-HTMA-0	1709	20.11 (26.3%)	1663	43.52 (56.9%)	1636	16.32 (16.7%)
DI-HTMA-1.0	1711	19.67 (25.0%)	1664	45.85 (58.3%)	1636	14.93 (16.7%)
DI-HTMA-2.0	1709	19.91 (25.2%)	1664	42.87 (54.2%)	1636	15.91 (20.6%)
DI-HTMA-4.0	1708	21.43 (26.6%)	1663	41.81 (52.0%)	1635	14.38 (21.4%)
SP-PBS-0.0	1696	34.53 (41.2%)	1662	32.36 (38.6%)	1635	13.73 (20.1%)
SP-PBS-0.7	1701	24.70 (32.0%)	1662	38.19 (49.5%)	1636	13.86 (18.5%)
SP-PBS-2.0	1705	16.83 (23.1%)	1662	41.47 (56.8%)	1636	12.79 (20.1%)
SP-PBS-3.4	1701	23.05 (30.4%)	1662	38.19 (48.7%)	1635	14.84 (21.0%)

5.3.4.4 Thermal and Photostability

The thermograms for the undoped samples (*e.g.* **DI-PBS-0.0**) are in excellent agreement with those previously reported for the undoped di-ureasil,[21,34] with the onset of sample decomposition observed at ~339 ˚C (**Fig. 5.12a)**. Incorporation of **PBS-PFP** or **PFP-HTMA** *via* either method yields a material with good thermal stability with the onset of thermal decomposition occurring between 337-352 ˚C. This thermal stability considerably surpasses the moderate operating temperatures (~65-140 ˚C[35, 36]) present in organic electronic devices. The photostability of the CPE-di-ureasils was also investigated. **Fig. 5.12b** shows the integrated emission intensity of **DI-PBS-4.0**, **SP-PBS-3.4**, **DI-HTMA-4.0** and a pure **PBS-PFP** film as a function of irradiation time upon excitation at 370 nm. Irradiation of the PBS-PFP film over time results in the growth of a green emission band centred at 560 nm that is characteristic of the formation of fluorenone defects on polyfluorene chains.[37-39] This band eventually becomes more intense than the initial blue- poly(fluorene) emission. Thus to examine purely the poly(fluorene) contribution to the emission, the integrated intensity for all samples was measured in the range 385-490 nm. The integrated intensity of the **PBS-PFP** film dropped gradually to 40% of the initial value in the first hour, and continued to decrease to 25% at the end of the irradiation period (2 h). This is in contrast to **DI-BPS-4.0**, **SP-PBS-3.4** and **DI-HTMA-4.0**, whose emission shows improved stability to extended irradiation, retaining >80% of the initial intensity at the end of the study.

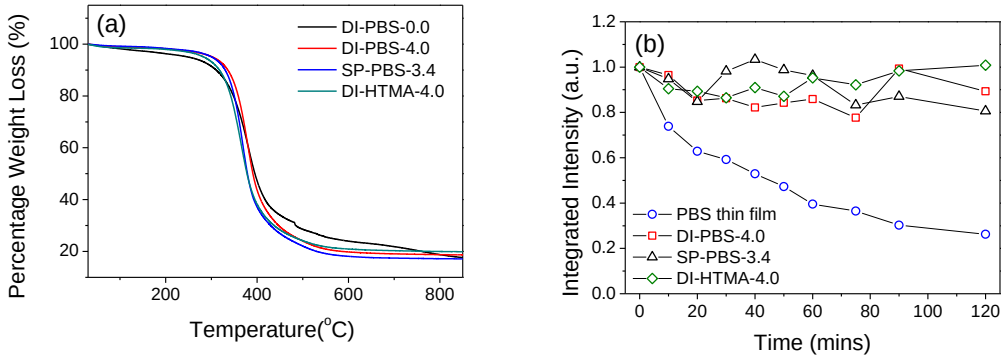

Figure. 5.12. (**a**) TGA thermograms of **DI-PBS-0.0** (blue line), **DI-PBS-4.0** (red line), **SP-PBS-3.4** (blue line) and **DI-HTMA-4.0** (cyan line). TGA measurements were performed in air at a heating rate of 10 ^{o}C min^{-1}. (**b**) Integrated emission intensity of a pure **PBS-PFP** thin film on glass (open blue circles), **DI-PBS-4.0** (open red squares), **SP-PBS-3.4** (open black triangles) and **DI-HTMA-4.0** (open green diamonds) under irradiation at 370 nm. The black lines serve only to guide the eye.

5.3.5 Photophysical Characterisation

5.3.5.1 Photoluminescence of CPEs in Solution

In general, the photophysical properties of CPEs are dependent on the repeat unit of the conjugated backbone, with similar spectra observed for CPEs with the same backbone structure.[40] However, due to their amphiphilic nature which gives rise to the tendency to aggregate in aqueous solution, their photophysical properties can also be dependent on interactions with the solvent.[40]

Fig. 5.13 shows the UV/Vis absorption and PL properties of **PBS-PFP** and **HTMA-PFP** in solution. Binary solvent systems of a polar solvent and a non-polar solvent were used to reduce polymer aggregation. The optimised solvent systems were chosen from the literature as 1,4-dioxane/H_2O (25:75% *v/v*) for **PBS-PFP**[41] and MeCN/H_2O (25:75% *v/v*) for **HTMA-PFP**.[42]

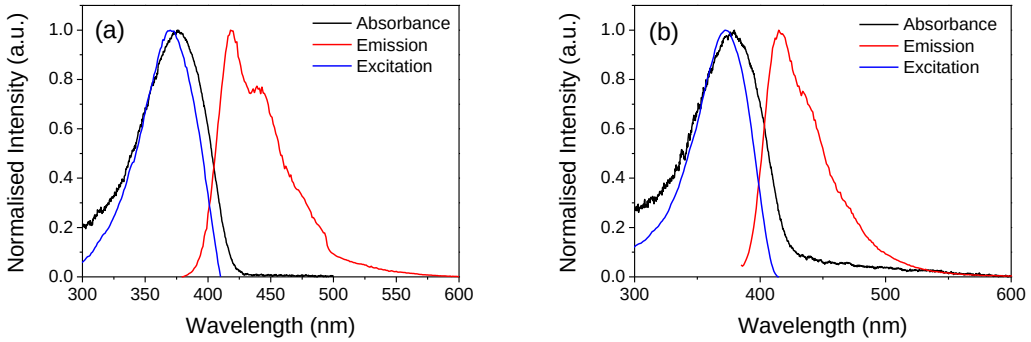

Figure 5.13. UV/Vis absorption (black lines), PL (λ_{ex} = 370 nm, red lines) and PL excitation (λ_{ex} = 420 nm, blue lines) spectra for (**a**) **PBS-PFP** in 1,4-dioxane/H_2O (25:75% *v/v*) and (**b**) **HTMA-PFP** in MeCN/H_2O (25:75% *v/v*).

Both CPEs exhibit a broad UV/Vis absorption band between 300–425 nm with a maximum at 375 nm for **PBS-PFP** and 378 nm for **HTMA-PFP**. The corresponding PL spectra show vibrational fine structure which is more pronounced in the spectrum of **PBS-PFP**. The maximum of the PL band lies at 411 nm for **PBS-PFP** and 415 nm for **HTMA-PFP**, while the maximum of the PL excitation band is found at 370 and 372 nm for **PBS-PFP** and **HTMA-PFP**, respectively.

5.3.5.2 Photoluminescence of Undoped Di-ureasils

The PL properties of **DI-PBS-0.0** are shown in **Fig. 5.14** as a representative example for the undoped di-uresil samples, all of which show comparable trends. The PL spectra exhibit a broad band between 340 and 575 nm, the maximum of which is strongly dependent on the excitation energy, red-shifting to longer wavelengths as λ_{ex} increases. This behaviour is characteristic of undoped di-ureasils.[19, 43] Gaussian deconvolution of the PL spectra has previously revealed the presence of two components contributing to the overall emission; a ‘blue’ component (2.5 to 3.1 eV) which is ascribed to donor-acceptor pair recombinations occurring in the NH/C=O groups of the urea linkages and a ‘blue-purple’ component (2.8 to 3.3 eV) attributed to donor-acceptor pair recombinations occurring in the oxygen-related defects in the siliceous nanodomains.[19, 43]

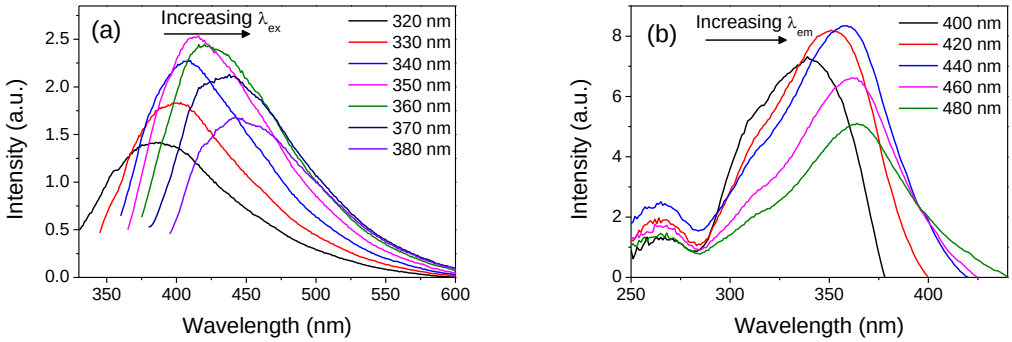

Figure 5.14. (**a**) PL spectra (λ_{ex} = 320, 330, 340, 350, 360,370 and 380 nm) and (**b**) PL excitation spectra (λ_{em} = 400, 420, 440, 460 and 480 nm) of **DI-PBS-0.0**.

A similar trend is observed in the corresponding excitation spectra which contain a broad band between 280 and 450 nm. As the monitoring energy decreases, the maximum of this band is red-shifted. As the band red-shifts, it simultaneously broadens further suggesting the presence of two emitting species.[18, 43] The higher and lower energetic bands have been assigned to the preferential excitation of the purple-blue (siliceous domains) and blue (NH groups) emission bands, respectively.[18, 43]

5.3.5.3 Photoluminescence of CPE-di-ureasils

Incorporation of **PBS-PFP** *via* the *DI* method causes the emission spectra to take on the characteristic polyfluorene emission profile, yielding a structured band between 380-500 nm (**Fig. 5.15a** and **c**). A slight blue-shift in the emission maximum is also observed on transferring the CPE from solution to the solid-state (~2 nm). A blue-shift in CPE emission has previously been attributed to break-up of polymer aggregates.[1, 2] This suggests that the break-up of larger CPE aggregates occurs upon incorporation into the di-ureasil. There is also a distinct contribution from the di-ureasil host to the emission spectrum. At lower excitation wavelengths, 320-350 nm (semi-selective for di-ureasil excitation), the high energy portion of the spectrum is considerably broadened, an attribute that is seen for the undoped di-ureasil host. It is also notable that on increasing the excitation wavelength (λ_{ex}= 320 – 380 nm) there is also a gradual broadening at the lower energy region of the spectrum. This trend is dependent on the CPE dopant concentration. As the concentration of **PBS-PFP** is increased, the broadening in the high energy region is reduced, while the effect in the lower energy region is increased, as shown for **DI-PBS-2.0** in **Fig. 5.15c**.

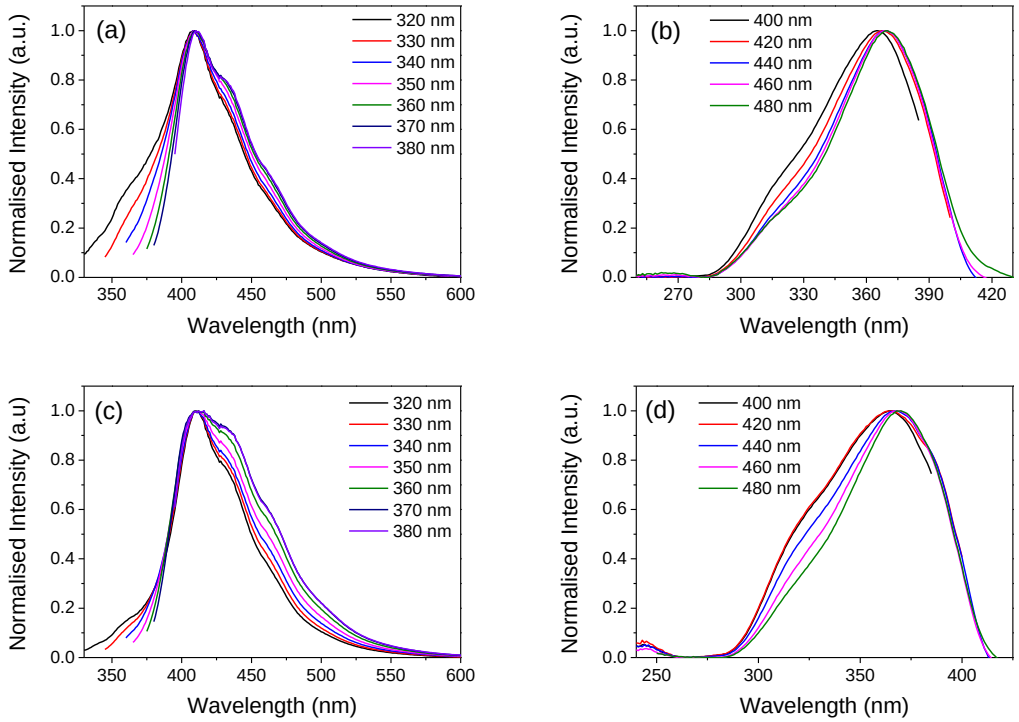

Figure 5.15. (**a**) PL (λ_{ex} = 320, 330, 340, 350, 360, 370 and 380 nm) and (**b**) PL excitation (λ_{em}= 400, 420, 440, 460 and 480 nm) spectra for **DI-PBS-1.0** and (**c**) PL (λ_{ex} = 320, 330, 340, 350, 360, 370 and 380 nm) and (**d**) PL excitation (λ_{em}= 400, 4200, 440, 460 and 480 nm) spectra for **DI-PBS-2.0**.

Similarly, the corresponding PL excitation spectra (**Fig. 5.15b** and **d**) are also very reminiscent of the CPE in solution (see **Fig. 5.13a**). Once again, a striking wavelength dependence is observed. As the emission wavelength is increased (λ_{em} = 420 – 480 nm), the shape of the spectrum changes from resembling the pure di-ureasil, to matching that of CPE. As the **PBS-PFP** concentration is increased the dominance of the CPE in the excitation spectra is clear, as shown for **DI-PBS-1.0** and **DI-PBS-2.0** in **Fig. 5.15b** and **d**, respectively. The PL and PL excitation spectra also show a similar wavelength dependence on incorporation of **PBS-PFP** *via* the *SP* method. However, the spectral broadening occurs to a lesser extent in both the high and low energy regions as shown for the highest concentration sample, **SP-PBS-3.4**, in **Fig. 5.16**.

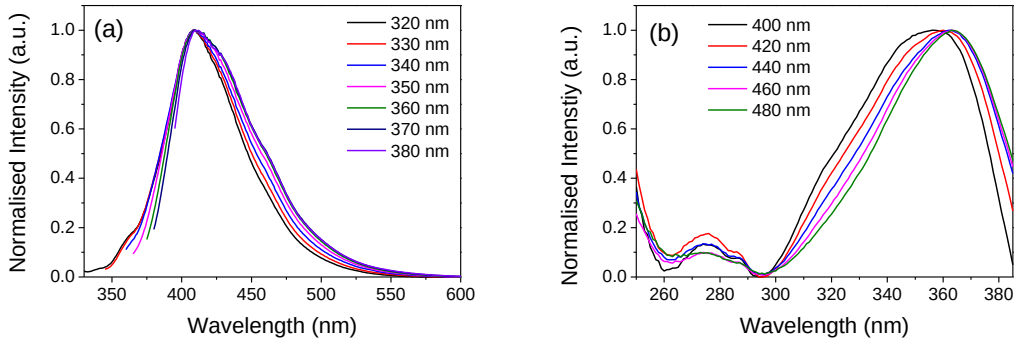

Figure 5.16. (**a**) PL (λ_{ex} = 320, 330, 340, 350, 360, 370 and 380 nm) and (**b**) PL excitation (λ_{em} = 400, 4200, 440, 460 and 480 nm) spectra for **SP-PBS-3.4**.

Similar trends are observed for the PL and PLE spectra of the **DI-HTMA-x** series. However, it must be noted that at the lowest concentration (**Fig. 5.17a** and **b**) the emission and excitation spectra do not show any CPE emission and resemble that of the undoped di-ureasil (**Fig. 5.14**). The appearance of the polyfluorene-like emission is only observed above a critical concentration of **HTMA-PFP** (see **Fig. 5.17c** and **d** for **DI-HTMA-2.0**). This suggests a potentially weaker interaction between **HTMA-PFP** and the di-ureasil host.

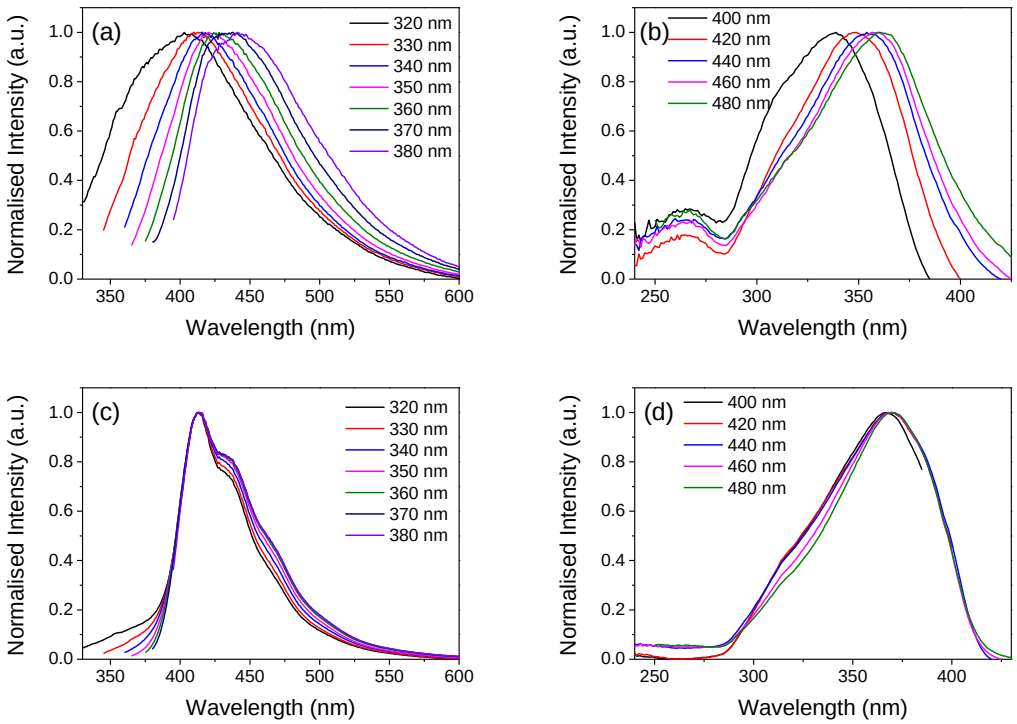

Figure 5.17. (**a**) PL (λ_{ex} = 320, 330, 340, 350, 360, 370 and 380 nm) and (**b**) PL excitation (λ_{em} = 400, 420, 440, 460 and 480 nm) spectra for **DI-HTMA-1.0** and (**c**) PL (λ_{ex} = 320, 330, 340, 350, 360, 370 and 380 nm) and (**d**) PL excitation (λ_{em} = 400, 4200, 440, 460 and 480 nm) spectra for **DI-HTMA-2.0**.

5.3.5.4 Photoluminescence Quantum Yield (PLQY)

Fig. 5.18 shows the measured photoluminescence quantum yields (PLQYs) for each sample series as a function of increasing CPE concentration (wt%). The undoped di-ureasils prepared *via* both methods show PLQYs of 2.3-6.8% matching those previously reported for di-ureasils.[16, 31] A dramatic increase in the PLQY is observed with increasing CPE concentration, which can be detected by the naked eye (**Fig. 5.19**). The PLQY values reached 56%, 47% and 46% for **DI-PBS-4.0**, **DI-HTMA-4.0** and **SP-PBS-3.4**, respectively. However, it must be noted that there is no increase in PLQY for **DI-HTMA-1.0** which remains similar to that of the undoped di-ureasil. This is consistent with the PL spectra for this sample which do not show any contribution from the CPE and resemble the undoped di-ureasil.

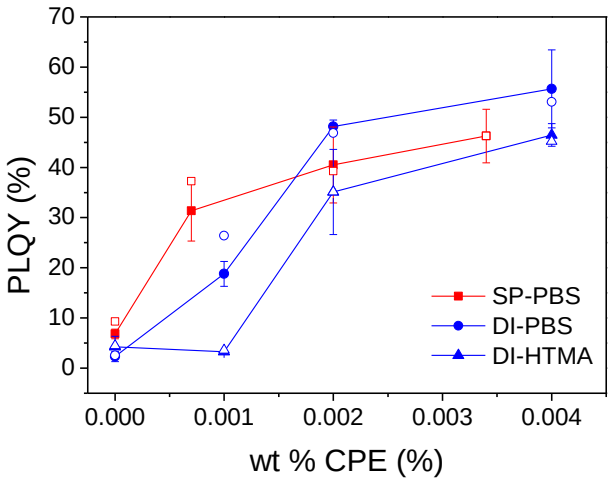

Figure 5.18. Measured PLQY (λ_{ex} = 370 nm) for **SP-PBS-x** (closed red squares**), DI-PBS-x** (closed blue circles) and **DI-HTMA-x** (closed blue triangles). The open symbols represent the corresponding PLQY values corrected for re-absorption/re-emission. The solid lines serve solely to guide the eye.

Due to their waveguiding nature and the possibility of self-absorption within these samples, the measured PLQY values were corrected for reabsorption as described in **Section 2.3.3**. However, as can be seen by the open symbols in **Fig. 5.18**, the effects of self-absorption for these samples are minimal resulting in negligible changes in the PLQY. The dramatic increase in the observed PLQY is not described simply by the sum of the contributions from each component. The PLQYs of the CPEs in solution were measured as 23.5% for **PBS-PFP** (1,4-dioxane/H_2O 25:75% *v/v*) and 28.7% for **HTMA-PFP** (MeCN/H_2O 25:75% *v/v*). Equally, solid-state films of the pure CPEs exhibit low PLQY values attributed increased value of aggregation, with the PLQY of **HTMA-PFP** films previously reported as ~7.5%.[44] If these values are merely combined with the PLQY values reported for undoped di-ureasils (4-10%[31]), the obtained PLQY would remain substantially lower than the values measured here. Thus, an alternative pathway must operate in the CPE-di-ureasils to produce this dramatic PLQY enhancement.

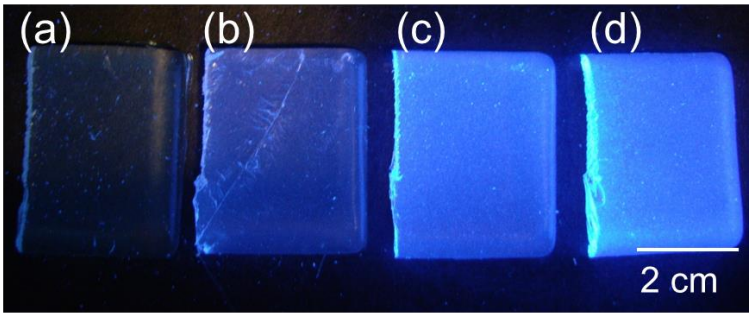

Figure 5.19. Photograph of (**a**) **DI-PBS-0.0**, (**b**) **DI-PBS-1.0**, (**c**) **DI-PBS-2.0** and (**d**) **DI-PBS-4.0** under UV-illumination (λ_{ex} = 365 nm).

5.3.5.5 Photoluminescence Lifetimes of CPE-di-ureasils

To further examine the mechanism responsible for the observed PLQY enhancement, picosecond time-correlated single photon counting (ps-TCSPC) emission lifetime measurements

were performed. The CPEs and di-ureasil relax over reasonably different time scales allowing distinct contributions from each component to the emission lifetime to be identified. Due to the experimental set-up, excitation was restricted to 365 nm, which meant that selective excitation was not possible due to strong overlap between the absorption bands of the two components (**Fig 5.20**).

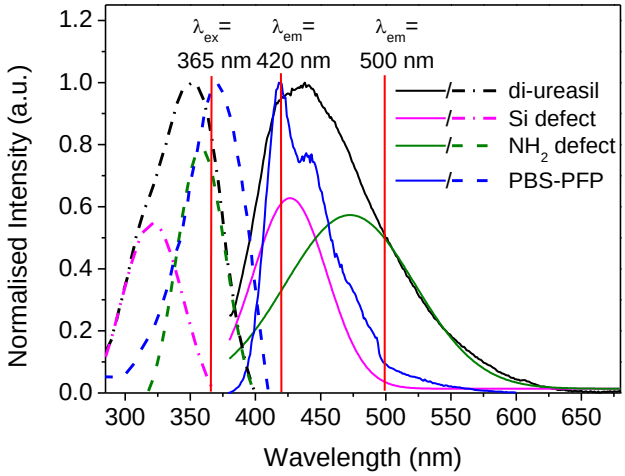

Figure 5.20. PL (λ_{ex} = 370 nm) and PL excitation (λ_{em} = 420 nm) spectra for **PBS-PFP** in 1,4 dioxane/H_2O 25:75% *v/v* (blue) and **DI-PBS-0.0** (black) showing the Gaussian peak fits for the two components that give rise to the di-ureasil emission and excitation spectra. These components are attributed to oxygen-related defects in the siliceous network (pink) and photoinduced proton transfer between NH_2 groups (dark green). The emission and excitation spectra are shown as solid and dashed lines, respectively. Red lines highlight the excitation (λ_{ex} = 365 nm) and emission wavelengths (λ_{em} = 420 and 500 nm) used in the TCSPC experiments.

However, the emission-excitation matrices (EEMs) suggest that variation of the monitoring wavelength should aid in distinguishing the two species (**Fig. 5.21**). EEMs plot the emission spectrum of the sample as a function of excitation wavelength as a 2D colour map, where different colours represent variations in the emission intensity and not the emission colour.

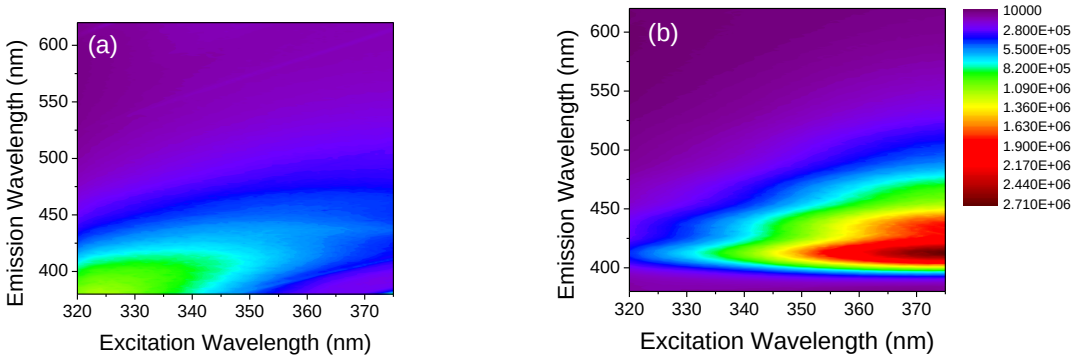

Figure 5.21. Emission-excitation matrices for (**a**) **DI-PBS-0.0** and (**b**) **DI-PBS-1.0**, where λ_{ex} = 320-375 nm and λ_{em} = 380-650 nm (both at 1 nm intervals).

Two weak emission contributions are observed for **DI-PBS-0.0** (**Fig. 5.21a**) located at 370-420 nm (λ_{ex} = 320-350 nm) and 425-500 nm (λ_{ex} = 350-370 nm). The EEM for **DI-PBS-1.0** shows a distinct band between 400- 420 nm which increases in intensity as the excitation wavelength increases to 370 nm (the absorbance maximum of the CPE) (**Fig. 5.21b**). A weaker

band between 470-500 nm is also observed for λ_{ex} = 350-370 nm. Based on these observations, emission wavelengths of 420 and 500 nm were chosen for TCSPC experiments to probe primarily the CPE and di-ureasil emission, respectively.

The photoluminescence decays and fits for **PBS-PFP** and **HTMA-PFP** in solution are shown in **Fig. 5.22**. The fitting procedure for all decays is described in detail in **Section 2.3.5**. CPEs can display complex decay curves, which often require three exponential components: τ_{CPE1} ~10-60 ps, assigned to fast intra/inter-chain energy migration and/ or conformational relaxation along the polymer backbone[45, 46]; τ_{CPE2} ~400 ps, attributed to radiative relaxation of aggregated polymer clusters[47, 48]; and τ_{CPE3} ~800 ps, attributed to radiative decay of isolated polymer chains.[46, 47] The relative contribution of τ_{CPE2} and τ_{CPE3} to the total decay is thus indicative of the extent of CPE aggregation.

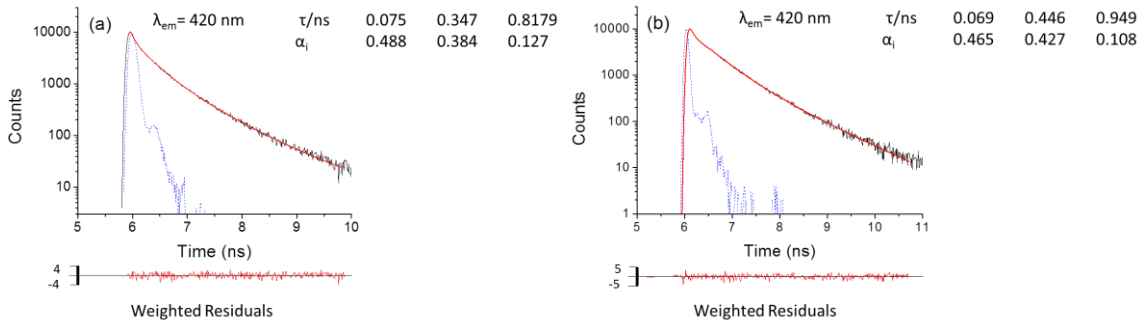

Figure 5.22. PL emission decay curves (solid black lines) (λ_{ex} = 365 nm and λ_{em} = 420 nm), and fits (red solid lines) for (**a**) **PBS-PFP** in 1,4-dioxane/H_2O (25:75% *v/v*) and (**b**) **HTMA-PFP** in MeCN/H_2O (25:75% *v/v*). The fitted decay times (τ_i), pre-exponential factors (α_i), fits, weighted residuals and instrument response function (dashed blue line) are also shown.

The undoped di-ureasils prepared *via* both methods exhibit similar lifetime components; see **Table 5.5** for the lifetime and pre-exponential values for **DI-PBS-0.0** as a representative example. Further fitting data and decay curves can be found in the Appendix. The values in **Table 5.5** are in good agreement with the values previously reported for undoped di-ureasils at room temperature, which also exhibit a tri-exponential decay curve in the solid-state, with τ_{DU1} <1 ns, τ_{DU2} ~3.0-3.5 ns and τ_{DU3} ~9.0-9.8 ns (λ_{em} = 400 nm).[13]

Table 5.5. PL lifetimes (τ_i) and pre-exponential coefficients (α_i) resulting from Global analysis of the photoluminescence decays (λ_{ex} = 365 nm) by linking the shortest lifetime component of **DI-PBS-0.0** (λ_{em} = 420 and 500 nm).

Sample	**λ_{em} (nm)**	**τ_{DU1} (ns)**	**τ_{DU2} (ns)**	**τ_{DU3} (ns)**	**α_{DU1} (ns)**	**α_{DU2} (ns)**	**α_{DU3} (ns)**
DI-PBS-0.0	420	0.45	2.46	9.89	0.74	0.21	0.05
	500	0.45	3.02	11.22	0.65	0.29	0.07

To identify the spectral regions dominated by contributions from the CPE and di-ureasil, respectively, emission decay curves were recorded for **DI-PBS-1.0** in the range 400-500 nm, varying the monitoring wavelength by 10 nm. Each decay curve is best fit with three exponential components; see Appendix **Fig. A.5.2** and **Table A.5.1** for decay curves, fits and fitting data. The tail fitting procedures used are discussed in **Section 2.3.5.4**.

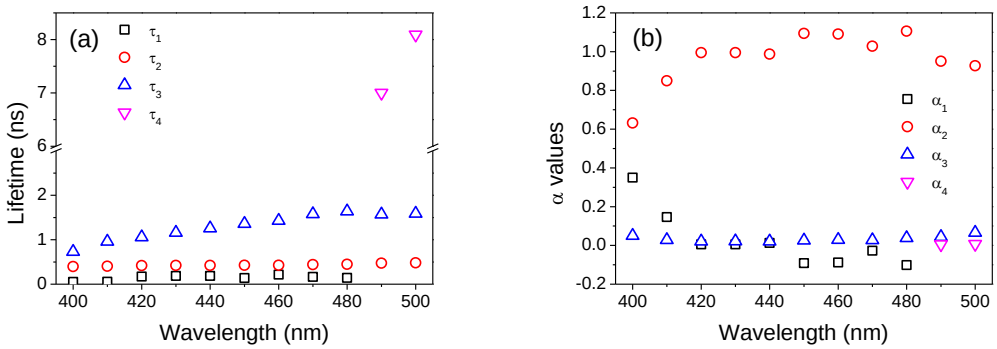

Figure 5.23. (**a**) Emission lifetimes, τ_i, and (**b**) corresponding pre-exponential α_i values determined from the fitting of tri-exponential functions to the fluorescence decays of the sample **DI-PBS-1.0** as a function of emission wavelength (λ_{em} = 400, 410, 420, 430, 440, 450, 460, 470, 480, 490 and 500 nm), (λ_{ex} = 365 nm).

The resultant lifetimes, τ_i, and pre-exponential contributions, α_i, display significant wavelength dependence (**Fig. 5.23**). In the range λ_{em} = 400-480 nm a short component of 50-200 ps (τ_1), an intermediate component of 400-440 ps (τ_2) and a longer component of 0.7-1.5 ns (τ_3) are observed. Each of these components becomes longer-lived as the emission wavelength is increased. The short component, τ_1, increases up to λ_{em} = 460 nm, and then decreases and disappears by λ_{em} = 490 nm. Comparison with the decay of **PBS-PFP** in solution highlights that τ_1 is reminiscent of τ_{CPE1} and is assigned to fast intra/-interchain energy migration. However, it is longer-lived, indicating that incorporation of the CPE into the di-ureasil decreases the rate of these relaxation processes. The intermediate lifetime, τ_2, is assigned to contributions from both τ_{CPE2} and τ_{DU1}, with the CPE providing the major contribution at λ_{em} <450 nm and the di-ureasil providing the major contribution at longer wavelengths. This is supported by the pre-exponential value for τ_1 which appears as a decay time at the onset of the emission band and a rise time at the end (indicated by the switch from a positive to negative α value). Simultaneously, the pre-exponential value α_2 increases in magnitude with wavelength, suggesting interconversion between the species responsible for these decay pathways. A much longer-lived component, τ_4 ~8 ns, appears at emission wavelengths >480 nm, coinciding with the disappearance of τ_1. The emission wavelength dependence and lifetimes of τ_3 and τ_4 are typical of τ_{DU2} and τ_{DU3}, respectively. These observations support the assignment of 420 and 500 nm as emission wavelengths to primarily probe the CPE and di-ureasil contributions, respectively.

To examine the effect of increasing CPE concentration, the PL decays for the **DI-PBS-x** series were measured at λ_{em} =420 and 500 nm. Global analysis of the decay curves reveals that at

420 nm, τ_1, τ_2 and τ_3 and their corresponding pre-exponential values remain effectively constant as the CPE concentration is increased (**Table 5.6**). At the highest concentration (8 $\times 10^{-3}$ wt%), α_1 decreases significantly which is accompanied by an increase in α_2 and α_3. While at λ_{em} = 500 nm, τ_2 and τ_3 remain constant and τ_4 decreases significantly from 5.5 to 2.2 ns (**Fig 5.24a**). This is accompanied by a decrease in α_2 and increase in α_3 (**Fig. 5.24b**).

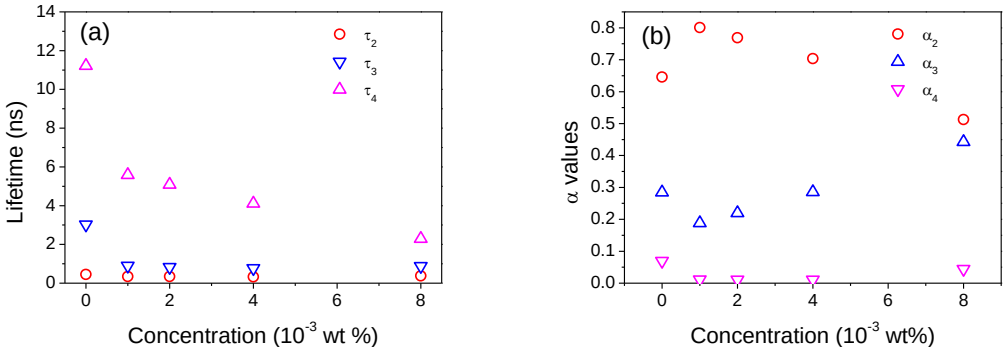

Figure 5.24. (**a**) Emission lifetimes, τ_i, and (**b**) corresponding pre-exponential α_i values determined from the fitting of tri-exponential functions to the fluorescence decays for the **DI-PBS-x** series at the di-ureasil emission wavelength (λ_{ex}= 365 nm, λ_{em}= 500 nm).

Table 5.6. PL lifetimes (τ_i) and pre-exponential coefficients (α_i) resulting from Global analysis (τ_{DU2} linked to τ_{DU1} at λ_{em} = 500 nm) of the photoluminescence decays (λ_{ex} = 365 nm) of **DI-PBS-x** (λ_{em} = 420 nm).

Sample	τ_{DU1} **(ns)**	τ_{DU2} **(ns)**	τ_{DU3} **(ns)**	α_{DU1} **(ns)**	α_{DU2} **(ns)**	α_{DU3} **(ns)**
DI-PBS-1.0	0.01	0.34	0.68	0.69	0.26	0.05
DI-PBS-2.0	0.02	0.34	0.63	0.61	0.31	0.09
DI-PBS-4.0	0.01	0.32	0.59	0.61	0.29	0.10
DI-PBS-8.0	0.04	0.37	0.64	0.28	0.58	0.14

Similar trends were observed for the **DI-HTMA-x** series, as shown in **Table 5.7** (see Appendix **Fig. A.5.3** for corresponding decays and fits). However, it must be noted that **DI-HTMA-1.0** displays di-ureasil-like decay times both at 420 and 500 nm (**Table 5.7**), which is consistent with the steady-state PL and PLQY measurements.

To examine the effect of incorporation method, the **SP-PBS-x** series was also examined, as summarised in **Table 5.8** (see Appendix **Fig A.5.4** for corresponding decays and fits). The trends in lifetime and pre-exponential values at both emission wavelengths are similar to those of **DI-PBS-x**, but occur to a reduced extent, suggesting a decreased electronic interaction between the CPE and the di-ureasil. Furthermore, at 420 nm the emission decays are longer and are dominated by τ_2 (~500 ps), suggesting that aggregation of the CPE chains is increased for the **SP-PBS-x** series. This is consistent with the confocal microscopy results, which show the CPE is confined to a surface layer following this incorporation method.

Table 5.7. PL lifetimes (τ_i), pre-exponential coefficients (α_i), fractional contribution (f_i) and chi squared (χ^2) values resulting from Global analysis (a single lifetime at λ_{em} = 420 nm was linked to a lifetime at λ_{em} = 500 nm) of the photoluminescence decays (λ_{ex} = 365 nm) of **DI-HTMA-x** at different emission wavelengths (λ_{em} = 420 and 500 nm).

Sample	τ_1 **(ns)**	τ_2 **(ns)**	τ_3 **(ns)**	α_1	α_2	α_3	f_1	f_2	f_3	χ^2
					λ_{em} = 420 nm					
PFP-HTMA solution	0.07 ±0.01	0.45 ±0.01	0.95 ±0.01	0.47 ±0.02	0.43 ±0.01	0.10 ±0.01	0.10 ±0.01	0.59 ±0.01	0.31 ±0.01	1.04
DI-HTMA-0.0	0.45 ±0.01	2.46 ±0.02	9.89 ±0.07	0.74 ±0.01	0.21 ±0.01	0.05 ±0.01	0.26 ±0.01	0.39 ±0.01	0.35 ±0.01	1.51
DI-HTMA-1.0	0.09 ±0.01	0.49 ±0.01	4.58 ±0.14	0.34 ±0.02	0.65 ±0.01	0.01 ±0.01	0.07 ±0.01	0.80 ±0.02	0.13 ±0.01	1.28
DI-HTMA-2.0	0.10 ±0.01	0.42 ±0.01	1.14 ±0.05	0.62 ±0.02	0.35 ±0.01	0.03 ±0.01	0.26 ±0.01	0.60 ±0.03	0.14 ±0.01	1.07
DI-HTMA-4.0	0.05 ±0.01	0.38 ±0.01	0.87 ±0.02	0.34 ±0.02	0.57 ±0.01	0.09 ±0.01	0.06 ±0.01	0.68 ±0.01	0.26 ±0.01	1.21
DI-HTMA-8.0	0.07 ±0.01	0.33 ±0.01	0.65 ±0.01	0.25 ±0.02	0.47 ±0.01	0.28 ±0.01	0.05 ±0.01	0.40 ±0.01	0.55 ±0.01	0.85
					λ_{em} = 500 nm					
DI-HTMA-0.0	0.45 ±0.02	3.02 ±0.03	11.22 ±0.07	0.64 ±0.03	0.29 ±0.01	0.07 ±0.01	0.15 ±0.01	0.45 ±0.01	0.40 ±0.01	1.67
DI-HTMA-1.0	0.49 ±0.01	2.45 ±0.03	10.64 ±0.14	0.72±0.02	0.08 ±0.01	0.20 ±0.01	0.13 ±0.01	0.08 ±0.01	0.79 ±0.01	1.33
DI-HTMA-2.0	0.26 ±0.01	1.14 ±0.01	7.87 ±0.14	0.67 ±0.03	0.31 ±0.01	0.02 ±0.01	0.25 ±0.01	0.51 ±0.01	0.24 ±0.01	1.27
DI-HTMA-4.0	0.38 ±0.01	1.12 ±0.01	4.75 ±0.06	0.65 ±0.03	0.33 ±0.01	0.02 ±0.01	0.36 ±0.02	0.53 ±0.01	0.11 ±0.01	1.35
DI-HTMA-8.0	0.33 ±0.01	1.00 ±0.01	4.06 ±0.20	0.57 ±0.03	0.41 ±0.01	0.02 ±0.01	0.28 ±0.01	0.60 ±0.01	0.12 ±0.01	1.06

Table 5.8. PL lifetimes (τ_i), pre-exponential coefficients (α_i), fractional contribution (f_i) and chi squared (χ^2) values resulting from individual fits to the photoluminescence decays (λ_{ex} = 365 nm) of **SP-PBS-x** at different emission wavelengths (λ_{em} = 420 and 500 nm).

Sample	τ_1 **(ns)**	τ_2 **(ns)**	τ_3 **(ns)**	α_1	α_2	α_3	f_1	f_2	f_3	χ^2
					λ_{em} = 420 nm					
PBS-PFP solution	0.08 ±0.01	0.35 ±0.02	0.82 ±0.02	0.48 ±0.01	0.38 ±0.01	0.14 ±0.01	0.14 ±0.01	0.49 ±0.03	0.37 ±0.02	1.03
SP-PBS-0.0	0.21 ±0.01	1.59 ± 0.02	8.77 ±0.1	0.62 ±0.10	0.32 ±0.04	0.06 ±0.01	0.12 ±0.02	0.44 ±0.05	0.44 ±0.04	2.52
SP-PBS-0.7	0.11 ±0.01	0.51 ±0.01	2.25 ±0.70	0.28 ±0.02	0.71 ±0.01	0.01 ±0.01	0.08 ±0.01	0.85 ±0.02	0.07 ±0.02	1.09
SP-PBS-2.0	0.01 ±	0.48 ±	1.00 ±	0.78 ±	0.19 ±	0.03 ±	0.01 ±	0.78 ±	0.21 ±	0.93
SP-PBS-7.0	0.01 ±0.01	0.48 ±0.01	0.79 ±0.01	0.62 ±0.04	0.31 ±0.01	0.07 ±0.01	0.03 ±0.01	0.71 ±0.01	0.26 ±0.01	0.95
					λ_{em} = 500 nm					
SP-PBS-0.0	0.39 ±0.02	2.16 ±0.04	9.30 ±0.15	0.56 ±0.03	0.37 ±0.01	0.07 ±0.01	0.13 ±0.01	0.48 ±0.01	0.39 ±0.01	1.53
SP-PBS-0.7	0.08 ±0.01	0.65 ±0.01	3.27 ±0.05	0.47 ±0.06	0.50 ±0.03	0.03 ±0.01	0.09 ±0.01	0.70 ±0.02	0.21 ±0.01	1.43
SP-PBS-2.0	0.02 ±0.01	0.61 ±0.01	2.90 ±0.05	0.59 ±0.05	0.39 ±0.2	0.02 ±0.01	0.05 ±0.01	0.76 ±0.02	0.19 ±0.01	1.67
SP-PBS-7.0	0.01 ±0.01	0.57 ±0.01	1.92 ±0.03	0.63 ±0.06	0.35 ±0.02	0.02 ±0.01	0.02 ±0.01	0.83 ±0.02	0.15 ±0.01	1.29

5.3.5.6 Discussion of the Mechanism of Photoluminescence Enhancement

The steady-state PL spectra clearly show that the CPE provides the major contribution to the emission spectra. However, the spectral broadening at both the high and low energy regions of the spectrum highlights the fact that the di-ureasil is an "active" host, which contributes to the emission profile of the CPE-di-ureasils. Significant spectral overlap between the CPE and the di-ureasil indicates the potential for energy transfer between the two components. The time-resolved PL measurements confirm this hypothesis. As the detection wavelength is increased, the emission decay profile transitions from CPE-like to more di-ureasil-like (**Fig. 5.23**), with the CPE emission effectively switched-off at 460 nm.

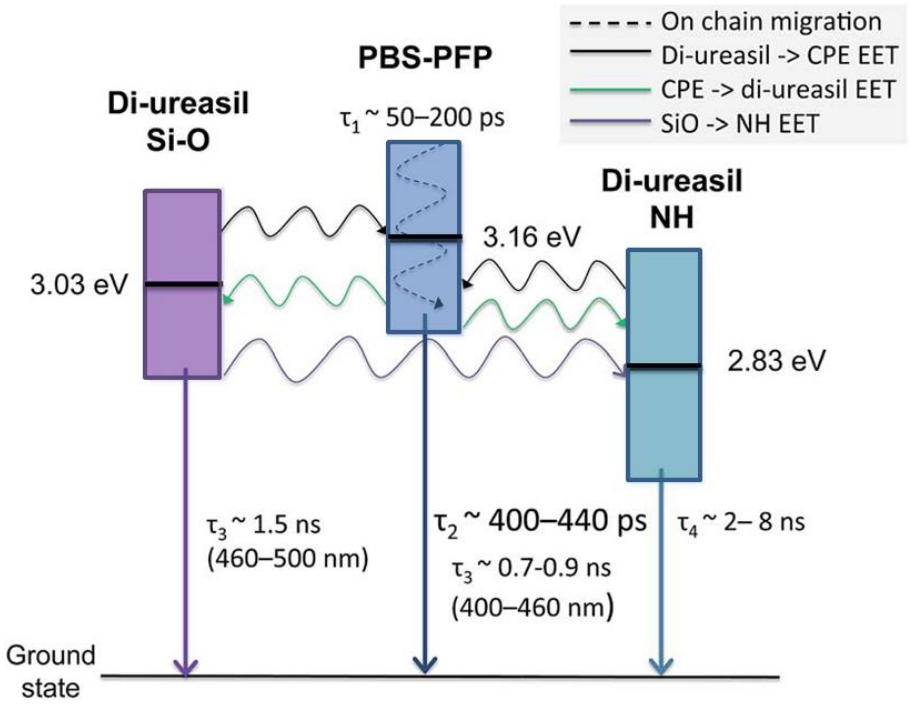

Figure. 5.25. Schematic energy level diagram showing proposed mechanism for energy transfer between **PBS-PFP** and the di-ureasil host. The solid black lines represent the tabulated energies for the emissive states taken from ref [49] for **PBS-PFP** and ref [50] for the di-ureasil. The shaded bands correspond to the FWHM values of the corresponding emission spectra.

Fig. 5.25 represents a schematic diagram for the proposed energy transfer mechanism in **DI-PBS-x**. Energy transfer and charge carrier trapping both rely on electronic coupling of the donor and the acceptor, the extent of which will depend on both the spatial distribution of the CPE within the di-ureasil matrix and the energy of the electronic states involved. As observed in the confocal microscopy experiments the *DI* method produces CPE domains within the di-ureasil that are well-distributed throughout the sample. The extended nature of the electronic states in conjugated polymers means that excitons are free to migrate along an individual backbone or to hop between chains.[51] Both **PBS-PFP** and **HTMA-PFP** have relatively short chain lengths, corresponding to ~8-9 r.u. Assuming a conjugation length of ~3-4 r.u. for a fluorene-phenylene copolymer[52], this implies that exciton migration along the polymer backbone should not be a significant prerequisite for energy transfer to the di-ureasil.

The strong spectral overlap means that it is challenging to unequivocally assign the direction of energy transfer upon excitation at 365 nm. However, the TCSPC experiments allow some conclusions to be drawn. The fast decay component for **DI-PBS-1.0**, τ_1, becomes a rise time at 440 nm (**Fig. 5.23**), and as α_2 simultaneously increases, it is reasonable to propose that interconversion occurs between these two species. This response is characteristic of exciton energy transfer (EET) from a high to a lower energy chromophore.[53] We therefore propose that τ_1 corresponds to a combination of EET from the CPE to the di-ureasil and on-chain exciton migration. The lifetime and contribution of the longer-lived components for this sample (τ_2, τ_3, τ_4) also depend on wavelength, which suggests that the absorbing and emitting species are chemically distinct.[54] The intermediate lifetime, τ_2, is similar to both τ_{CPE2} (polymer clusters) and τ_{DU1} and based on the steady state PL spectra (**Fig. 5.20**), it seems reasonable that the CPE contribution dominates at λ_{em} <450 nm, and switches to the di-ureasil at longer wavelengths. At a monitoring wavelength of 420 nm the corresponding pre-exponential value, α_2, is effectively independent of the CPE concentration. Also at this wavelength, τ_3 is independent of CPE concentration and comparable to the reported lifetime for radiative relaxation of isolated CPE chains (τ_{CPE3}).[46, 47] These trends suggest that the di-ureasil matrix is extremely effective at inhibiting aggregation of the CPE. Between 440-500 nm, τ_3 becomes longer-lived (1.3-1.6 ns) and is more reminiscent of the reported di-ureasil lifetime, τ_{DU2}.[13] At the di-ureasil emission wavelength, λ_{em} = 500 nm, τ_4 decreases significantly as the CPE concentration increases, with a concomitant rise in α_3. This trend indicates that the longest-lived di-ureasil component undergoes energy transfer to isolated CPE chains rather than CPE clusters, which is supported by the constant α_2 value at 420 nm. The fact that the di-ureasil can energy transfer to the CPE is fully consistent with the description of localised excited states in the inorganic moiety.[55] The fact that these emissive sites in di-ureasils are relatively localised within thermally accessible trap states,[55] provides the possibility of enhancing yields in electroluminescent devices baed on these materials. This is similar to the thermally activated delayed fluorescence (TADF) mechanism recently reported by Uoyama *et al*.[56]

The CPE emission profile dominates the steady-state photoluminescence spectra of the CPE-di-ureasil composites and must provide the major contribution to the PLQY. The quenching of excitons at non-emissive defect sites is one of the key processes that control the PLQY of emissive conjugated polymers.[57] Aggregation can increase the rate of exciton migration, leading to a decrease in the PLQY due to trapping at these sites. An increase in aggregation is expected on increasing the CPE concentration. However, this trend is not indicated in the TCSPC experiments. The lifetime data indicate that the di-ureasil matrix is in fact very efficient at inhibiting CPE aggregation. Moreover, the FTIR data reveal a high degree of hydrogen-bonding is present in our system, and indeed this may be attributed in part to interactions between the di-ureasil and the polar terminal groups on the side chains of both CPEs. Particularly at higher concentrations, **DI-PBS-x** samples possess a less ordered di-ureasil matrix, suggesting greater interaction between

CPE and host when compared with their **DI-HTMA-x** counterparts. Matrix-inhibited aggregation has recently been demonstrated as an effective mechanism to isolate CPE chains in poly(vinyl alcohol) (PVA) films.[44] A significant increase in the PLQY was observed for water-soluble poly(fluorenephenylene) CPEs (including **HTMA-PFP** and **PBS-PFP**) upon their incorporation into the rigid, hydrogen-bonded PVA matrix, which was attributed to a combined reduction in chain flexibility and increase in chain isolation upon incorporation.[44] Di-ureasils have also been shown to effectively inhibit the aggregation of molecular organic dyes (*e.g.* Rhodamine B).[58]

The TCSPC data indicate an energy transfer process also contributes to the enhanced PLQY. It is reasonable to assume that the CPE is the primary light-absorbing component and that after photogeneration, excitons migrate to lower energy subunits. Given the relatively short conjugation length of the CPEs used, it is reasonable to suggest that EET to the di-ureasil will be as, if not more, important than on-chain exciton migration. Owing to their complex nature, the individual lifetime components of the pure di-ureasil hybrid at room temperature have yet to be formally assigned.[13] Time-resolved emission measurements at 14 K have shown the existence of two components in the di-ureasil emission. The emission from the siliceous domains is distinctly observed at 1-5 ms while at longer delays (>10 ms) the emission from the NH defects dominates the spectrum.[19] These lifetimes decrease abruptly for temperatures higher than 220 K, falling abruptly from the milli- to nanosecond timescale.[16] It is therefore tempting to assign τ_4 at 500 nm to this emission component. The decrease in τ_4 with increasing CPE concentration, in conjunction with the increase in increase in α_3, would suggest that energy transfer additionally occurs from the NH-centred trap states to the CPE. At first glance, analysis of the relative energy levels of the individual components indicates that this would require an uphill jump in energy. However, strong electronic coupling results in excitation sharing across a large number of sub-units (in both the CPE and the di-ureasil), meaning that there are a significant number of electronic energy levels in each exciton manifold.[59] As such, a band structure description, rather than discrete energy levels, is more appropriate for this system. In this case, at room temperature (k_BT ~0.03 eV), there is sufficient band overlap to facilitate forward and thermally-activated reverse energy transfer between all components, provided that the long-range Coulomb transfer integrals are sufficient.[59] This suggests that EET occurs to an isolated CPE chain (as indicated by the lifetime data), which has a high radiative probability, giving rise to a long emission lifetime (τ_3) and correspondingly high PLQY.

5.4 Conclusions

CPE-di-ureasils were successfully prepared *via* two different methods; *Direct Insertion* and *Solvent Permeation*. Both methods utilise a mild, sol-gel process to provide transparent, elastomeric monoliths. Confocal microscopy was used to probe the localisation of the CPE within the di-ureasil network. The *DI* method leads to a homogeneous distribution of CPE domains

throughout the entire di-ueasil host, while the *SP* method yields a confined layer of CPE at the di-ureasil surface. Release studies indicate that the CPEs are effectively retained within the di-ureasil matrix following incorporation. Through a combination of XRD, ss-NMR and FTIR, the incorporation of the CPEs was found to have no adverse effect on the structural properties of the di-ureasil. However, further fitting of the Amide I region of the FTIR spectra showed that the *SP* method does lead to disruption and reordering of the disordered hydrogen-bonded POE/urea associations present within the di-ureasil network which is consistent with the swelling and contraction occurring during sample preparation.

Examination of the photophysical characteristics of the CPE-di-ureasils indicate that both CPE and di-ureasil components contribute to the photoluminescence properties which gives rise to a dramatic enhancement of the PLQY. This is in part due to effective prevention of aggregation of CPE chains through weak physical interactions with the di-ureasil matrix, which are more favourable for **PBS-PFP** than **HTMA-PFP**. Steady-state PL and TCSPC measurements also indicate that cooperative electronic interactions between the two components are important. The PL emission spectra are dominated by contributions from the CPE, while the excitation wavelength dependence and red- and blue-edge band broadening are characteristic of di-ureasil contribution. PL decays of **DI-PBS-1.0** as a function of increasing emission wavelength were examined to further probe each of these contributions to the overall CPE-di-ureasil emission. These measurements suggest that the decay profile transitions from CPE-like to more di-ureasil-like with increasing monitoring wavelength, with the CPE emission effectively switched off at 460 nm. Thus, monitoring wavelengths of 420 and 500 nm were chosen to represent contributions from the CPE and contributions characteristic of the di-ureasil, respectively. As the CPE concentration is increased the lifetime components at the CPE emission wavelength, 420 nm, remain reasonably unaffected. While at 500 nm the longer component of the di-ureasil lifetime decreases dramatically with increasing CPE concentration. The pre-exponential values indicate an effective isolation of CPE chains, yielding emissive sites that have a high radiative probability. Similar trends are evident for all three series investigated. However, the trends occur to a lesser extent for the **SP-PBS-x** series, indicating reduced electronic interaction between the CPE and the di-ureasil through this incorporation method. The lifetime of the aggregated CPE species dominates the *SP* decays at 420 nm suggesting CPE aggregation is increased in this series, consistent with the CPE surface layer exhibited by these samples. It was also noted that the PL decays of **DI-HTMA-1.0** display di-ureasil-like characteristics at both 420 nm and 500 nm, which is in accordance with the steady-state PL spectra and PLQY value of this sample which resembles that of the undoped di-ureasil.

The electronic coupling between the CPE and the di-ureasil suggest that CPE-di-ureasils offer a wealth of potential applications from composite photovoltaics, to luminescent solar concentrators and optical sensors. The power of the approach presented in this chapter lies in both its simplicity and versatility. Through rational selection of the constituents, it is possible to tailor

the optical properties (*e.g.* emission colour, energy transfer, PLQY) for a targeted application, as will be discussed in the following chapter. Furthermore, a wide variety of Jeffamine® precursors[60] are commercially available, which makes tuning of the mechanical properties possible. While the confinement of the CPE within a specific region of an active layer offers the potential to reduce the complexity of multi-layer device architectures and may yield improved device performance.

5.5 References

1. H. D. Burrows, V. M. M. Lobo, J. Pina, M. L. Ramos, J. S. de Melo, A. J. M. Valente, M. J. Tapia, S. Pradhan and U. Scherf, *Macromolecules*, 2004, **37**, 7425-7427.
2. H. D. Burrows, M. J. Tapia, S. M. Fonseca, A. J. Valente, V. M. Lobo, L. L. Justino, S. Qiu, S. Pradhan, U. Scherf, N. Chattopadhyay, M. Knaapila and V. M. Garamus, *ACS Appl. Mater. Interfaces*, 2009, **1**, 864-874.
3. H. A. Attar and A. P. Monkman, *J. Phys. Chem. B*, 2007, **111**, 12418-12426.
4. H. D. Burrows, M. J. Tapia, C. L. Silva, A. A. Pais, S. M. Fonseca, J. Pina, J. S. de Melo, Y. Wang, E. F. Marques, M. Knaapila, A. P. Monkman, V. M. Garamus, S. Pradhan and U. Scherf, *J. Phys. Chem. B*, 2007, **111**, 4401-4410.
5. B. H. Hamadani, S. Jung, P. M. Haney, L. J. Richter and N. B. Zhitenev, *Nano Lett.*, 2010, **10**, 1611-1617.
6. G. Li, V. Shrotriya, J. Huang, Y. Yao, T. Moriarty, K. Emery and Y. Yang, *Nat. Mater.*, 2005, **4**, 864-868.
7. M. Álvaro, A. Corma, B. Ferrer, M. S. Galletero, H. García and E. Peris, *Chem. Mater.*, 2004, **16**, 2142-2147.
8. E. Dovgolevsky, S. Kirmayer, E. Lakin, Y. Yang, C. J. Brinker and G. L. Frey, *J. Mater. Chem.*, 2008, **18**, 423-436.
9. R. C. Evans and P. C. Marr, *Chem. Commun.*, 2012, **48**, 3742-3744.
10. T. Q. Nguyen, J. Wu, S. H. Tolbert and B. J. Schwartz, *Adv. Mater.*, 2001, **13**, 609-611.
11. J. Wu, A. F. Gross and S. H. Tolbert, *J. Phys. Chem. B*, 1999, **103**, 2374-2384.
12. R. C. Evans, *J. Mater. Chem. C*, 2013, **1**, 4190-4200.
13. L. Fu, R. A. S. Ferreira, M. Fernandes, S. C. Nunes, V. de Zea Bermudez, G. Hungerford, J. Rocha and L. D. Carlos, *Opt. Mater.*, 2008, **30**, 1058-1064.
14. C. Sanchez, P. Belleville, M. Popall and L. Nicole, *Chem. Soc. Rev.*, 2011, **40**, 696-753.
15. Y. J. Cui, M. Q. Wang, L. J. Chen and G. D. Qian, *Dyes Pigments*, 2004, **62**, 43-47.
16. L. D. Carlos, R. A. S. Ferreira, V. de Zea. Bermudez and S. J. L. Ribeiro, *Adv. Funct. Mater.*, 2001, **11**, 111-115.
17. V. de Zea Bermudez, L. D. Carlos and L. Alcácer, *Chem. Mater.*, 1999, **11**, 569-580.
18. P. P. Lima, R. A. S. Ferreira, S. A. Júnior, O. L. Malta and L. D. Carlos, *J. Photochem. Photobiol. A*, 2009, **201**, 214-221.
19. L. D. Carlos, V. de Zea Bermudez, R. A. S. Ferreira, L. Marques and M. Assunção, *Chem. Mater.*, 1999, **11**, 581-588.
20. M. C. Neves, M. A. Martins, P. C. Soares-Santos, P. Rauwel, R. A. S. Ferreira, T. Monteiro, L. D. Carlos and T. Trindade, *Nanotechnology*, 2008, **19**, 155601.
21. M. E. Mesquita, S. S. Nobre, M. Fernandes, R. A. S. Ferreira, S. C. G. Santos, M. O. Rodrigues, L. D. Carlos and V. de Zea. Bermudez, *J. Photochem. Photobiol. A*, 2009, **205**, 156-160.
22. S. F. H. Correia, P. P. Lima, P. S. André, M. R. S. Ferreira and L. A. D. Carlos, *Sol. Energ. Mat. Sol. Cells*, 2015, **138**, 51-57.
23. A. Garcia, J. Z. Brzezinski and T.-Q. Nguyen, *J. Phys. Chem. C*, 2009, **113**, 2950-2954.
24. R. Yang, H. Wu, Y. Cao and G. C. Bazan, *J. Am. Chem. Soc.*, 2006, **128**, 14422-14423.
25. N. Willis-Fox, A. T. Marques, J. Arlt, U. Scherf, L. D. Carlos, H. D. Burrows and R. C. Evans, *Chem. Sci.*, 2015, **6**, 7227-7237.
26. J. E. Lofgreen and G. A. Ozin, *Chem. Soc. Rev.*, 2014, **43**, 911-933.
27. Z. G. Wu, N. Bouklas and R. Huang, *Int. J. Solids Struct.*, 2013, **50**, 578-587.

28. D. Saikia, H.-Y. Wu, Y.-C. Pan, C.-C. Liao, C.-F. Chen, G. T. K. Fey and H.-M. Kao, *Electrochim. Acta*, 2009, **54**, 7156-7166.
29. Y. Ding, Y. Li, M. Qin, Y. Cao and W. Wang, *Langmuir*, 2013, **29**, 13299-13306.
30. K. N. Plunkett, M. L. Kraft, Q. Yu and J. S. Moore, *Macromolecules*, 2003, **36**, 3960-3966.
31. L. Fu, R. A. S. Ferreira, N. J. O. Silva, L. D. Carlos, V. de Zea Bermudez and J. Rocha, *Chem. Mater.*, 2004, **16**, 1507-1516.
32. Scherrer equation: $L = 0.94\lambda/(A\cos\theta)$, where A (in radians) is the full-width-half-maximum of the Bragg peak. See A. Guinier, X-ray Diffraction in Crystals, Imperfect Crystals and Amorphous Bodies, Dover, New York 1994.
33. K. Dahmouche, L. D. Carlos, V. de Zea Bermudez, R. A. S. Ferreira, C. V. Santilli and A. F. Craievich, *J. Mater. Chem.*, 2001, **11**, 3249-3257.
34. M. Fernandes, V. de Zea.. Bermudez, R. A. S. Ferreira, L. D. Carlos and N. V. Martins, *J. Lumin.*, 2008, **128**, 205-212.
35. I. T. Sachs-Quintana, T. Heumüller, W. R. Mateker, D. E. Orozco, R. Cheacharoen, S. Sweetnam, C. J. Brabec and M. D. McGehee, *Adv. Funct. Mater*, 2014, **24**, 3978-3985.
36. D. E. Loy, B. E. Koene and M. Thompson, *Adv. Funct. Mater.*, 2002, **12**, 245-249.
37. M. Kuik, G. A. H. Wetzelaer, J. G. Laddé, H.T. Nicolai, J. Wildeman, J. Sweelssen and P. W. M. Blom, *Adv. Funct. Mater.*, 2011, **21**, 4502-4509.
38. K. L. Chan, M. Sims, S. I. Pascu, M. Ariu, A. B. Holmes and D. D. C. Bradley, *Adv. Funct. Mater.*, 2009, **19**, 2147-2154.
39. X. H. Yang, F. Jaiser, D. Neher, P. V. Lawson, J. Brédas, E. Zojer, R. Güntner, P. S. de Freitas, M. Forster and U. Scherf, *Adv. Funct. Mater.*, 2004, **14**, 1097-1104.
40. H. Jiang, P. Taranekar, J. R. Reynolds and K. S. Schanze, *Angew. Chem. Int. Ed.*, 2009, **48**, 4300-4316.
41. H. D. Burrows, S. M. Fonseca, C. L. Silva, A. A. Pais, M. J. Tapia, S. Pradhan and U. Scherf, *Phys. Chem. Chem. Phys.*, 2008, **10**, 4420-4428.
42. M. L. Davies, H. D. Burrows, S. Cheng, M. C. Moran, G. Miguel Mda and P. Douglas, *Biomacromolecules*, 2009, **10**, 2987-2997.
43. L. D. Carlos, R. A. S. Ferreira, R. N. Pereira, M. Assunção and V. de Zea Bermudez, *J. Phys. Chem. B*, 2004, **108**, 14924-14932.
44. H. A. Al-Attar and A. P. Monkman, *Adv. Funct. Mater.*, 2012, **22**, 3824-3832.
45. T. Costa, A. T. Marques, J. S. de Melo, A. W. Thomas, L. E. Garner, U. Scherf, G. C. Bazan and H. D. Burrows, *J. Phys. Chem. B*, 2014, **118**, 613-623.
46. M. L. Davies, P. Douglas, H. D. Burrows, G. Miguel Mda and A. Douglas, *J. Phys. Chem. B*, 2011, **115**, 6885-6892.
47. H. A. A. Attar and A. P. Monkman, *Adv. Funct. Mater.*, 2008, **18**, 2498-2509.
48. A. T. Marques, H. D. Burrows, J. S. de Melo, A. J. Valente, L. L. Justino, U. Scherf, E. Fron, S. Rocha, J. Hofkens, E. W. Snedden and A. P. Monkman, *J. Phys. Chem. B*, 2012, **116**, 7548-7559.
49. S. M. Fonseca, J. Pina, L. G. Arnaut, J. S. de Melo, H. D. Burrows, N. Chattopadhyay, L. Alcácer, A. Charas, J. Morgado, A. P. Monkman, U. Asawapirom, U. Scherf, R. Edge and S. Navaratnam, *J. Phys. Chem. B*, 2006, **110**, 8278-8283.
50. S. S. Nobre, P. P. Lima, L. Mafra, R. A. S. Ferreira, R. O. Freire, L. Fu, U. Pischel, V. de Zea Bermudez, O. L. Malta and L. D. Carlos, *J. Phys. Chem. C*, 2007, **111**, 3275-3284.
51. T. Q. Nguyen, J. Wu, V. V. Doan, B. J. Schwartz and S. H. Tolbert, *Science*, 2000, **288**, 652-656.
52. S. M. Pinto, H. D. Burrows, M. M. Pereira, S. M. Fonseca, F. B. Dias, R. Mallavia and M. J. Tapia, *J. Phys. Chem. B*, 2009, **113**, 16093-16100.
53. E. W. Snedden, L. A. Cury, K. N. Bourdakos and A. P. Monkman, *Chem. Phys. Lett.*, 2010, **490**, 76-79.
54. S. J. Strickler and R. A. Berg, *J. Chem. Phys.*, 1962, **37**, 814.
55. R. A. S. Ferreira, A. L. Ferreira and L. D. Carlos, *Eur. Phys. J. B*, 2006, **50**, 371-378.
56. H. Uoyama, K. Goushi, K. Shizu, H. Nomura and C. Adachi, *Nature*, 2012, **492**, 234-238.
57. S. I. Hintschich, C. Rothe, S. Sinha, A. P. Monkman, P. Scandiucci de Freitas and U. Scherf, *J. Chem. Phys.*, 2003, **119**, 12017-12022.

58. J. Fernándes, S. García-Revilla, L. D. Carlos, E. Pecoraro, M. A. Arriandiaga and R. Balda, *Laser Photon. Rev.*, 2014, **8**, L32-L36.
59. G. D. Scholes and G. Rumbles, *Nat. Mater.*, 2006, **5**, 683-696.
60. Huntsman International LLC, Products, http://www.huntsman.com/performance_products/a/Products, (acessed August 2015).

Chapter Six

……

Caught Red Handed: Tuneable White-Light Emission due to Incomplete Energy Transfer from Di-ureasils to Red-Emitting Conjugated Polymers

6.1 Introduction

The development of white-light emitting CP-based materials has attracted considerable interest due to their applications in next generation solid-state lighting,[1] back-lighting for liquid-crystal displays[2] and full-colour flat-panel electroluminescence.[3] White-light emitting systems usually depend on the principle of additive colour mixing, in which multiple components that emit either three primary colours (red, green and blue)[2, 4] or two complementary colours (*e.g.* blue and orange)[2] are combined. This requirement for multiple emissive species naturally gives rise to a multi-layer device architecture in which each layer emits a distinct colour, which when combined produces white light.[5] The performance of CP-based electronic devices is inherently linked to the morphology of each CP layer.[6] As such, to prevent modification of the morphology of initially cast layers by those deposited subsequently, the use of orthogonal solvents is required.[7] Alternatively, initial layers must be rendered insoluble after deposition, by processes such as 'hard-baking' or cross-linking reactions.[8] This introduces a further level of complexity into the device fabrication process. To circumvent these challenges, conjugated polymer white-light emitting devices have been produced by blending either a range of different polymers or a single polymer host with a dopant molecular dye.[5] However, these systems suffer from intrinsic phase separation[2] and as such, there are increasing reports of white-emitting polymers in which several chromophores emitting in either the primary or complementary spectral regions are incorporated within a single polymer chain.[9] Nonetheless, these polymers present a significant synthetic challenge and do not overcome the inherent instability possessed by CP-based devices.

In an effort to produce a single-layer white-light emitting material, this work focusses on the incorporation of red-emitting CPs into the blue-emitting di-ureasil host introduced in the previous chapter. In **Chapter 5** the possibility of energy transfer between CP and di-ureasil host was demonstrated. The excitation wavelength dependence of the di-ureasil emission has previously been exploited to modulate energy transfer between the di-ureasil host and a variety of guest species such as lanthanide complexes[10, 11] and quantum dots.[12] This is a significant advantage as it is synthetically challenging to produce individual CPs exhibiting tunable emission.[13-15] Moreover, incorporation of the CP within the di-ureasil host may give rise to improved thermal and photostability of the resulting active layer. Given the simple, solution-based fabrication method and the structural tunability of the two components, this approach has the potential to be a versatile and efficient route to highly desirable white-light emitting CP-di-ureasil materials, whose optoelectronic properties may be tuned across a wide spectral region.

6.1.1 Aims

In this chapter, the synthesis of CP-di-ureasil composite materials incorporating two different red-emitting CPs, **P3TMAHT** and **MEH-PPV** (**Fig. 6.1**), is presented in an effort to extend the emission profile from the blue emission of the di-ureasil host further across the visible

spectrum. The structural and optical characterisation of the CP-di-ureasils will be investigated as a function of CP concentration. The thermal and photostability of the resulting composite material will be considered. Steady-state photoluminescence and time-resolved emission studies will be used to investigate energy transfer between the di-ureasil host and CP guest.

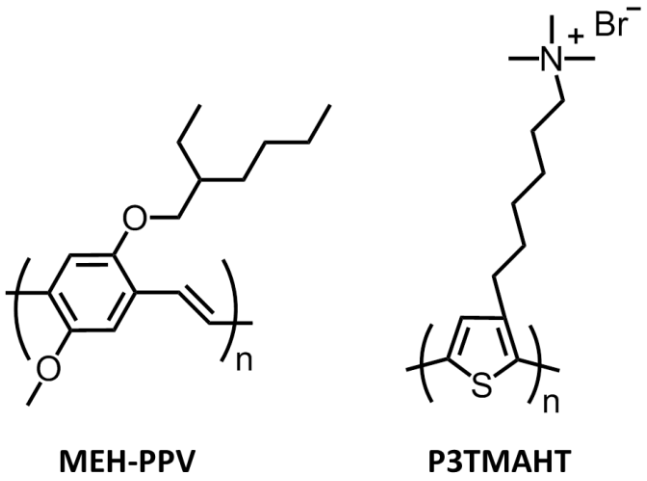

Figure 6.1. Chemical structures of the CPs investigated.

6.2 Experimental

6.2.1 Polymers

Poly[3-(6-triethylammoniumhexyl)thiophene] bromide (**P3TMAHT**) with an M_n = 17,000 g mol^{-1} determined by gel permeation chromatography (~304 g mol^{-1} repeat units (r.u.)) was synthesised by Mario Kraft (Bergische Universität Wuppertal, Germany) as previously reported.[16, 17] Methoxy-5-(2-ethylhexyloxy-1,4-phenylenevinylene) (**MEH-PPV**) with a M_w >100,000 (~260 g mol^{-1} repeat units (r.u.)) was purchased from American Dye Source, Inc. and used as received.

6.2.2 Synthesis of CP-di-ureasils

A series of CP-di-ureasils were prepared *via* the *Direct Insertion* method described in the previous chapter (**Section 5.2.2**).[18] To prepare these samples a fixed volume of CP solution was added to the d-UPTES precursor solution (6.9 ml), prior to addition of the gelation agents which then form the condensed di-ureasil network around the CP which is *in situ*. The volume of the CP solution, was varied to produce CP-di-ureasils with the doped wt% described in **Table 6.1**. The samples are denoted **P3T-x** and **MEH-x** for **P3TMAHT** and **MEH-PPV**, respectively, where x represents the concentration (in 10^{-3} wt%) of the CP within the di-ureasil. Following the literature convention, the undoped di-ureasil prepared from Jeffamine ED-600 is denoted as **d-U(600)**.[11, 19]

Table 6.1. Composition of CP-di-ureasils prepared in this study. [CP] is the concentration of the CP stock solution (in mM repeat units (r.u.)) added to the d-UPTES stock solution. The incorporated CP weight percent (wt%) was estimated from [CP] and the mass of the dry CP-di-ureasil.

Polymer	Sample	[CPE] (mM (r.u.))	CPE wt%
Undoped di-ureasil	d-U(600)	0.0	0
P3TMAHT	P3T-0.6	0.33	0.6×10^{-3}
	P3T-1.2	0.65	1.2×10^{-3}
	P3T-1.8	0.87	1.8×10^{-3}
	P3T-2.4	1.31	2.4×10^{-3}
	P3T-3.3	1.74	3.3×10^{-3}
	P3T-6.6	3.47	6.6×10^{-3}
MEH-PPV	MEH-0.2	0.15	0.2×10^{-3}
	MEH-0.5	0.30	0.5×10^{-3}
	MEH-0.7	0.40	0.7×10^{-3}
	MEH-1.0	0.45	1.0×10^{-3}
	MEH-1.3	0.81	1.3×10^{-3}
	MEH-2.7	1.62	2.7×10^{-3}

6.3 Results and Discussion

6.3.1 Potential Energy Transfer between CP and Di-ureasil Host

P3TMAHT and **MEH-PPV** were selected based on the significant overlap of their absorption bands with the emission spectrum of the di-ureasil (**Fig. 6.2**), the origin and nature of which has been described in **Section 5.3.5.2**, which gives rise to the possibility of energy transfer between the two species.

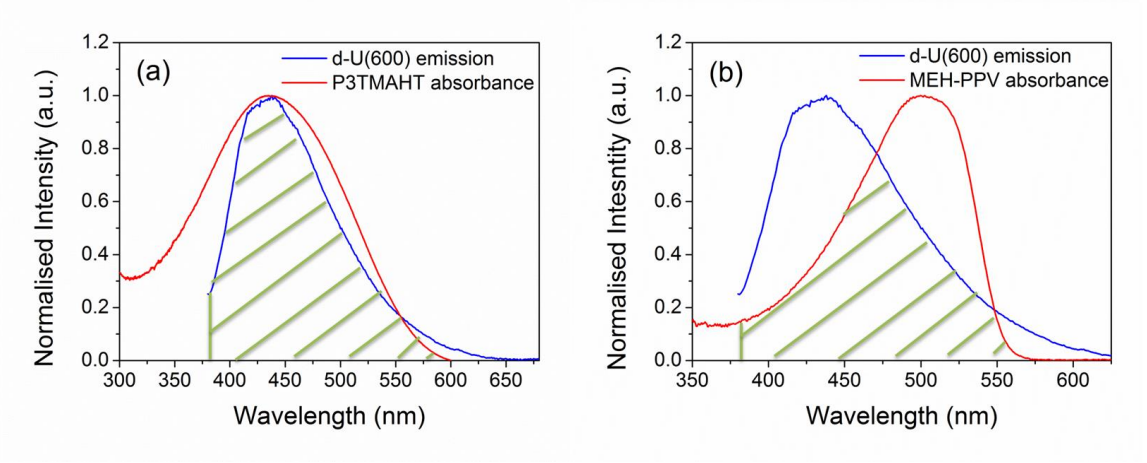

Figure 6.2. Spectral overlap between the emission spectrum of **d-U(600)** (blue line, λ_{ex} = 370 nm) and UV/Vis absorption spectrum of (**a**) **P3TMAHT** (red line λ_{ex} = 430 nm in aqueous solution) and (**b**) **MEH-PPV** (red line λ_{ex} = 480 nm in THF). The green shaded regions highlight the spectral overlap.

Di-ureasils have been shown to act as efficient energy donors while functioning as host matrices for a diverse range of lanthanide ions or complexes and nanoparticles.[10, 12, 20] In conjugated polymers, excitation energy transfer between donors (*D*) and acceptors (*A*) is favoured by Förster-type resonance energy transfer (FRET) based on long-range dipole-dipole interactions,[21, 22] which requires a strong overlap between donor emission and the acceptor absorption spectra.[21] As described earlier, this condition is met by the di-ureasil donor and CP acceptor pairs chosen here (**Fig. 6.2**). The FRET efficiency is also highly dependent on the centre to centre distance between *D* and *A*.[21] The spectral overlap integral, J_{DA}, was quantified for both di-ureasil-CP pairs using **Eqn. 1.7**. Following this the Förster distance, R_0, was calculated using **Eqn. 1.6**. For this calculation the refractive index of the di-ureasil host was taken from the literature to be 1.5[23, 24] and the orientation factor, κ, describing the relative orientation of the transition dipoles of the donor and acceptor, due to the amorphous nature of the material, was taken to be 2/3 which is appropriate for dynamic random averaging of the donor and acceptor.[21] The calculated spectral overlap integrals and Förster distances are shown in **Table 6.2**. The Förster distances are slightly smaller than those found for systems of blended polymers in which **MEH-PPV** acts as the acceptor, which range from R_0 ~5.1 nm when poly(*N*-vinylcarbazole) (PVK) acts as the energy donor[22] to ~6 nm when poly(9,9-di-*n*-octylfluorenyl-2,7-diyl) is the donor.[25] However, the R_0 values obtained here are very similar to those obtained for energy transfer from oligonucleotides to a zwitterionic polythiophene derivative (R_0 = 2.54 – 2.68 nm).[26] The spectral overlap intergral and R_0 values in **Table 6.2** confirm the possibility of energy transfer between the chosen CPs and the di-ureasil host.

Table 6.2. Calculated spectral overlap integrals, J_{DA}, and Förster radii, R_0, for **P3TMAHT** and **MEH-PPV** with **d-U(600)** host.

CP	J_{DA} (M^{-1} cm^3)	R_0 (nm)
P3TMAHT	1.5×10^{-14}	2.3
MEH-PPV	2.7×10^{-14}	3.7

6.3.2 Physical Characterisation

6.3.2.1 Confocal Microscopy

The distribution of the CP within the di-ureasil was first investigated using confocal microscopy. CP-di-ureasils were directly excited within the CP absorption band (λ_{ex} = 488 nm) and observed using a red filter which isolates emission wavelengths in the range 550-740 nm. Intense red emission was observed from distinct domains of *ca*. 2-5 μm in diameter, which are homogeneously distributed throughout the di-ureasil matrix (shown in **Fig. 6.3a**, for **P3T-6.6**). Each domain is anticipated to comprise multiple CP chains. Selective excitation of the di-ureasil (λ_{ex} = 405 nm) also resulted in the observation of red emission from the same isolated domains

attributed to the CP. An overlay of the images collected on excitation of the di-ureasil and the CP, respectively, exhibits identical emission from the domains attributed to the CP, providing preliminary evidence for the occurrence of energy transfer from the di-ureasil host to the incorporated CP (**Fig. 6.3b**).

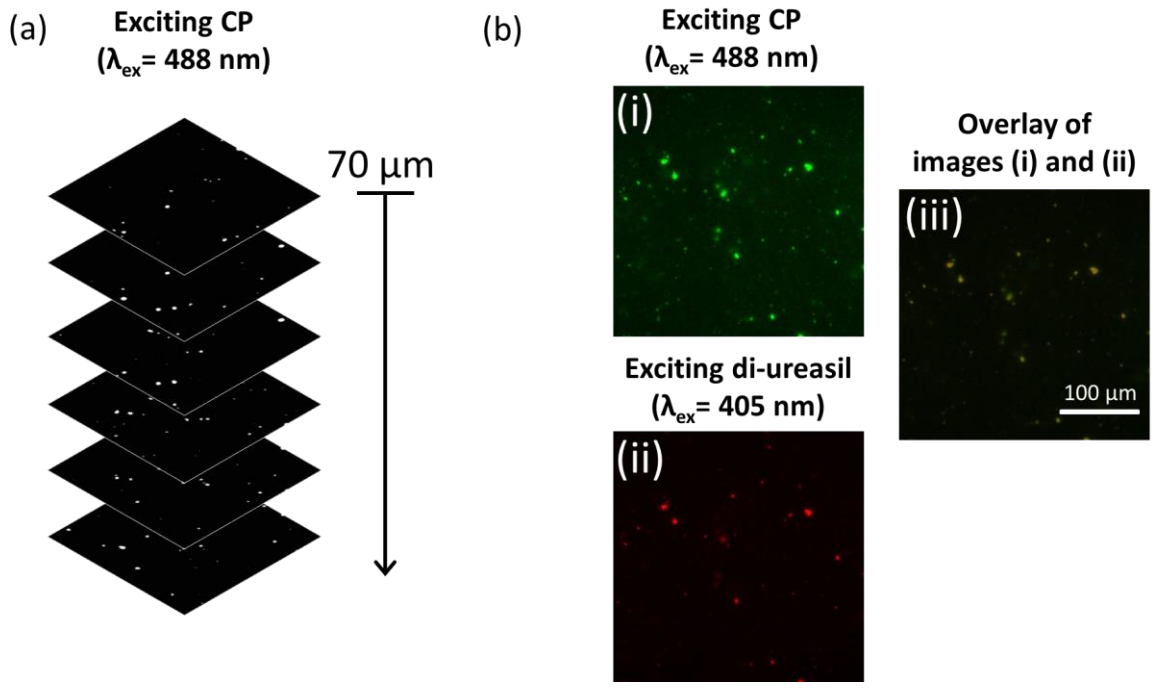

Figure 6.3. Confocal microscopy images for **P3T-6.6** (**a**) up to a depth of 70 µm from the sample surface (λ_{ex} = 488 nm) and (**b**) from 40 µm below the surface: (**i**) λ_{ex} = 488 nm, red emission filter 550-740 nm, (**ii**) λ_{ex} = 405 nm, red emission filter 550-740 nm and (**iii**) overlay of images (**i**) and (**ii**) showing emission from identical local domains.

6.3.2.2 Powder X-Ray Diffraction

The PXRD patterns for all samples match those discussed in **Section 5.3.4.1** and in the literature.[11, 27-29] The patterns exhibit a primary band centred at 21.1˚, with a shoulder at 11.0-15.0˚ (**Fig. 6.4**). The structural unit distance, *d*, was determined from the main peak at 21.1˚ to be 4.2 ± 0.1 Å (from Bragg's Law). The shoulder between 11.0˚ and 15.0˚ gives rise to a characteristic distance of 3.4 ± 0.5 Å matching those reported previously.[11, 29] The coherent length over which the structural unit survives in the di-ureasil was estimated to be 11.1 ± 1 Å (from the Scherrer equation).[30] This value is similar to that previously reported for di-ureasils prepared *via* carboxylic acid solvolysis.[29] These results suggest that the incorporation of the CPs, within the concentration range examined in this study, does not induce significant structural changes in the di-ureasil host.

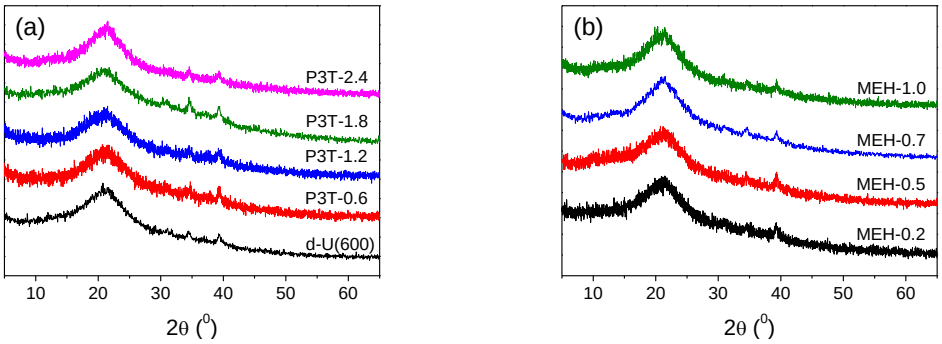

Figure 6.4. Powder X-ray patterns for samples (**a**) **d-U(600)**, **P3T-0.6**, **P3T-1.2**, **P3T-1.8** and **P3T-2.4** and (**b**) **MEH-0.2**, **MEH-0.5**, **MEH-0.7** and **MEH-1.0** in the range 2θ = 5-65^0.

6.3.2.3 Solid-State NMR

The ^{29}Si MAS-NMR spectra of all CP-di-ureasils studied contain three broad signals characteristic of T_1, T_2 and T_3 units (**Fig. 6.5**). The assignment of these signals is equivalent to those discussed in **Section 5.3.4.2**. The T_2 and T_3 signals (at –58.1 ppm and –66.6 ppm, respectively) are the dominant environments with a negligible contribution from T_1 at –49.4 ppm, as is the case for lanthanide complex doped di-ureasils.[11] The absence of the T_0 signal confirms that there is no unreacted precursor remaining.[11]

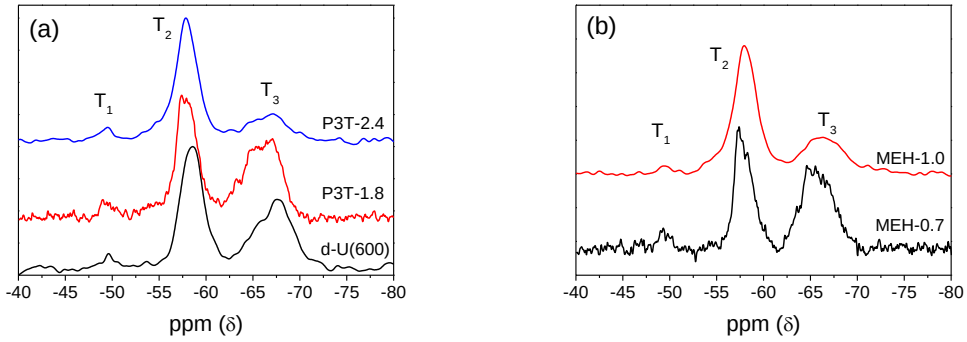

Figure 6.5. ^{29}Si solid-state MAS NMR spectra for (**a**) **d-U(600)**, **P3T-1.8** and **P3T-2.4** and (**b**) **MEH-0.**7 and **MEH-1.0**.

The degree of condensation, *C*, of the siliceous network was determined as described in **Section 5.3.4.2**, using Gaussian deconvolution of the peaks to determine the relative population of each organosiloxane species, the result of which is presented in **Table 6.3**. The *C* values obtained [73-83%] are in good agreement with those previously observed for poly(fluorene)-di-ureasils (**Section 5.3.4.2**). No linear relationship between *C* and wt% of CP incorporated is observed, even on the incorporation of the much higher molecular weight **MEH-PPV**. This is contrary to previous studies with lanthanide complexes of varying sizes in which the degree of condensation decreased with increasing complex size.[31] This is most likely due to the differing level of interaction between the CP and the di-ureasil. In particular, the di-ureasil is able to interact strongly with Eu^{III}-containing

complexes *via* the incorporation of its C=O groups into the coordination sphere of the metal complex,[31] a situation that is impossible for the non-metal containing CPs investigated here.

Table 6.3. ^{29}Si MAS NMR chemical shifts (ppm *vs.* TMS), population of different T_n species (%), T_n species ratios, and degree of condensation, *C* (%) of CP-di-ureasils.

Sample	T_1 (%)	T_2 (%)	T_3 (%)	T_1: T_2: T_3	C (%)[a]
d-U(600)	-49.7 (3.4)	-58.6 (55.0)	-67.4 (41.6)	1: 16.1:12.2	79.4
P3T-1.8	-49.4 (3.8)	-57.9 (41.3)	-66.8 (54.9)	1: 10.8: 14.4	83.7
P3T-2.4	-49.3 (3.8)	-57.9 (67.0)	-66.9 (29.2)	1: 17.6: 7.7	75.1
MEH-0.7	-49.1 (8.1)	-57.9 (37.6)	-66.9 (54.2)	1: 4.6: 6.7	82.0
MEH-1.0	-49.6 (2.6)	-58.0 (62.8)	-66.2 (34.6)	1: 24.2: 13.	77.3

[a] $C = 1/3(\%T_1+2\%T_2+3\%T_3)$[11]

The ^{13}C CP/MAS-NMR spectra are in excellent agreement with those previously reported for di-ureasils of this type[28] (**Fig. 6.6**). The assignment of the main peaks can be found in **Table 6.4**. Once again, no significant changes in the peaks are observed on comparison between the two CP-di-ureasil series and **d-U(600)**, further indicating that the hybrid structure is not chemically modified upon CP incorporation.

Table 6.4. ^{13}C solid-state CP-MAS NMR chemical shifts (ppm *vs.* TMS) and assignments of CP-di-ureasils.

Signal assignment	d-U(600)	P3T-1.8	P3T-2.4	MEH-0.7	MEH-1.0
-OCH	75.7	75.7	75.5	75.7	75.7
-(OCH_2CH_2)	71.1	71.0	71.0	71.2	71.0
-NCH_2 in -$N(CH_2)_3Si$	46.3	46.3	-	46.5	-
-'CH_2 in -$N(CH_2)_3Si$	24.8	24.6	25.1	24.8	-
-CH_3 in – $OCH_2CH(CH_3)$	19.0	18.8	19.3	19.0	19.0
-CH_3 in – $(CH_3CH_2O)_3Si$	17.8	17.7	17.7	18.0	17.8
-CH_2Si in – $N(CH_2)_3Si$	11.4	11.1	-	11.3	-

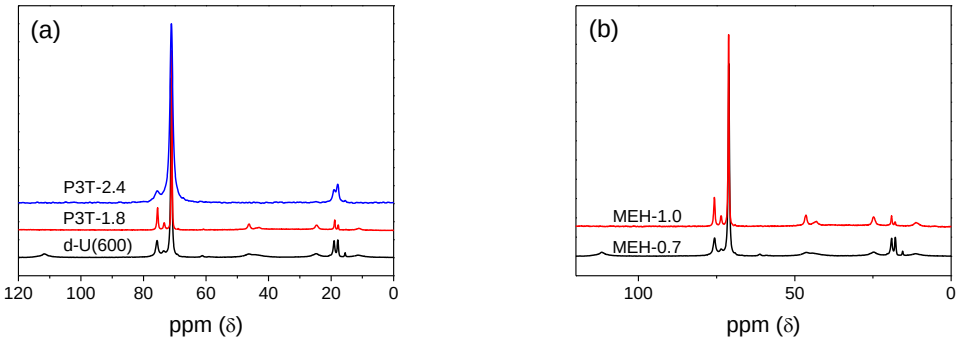

Figure 6.6. ^{13}C solid-state CP/MAS NMR spectra for (**a**) **d-U(600)**, **P3T-1.8** and **P3T-2.4** and (**b**) **MEH-0.7** and **MEH-1.0**.

6.3.2.4 Fourier Transform Infrared Spectroscopy

The FTIR spectra for the CP-di-ureasils, **Fig. 6.7**, match those of undoped di-ureasils.[32] Gaussian deconvolution of the Amide I region (1610-1770 cm^{-1}) of the spectra yielded three components at 1714, 1667 and 1638 cm^{-1} (see **Fig. A.6.1** in the appendix for **P3T-1.8** as a representative example). The first two of these bands are ascribed to the vibrations of C=O groups within disordered hydrogen-bonded urea-polyether associations of increasing strength, while the component at 1638 cm^{-1} is attributed to strong self-associated hydrogen-bonded urea-urea associations.[11, 28, 32] There is no noticeable change in the position or contribution of any of these bands as a function of CP concentration, **Table 6.5**, suggesting no significant effect on hydrogen bonding interactions within the di-ureasil on CP incorporation.

Table 6.5. Results of the curve fitting performed in the 'Amide I' band of **MEH-x** and **P3T-x** CP-di-ureasils. The peak position, area and % contribution for each component resolved are shown.

Sample	Peak (cm^{-1})	Area (% of total area)	Peak (cm^{-1})	Area (% of total area)	Peak (cm^{-1})	Area (% of total area)
d-U(600)	1714	0.65 (19.1%)	1665	2.06 (60.4%)	1636	0.70 (20.5%)
P3T-0.6	1713	0.62 (17.8%)	1666	2.16 (61.9%)	1638	0.71 (20.3%)
P3T-1.2	1710	0.41 (12.1%)	1664	2.23 (66.0%)	1637	0.74 (21.9%)
P3T-1.8	1714	0.80 (24.5%)	1666	1.85 (56.7%)	1638	0.61 (18.7%)
P3T-2.4	1714	0.56 (18.8%)	1666	1.86 (62.4%)	1638	0.56 (18.8%)
MEH-0.2	1715	0.39 (21.9%)	1669	1.01 (56.7%)	1639	0.38 (21.3%)
MEH-0.5	1715	0.48 (22.7%)	1668	1.20 (56.9%)	1639	0.43 (20.4%)
MEH-0.7	1714	0.26 (8.4%)	1667	2.09 (67.4%)	1639	0.75 (24.2%)
MEH-1.0	1715	0.69 (21.4%)	1668	1.78 (55.1%)	1639	0.76 (23.5%)

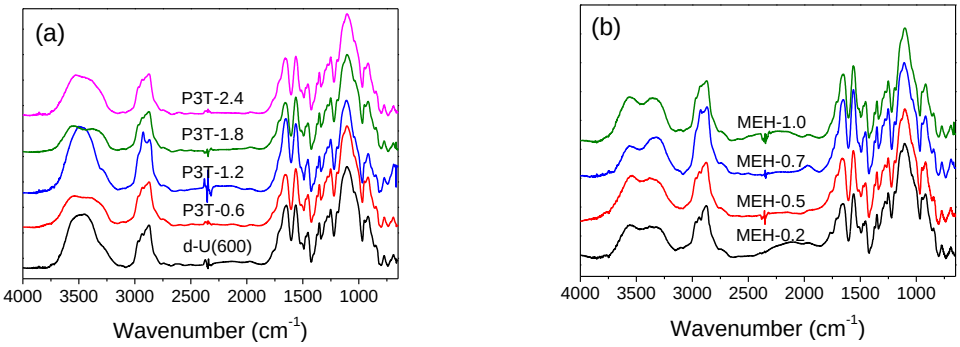

Figure 6.7. FTIR spectra for (**a**) **d-U(600)**, **P3T-0.6**, **P3T-1.2**, **P3T-1.8** and **P3T-2.4** and (**b**) **MEH-0.2**, **MEH-0.5**, **MEH-0.7** and **MEH-1.0** over the range 4000-400 cm^{-1}. All spectra taken at a resolution of 4 cm^{-1}.

6.3.3 Photophysical Characterisation

6.3.3.1 Photoluminescence of CP-di-ureasils

Fig. 6.8a and **6.8c** show the PL spectra for **P3T-1.8** and **MEH-0.5** as a function of excitation wavelength, as representative samples for the P3T-x and MEH-x series, respectively. On addition of the CPs to the di-ureasil host matrix, the PL spectra retain a broad emission band in the blue spectral region, whose excitation wavelength dependence indicates that it may be ascribed to the di-ureasil emission. Previously, energy transfer from a di-ureasil host to a dopant species has been inferred from the presence or absence of the di-ureasil band in the emission spectrum.[10, 33] For di-ureasils doped with an Eu(1-(2-napththyl)-4,4,4-trifluoro-1,3-butanedionate)$_3$·2,2′-bipyridine complex the di-ureasil emission is completely absent,[33] while this phenomenon occurs only at high dopant concentrations for the analogous Cu(CF_3SO_3)$_3$-di-ureasils, suggesting that energy transfer is less efficient in the latter system.[10] The detection of the di-ureasil emission in the PL spectra of MEH-x and P3T-x di-ureasils suggests incomplete energy transfer in this case. This is advantageous as the di-ureasil emission provides a significant contribution to the total sample emission, which is necessary for the generation of white light. The emission spectra also exhibit a broad emission band in the orange-red spectral region, which is attributed to emission from the CP (see appendix **Fig. A.6.2** for the PL properties of **P3TMAHT** and **MEH-PPV** in solution, respectively). The emission maximum of this band is relatively insensitive to the excitation wavelength.

The excitation spectra for P3T- and MEH-di-ureasils monitored specifically in the CP emission region (500–580 nm) exhibit a major component centred at 430-450 nm assigned to direct CP excitation (see **Fig. 6.8b** and **Fig.6.8d** for **P3T-1.8** and **MEH-0.5**, respectively, as representative examples). However, a shoulder at ~370 nm is also observed, which is reminiscent of the **d-U(600)** excitation band (**Fig. 5.14b**). The contribution from this shoulder increases as the monitoring wavelength is moved towards the di-ureasil emission range (400-440 nm), further supporting this assignment. The presence of this di-ureasil band in the excitation spectrum while

monitoring the CP emission, even at the highest CP concentrations examined (see appendix **Fig. A.6.4** and **Fig. A.6.6**), supports the occurrence of di-ureasil to CP energy transfer.[10]

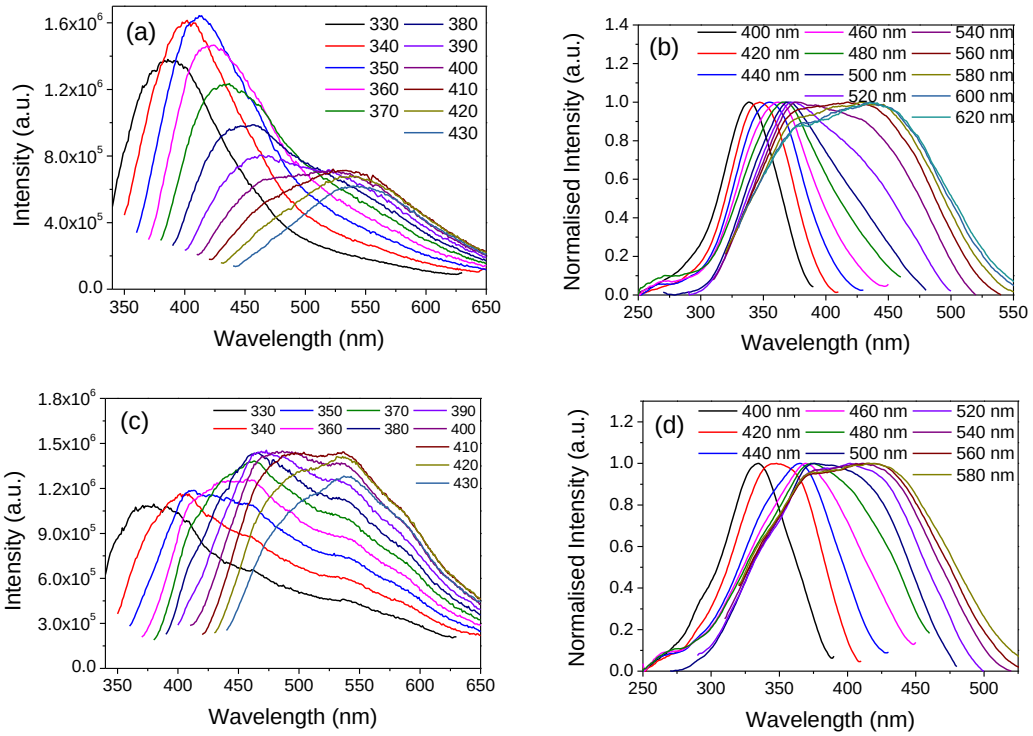

Figure 6.8. (**a**) PL spectra (λ_{ex} = 330, 340, 350, 360, 370, 380, 390, 400, 410, 420 and 430 nm) of **P3T-1.8**. (**b**) PL excitation spectra (λ_{em} = 400, 420, 440, 460, 480, 500, 520, 540, 560, 580, 600 and 620 nm) of **P3T-1.8**. (**c**) PL spectra (λ_{ex} = 330, 340, 350, 360, 370, 380, 390, 400, 410, 420 and 430 nm) of **MEH-0.5**. (**d**) PL excitation spectra (λ_{em} = 400, 420, 440, 460, 480, 500, 520, 540, 560 and 580 nm) of **MEH-0.5**.

It is important to note that the spectral overlap for di-ureasil-**MEH-PPV** is almost twice that calculated for the di-ureasil-**P3TMAHT** combination (**Table 6.2**), suggesting the energy transfer to **MEH-PPV** should be more efficient. However, in the case of both CPs studied here, we note that the absorption band of the CP partially overlaps with that of the di-ureasil (310-450 nm). As such, at these wavelengths, selective excitation of the di-ureasil is not possible. However, at the lowest excitation wavelengths (250-380 nm), where the CP absorption is minimal, significant CP emission is still observed, further suggesting the existence of energy transfer. It should also be noted that at low dopant concentrations the CP emission maximum is significantly blue-shifted on incorporation into the di-ureasil compared to the parent stock solutions (~65 and 75 nm for **P3TMAHT** and **MEH-PPV**, respectively). However, as the CP dopant wt% is increased, the emission maximum subsequently red-shifts (**Fig. 6.9**). A blue-shift in the emission maximum is often attributed to the break-up of polymer aggregates, which decreases the effective conjugation length.[34] Similarly large spectral shifts have been reported for the **P3TMAHT** emission band in a related di-block copolymer upon interaction with DNA, which changes the aggregate structure.[35] A large blue-shift (86 nm) in the emission maximum has also previously been observed on incorporation of

MEH-PPV into a PVK matrix.[36] As expected the magnitude of the emission signal in the red region of the spectrum increases with increasing CP dopant concentration (see Appendix **Fig. 6.3** and **A.6.4** for P3T-di-ureasils and **Fig. A.6.5** and **A.6.6** for MEH-di-ureasils).

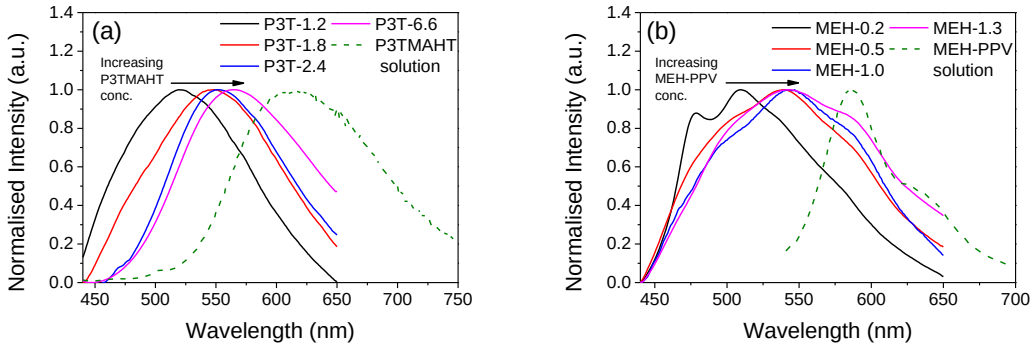

Figure 6.9. Photoluminescence spectra (λ_{ex} = 430 nm) of (**a**) **P3T-1.2**, **P3T-1.8**, **P3T-2.4**, **P3T-6.6** and **P3TMAHT** in aqueous solution (16 μM) and (**b**) **MEH-0.2**, **MEH-0.5**, **MEH-1.0**, **MEH-1.3** and **MEH-PPV** in THF (5 μM).

Fig. 6.10 shows the emission-excitation matrices (EEMs) for **P3T-1.8** and **MEH-0.5** as representative examples. The EEMs illustrate that through careful selection of the excitation wavelength, the resulting emission of the CP-di-ureasil can be tuned across the entire visible spectrum. The EEM of **P3T-1.8** (**Fig. 6.10a**) shows emission from the di-ureasil host in the region 380 to 475 nm (λ_{ex} = 330-370 nm), which reaches a maximum at λ_{ex} = 350 nm and then subsequently reduces in intensity. Moreover, there is an increase in the emission originating from the CP in the green-red region (475-625 nm) as the excitation wavelength increases. The reduction in di-ureasil emission at λ_{ex}>350 nm, accompanied by the increase in CP emission leads to similar emission intensity across the emission range investigated. The EEM of **MEH-0.5** (**Fig. 6.10b**) is slightly different as the CP emission dominates the entire emission spectrum, which increases in intensity across the excitation wavelength range studied (330-370 nm). However, the di-ureasil contribution is still visible for **MEH-0.5** between 420-480 nm. This band merges with the CP emission at λ_{ex}>350 nm, again leading to similar emission intensity across the emission range investigated at higher excitation wavelengths.

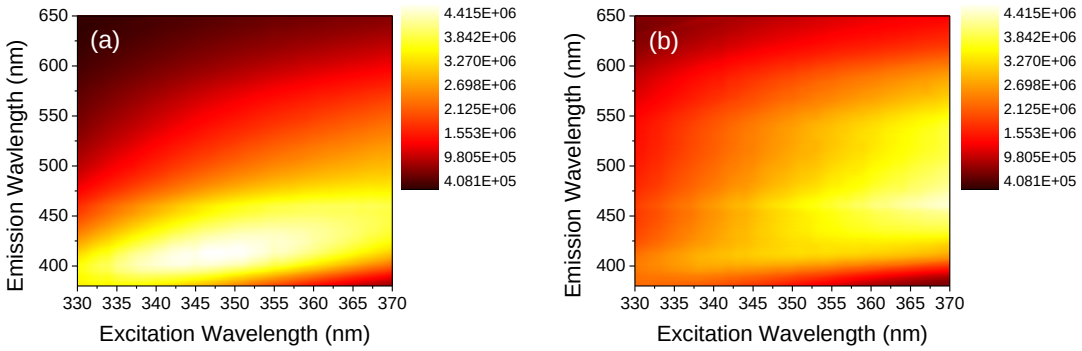

Figure 6.10. Emission-excitation matrices for (**a**) **P3T-1.8** and (**b**) **MEH-0.5**, where λ_{ex} = 330–370 nm and λ_{em} = 380–650 nm (both at 1 nm intervals).

6.3.3.2 CIE (1931) Colour Coordinates

Fig. 6.11 plots the Commission Internationale d'Éclairage (CIE) 1931 *xy* chromaticity diagrams for representative P3T- and MEH-di-ureasils as a function of excitation wavelength and CP doping wt%. The CIE (1931) colour coordinates were determined as outlined in **Section 2.3.4**.

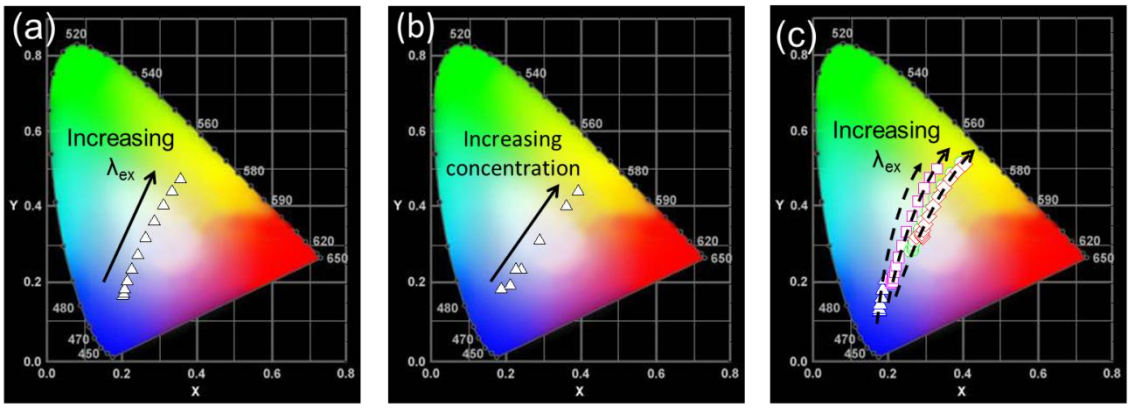

Figure 6.11. CIE *x,y* chromaticity diagrams for (**a**) **P3T-1.8** as a function of increasing excitation wavelength (λ_{ex} = 330, 340, 350, 360, 370, 380, 390, 400, 410, 420 and 430 nm); (**b**) **d-U(600)**, **P3T-0.6**, **P3T-1.2**, **P3T-1.8**, **P3T-2.4**, **P3T-3.3** and **P3T-6.6** at a fixed excitation wavelength (λ_{ex} = 370 nm); (**c**) **MEH-0.0** (open triangles), **MEH-0.2** (open squares), **MEH-0.7** (open circles) and **MEH-2.7** (open diamonds) as a function of excitation wavelength (**MEH-0.0**: λ_{ex} = 330, 340, 350, 360, 370, 380, 390 nm; **MEH-0.2**, **MEH-0.7** and **MEH-2.7**: λ_{ex} = 330, 340, 350, 360, 370, 380, 390, 400, 410, 420 and 430 nm). The dashed arrows serve only to guide the eye.

Taking **P3T-1.8** as an example, **Fig. 6.11a** shows that by taking advantage of the excitation wavelength dependence of the di-ureasil emission, the emission colour can be tuned from the blue (0.19, 0.16) to the yellow (0.31, 0.43) region, through white (0.23, 0.30). As the excitation wavelength is increased, the 'blue' emission of the di-ureasil is shifted towards the red spectral region where the CP emits; when the contributions from both CP and di-ureasil are roughly equal, white-light is produced. Moreover, if the excitation wavelength is fixed (370 nm), and the CP dopant wt% is varied, the emission of the CP-di-ureasil can be modulated further (see **Fig. 6.11b** for the **P3T-x** series). At low dopant concentrations, the di-ureasil emission dominates, giving rise to CIE *x,y* coordinates in the blue region (0.21, 0.20). As the CP concentration is increased, emission in the red gamut becomes more important, shifting the colour coordinates to (0.39, 0.44), through white (0.29, 0.31). **Fig. 6.11c** shows comparable trends with excitation wavelength and dopant concentration for the **MEH-x** series. As the **MEH-PPV** concentration increases the colour coordinates move from blue to yellow on a path that passes increasingly close to pure white light, (0.33, 0.33).[37] However, this effect appears to saturate at a dopant concentration of 0.007 wt%.

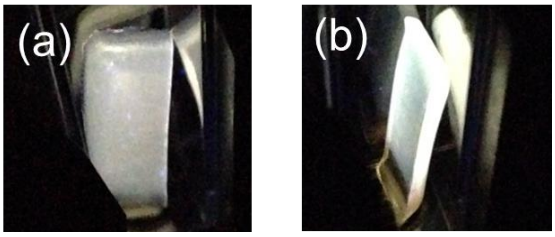

Figure 6.12. Photographs of (**a**) **P3T-1.8** and (**b**) **MEH-2.7** under UV-illumination (λ_{ex} = 385 nm).

Combined emission from direct excitation of the di-ureasil host and the CP emission resulting from *D-A* energy transfer gives rise to a broad emission band covering the majority of the visible spectrum. Judicious selection of the excitation wavelength and CP dopant concentration provide two independent modes for tuning the emission colour of CP-di-ureasils to generate a white-light emitting material. The photographs in **Fig. 6.12a** and **6.12b** show the white-light produced from **P3T-1.8** (cool) and **MEH-2.7** (warm), respectively, upon excitation at 385 nm. This approach provides a simple and elegant method to produce a single layer, white-light emitting material.

6.3.3.3 Photoluminescence Lifetimes of CP-di-ureasils

As indicated above, both CPs absorb light to some extent at the wavelengths used to directly excite the di-ureasil. Thus, to further investigate the origin of the CP emission, (host-guest energy transfer *vs.* direct excitation), ps-TCSPC experiments were carried out. Photoluminescence decays were measured for the **P3T-x** and **MEH-x** series, upon excitation at 365 nm and detection at 420 and 600 nm, which correspond predominantly to the di-ureasil and CP emission, respectively (**Fig. 6.13**).

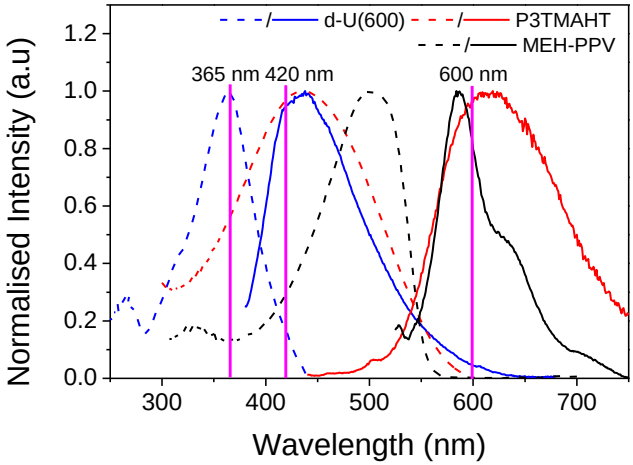

Figure 6.13. Emission and excitation spectra for **d-U(600)** (blue, λ_{ex} = 365 nm, λ_{em} = 420 nm) and UV/Vis absorption and emission spectra for **MEH-PPV** (black, λ_{ex} = 480 nm in THF) and **P3TMAHT** (red, λ_{ex} = 430 nm in aqueous solution). Emission spectra are shown as solid lines and excitation and UV/Vis absorption spectra are shown as dashed lines. The pink lines highlight the excitation (λ_{ex}) and emission (λ_{em}) wavelengths used in the ps-TCSPC experiments.

All decay curves displayed complex multi-exponential behaviour, requiring a minimum of three exponential components to fit the data. In some instances it was not possible to obtain satisfactory fits to the data at short times after the pulse (<90 ps). This arises due to the nature of the samples themselves, which makes it impossible to completely eliminate contributions from scattering at the shortest timescales. For these samples, tail fits to the decay curves were used instead.

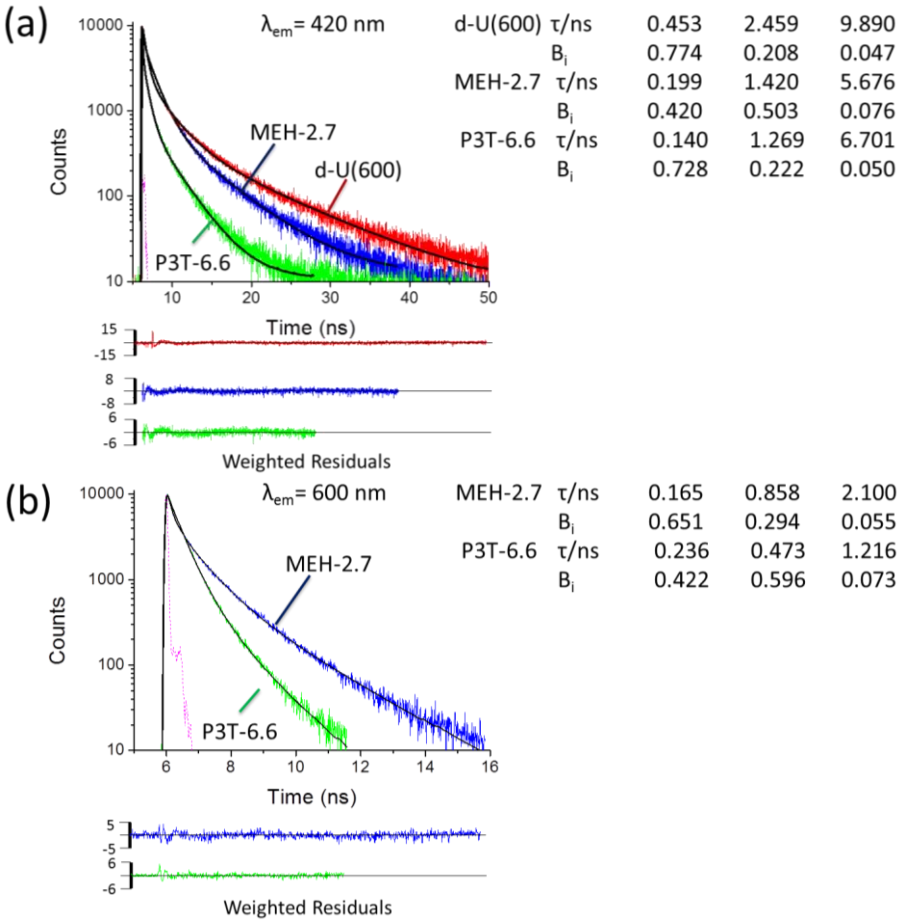

Figure 6.14. PL emission decay curves for (**a**) **d-U(600)** (red), **MEH-2.7** (blue) and **P3T-6.6** (green) detected at λ_{em} = 420 nm and (**b**) **MEH-2.7** (blue) and **P3T-6.6** (green) detected at λ_{em} = 600 nm. The resulting decay times (τ), fits (black lines), weighted residuals and instrument response function (IRF, pink dash) are also shown. λ_{ex} = 365 nm.

Fig. 6.14 presents the decay curves and fits obtained for **d-U(600)**, **P3T-6.6** and **MEH-2.7** at room-temperature. The undoped **d-U(600)** exhibits a tri-exponential decay curve at λ_{em} = 420 nm, with components at τ_{dU1} ~400 ps, τ_{dU2} ~2.5 ns and τ_{dU3} ~9.9 ns. These lifetimes are extremely similar to those reported for undoped di-ureasils prepared *via* formic acid solvolysis.[28] The pre-exponential factors (α_i) show that τ_{dU1} is the primary component in the emission decay (α_{dU1} ~0.75), with τ_{dU2} (α_{dU2} ~0.20) and τ_{dU3} (α_{dU3} ~0.05) providing lesser contributions. Photoluminescence decays for the CPs in solution were also measured by selective excitation at 460 nm and monitoring the decay at 600 nm, the spectral region dominated by the CP emission (**Fig. 6.15**). The decays also exhibit complex tri-exponential behaviour, comprising a long lifetime component (τ_{CP3}) of ~600 ps for **P3TMAHT** and ~800 ps for **MEH-**

PPV, ascribed to emission from isolated polymer chains,[38, 39] an intermediate lifetime (τ_{CP2}) of ~200 ps attributed to radiative relaxation of aggregated polymer species,[38, 39] and a short component (τ_{CP1}) of ~25 ps. Very short lifetimes (~10-30 ps) have previously been assigned to conformational relaxation and/or energy migration along the polymer chain.[38, 40]

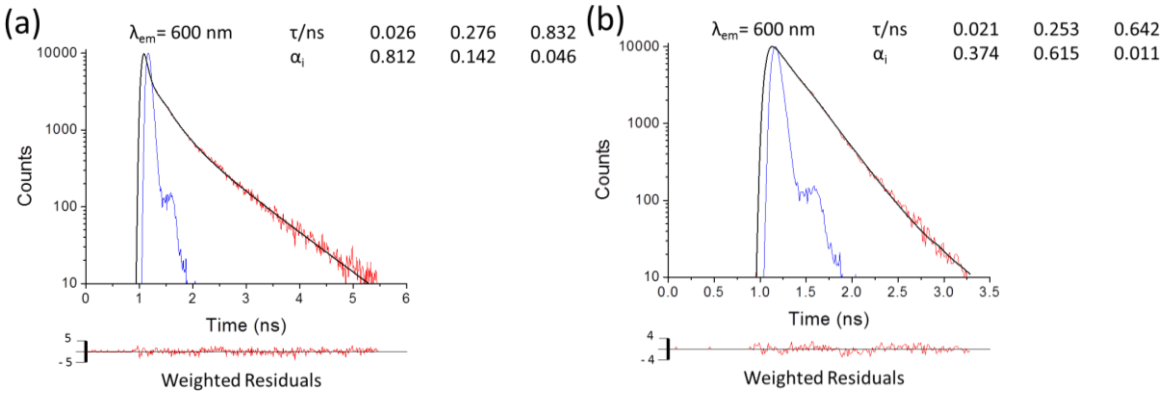

Figure 6.15. PL emission decay curves (solid red lines) (λ_{ex}= 460 nm and λ_{em}= 600 nm), and fits (solid black lines) for (**a**) **P3TMAHT** in water and (**b**) **MEH-PPV** in THF. The fitted decay times (τ_i), (α_i), fits, weighted residuals and instrument response function (solid blue line) are also shown.

Addition of **P3TMAHT** or **MEH-PPV** to the di-ureasil host results in a significant decrease in the lifetime measured at λ_{em}= 420 nm (**Fig. 6.14a**). **Fig. 6.16** shows the lifetimes and pre-exponential contributions obtained for multi-exponential fits to the **P3T-x** series. Over the concentration range examined, τ_{dU3} decreases considerably from 9.9 ns in the pure di-ureasil to 6.7 ns at the highest CP wt% for the **P3T-x** series (**Fig. 6.16a**). The two shorter di-ureasil species remain reasonably constant with the exception of the highest **P3TMAHT** concentration (6.6×10^{-3} wt%), where τ_{dU1} drops considerably to 140 ps. Similar trends are observed for **MEH-x** for both τ_i and α_i upon detection at 420 nm (**Table 6.6**). The apparent decrease in the emission lifetime of the di-ureasil donor in the presence of the CP acceptor is clear evidence for the occurrence of energy transfer. The strong dependence of τ_{dU3} on CP concentration upon detection in the di-ureasil emission band further supports energy transfer between the two species.

The decay curves measured at 600 nm for the **P3T-x** series also require tri-exponential fits, whose lifetimes are denoted as τ_2, τ_3, and τ_4. The shortest lifetime component observed for the CP in solution, τ_{CP1}, disappears and is replaced by a fourth long-lived species, τ_4, which provides a minor contribution to the overall decay (~1%) (**Fig. 6.16d**). This long lifetime component (4.4 ns) is significantly longer than typically observed for CPs and is more reminiscent of the longest-lived di-ureasil component (τ_{dU3}). Although the CP emission dominates at this monitoring wavelength, there may be some residual emission from the di-ureasil present, making it reasonable to assign τ_4 to this contribution. This lifetime is similar to those discussed in **Chapter 5** (**Section 5.3.5.5**) for poly(fluorene)-phenylene-doped di-ureasils. The magnitude of τ_4 decreases significantly from 4.4 ns to 1.2 ns as the CP wt% increases (**Fig. 6.16c**), suggesting increasingly efficient energy transfer from the di-ureasil to the CP. The fact that the di-ureasil continues to contribute to the emission at

600 nm makes it difficult to unequivocally assign the lifetime components to individual emitting species. However, when comparing the lifetimes of the parent CP stock solutions and the corresponding CP-di-ureasils, it is noted that both the shortest component, τ_2 (which resembles and may contain a contribution from τ_{CP2}) and the intermediate lifetime, τ_3 (which is similar to τ_{CP3}), decrease steadily with increasing CP concentration. The decrease in τ_2 and τ_3 with increasing concentration thus suggest an increase in CP aggregation. This is supported by the PL spectra which suggest an initial deaggregation of the polymer species upon incorporation into the di-ureasil at the lowest concentration, followed by re-aggregation with increasing CP concentration (**Fig. 6.9**). This is similar to the behaviour previously reported for **MEH-PPV** in a PVK matrix.[36] Similar trends in τ_i and α_i are observed for the **MEH-x** series upon detection at 600 nm (**Table 6.7**). However, τ_4 is much shorter for **MEH-PPV** (3.1 ns), suggesting more efficient energy transfer in this system, which is in line with the larger spectral overlap integral.

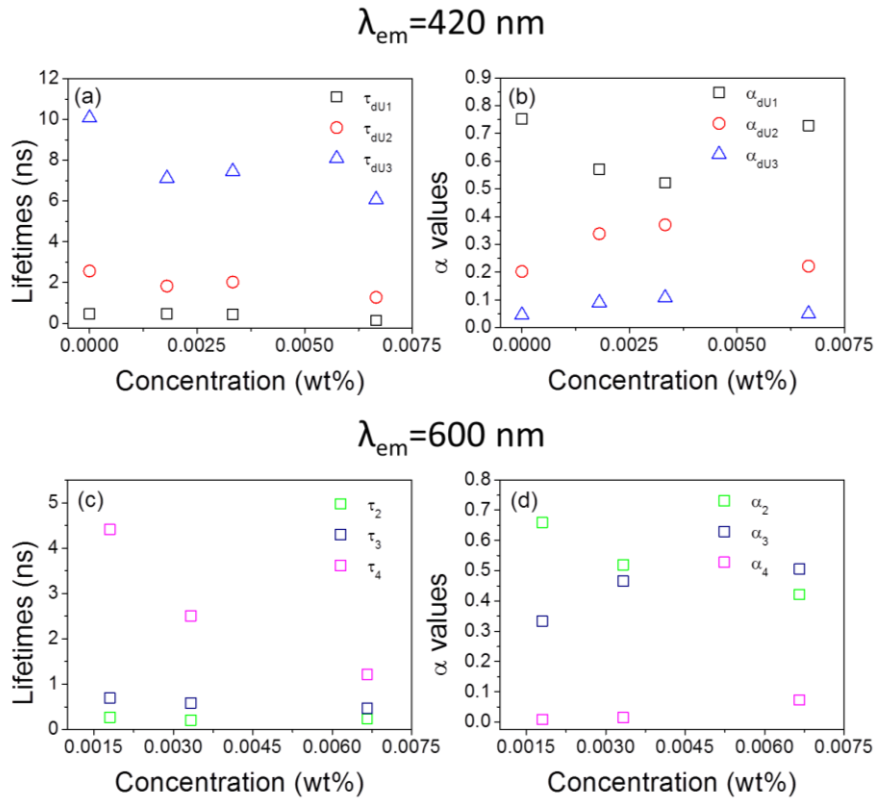

Figure 6.16. Emission lifetimes (τ_i) and corresponding pre-exponential factors (α_i) determined from tri-exponential fits to the fluorescence decays measured for the **P3T-x** series at (**a**, **b**) λ_{ex} = 365 nm and λ_{em} = 420 nm (di-ureasil emission) and (**c**, **d**) λ_{ex} = 365 nm and λ_{em} = 600 nm (CP emission band).

The occurrence of energy transfer within a system is often indicated by a rise time detected in the decay profile of the acceptor species. Energy transfer from highly planarised, aggregated chain segments of **MEH-PPV** to disordered, unaggregated chain segments has been shown to occur on a <1 ps timescale.[41] Thus, the lack of a rise time in the decay curves measured here does not indicate an absence of energy transfer, but rather that it occurs on a timescale that is beyond the resolution of our experimental set-up. Overall, the ps-TCSPC data suggest that the origin of the CP emission is not solely due to direct excitation, but also arises due to host-guest energy transfer.

Table 6.6. PL lifetimes (τ_i), pre-exponential coefficients (α_i), fractional contribution (f_i) and chi squared (χ^2) values obtained from fitting of the photoluminescence decays (λ_{ex} = 365 nm) of **MEH-*x*** at λ_{em} = 420 nm.

Sample	τ_1 **(ns)**	τ_2 **(ns)**	τ_3 **(ns)**	α_1	α_2	α_3	f_1	f_2	f_3	χ^2
d-U(600)	0.45 ±0.01	2.46 ±0.02	9.89 ±0.07	0.74 ±0.01	0.21 ±0.01	0.05 ±0.01	0.26 ±0.01	0.40 ±0.01	0.36 ±0.01	1.51
MEH-0.7	0.22 ±0.01	1.40 ±0.01	5.98 ±0.03	0.47 ±0.01	0.45 ±0.01	0.08 ±0.01	0.09 ±0.01	0.53 ±0.02	0.38 ±0.03	1.32
MEH-1.3	0.28 ±0.01	1.67 ±0.02	7.02 ±0.03	0.48 ±0.01	0.43 ±0.01	0.09 ±0.01	0.09 ±0.01	0.49 ±0.02	0.42 ±0.04	1.28
MEH-2.7	0.20 ±0.01	1.42 ±0.01	5.68 ±0.03	0.42 ±0.01	0.50 ±0.01	0.08 ±0.01	0.07 ±0.01	0.58 ±0.02	0.35 ±0.03	1.34

Table 6.7. PL lifetimes (τ_i), pre-exponential coefficients (α_i), fractional contribution (f_i) and chi squared (χ^2) values obtained from fitting of the photoluminescence decays (**MEH-*x*** λ_{ex}= 365 nm and **MEH-PPV** solution λ_{ex}= 460 nm) at λ_{em} = 600 nm.

Sample	τ_1 **(ns)**	τ_2 **(ns)**	τ_3 **(ns)**	τ_4 **(ns)**	α_1	α_2	α_3	α_4	f_1	f_2	f_3	f_4	χ^2
MEH-PPV solution	0.02 ±0.01	0.25 ±0.01	0.64 ±0.04		0.37 ±0.03	0.62 ±0.02	0.01 ±0.01		0.05 ±0.01	0.91 ±0.01	0.04 ±0.01		1.07
MEH-0.7		0.27 ±0.01	1.05 ±0.01	3.07 ±0.06		0.54 ±0.02	0.43 ±0.01	0.03 ±0.01		0.21 ±0.01	0.65 ±0.01	0.13 ±0.01	1.14
MEH-1.3		0.18 ±0.01	0.74 ±0.01	2.10 ±0.03		0.64 ±0.02	0.31 ±0.01	0.05 ±0.02		0.25 ±0.01	0.51 ±0.01	0.24 ±0.01	1.22
MEH-2.7		0.17 ±0.01	0.86 ±0.01	2.10 ±0.03		0.65 ±0.02	0.29 ±0.01	0.06 ±0.02		0.23 ±0.01	0.53 ±0.01	0.24 ±0.01	1.22

6.3.4 Improved Stability of the CP within the Di-ureasil Matrix

6.3.4.1 Thermal Stability

The thermograms for **d-U(600)** match those previously reported,[20, 42, 43] with the onset of sample decomposition at ~339 ˚C (**Fig. 6.17** and **Table 6.8**). The thermograms of the pure CPs exhibit two major decomposition events, at 220 and 435 ˚C for **P3TMAHT** and 300 and 508 ˚C for **MEH-PPV**, which is in good agreement with previous reports for **MEH-PPV**[44] and the related poly(thiophene) P3HT.[45] The first step is attributed to the loss of side chains attached to the polymer backbone, while the second is associated with decomposition of the polymer backbone. Doping of related ED-900-based di-ureasils with lithium salts has previously been shown to thermally destabilise the matrix.[42] However, for P3T-di-ureasils, incorporation of the CP yields a material that has a significantly higher thermal stability than the CP alone, with the main decomposition occurring at ~335 ˚C (**Fig. 6.17a**), which represents an increase in thermal stability of ~120˚C.

Since **MEH-PPV** has an intrinsically higher thermal stability than **P3TMAHT**, this effect is less pronounced for MEH-di-ureasils, with the onset of thermal decomposition increasing by ~30 °C (**Fig. 6.17b**). No direct relationship between the CP doping wt% and the improvement in the thermal stability is observed (**Table 6.8**).

Table 6.8. TGA results showing the onset temperature (T_{os}) and weight loss percentage (%) for CP-di-ureasil samples and the pure CPs.

Sample	T_{os} (˚C) Step One	Weight loss (%)	T_{os} (˚C) Step Two	Weight loss (%)
P3TMAHT	221.8	27.2	435.5	34.6
d-U(600)	334.8	59.4		
P3T-0.6	336.9	65.8		
P3T-1.2	337.4	59.7		
P3T-1.8	337.5	50.6		
P3T-2.4	328.9	63.8		
MEH-PPV	303.7	52.2	508.4	41.3
MEH-0.2	336.1	66.7		
MEH-0.5	335.2	65.1		
MEH-0.7	323.8	66.8		
MEH-1.0	343.9	67.6		

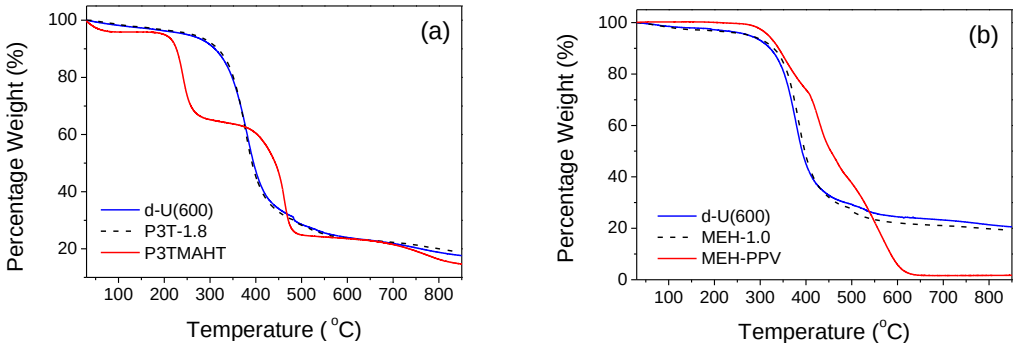

Figure 6.17. TGA thermograms of (**a**) **d-U(600)** (blue line), **P3T-1.8** (black dash line) and **P3TMAHT** (red line) and (**b**) **d-U(600)** (blue line), **MEH-1.0** (black dash line) and **MEH-PPV** (red line). TGA measurements were performed in air at a heating rate of 10 ^{o}C min^{-1}.

6.3.4.2 Photostability

The photostability of the CP-di-ureasils was also investigated. The integrated emission intensity of the pure **P3TMAHT** film dropped rapidly during the first 30 min of irradiation (λ_{ex} = 450 nm) to 30% of the initial value, and continued to decrease steadily to 20% at the end of the irradiation period (2 h) (**Fig. 6.18a**). This is in stark contrast to the integrated emission intensity of the **P3T-6.6** sample, which remains almost constant throughout the observation window. Similar trends were observed on comparison of **MEH-2.7** and the **MEH-PPV** film (**Fig. 6.18b**); however, the **MEH-PPV** film was less susceptible to photodegradation, dropping to 55% of the initial value within the 2 h period. Polythiophenes and PPV-type polymers are both susceptible to chemical attack under UV/visible irradiation; however, the archetypical polythiophene P3HT is typically more stable than **MEH-PPV**.[46] The origin of the reduced photostability of the **P3TMAHT** film is unclear at present, but it is possible that the ionic side groups of the polyelectrolyte may promote photodegradation, for example by expediting the diffusion of oxygen and/or water into the film. However, the photostability of both **MEH-PPV** and P3HT can be improved on blending with other species, such as fullerenes,[47] graphene oxide,[48] or other polymers[49] which facilitate the trapping of reactive intermediates. The enhanced photostability observed here for MEH- and P3T-di-ureasils is most likely to result from a similar mechanism.

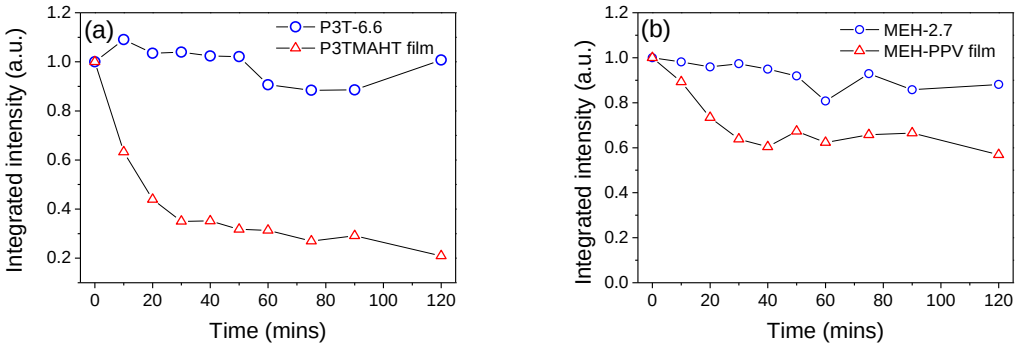

Figure 6.18. Integrated emission intensity of (**a**) a **P3TMAHT** thin film on glass (open red triangles) and **P3T-6.6** (open blue circles) under irradiation at 450 nm. and (**b**) a **MEH-PPV** thin film on glass (open red triangles) and **MEH-2.7** (open blue circles) under 500 nm irradiation. The black lines serve only to guide the eye.

6.4 Conclusions

CP-di-ureasils were successfully prepared *via* the *Direct Insertion* method in a simple one-pot solution process that yielded elastomeric monoliths exhibiting a tunable emission colour caused by incomplete energy transfer between the host and guest. Confocal microscopy revealed a homogeneous distribution of the CP within the di-ureasil. Selective excitation of the di-ureasil showed emission from CP domains throughout the di-ureasil, indicating the presence of energy transfer within the system. Through a combination of XRD, ss-NMR and FTIR, the incorporation of the CPs was found to have no adverse effect on the structural properties of the di-ureasil. Despite the larger molecular weight of **MEH-PPV**, bulk samples retain the structural and mechanical properties of the organic-inorganic hybrid host. Furthermore, P3T- and MEH-di-ureasils exhibit significantly superior thermal and photostability in comparison to the parent conjugated polymers, providing a route to light-emitting materials with an extended shelf-life.

Investigation of the photophysical characteristics of the CP-di-ureasils indicate that both CP and di-ureasil components contribute to the photoluminescence properties. Although large spectral overlap integrals are calculated for the **d-U(600)** host with both **MEH-PPV** and **P3TMAHT**, incomplete energy transfer from the di-ureasil host to the CP dopant results in emission from both species on direct excitation of the di-ureasil matrix. The contribution from each of these species can be modulated through judicious selection of the CP concentration or excitation wavelength. CIE chromaticity diagrams show that the subsequent emission colour is tunable from the blue to the yellow spectral region, along a trajectory that passes through white. As both CPs absorb to some extent at the wavelengths used to directly excite the di-ureasil, ps-TCSPC measurements were carried out to examine the origin of the CP emission. The PL lifetime at 420 nm, which is selective for di-ureasil emission, is reduced significantly with increasing CP concentration, indicating the occurrence of energy transfer. At the CP emission wavelength, 600 nm, a long lived species appears that is attributed to the di-ureasil for which there is residual emission at this wavelength. The magnitude of this long lived component

decreased significantly as the CP wt% was increased, suggesting progressively more efficient energy transfer from the di-ureasil to the CP. Also at this emission wavelength the lifetime of the species attributed to CP aggregates and isolated chains decreased with increasing concentration, suggesting an increase in CP aggregation. This is supported by the PL spectra which suggested an initial deaggregation of the polymer species upon incorporation into the di-ureasil at the lowest concentration, followed by re-aggregation with increasing CP concentration.

In addition to the monolithic samples discussed here, it is also possible to spin coat the CP-d-UPTES precursor solution as a homogeneous thin film onto different substrates, making these material a promising candidate for use in thin film devices. The facile synthetic approach, improved thermal and photostability of the resulting composite, the possibility to cast from solution as a single layer film and the tunable emission colour demonstrate that CP-di-ureasils are a versatile and efficient route to highly desirable white-light-emitters.

6.5 References

1. M. C. Gather, A. Kohnen and K. Meerholz, *Adv. Mater.*, 2011, **23**, 233-248.
2. L. Ying, C. L. Ho, H. Wu, Y. Cao and W. Y. Wong, *Adv. Mater.*, 2014, **26**, 2459-2473.
3. S. H. Wu, M. Aonuma, Q. S. Zhang, S. P. Huang, T. Nakagawa, K. Kuwabara and C. Adachi, *J. Mater. Chem. C*, 2014, **2**, 421-424.
4. Y. S. L. V. Narayana, S. Basak, M. Baumgarten, K. Mullen and R. Chandrasekar, *Adv. Funct. Mater.*, 2013, **23**, 5875-5880.
5. H. Wu, L. Ying, W. Yang and Y. Cao, *Chem. Soc. Rev.*, 2009, **38**, 3391-3400.
6. B. H. Hamadani, S. Jung, P. M. Haney, L. J. Richter and N. B. Zhitenev, *Nano Lett.*, 2010, **10**, 1611-1617.
7. C. Duan, K. Zhang, C. Zhong, F. Huang and Y. Cao, *Chem. Soc. Rev.*, 2013, **42**, 9071-9104.
8. R. Trattnig, L. Pevzner, M. Jager, R. Schlesinger, M. V. Nardi, G. Ligorio, C. Christodoulou, N. Koch, M. Baumgarten, K. Mullen and E. J. W. List, *Adv. Funct. Mater.*, 2013, **23**, 4897-4905.
9. E. Ravindran, S. J. Ananthakrishnan, E. Varathan, V. Subramanian and N. Somanathan, *J. Mater. Chem. C*, 2015, **3**, 4359-4371.
10. M. C. Goncalves, V. de Zea Bermudez, R. A. S. Ferreira, L. D. Carlos, D. Ostrovskii and J. Rocha, *Chem. Mater.*, 2004, **16**, 2530-2543.
11. P. P. Lima, R. A. S. Ferreira, S. A. Júnior, O. L. Malta and L. D. Carlos, *J. Photochem. Photobiol. A*, 2009, **201**, 214-221.
12. M. C. Neves, M. A. Martins, P. C. Soares-Santos, P. Rauwel, R. A. S. Ferreira, T. Monteiro, L. D. Carlos and T. Trindade, *Nanotechnology*, 2008, **19**, 155601.
13. A. Gutacker, S. Adamczyk, A. Helfer, L. E. Garner, R. C. Evans, S. M. Fonseca, M. Knaapila, G. C. Bazan, H. D. Burrows and U. Scherf, *J. Mater. Chem.*, 2010, **20**, 1423-1430.
14. M. Knaapila, R. C. Evans, A. Gutacker, V. M. Garamus, M. Torkkeli, S. Adamczyk, M. Forster, U. Scherf and H. D. Burrows, *Langmuir*, 2010, **26**, 5056-5066.
15. U. Scherf, A. Gutacker and N. Koenen, *Acc.Chem. Res.*, 2008, **41**, 1086-1097.
16. R. C. Evans, M. Knaapila, N. Willis-Fox, M. Kraft, A. Terry, H. D. Burrows and U. Scherf, *Langmuir*, 2012, **28**, 12348-12356.
17. L. Zhai and R. D. McCullough, *Adv. Mater.*, 2002, **14**, 901-905.
18. N. Willis-Fox, A. T. Marques, J. Arlt, U. Scherf, L. D. Carlos, H. D. Burrows and R. C. Evans, *Chem. Sci.*, 2015, **6**, 7227-7237.

19. N. Willis-Fox, M. Kraft, J. Arlt, U. Scherf and R. C. Evans, *Adv. Funct. Mater.*, 2015, 10.1002/adfm.201504017.
20. M. E. Mesquita, S. S. Nobre, M. Fernandes, R. A. S. Ferreira, S. C. G. Santos, M. O. Rodrigues, L. D. Carlos and V. de Zea Bermudez, *J. Photochem. Photobiol. A*, 2009, **205**, 156-160.
21. H. Y. Byun, I. J. Chung, H. K. Shim and C. Y. Kim, *Macromolecules*, 2004, **37**, 6945-6953.
22. F. Kong, Y. M. Sun and R. K. Yuan, *Nanotechnology*, 2007, **18**, 265707.
23. R. A. S. Ferreira, D. C. Oliveira, L. Q. Maia, C. M. S. Vicente, P. S. André, V. de Zea Bermudez, S. J. L. Ribeiro and L. D. Carlos, *Opt. Mater.*, 2010, **32**, 1587-1591.
24. D. C. Oliveira, A. G. Macedo, N. J. O. Silva, C. Molina, R. A. S. Ferreira, P. S. André, K. Dahmouche, V. de Zea Bermudez, Y. Messaddeq, S. J. L. Ribeiro and L. D. Carlos, *Chem. Mater.*, 2008, **20**, 3696-3705.
25. M. Wu, X. Xu, J. Wang and L. Li, *ACS Appl. Mater. Interfaces*, 2015, **7**, 8243-8250.
26. K. F. Karlsson, P. Asberg, K. P. R. Nilsson and O. Inganas, *Chem. Mater.*, 2005, **17**, 4204-4211.
27. L. D. Carlos, V.de Zea Bermudez, R. A. S. Ferreira, L. Marques and M. Assuncao, *Chem. Mater.*, 1999, **11**, 581-588.
28. L. Fu, R. A. S. Ferreira, M. Fernandes, S. C. Nunes, V. de Zea Bermudez, G. Hungerford, J. Rocha and L. D. Carlos, *Opt. Mater.*, 2008, **30**, 1058-1064.
29. L. Fu, R. A. S. Ferreira, N. J. O. Silva, L. D. Carlos, V. de Zea Bermudez and J. Rocha, *Chem. Mater.*, 2004, **16**, 1507-1516.
30. Scherrer equation: $L = 0.94\lambda/(A\cos\theta)$, where A (in radians) is the full-width-half-maximum of the Bragg peak. See A. Guinier, X-ray Diffraction in Crystals, Imperfect Crystals and Amorphous Bodies, Dover, New York 1994.
31. P. P. Lima, S. A. Junior, O. L. Malta, L. D. Carlos, R. A. S. Ferreira, R. Pavithran and M. L. P. Reddy, *Eur. J. Inorg. Chem.*, 2006, **2006**, 3923-3929.
32. V. de ZeaBermudez, L. D. Carlos and L. Alcacer, *Chem. Mater.*, 1999, **11**, 569-580.
33. L. Fu, R. A. S. Ferreira, N. J. O. Silva, A. J. Fernandes, P. Ribeiro-Claro, I. S. Gonçalves, V. de Zea Bermudez and L. D. Carlos, *J. Mater. Chem.*, 2005, **15**, 3117–3125.
34. H. D. Burrows, V. M. M. Lobo, J. Pina, M. L. Ramos, J. S. de Melo, A. J. M. Valente, M. J. Tapia, S. Pradhan and U. Scherf, *Macromolecules*, 2004, **37**, 7425-7427.
35. M. Knaapila, T. Costa, V. M. Garamus, M. Kraft, M. Drechsler, U. Scherf and H. D. Burrows, *J. Phys. Chem. B*, 2015, **119**, 3231-3241.
36. U. Balderas, C. Falcony, I. Moggio, E. Arias and M. Mondragón, *Polymer*, 2013, **54**, 2062-2066.
37. R. W. G. Hunt, *Measuring Colour*, Ellis Horwood, Chichester, 1991.
38. B. Ferreira, P. F. da Silva, J. S. S. de Melo, J. Pina and A. Macanita, *J. Phys. Chem. B*, 2012, **116**, 2347-2355.
39. A. T. Marques, H. D. Burrows, J. S. S. de Melo, A. J. Valente, L. L. Justino, U. Scherf, E. Fron, S. Rocha, J. Hofkens, E. W. Snedden and A. P. Monkman, *J. Phys. Chem. B*, 2012, **116**, 7548-7559.
40. T. Costa, A. T. Marques, J. S. S. de Melo, A. W. Thomas, L. E. Garner, U. Scherf, G. C. Bazan and H. D. Burrows, *J. Phys. Chem. B*, 2014, **118**, 613-623.
41. T. Unger, F. Panzer, C. Consani, F. Koch, T. Brixner, H. Bassler and A. Kohler, *Acs Macro. Lett.*, 2015, **4**, 412-416.
42. P. C. Barbosa, L. C. Rodrigues, M. M. Silva and M. J. Smith, *J. Power Sources*, 2008, **180**, 607-611.
43. M. Fernandes, V. de Zea Bermudez, R. A. S. Ferreira, L. D. Carlos and N. V. Martins, *J. Lumin.*, 2008, **128**, 205-212.
44. S. Chuangchote, T. Srikhirin and P. Supaphol, *Macromol. Rapid Commun.*, 2007, **28**, 651-659.
45. B. K. Kuila and A. K. Nandi, *J. Phys. Chem. B*, 2006, **110**, 1621-1631.
46. M. Jorgensen, K. Norrman and F. C. Krebs, *Sol. Energy Mater. Sol. Cells*, 2008, **92**, 686-714.
47. E. T. Hoke, I. T. Sachs-Quintana, M. T. Lloyd, I. Kauvar, W. R. Mateker, A. M. Nardes, C. H. Peters, N. Kopidakis and M. D. McGehee, *Adv. Energy Mater.*, 2012, **2**, 1351-1357.

48. C. Ran, M. Wang, W. Gao, J. Ding, Y. Shi, X. Song, H. Chen and Z. Ren, *J. Phys. Chem. C*, 2012, **116**, 23053-23060.
49. X. Wang, L. C. Groff and J. D. McNeill, *Langmuir*, 2013, **29**, 13925-13931.

Chapter Seven

A Hard Graft: Attaching a Polyfluorene to the Very Backbone of a Di-ureasil Matrix

7.1 Introduction

In **Chapters 5** and **6**, it was demonstrated that incorporation of conjugated polymers into a di-ureasil host matrix resulted in materials in which a synergistic interaction between the two components led to enhanced optical properties. The exhibited properties of organic-inorganic hybrids such as these depend not only on the nature of the individual components, but also on the interaction and interface between the two species.[1] As discussed previously, the nature of these interfaces has been used to divide hybrid materials into two different classes.[1, 2] *Class I* hybrids are defined as materials in which there are no covalent or iono-covalent bonds between the organic and inorganic species.[2, 3] In these materials the components exchange only weak bonds (van der Waals forces, hydrogen bonding or electrostatic forces).[1, 3] In contrast, hybrid materials in which the two phases are totally or partly linked through strong chemical bonds (covalent or iono-covalent bonds) are designated as *Class II* hybrids.[1, 3] Undoped di-ureasils fall under this category as the organic component, ED-600, is covalently bound to the siliceous network *via* two urea linkages.

Di-ureasils are a subset of a larger group of *Class II* materials, called polysilsesquioxanes, which are a family of organic-inorganic materials prepared *via* the hydrolysis and condensation of monomers containing an organic bridging group with two or more functional silyl groups.[4, 5] Through the variety of chemical and structural properties of polysilsesquioxanes accessible by variation of the organic bridging unit or functionalised silyl groups, they have found use in a wide range of applications such as separation membranes,[6] thermal insulation coatings[7] and photo-patternable materials.[8] The inclusion of π-conjugated bridging species, such as 1-cyano-1,2-bisbiphenyl-ethylene derivatives into a *Class II* hybrid, has led to highly fluorescent materials derived from strong π-π interactions between conjugated species giving rise to aggregation-induced emission.[9] Alternatively, covalently binding carbazole units to a polysiloxane network, to form a phosphorescent OLED with an iridium bis(4,6-difluorophenyl)pyridinato-N,C^2 picolinate (FIrpic) dopant, has been shown to break up the π-π interactions between the chromophoric units giving rise to a host material with high triplet energies. This prevents back energy transfer to the host, confining the triplet exciton on the FIrpic. This gives rise to a phosphorescent organic light-emitting diode with greater maximum quantum efficiency when compared to identical devices with different polymeric host networks.[10, 11]

The CP-doped samples discussed in **Chapter 5** and **6** can be described as *Class I* hybrid materials with respect to the incorporated CP and the host matrix, as there are only weak interactions such as van der Waals forces and hydrogen bonding between them. However, it is also possible to create a *Class II* hybrid in which the CP is chemically bound directly to the di-ureasil. Oligothiophene species have recently been introduced into a polysiloxane network to form *Class II* hybrids in an effort to increase the conductivity of the resulting material.[12] However, it was found that the rigidity of the siloxane network disturbs the effective conjugation in the oligothiophenes

reducing the overall conductivity. An alternative preparation allows the formation of *Class II* hybrid nanoparticles through base-catalysed nanoprecipitation of a polyfluorene with pendant triethoxysilyl groups.[13] The photophysical properties of these hybrid nanoparticles were found to be dependent on the relative amounts of their inorganic and organic components, highlighting the dependence of the photophysical properties on the interaction between the two phases. Thus, the covalent grafting of a polyfluorene based CP into the siloxane structure of a di-ureasil host has the potential to further modulate the interaction between the CP guest and the flexible di-ureasil host network.

7.1.1 Aims

In this chapter, the incorporation of a blue-emitting, polyfluorene conjugated polymer, **PF2/6-NH_2** (**Fig. 7.1**), within a di-ureasil host matrix will be examined. Two distinct incorporation methods are discussed, to produce Class I and Class II hybrid materials. The synthesis, structural characterisation and optical properties of these PF-di-ureasils will be investigated as a function of PF concentration, in an effort to examine any differing interaction between the PF and di-ureasil host arising from the structural differences between Class I and Class II hybrid materials.

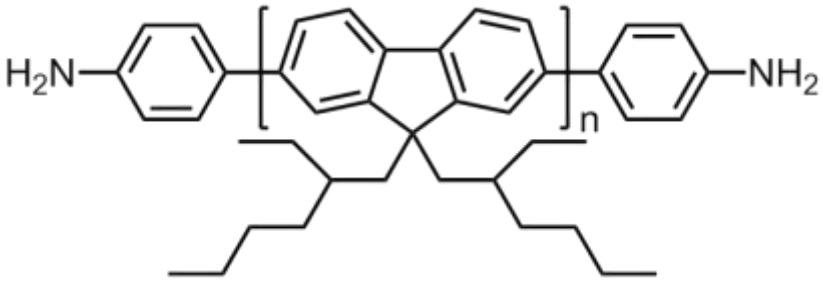

Figure 7.1. Chemical structure of 4-aminophenyl end-capped poly[9,9-bis(2-ethylhexyl)fluorene-2,7-diyl] (**PF2/6-NH_2**).

7.2 Experimental

7.2.1 Polymer

4-aminophenyl end-capped poly[9,9-bis(2-ethylhexyl)fluorene-2,7-diyl] (**PF2/6-NH_2**) with an M_n of 16,900 g mol^{-1}(~388 g mol^{-1} (r.u.)), was synthesised by Dr. Ana-Teresa Marques following the previously reported method.[14, 15]

7.2.2 Synthesis of PF-Di-ureasils

PF-di-ureasils were prepared *via* two different methods identified as *Direct Insertion* (*DI*), described in **Section 5.2.2**, and *Grafting* (*GF*). The samples created *via* the *DI* method were prepared by adding a fixed volume of PF solution in THF (5.2 mM r.u.) to the d-UPTES precursor solution (6.9 ml), prior to addition of the gelation agents, which then formed the condensed di-ureasil network around the PF *in situ*. The volume of the CP solution was varied to produce CP-di-

ureasils with the doped wt% described in **Table 7.1**. The samples are denoted **DI-PF-x**, where x represents the concentration (in 10^{-2} wt%) of the PF within the di-ureasil.

In the *GF* method a fixed volume of PF solution in THF (3.6 mM r.u.), *V*, was reacted with 2 equivalents of ICPTES, to produce a d-UPTES-like solution, in which the ED-600 component is replaced by **PF2/6-NH_2**. This mixture was then added to a previously prepared solution of conventional d-UPTES ('6.9 – *V*' ml). To this mixture of d-UPTES and **PF2/6-NH_2**-d-UPTES, the gelation agents ethanol (0.409 ml, 7 mmol), HCl (0.5 M, 0.040 ml) and H_2O (0.095 ml, 5.3 mmol) were added. This corresponds to a ratio of 1 ICPTES: 2.3 EtOH: 1.8 H_2O: 0.006 HCl molar equivalents, where the ICPTES concentration includes that used in both the conventional d-UPTES and the **PF2/6-NH_2**-d-UPTES. The volume of the initial PF solution was varied to produce PF-di-ureasils with the doped wt% described in **Table 7.1**. The samples for the *GF* method are denoted **GF-PF-x** where x represents the concentration (in 10^{-2} wt%) of the PF within the di-ureasil.

Table 7.1. Composition of PF-di-ureasils prepared in this study. [PF] is the concentration of the stock PF solution (in mM (r.u.)), that is either added to the d-UPTES intermediate (*DI* method) or in which **PF2/6-NH_2** is reacted with ICPTES (*GF* method).

Method	Sample	[PF] (mM (r.u.))	CPE wt%
Undoped di-ureasil	d-U(600)	0.0	0
Direct Insertion	DI-PF-0.16	0.12	0.16×10^{-2}
	DI-PF-0.31	0.24	0.31×10^{-2}
	DI-PF-0.47	0.36	0.47×10^{-2}
	DI-PF-1.60	1.21	1.6×10^{-2}
	DI-PF-3.90	3.02	3.9×10^{-2}
Grafted	GF-PF-0.16	0.12	0.16×10^{-2}
	GF-PF-0.31	0.24	0.31×10^{-2}
	GF-PF-0.47	0.36	0.47×10^{-2}
	GF-PF-1.60	1.21	1.6×10^{-2}
	GF-PF-3.90	3.02	3.9×10^{-2}
	GF-PF-15.0	26.80	1.5×10^{-1}

7.3 Results and Discussion

7.3.1 Incorporation of the PF within the Di-ureasil

A schematic representation of the two incorporation methods used to prepare PF-di-ureasils is shown in **Fig. 7.2**. The *DI* method involves the condensation of the d-UPTES solution around the CPE *in situ*. In this method the PF is permanently encased in the di-ureasil network, albeit without formal chemical bonding between the PF guest and the di-ureasil host. In contrast, the *GF* method involves covalently bonding **PF2/6-NH_2** to the ICPTES starting material and the co-

condensation of this new species with the conventional d-UPTES. This forms a sample in which the PF is chemically linked to the host siliceous network *via* two urea linkages.

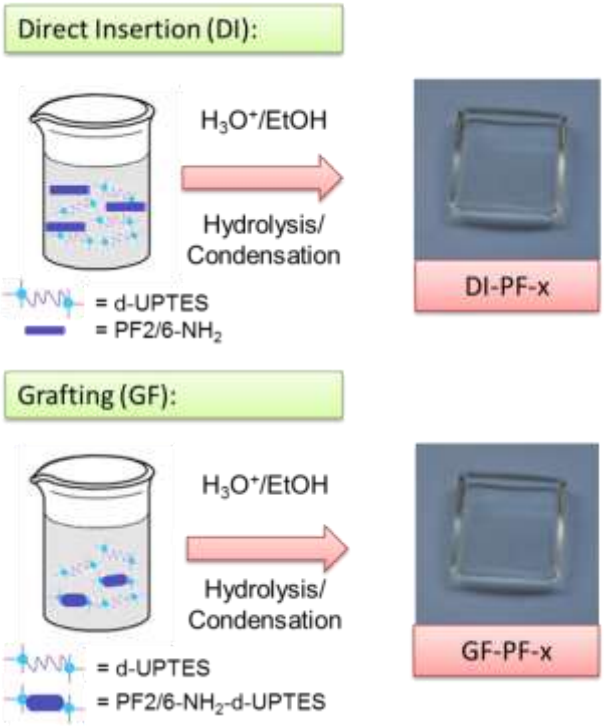

Figure 7.2. Schematic representation of the two synthetic methods used to prepare PF-di-ureasils.

7.3.1.1 Preparation of PF2/6-NH_2-d-UPTES Solution

The mechanism for the reaction between **PF2/6-NH_2** and ICPTES to form the **PF2/6-NH_2**-d-UPTES precursor solution (**Scheme 7.1**) is similar to that for the preparation of conventional d-UPTES, shown previously in **Scheme 5.1**. The reaction was followed by FTIR spectroscopy through the disappearance of the band at 2270 cm^{-1} corresponding to the isocyanate stretching frequency (**Fig. 7.3**). During the reaction between **PF2/6-NH_2** and ICPTES takes > 120 h for the isocyanate band to disappear.

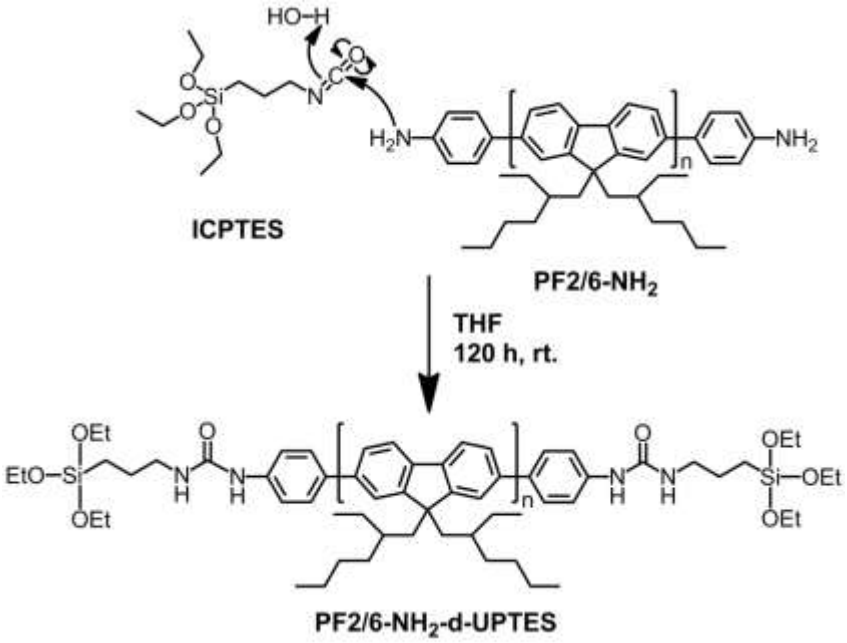

Scheme 7.1. The nucleophilic attack of ICPTES by **PF2/6-NH$_2$**, forming the urea linkages of the precursor solution, **PF2/6-NH$_2$**-d-UPTES.

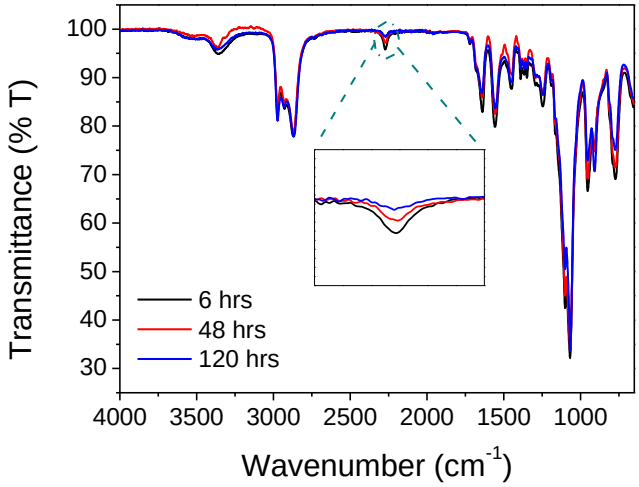

Figure 7.3. FTIR spectra of the **PF2/6-NH$_2$**-d-UPTES reaction mixture at increasing time following initiation of the reaction. The inset shows an expanded region of the spectrum (2200 to 2350 cm^{-1}), highlighting the disappearance of the stretch attributed to the N=C=O group of ICPTES.

7.3.1.1.1 Solution-Phase NMR: Confirmation of PF2/6-NH$_2$-d-UPTES

In order to further examine the chemical binding of **PF2/6-NH$_2$** to ICPTES, solution phase ^{1}H NMR and ^{13}C NMR studies were carried out. However, at the quantities of **PF2/6-NH$_2$** available, the signals in the NMR spectra for all species under investigation at the corresponding concentrations were expected to be extremely low, with the possibility that they would be completely swamped by solvent peaks. Thus, to ascertain the peak positions for the starting materials and that of the d-UPTES product, the initial NMR spectra for the liquid phase starting materials were carried out in the absence of solvent. The ^{13}C NMR of ED-600 and ICPTES are

shown in **Fig. 7.4a** and **b**, respectively. The assignments shown in **Fig. 7.4** were determined using ^{1}H NMR, DEPT 13 and CH COSY spectra (see Appendix, **Fig. A.7.1** and **A.7.2**).

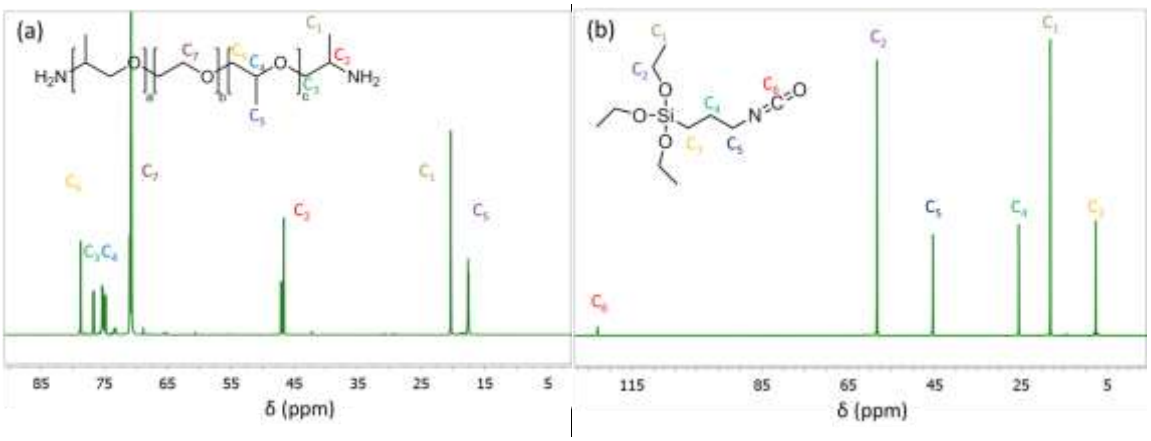

Figure 7.4. ^{13}C NMR spectra for (**a**) ED-600 and (**b**) ICPTES in the absence of solvent at 298 K.

The interaction between these two starting materials to form the precursor solution was followed over the course of the reaction. The assignments for the ^{13}C NMR and ^{1}H NMR for d-UPTES, shown in **Fig. 7.5** were determined with the help of CH COSY spectra (see Appendix **Fig. A.7.3**). The appearance of a peak at ~159 ppm in the ^{13}C spectrum confirms the formation of the carbonyl group of the urea linkages. The ^{1}H NMR spectra for polymeric species, such as d-UPTES (**Fig. 7.5b**), show broader signals than those observed for small molecules.[16] Koldemir *et. al*. have previously shown that the overlap of such signals makes it difficult to accurately determine integration values[17] and as such they are not discussed here. However, a number of subtle changes in the ^{1}H spectrum are observed as the reaction proceeds, particularly to the protons closest to the newly forming urea linkages. The peak associated with protons on C_4 (1.03 ppm) disappears and a new band appears downfield (1.18 ppm). There is also a change at ~2.6 ppm, the band attributed to the protons on C_5 and C_7, which is difficult to see clearly as it is swamped by other proton signals. Finally, two distinct signals appear at 5.4 and 5.7 ppm which are attributed to the NH protons of the urea groups. This confirms the presence of the urea linkages. The occurrence of each of these spectral changes, which develop during the reaction, is shown in **Fig. 7.5b** (t = 10 min -24 h), with the dashed orange lines highlighting the appearance of new signals.

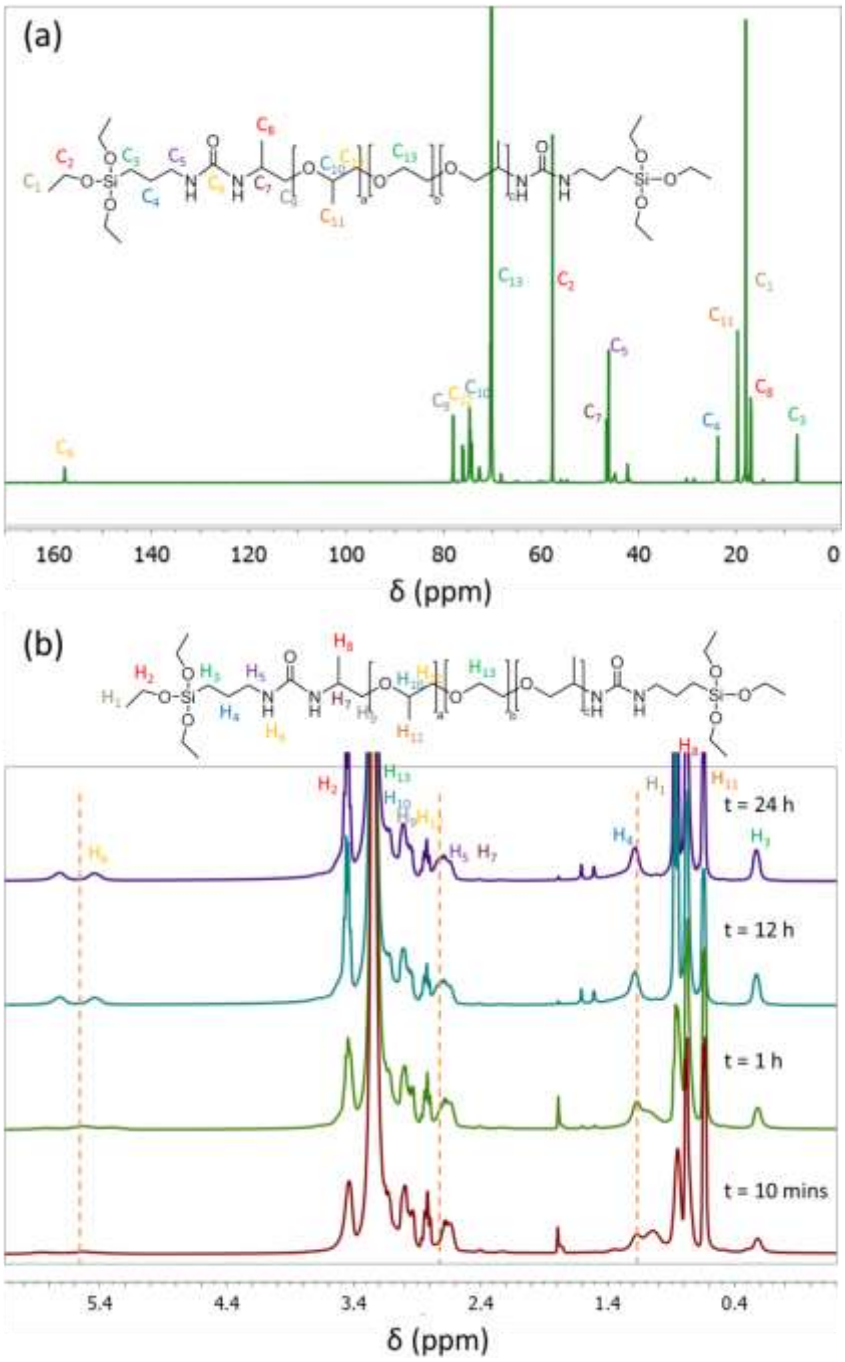

Figure 7.5. (**a**) ^{13}C NMR spectrum for d-UPTES and (**b**) ^{1}H NMR spectrum for the reaction between ED-600 and ICPTES to form d-UPTES over time with no solvent at 298 K. The dashed lines highlight the formation of new signals during the course of the reaction and serve only to guide the eye.

The reaction between **PF2/6-NH$_2$** and excess ICPTES to form **PF2/6-NH$_2$**-d-UPTES was studied *in situ* in d_8-THF (rt., 120 h). As expected the signal intensity was very low; however, the presence of **PF2/6-NH$_2$** is confirmed by the appearance of the aromatic peaks at 141-120 ppm in the ^{13}C NMR spectrum (**Fig. 7.6**).[18] Moreover, while signals attributable to the NH protons of the urea group are too weak to be seen in the ^{1}H NMR spectrum, formation of the carbamide bond is confirmed by the appearance of a signal at 152 ppm in the ^{13}C spectrum, which is assigned to the carbonyl of the urea moiety (**Fig. 7.6**).

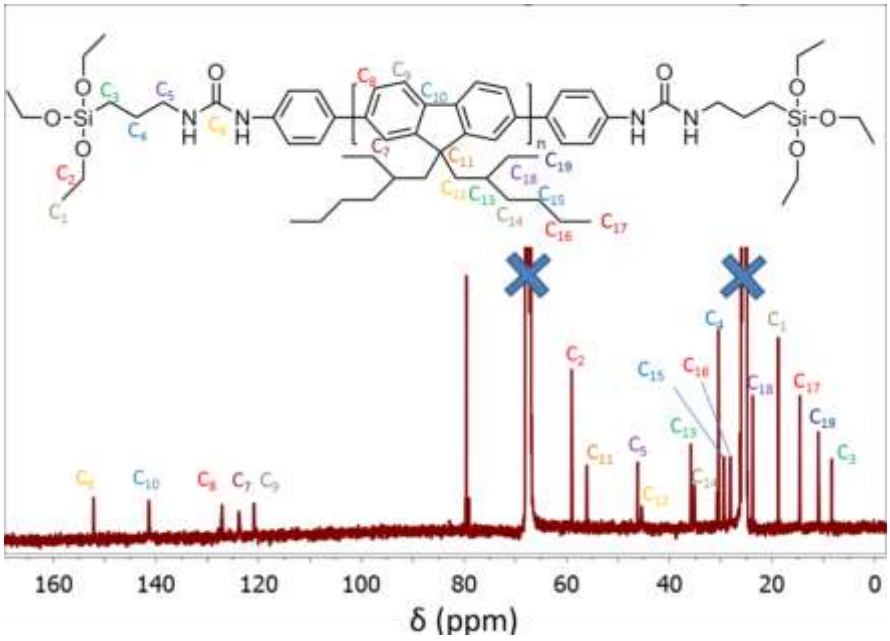

Figure 7.6. ^{13}C NMR spectrum for **PF2/6-NH$_2$**-d-UPTES in d_8-THF at 298 K.

7.3.1.1.2 Solution-Phase NMR: Confirmation of PF2/6-NH$_2$-d-UPTES Mixture with No Chemical Bond between the Two Species

For the *DI* method, ^{13}C NMR spectra were recorded on addition of **PF2/6-NH$_2$** (d_8-THF, 5.2 mM r.u.) to a solution of conventional d-UPTES (d_8-THF, 36 mM) to confirm that this does not create a mixture in which the **PF2/6-NH$_2$** is chemically bound to ICPTES. The ^{13}C spectrum of the initial d-UPTES solution matches that described above (**Fig. 7.5**). Upon addition of **PF2/6-NH$_2$** to the d-UPTES solution, the characteristic aromatic signals of **PF2/6-NH$_2$** are observed (141-120 ppm) (**Fig. 7.7a**). The absence of chemical binding between **PF2/6-NH$_2$** and any unreacted ICPTES is confirmed by the absence of a signal at 152 ppm in the ^{13}C spectrum (**Fig. 7.7b**), which would indicate a urea linkage between the two species.

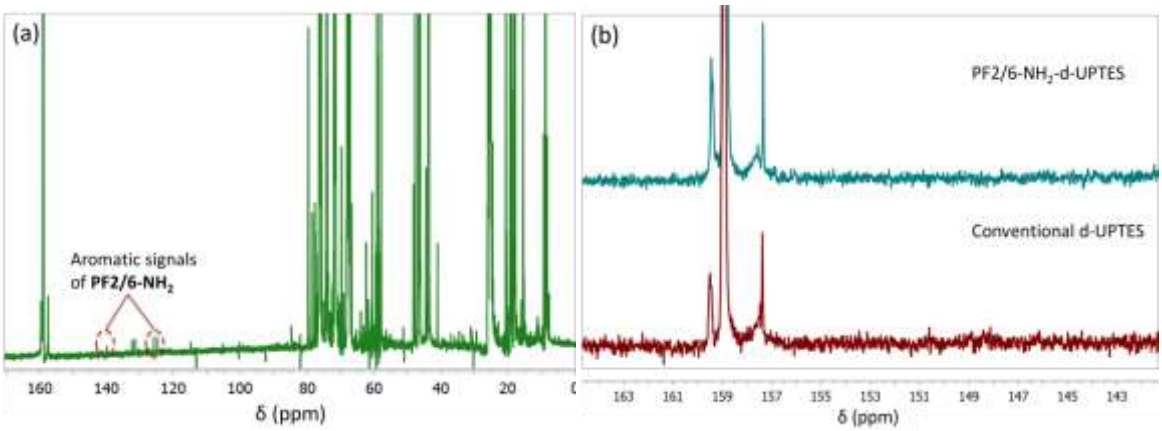

Figure 7.7. (**a**) ^{13}C NMR spectrum for **PF2/6-NH$_2$** mixed with conventional d-UPTES for the *DI* method in d_8-THF at 298 K and (**b**) comparison of the 142-162 ppm region of the ^{13}C NMR spectrum for **PF2/6-NH$_2$**-d-UPTES and a mixture of **PF2/6-NH$_2$** and conventional d-UPTES showing no signal at 152 ppm which would be indicative of a urea linkage to **PF2/6-NH$_2$**.

7.3.2 Physical Characterisation

Once the chemical grafting of **PF2/6-NH_2** to ICPTES to form the di-ureasil precursor was confirmed (*GF* method) or shown not to occur (*DI* method), using the solution phase techniques described above, solid-state monoliths were prepared as described in **Section 7.2.2**. The bulk structural properties of these solid-state samples were then examined as outlined below.

7.3.2.1 Powder X-Ray Diffraction

The PXRD patterns for all samples match those discussed in **Sections 5.3.4.1** and **6.3.2.2** and in the literature.[19-21] The patterns exhibit a primary band centred at 21.0°, with a shoulder at 10.0-15.0° (**Fig. 7.8**). The structural unit distance, *d*, was determined from the main peak at 21.0° to be 4.2 ± 0.1 Å (from Bragg's Law). The shoulder between 10.0° and 15.0° gives rise to a characteristic distance of 3.4 ± 0.5 Å, matching those reported previously for in-plane ordering of additional intra-siloxane domains.[20, 21] The coherent length over which the structural unit survives in the di-ureasil was estimated to be 12.7 ± 1 Å (from the Scherrer equation).[22] This value is similar to that previously reported for di-ureasils prepared *via* carboxylic acid solvolysis.[20] These results suggest that incorporation of the PF *via* either the *DI* method, or through grafting directly to the di-ureasil matrix, does not induce significant structural changes in the di-ureasil host.

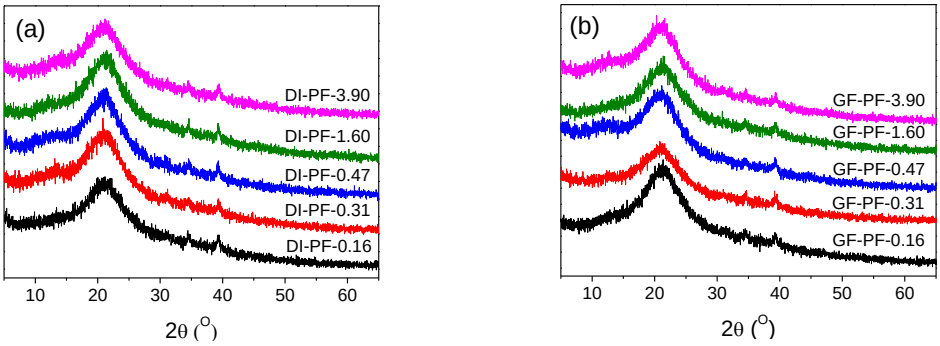

Figure 7.8. Powder X-ray diffraction patterns for (**a**) **DI-PF-0.16**, **DI-PF-0.31**, **DI-PF-0.47**, **DI-PF-1.60** and **DI-PF-3.90** and (**b**) **GF-PF-0.16**, **GF-PF-0.31**, **GF-PF-0.47**, **GF-PF-1.60** and **GF-PF-3.90** in the range 2θ = 5-65º. Artefacts in the powder pattern are observed at 34.5 and 39.4 2θ due to a misalignment in the instrumental setup.

7.3.2.2 Solid-State NMR

The ^{29}Si MAS-NMR spectra of all PF-di-ureasils studied contain three broad signals characteristic of T_1, T_2 and T_3 units (**Fig. 7.9**) at -49.6, –58.3 and –67.4 ppm, respectively. [20, 21] The absence of the T_0 signal confirms that there is no unreacted d-UPTES remaining.[21]

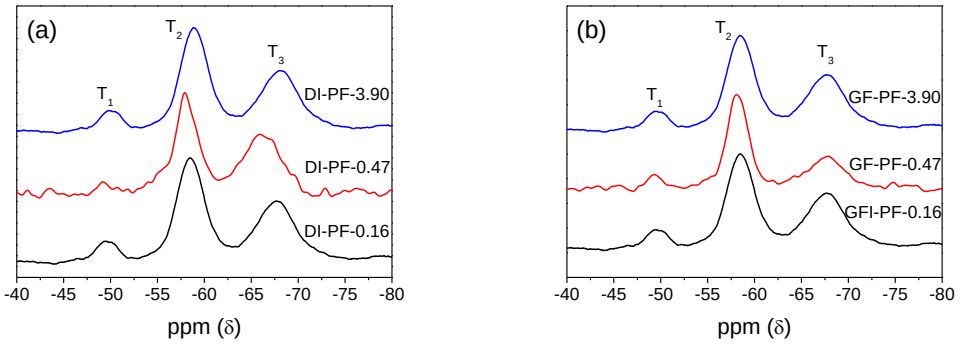

Figure 7.9. ^{29}Si solid-state MAS NMR spectra for (**a**) **DI-PF-0.16**, **DI-PF-0.47** and **DI-PF-3.90** and (**b**) **GF-PF-0.16**, **GF-PF-0.47** and **GF-PF-3.90**.

The degree of condensation, *C*, of the siliceous network was determined as described in **Section 5.3.4.2**, using Gaussian deconvolution of the peaks to determine the relative population of each organosiloxane species, the result of which is presented in **Table 7.2**. The *C* values obtained [76-81%] are in good agreement with those previously observed for poly(fluorene)-di-ureasils (**Section 5.3.4.2**). In contrast, they are slightly higher than those observed in **Section 6.3.2.3**, which is consistent with the lower M_w of **PF2/6-NH$_2$** (16,900 g mol^{-1}) when compared, in particular, to **MEH-PPV** (>100,000 g mol^{-1}). No linear relationship between *C* and wt% of PF incorporated is observed for either incorporation method.

Table 7.2. ^{29}Si MAS NMR chemical shifts (ppm *vs.* TMS), population of different T_n species (%), T_n species ratios, and degree of condensation, *C* (%) of **DI-PF-x** and **GF-PF-x**.

Sample	T_1 (%)	T_2 (%)	T_3 (%)	T_1: T_2: T_3	*C* (%)[a]
d-U(600)	-49.7 (3.4)	-58.6 (55.0)	-67.4 (41.6)	1: 16.1:12.2	79.4
DI-PF-0.16	-49.6 (6.0)	-58.5 (52.2)	-67.6 (41.8)	1: 8.6: 6.9	78.6
DI-PF-0.47	-46.9 (2.9)	-58.1 (50.8)	-66.1 (46.3)	1: 17.7:16.1	81.1
DI-PF-3.90	-49.6 (6.0)	-58.2 (53.0)	-67.5 (41.3)	1: 9.3: 7.3	78.5
GF-PF-0.16	-49.4 (5.7)	-58.5 (53.0)	-67.8 (42.3)	1: 9.3: 7.2	78.5
GF-PF-0.47	-49.4 (4.9)	-58.2 (61.7)	-67.5 (33.4)	1: 12.7: 6.9	76.2
GF-PF-3.90	-49.6 (5.4)	-58.4 (53.7)	-67.8 (40.9)	1: 9.9: 7.6	78.5

The ^{13}C CP/MAS-NMR spectra are in excellent agreement with those previously reported for di-ureasils[20] (**Fig. 7.10**). The assignments for the main peaks are shown in **Table 7.3**. No significant changes in the bands are observed on PF incorporation for either synthetic method, indicating that the di-ureasil structure is not drastically modified upon grafting the PF directly into the siliceous network.

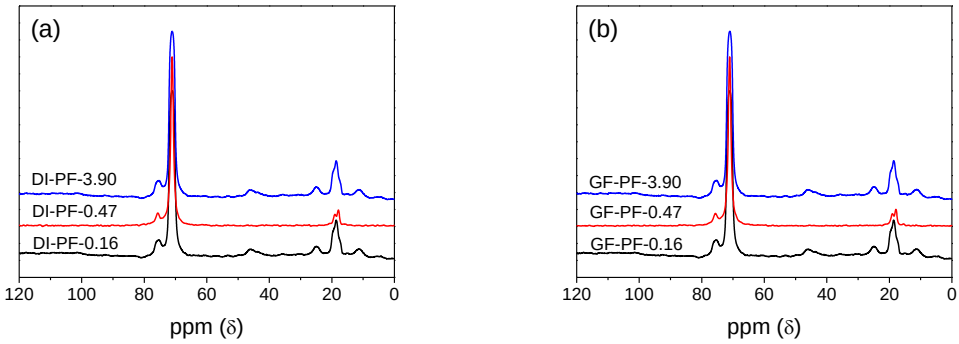

Figure 7.10. ^{13}C solid-state CP/MAS NMR spectra for (**a**) **DI-PF-0.16**, **DI-PF-0.47** and **DI-PF-3.90** and (**b**) **GF-PF-0.16**, **GF-PF-0.47** and **GF-PF-3.90**.

Table 7.3. ^{13}C solid-state CP-MAS NMR chemical shifts (ppm *vs.* TMS) of PF-di-ureasils.

Signal assignment	**d-U(600)**	**DI-PF-0.16**	**DI-PF-0.47**	**DI-PF-3.90**	**GF-PF-0.16**	**GF-PF-0.47**	**GF-PF-3.90**
-OCH	75.7	75.2	75.6	75.7	75.7	75.6	75.7
-(OCH_2CH_2)	71.1	71.3	71.1	71.3	71.3	71.1	70.8
-NCH_2 in $N(CH_2)_3Si$	46.3	46.3	-	46.4	46.4	-	45.9
-'CH_2 in $N(CH_2)_3Si$	24.8	24.9	-	24.9	24.9	-	24.9
-CH_3 in – $OCH_2CH(CH_3)$	19.0	18.5	18.9	19.1	19.1	19.2	18.5
-CH_3 in – $(CH_3CH_2O)_3Si$	17.8	-	17.8	-	-	17.8	-
-CH_2Si in – $N(CH_2)_3Si$	11.4	10.7	-	11.2	11.2	-	11.7

7.3.2.3 Fourier Transform Infrared Spectroscopy

The FTIR spectra for the PF-di-ureasils, **Fig. 7.11**, match those of undoped di-ureasils.[23] Gaussian deconvolution of the Amide I region (1610-1770 cm^{-1}) of the spectra yielded three components at 1712, 1668 and 1637 cm^{-1} (**Fig. 7.11** shows the fit to **DI-PF-0.47** as a representative example). The first two of these bands are ascribed to the vibrations of C=O groups within disordered hydrogen-bonded urea-polyether associations of increasing strength, while the component at 1637 cm^{-1} is attributed to strong self-associated hydrogen-bonded urea-urea associations.[21, 23] There is no noticeable change in the position or contribution of any of these bands as a function of PF concentration (**Table 7.4**) suggesting no significant changes occur in the hydrogen bonding interactions within the di-ureasil upon CP incorporation for either Class I or Class II hybrid materials.

Table 7.4. Results of the curve fitting performed in the 'Amide I' band of **DI-PF-x** and **GF-PF-x** PF-di-ureasils. The peak position, area and % contribution for each component resolved are shown.

Sample	Peak (cm^{-1})	Area (% of total area)	Peak (cm^{-1})	Area (% of total area)	Peak (cm^{-1})	Area (% of total area)
d-U(600)	1714	0.65 (19.1%)	1668	2.06 (60.4%)	1640	0.70 (20.5%)
DI-PF-0.16	1717	0.07 (18.9%)	1672	0.24 (64.9%)	1638	0.06 (16.2%)
DI-PF-0.31	1714	0.12 (12.5%)	1666	0.65 (67.7%)	1637	0.19 (19.8%)
DI-PF-0.47	1713	0.42 (11.5%)	1665	2.44 (67.0%)	1637	0.78 (21.5%)
DI-PF-1.60	1714	0.19 (17.9%)	1668	0.69 (65.1%)	1638	0.18 (17.0%)
DI-PF-3.90	1712	0.14 (19.7%)	1666	0.44 (62.0%)	1636	0.13 (18.3%)
GF-PF-0.16	1717	0.07 (18.9%)	1672	0.24 (64.9%)	1638	0.06 (16.2%)
GF-PF-0.31	1715	0.05 (10.6%)	1672	0.33 (70.2%)	1637	0.09 (19.2%)
GF-PF-0.47	1712	0.11 (21.6%)	1667	0.29 (56.9%)	1638	0.11 (21.5%)
GF-PF-1.60	1714	0.19 (17.9%)	1668	0.69 (65.1%)	1638	0.18 (17.0%)
GF-PF-3.90	1715	0.15 (17.8%)	1667	0.56 (65.9%)	1637	0.14 (16.5%)

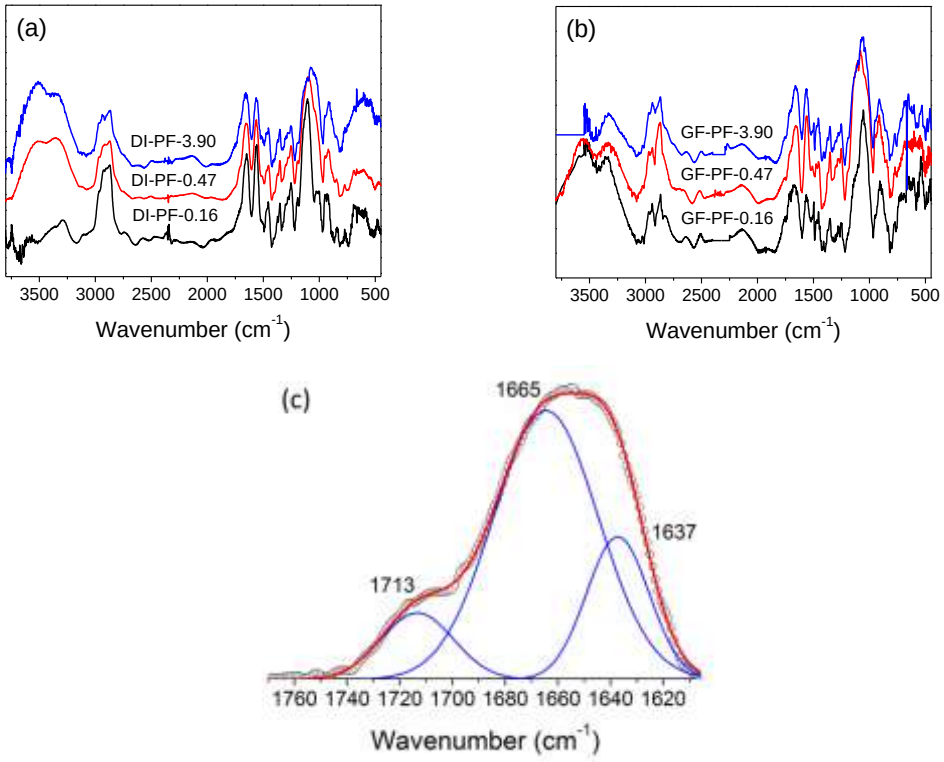

Figure 7.11. FTIR spectra for (**a**) **DI-PF-0.16**, **DI-PF-0.47**, and **DI-PF-3.90** and (**b**) **GF-PF-0.16**, **GF-PF-0.47** and **GF-PF-3.90** over the range 3800-450 cm^{-1} at a resolution of 4 cm^{-1}. (**c**) Results of curve-fitting preformed in the 'Amide I' region of the sample **DI-PF-0.47**. The numbers describe the maxima of the deconvoluted peaks.

7.3.3 Photophysical Characterisation

7.3.3.1 Steady-State UV/Vis Absorption and Photoluminescence Studies

The PL properties of PF are highly dependent on the molecular structure and morphology of the polymer.[24-26] In THF, **PF2/6-NH$_2$** exhibits the characteristic PF absorption and excitation band with a maximum at 380 nm in both spectra. The maximum of the PL band lies at 415 nm with shoulders at 437 and 465 nm corresponding to 0-0, 0-1 and 0-2 vibronic transitions, respectively (**Fig. 7.12**).[24, 27, 28] These optical properties are characteristic of the disordered α-phase exhibited by most PFs in solution.[25, 27]

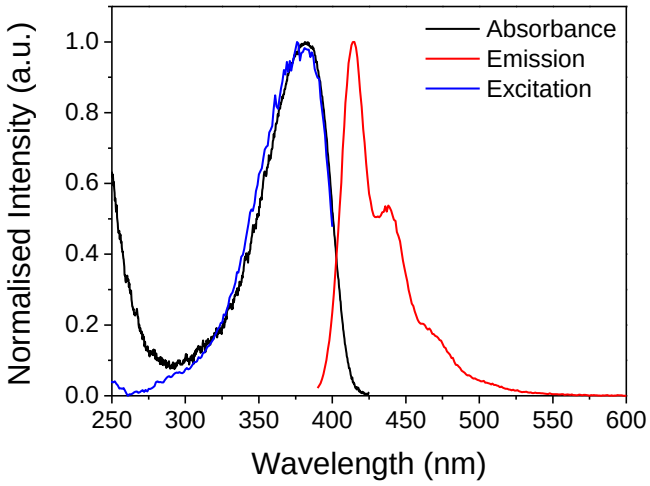

Figure 7.12. UV/Vis absorption (black line), PL (λ_{ex} = 380 nm, red line) and PL excitation (λ_{em} = 415 nm, blue line) spectra for **PF2/6-NH$_2$** in THF (4.3×10^{-3} mM r.u.).

Fig. 7.13 a and **b** show the emission and excitation spectra of **DI-PF-0.16**. On comparison with the solution phase spectra, a moderate red-shift (~5 nm) is observed for all 3 peaks in the PL spectrum (**Fig. 7.13a**) while a shoulder at 400 nm appears in the excitation spectrum (**Fig.7.13b**). On increasing the **PF2/6-NH$_2$** concentration, the relative intensities of the 0-0 and 0-1 vibronic band are inverted and the contribution of the new shoulder in the excitation band increases, (see **Fig. 7.13c** and **d** for **DI-PF-3.90** as a representative example). This behaviour is attributed to increasing self-absorption which has previously been reported for PF2/6 in polyethylene blends[29] and for poly(9,9-di-*n*-octylfluorenyl-2,7-diyl) (PFO) in a sugar derived organogel.[28] A distinct change in the optical properties may also be attributed to the formation of the β-phase. When compared to the disordered α-phase, the β-phase contains more rigid planar, stacked PF segments, giving rise to distinct optical properties. However, previous studies on **PF2/6-NH$_2$** have shown that the bulky side chains prevent the formation of this stacked phase.[30] The lack of β-phase formation is further confirmed for the DI samples through the absence of a new characteristic band centred at 435 nm in the excitation spectra.

Due to the similar nature of the CP backbone of **PF2/6-NH$_2$** to the CPs used in **Chapter 5**, similar optical properties may be expected, with contributions from both the CP and the di-ureasil host. However, contributions from the di-ureasil, identified as a considerable broadening at the high energy portion of the spectrum at lower excitation wavelengths, 320-350 nm (semi-selective for di-ureasil excitation), along with a broadening of the spectrum in the lower energy region, are only observed for the lower concentration samples, (**Fig. 7.13a** for **DI-PF-0.016**). This is most likely due to the much higher PF concentrations used during this work (~10 times higher). As noted in **Section 5.3.5.3** the optical properties of the polymer began to dominate at higher CP concentrations, explaining the dominance of the PF signal here and the smaller contribution from the di-ureasil.

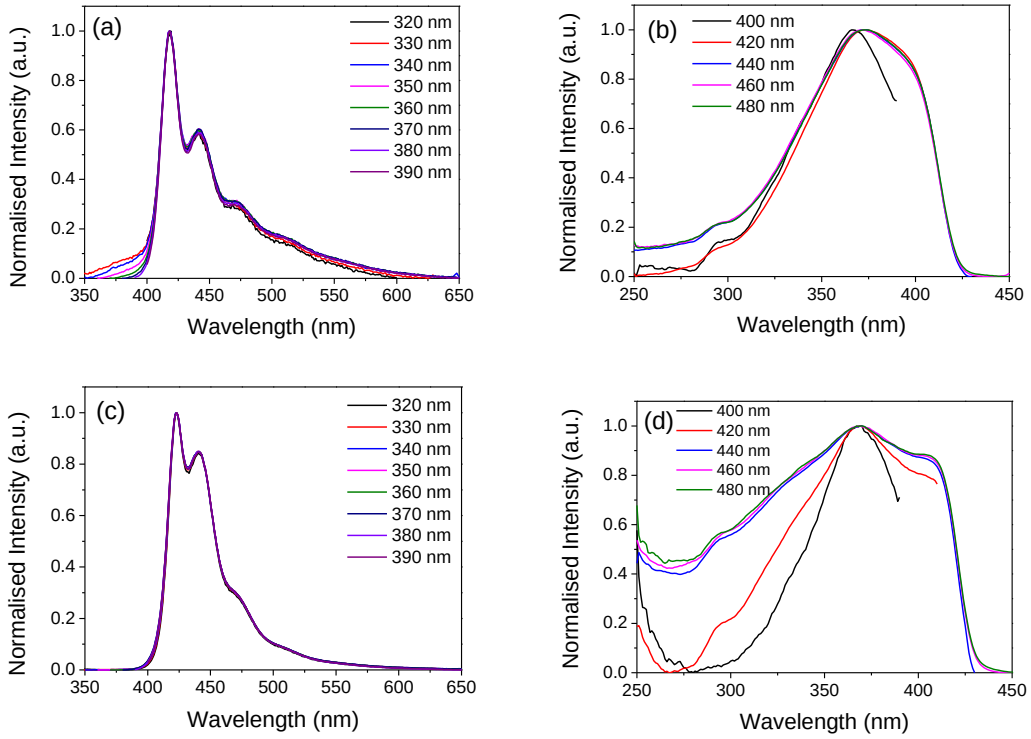

Figure 7.13. (**a**) PL (λ_{ex} = 320, 330, 340, 350, 360, 370, 380 and 390 nm) and (**b**) PL excitation (λ_{em}= 400, 420, 440, 460 and 480 nm) spectra for **DI-PF-0.16** and (**c**) PL (λ_{ex} = 320, 330, 340, 350, 360, 370, 380 and 390 nm) and (**d**) PL excitation (λ_{em}= 400, 4200, 440, 460 and 480 nm) spectra for **DI-PF-3.90**.

The same trends were observed for the samples prepared *via* the *GF* method. The high concentration of the PF also causes its signal to swamp any observable contribution from the di-ureasil in the PL spectrum, as can be seen for **GF-PF-3.90** in **Fig. 7.14**. However, for both sets of samples, **DI-PF-x** and **GF-PF-x**, a slight red shift and broadening is observed in the excitation spectrum with increasing emission wavelength. This is indicative of contribution from the di-ureasil host as discussed previously in **Section 5.3.5.3**.

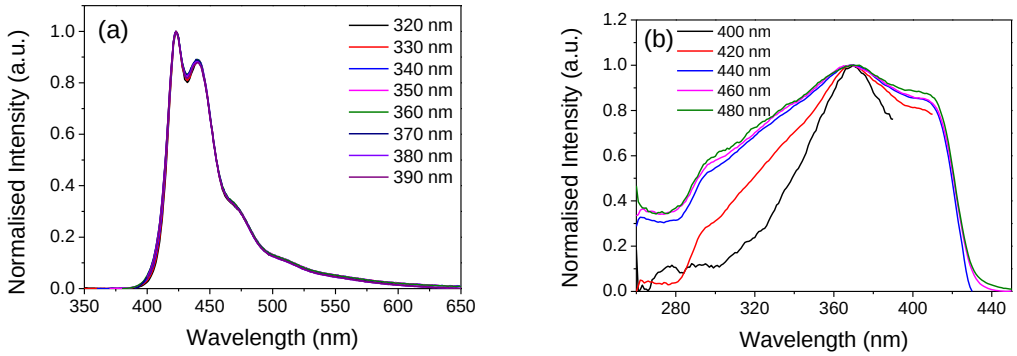

Figure 7.14. (**a**) PL (λ_{ex} = 320, 330, 340, 350, 360, 370, 380 and 390 nm) and (**b**) PL excitation (λ_{em}= 400, 420, 440, 460 and 480 nm) spectra for **GF-PF-3.90**.

7.3.3.2 Photoluminescence Quantum Yield (PLQY)

The PLQY value for **PF2/6-NH$_2$** in THF solution (4.3 × 10^{-3} mM r.u.) was measured as 85.5%, in good agreement with values previously reported in decalin and toluene.[31] On deposition of a thin film of **PF2/6-NH$_2$** (10 mg/ml in THF) on glass the measured PLQY value drops to 19.8%. **Fig. 7.15** shows the PLQY values for samples prepared *via* both preparation methods as a function of increasing PF concentration (wt%). The open symbols represent the measured values; however, as discussed above these samples undergo some self-absorption and the PLQY values corrected for self-absorption (as described in **Section 2.3.3**), are shown as solid symbols. The PLQY for the undoped di-ureasil, **d-U(600)** (3.4%), compares well to that previously reported.[20, 32] Upon incorporation of **PF2/6-NH$_2$** the PLQY increases with increasing concentration for both methods, which can be detected by the naked eye (**Fig. 7.16**). However, this trend appears to plateau at a concentration of 0.16 wt%, yielding a PLQY of 40%.

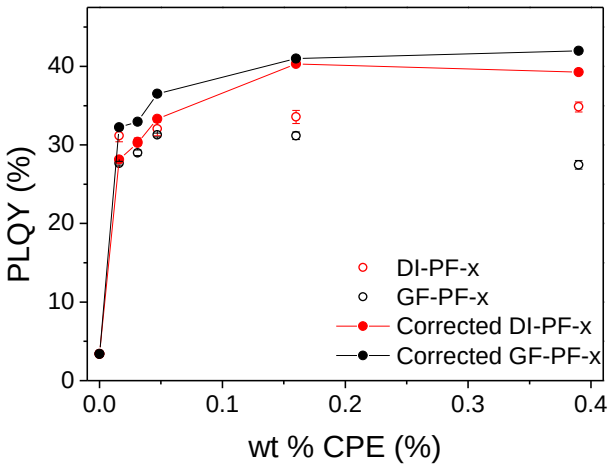

Figure 7.15. Measured PLQY (λ_{ex} = 370 nm) (open symbols) and PLYQ values corrected for re-absorption/re-emission (closed symbols) for **DI-PF-x** (red circles**)** and **GF-PF-x** (black circles). The solid lines serve solely to guide the eye.

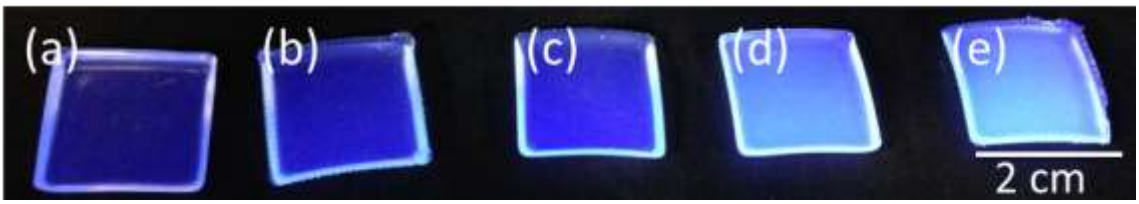

Figure 7.16. Photograph of (**a**) **DI-PF-0.16**, (**b**) **DI-PF-0.31**, (**c**) **DI-PF-0.47**, (**d**) **DI-PF-1.60** and (**e**) **DI-PF-3.90** under UV-illumination (λ_{ex} = 365 nm).

7.3.3.3 Photoluminescence Lifetimes of PF-di-ureasils

In an effort to further examine the mechanism behind the optical properties of the PF-di-ureasil samples, ps-TCSPC experiments were carried out. Decays were measured for the **DI-PF-x** and **GD-PF-x** series, upon excitation at 370 nm and detection at 420 nm and 500 nm, which correspond predominantly to the PF and di-ureasil emission, respectively (**Fig. 7.17**).

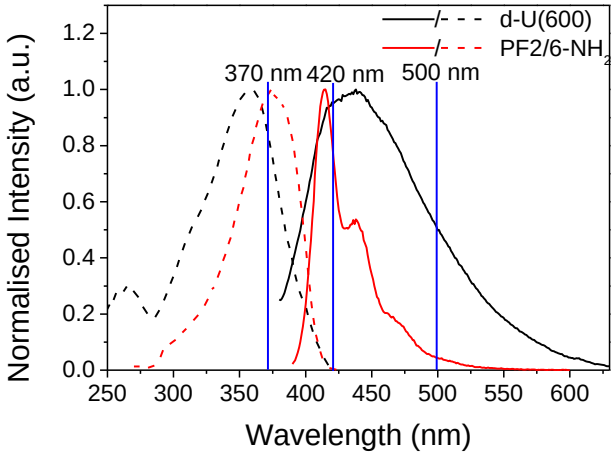

Figure 7.17. Emission and excitation spectra for **d-U(600)** (black, λ_{ex} = 370 nm, λ_{em} = 420 nm) and UV/Vis absorption and emission spectra for **PF2/6-NH$_2$** (red, λ_{ex} = 370 nm in THF). Emission spectra are shown as solid lines and excitation and UV/Vis absorption spectra are shown as dashed lines. The blue lines highlight the excitation (λ_{ex}) and emission (λ_{em}) wavelengths used in the ps-TCSPC experiments.

The solution of **PF2/6-NH$_2$** in THF exhibited a mono-exponential decay, (**Fig. 7.18a**), with a lifetime of 423 ps. This matches that reported by Pina *et. al.* for the same polymer with a similar M_w in toluene.[31] This lifetime is associated with the relaxed structure of the excited chromophoric segments of the polymer.[31, 33] A fast decay component (~40 ps) is also frequently observed in more viscous solvents attributed to contributions from fast conformational relaxation and solvation dynamics,[31, 33] however, this was not observed here. The decay of the undoped **d-U(600)** has previously been discussed in **Section 5.3.5.5** and showed a tri-exponential decay both at 420 and 500 nm. The lifetime values are shown in **Table 5.5**.

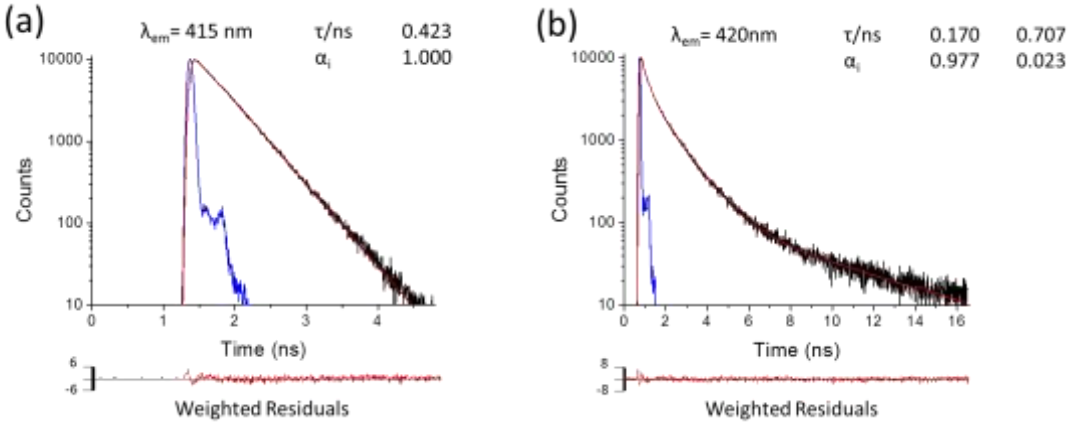

Figure 7.18. PL emission decay curves (solid black lines), and fits (red solid lines) for (**a**) **PF2/6-NH$_2$** in THF (λ_{ex} = 365 nm and λ_{em} = 415 nm) and (**b**) **DI-PF-0.47** (λ_{ex} = 370 nm and λ_{em} = 420 nm). The fitted decay times (τ_i), pre-exponential factors (α_i), fits, weighted residuals and instrument response function (blue line) are also shown.

Addition of **PF2/6-NH$_2$** to the di-ureasil host *via* either method results in a significant decrease in the lifetime measured at λ_{em}= 420 nm (see **Fig. 7.19a** for the **DI-PF-x** series as a representative example). At this emission wavelength the decays for each of the PF-di-ureasil samples were well fitted to the sum of two exponentials. Similar trends in the lifetime values and pre-exponential factors were observed for both the **DI-PF-x** and **GF-PF-x** series. The shorter of the decay components, τ_1, exhibited a lifetime of ~170-200 ps and accounts for >95% of the decay for both sample series. A longer lived component (τ_2) of ~600-800 ps is also observed which contributes the remaining <5% of the decay (**Table 7.5**). Neither of these species resembles the components previously noted for the di-ureasil host (**Table 5.5**) suggesting that they contain contributions primarily from the polymer species. A similar dominance of contributions from the CP at the polymer emission maximum was previously observed in **Chapter 5**. The shortening of the **PF2/6-NH$_2$** lifetime from 423 ps in solution to ~200 ps in the solid-state indicates an increase in PF aggregation. This is supported by the reduced PLQY values in the solid-state di-ureasils compared to the solution phase. There are two possibilities to account for the appearance of the second longer lived component (~600-800 ps). Firstly, the fact that it is just over twice the value of τ_1, corresponding to the major PF lifetime, may suggest that it arises due to emission following self-absorption, as indicated in the PL spectra. Similar lengthening of the acceptor lifetime is often seen in systems based on FRET from metal containing systems in which the acceptor lifetime is increased by the magnitude of the donor lifetime.[33, 34] In the event of self-absorption, the PF acts as both the donor and acceptor and thus the lifetime of the 'acceptor PF' species should be increased by the lifetime of the 'donor PF' species, *i.e.* it should be roughly doubled. However, in the emission spectra the effects of self-absorption increase with increasing PF concentration. Thus, the lifetime contribution from a species emitting following self-absorption may also be expected to increase with PF concentration. This is not observed for either the **DI-PF-x** or **GF-PF–x** series (**Table 7.5**). A second possible explanation for

the longer lived component is that the shortest di-ureasil lifetime, τ_{DU1} ~400 ps, acts as the donor once again to a 'PF acceptor' species. The ~600-800 ps lifetime observed here may have some contribution from the τ_{DU1} component populating the **PF2/6-NH$_2$** exited state. However, due to the strong spectral overlap between the PF and the di-ureasil and the extreme dominance of the PF contribution to both the PL and lifetime results, it is possible that the PF contribution swamps any observable changes arising from self-absorption or contributions from the di-ureasil. Thus, it is extremely difficult to unequivocally assign this longer lifetime component which may in fact arise as a combination of the above scenarios.

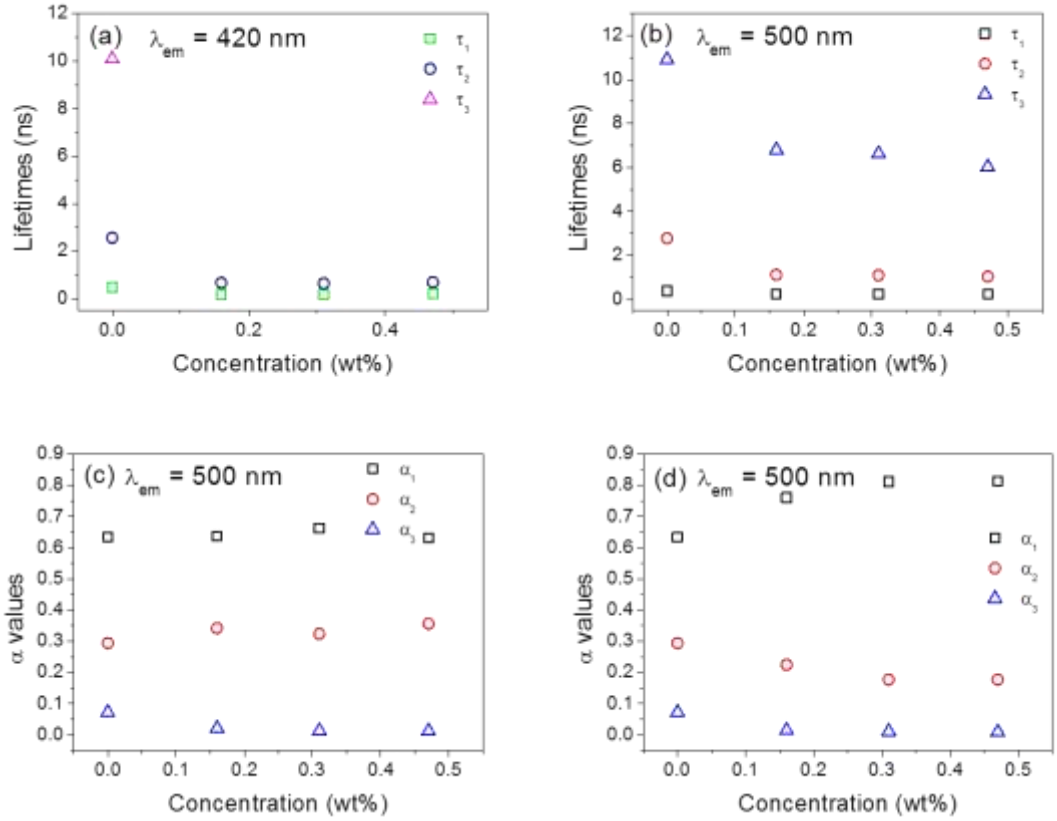

Figure 7.19. Emission lifetimes (τ_i) determined from di- and tri-exponential fits to the fluorescence decays measured for the **DI-PF-x** series at (**a**) λ_{ex} = 370 nm and λ_{em} = 420 nm (PF emission) and (**b**) λ_{ex} = 370 nm and λ_{em} = 500 nm (di-ureasil emission). Pre-exponential values (α_i) determined from tri-exponential fits to the fluorescence decays measured for the (**c**) **DI-PF-x** and (**d**) **GF-PF-x** series at λ_{ex} = 370 nm and λ_{em} = 500 nm (di-ureasil emission).

The decay curves measured at 500 nm for both series required tri-exponential fits, similar to that of the undoped **d-U(600)**. On incorporation of **PF2/6-NH$_2$** the longest lived component of the **d-U(600)** decay decreased from 11.22 ns to 5.56 ns in **DI-PF-0.47** (**Fig. 7.19b**) and to 6.03 ns for **GF-PF-0.47** (**Table 7.6**). The two shorter components at ~250 ps and 1.1 ns are also slightly reduced when compared with **d-U(600)b,** but remain unchanged with increasing PF concentration. The contribution for all three of the components remains reasonably constant for the **DI-PF-x** series. While for the **GF-PF-x** series, the contribution of the shortest component increases at the expense of the two longer components (**Fig. 7.19d**). The decrease in the di-ureasil lifetime with increasing PF concentration, identical to

that observed in **Chapters 5** and **6**, is evidence of energy transfer from the di-ureasil host to **PF2/6-NH$_2$**. Similar to the findings in **Chapter 5**, the increase in PLQY noted for the PF in the di-ureasil, compared to that of a pure PF thin film, may be attributed to this observed energy transfer. The magnitude of the increase in PLQY observed here is less than that measured in **Chapter 5**. This is most likely due to the higher concentration of CP dopant, which leads to self-absorption. This is mirrored by the smaller decrease in di-ureasil lifetime, thus indicating reduced energy transfer between the di-ureasil and **PF2/6-NH$_2$**. The large decrease in τ_3 with increasing PF concentration indicates the involvement of the NH species of the di-ureasil in the energy transfer process. It should be noted that the decrease in τ_3 is larger in the case of the **DI-PF-x** series when compared to the **GF-PF-x** series, suggesting more efficient energy transfer in the former sample set. The differing magnitude of energy transfer between the two series potentially suggests differing location of the PF species for both sets of samples with the PF potentially sitting further into the organic domains in the case of the **DI-PF-x** series, allowing it a greater interaction with the NH species undergoing photoinduced proton transfer. It is also possible that grafting of the PF directly to the matrix restricts possible motion and subsequent interaction with such components partaking in photoinduced proton transfer.

7.3.4 Thermal and Photostability

The thermogram for the **d-U(600)** sample is in excellent agreement with that previously reported[36, 37] with the onset of sample decomposition observed at ~339 °C (**Fig. 7.20**). Incorporation of **PF2/6-NH$_2$** *via* either method yields a material with good thermal stability with the onset of thermal decomposition occurring between 340-354 °C. This thermal stability is extremely similar to the PF containing CPE-di-ureasils discussed in **Section 5.3.4.4**, considerably surpassing the moderate operating temperatures (~65-140 °C[38, 39]) present in most organic electronic devices.

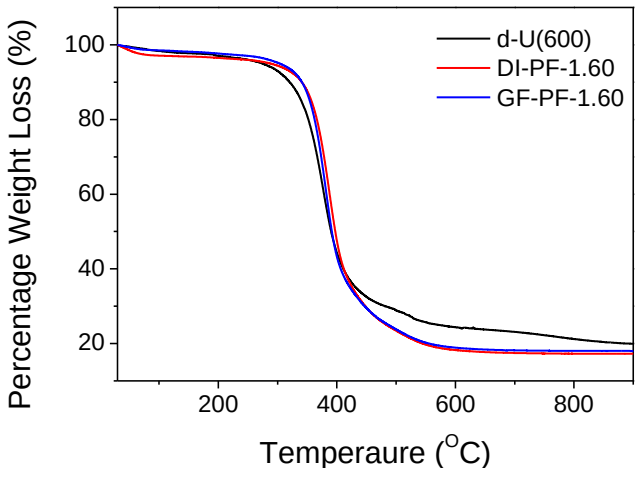

Figure. 7.20. TGA thermograms of **d-U(600)** (black line), **DI-PF-1.60** (red line) and **GF-PF-1.60** (blue line). TGA measurements were performed in air at a heating rate of 10 °C min^{-1}.

Table 7.5. PL lifetimes (τ_i), pre-exponential coefficients (α_i), fractional contribution (f_i) and chi squared (χ^2) values obtained from fitting of the photoluminescence decays (λ_{ex} = 370 nm) of **DI-PF-x** and **GF-PF-x** at λ_{em} = 420 nm.

Sample	τ_1 **(ns)**	τ_2 **(ns)**	α_1	α_2	f_1	f_2	χ^2
PF2/6-NH_2	0.42 ± 0.01		1.00 ± 0.01		1.00 ± 0.01		1.03
DI-PF-0.16	0.15 ± 0.01	0.80 ± 0.02	0.97 ± 0.01	0.03 ± 0.01	0.87 ± 0.02	0.13 ± 0.01	1.69
DI-PF-0.31	0.19 ± 0.01	0.64 ± 0.01	0.97 ± 0.01	0.03 ± 0.01	0.91 ± 0.01	0.09 ± 0.01	1.12
DI-PF-0.47	0.17 ± 0.01	0.71 ± 0.02	0.98 ± 0.01	0.02 ± 0.01	0.91 ± 0.01	0.09 ± 0.01	1.12
GF-PF-0.16	0.18 ± 0.01	0.66 ± 0.01	0.95 ± 0.01	0.05 ± 0.01	0.83 ± 0.01	0.17 ± 0.01	1.26
GF-PF-0.31	0.17 ± 0.01	0.64 ± 0.01	0.96 ± 0.01	0.04 ± 0.01	0.86± 0.01	0.14 ± 0.01	1.18
GF-PF-0.47	0.21 ± 0.01	0.68 ± 0.01	0.97 ± 0.01	0.03 ± 0.01	0.87 ± 0.01	0.13 ± 0.01	0.91

Table 7.6. PL lifetimes (τ_i), pre-exponential coefficients (α_i), fractional contribution (f_i) and chi squared (χ^2) values obtained from fitting of the photoluminescence decays (λ_{ex} = 370 nm) of **DI-PF-x** and **GF-PF-x** at λ_{em} = 500 nm.

Sample	τ_1 **(ns)**	τ_2 **(ns)**	τ_3 **(ns)**	α_1	α_2	α_3	f_1	f_2	f_3	χ^2
DI-PF-0.16	0.21 ± 0.01	1.07 ± 0.02	5.88 ± 0.18	0.64 ± 0.03	0.34 ± 0.01	0.02 ± 0.01	0.21 ± 0.01	0.59 ± 0.02	0.20 ± 0.01	1.10
DI-PF-0.31	0.25 ± 0.01	1.12 ± 0.01	5.72 ± 0.14	0.66 ± 0.02	0.33 ± 0.01	0.01 ± 0.01	0.27 ± 0.01	0.60 ± 0.01	0.13 ± 0.01	1.28
DI-PF-0.47	0.24 ± 0.01	1.11 ± 0.01	5.56 ± 0.13	0.63 ± 0.02	0.36 ± 0.01	0.01 ± 0.01	0.25 ± 0.01	0.64 ± 0.01	0.11 ± 0.01	1.16
GF-PF-0.16	0.24 ± 0.01	1.12 ± 0.01	6.80 ± 0.14	0.76 ± 0.02	0.23 ± 0.01	0.01 ± 0.01	0.34 ± 0.01	0.48 ± 0.01	0.18 ± 0.01	1.23
GF-PF-0.31	0.24 ± 0.01	1.11 ± 0.02	6.62 ± 0.17	0.81 ± 0.02	0.18 ± 0.01	0.01 ± 0.01	0.42 ± 0.01	0.42 ± 0.01	0.16 ± 0.01	1.44
GF-PF-0.47	0.25 ± 0.01	1.05 ± 0.01	6.03 ± 0.16	0.81 ± 0.02	0.18 ± 0.01	0.01 ± 0.01	0.46 ± 0.01	0.42 ± 0.01	0.13 ± 0.01	1.26

The photostability of the PF-di-ureasils was also investigated. Irradiation of a pure **PF2/6-NH$_2$** film over time, at a constant excitation wavelength of 370 nm, results in the growth of a second emission band (**Fig. 7.21**) centred at 550 nm. This is characteristic of the formation of fluorenone defects on the polyfluorene chains.[40-42]

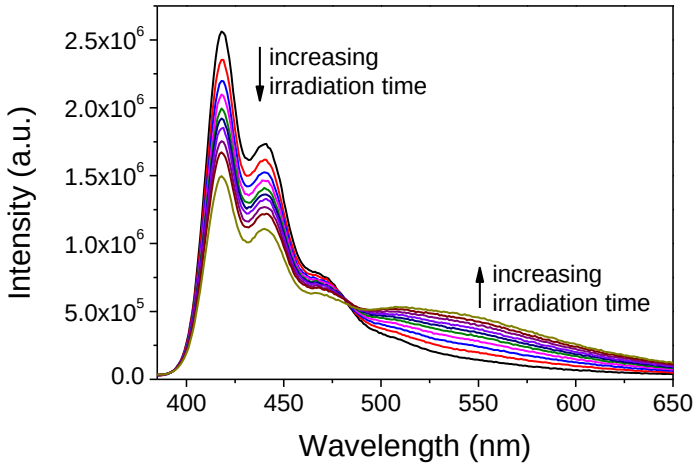

Figure. 7.21. PL spectra (λ_{ex} = 370 nm) of a film of pure **PF2/6-NH$_2$**.as a function of increasing irradiation time (t = 0, 10, 20, 30, 40, 50, 60 ,75, 90 and 180 min).

Thus to examine purely the poly(fluorene) contribution to the emission, the integrated intensity for all samples was measured in the range 385-460 nm. **Fig. 7.22a** shows this integrated emission intensity for **DI-PF-0.16**, **GF-PF-0.16** and a pure **PF2/6-NH$_2$** film as a function of irradiation time. The integrated intensity of the **PF2/6-NH$_2$** film dropped steadily to ~60% of the initial value over the irradiation period (2 h). Both **DI-PF-0.16** and **GF-PF-0.16** exhibit improved stability when compared to **PF2/6-NH$_2$** retaining ~75% of the initial intensity at the end of the study. Throughout the investigation, **GI-PF-0.16** display a slightly higher integrated intensity when compared to its *DI* counterpart, suggesting that chemically grafting the PF to the di-ureasil matrix offers improved stability. In addition to offering improved photostability when considering emission in the blue spectral region, both incorporation methods show a much greater resistance to formation of the green fluorenone defect emission band. **Fig. 7.22b** shows the emission intensity at 550 nm normalised to the initial sample intensity as a function of irradiation time. Following encapsulation of the PF within the di-ureasil *via* either method the growth of a fluorenone emission band at 550 nm is not observed, unlike the results obtained for the pure **PF2/6-NH$_2$** film. The fluorenone species are a degradation product formed through oxidative interactions between the polymer in its excited state and oxygen in the atmosphere to form superoxide radicals which further degrade the polymer.[41, 43, 44] The presence of these defects has been shown to be supressed in nitrogen or vacuum.[41] Hence it is possible that blending of **PF2/6-NH$_2$** with the di-ureasil host may reduce its interaction with ambient oxygen, thus preventing the formation of the fluorenone

species. This is a substantial advantage over pure **PF2/6-NH$_2$** films as the growth of the ketone emission band seriously degrades colour purity of the film.

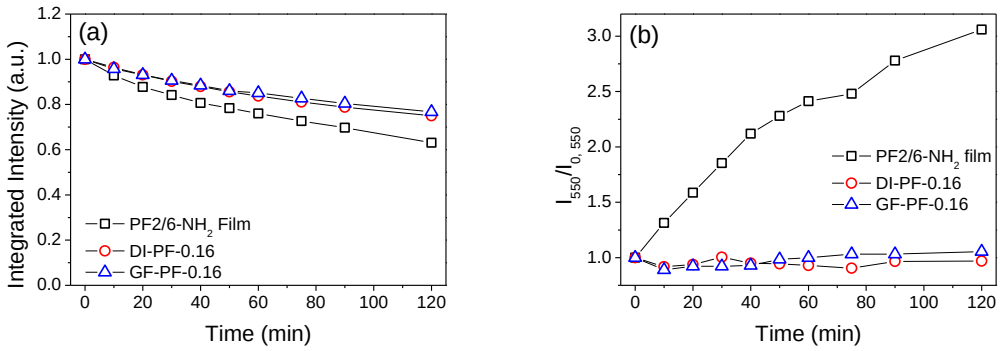

Figure 7.22. (**a**) Integrated emission intensity of a pure **PF2/6-NH$_2$** thin film on glass (open black squares), **DI-PF-0.16** (open red circles) and **GF-PF-0.16** (open blue triangles) under irradiation at 370 nm. (**b**) Emission intensity at 550 nm normalised to the initial emission intensity at 550 nm, $I_{0,550}$, under irradiation at 370 nm. The black lines serve only to guide the eye.

7.4 Conclusions

PF-di-ureasils were successfully prepared *via* two different methods; *Direct Insertion* and *Grafting*. Both methods utilise the same sol-gel process to create the final elastomeric monolith, however, the methods differ in whether the PF is covalently bound to the final di-ureasil network or not. ^{13}C and ^{1}H NMR studies were carried out to confirm the presence of a chemical bond between **PF2/6-NH$_2$** and the di-ureasil host. Through a combination of XRD, ss-NMR and FTIR, the incorporation of the CPs *via* either method was found to have no adverse effect on the bulk structural properties of the di-ureasil. Despite the different structures provided by the two methods, both sample series retain the structural and mechanical properties of the organic-inorganic hybrid host.

Investigation of the photophysical characteristics of the PF-di-ureasils indicated that the PF provides the major contribution to the optical properties. A small contribution from the di-ureasil host was observed at the lowest concentration in the PL spectra, while a broadening and a small red shift in the excitation spectra also indicate a contribution from the di-ureasil host. On incorporation of PF within the di-ureasil a red shift in the emission peak position was observed, while on increasing the PF concentration the relative intensities of the 0-0 and 0-1 vibronic band become inverted, indicating increasing self-absorption. Similar trends in the optical properties were observed for both methods, most likely due to the fact that the high concentration of **PF2/6-NH$_2$** and subsequent self-absorbance masks any possible subtle differences between the two methods. The PLQY values for the PF-di-ureasils were found to increase with increasing **PF2/6-NH$_2$** concentration and plateau at 40% at 0.16 wt%. The values for each of the PF-di-ureasils were at least 10% higher than that found for a thin film of the pure polymer (20%). This is attributed to

energy transfer between the di-ureasil and the PF species, which was indicated by ps-TCSPC measurement through a decrease in the di-ureasil lifetime at 500 nm. The magnitude of this energy transfer was found to be greater for the **DI-PF-x** series. This may suggest that the PF sits further into the organic domains of the di-ureasil allowing it a greater interaction with the NH species undergoing photoinduced proton transfer. Such an increase in interaction may also be attributed to the greater freedom of the PF in the **DI-PF-x** series which is unbound to the di-ureasil matrix.

Along with increased PLQY in the solid state, the PF-di-ureasils also exhibit excellent thermal properties remaining stable up to temperatures of 340-351 °C. These samples also showed increased photostability when compared to a thin film of pure **PF2/6-NH$_2$**. Once encapsulated within the di-ureasil, the PF shows resistance to ketone defect formation and the concomitant green emission band which causes a degradation of colour purity in PF-based devices.

Although the organic-inorganic interface between the CP and the di-ureasil network differs between the two preparation methods discussed here, there is very little difference in the optical or bulk structural properties. This suggests that the dopant concentration is too low to noticeably affect the bulk structural properties. On the other hand, it is high enough to cause self-absorption of the polymer species in both sets of samples which possibly masks any differences in the optical properties. This would seem to suggest that there is little advantage to using the more synthetically complex *Grafting* method. However, covalently binding a perylene bisimide species to a siloxane network has recently been shown to increase the conductivity through the organic-inorganic hybrid material.[45] Moreover, directing the placement of conjugated polymers within a silica matrix through surfactant templating has been shown to control the emission and diode behaviour of the devices prepared.[46] Thus, it is possible that the **GF-PF-x** samples may yet show improved conductivity and LED performance. Further investigations into device preparation are currently underway.

7.5 References

1. C. Sanchez, F. Ribot and B. Lebeau, *J. Mater. Chem.*, 1999, **9**, 35–44.
2. C. Sanchez, P. Belleville, M. Popall and L. Nicole, *Chem. Soc. Rev.*, 2011, **40**, 696–753.
3. P. Judeinstein and C. Sanchez, *J. Mater. Chem.*, 1996, **6**, 511-525.
4. D. A. Loy and K. J. Shea, *Chem. Rev.*, 1995, **95**, 1431-1442.
5. K. J. Shea and D. A. Loy, *Acc. Chem. Res.*, 2001, **34**, 707-716.
6. R. Xu, S. M. Ibrahim, M. Kanezashi, T. Yoshioka, K. Ito, J. Ohshita and T. Tsuru, *ACS Appl. Mater. Interfaces*, 2014, **6**, 9357-9364.
7. J. P. Randall, M. A. Meador and S. C. Jana, *ACS Appl. Mater. Interfaces*, 2011, **3**, 613-626.
8. L. Zhao, M. Vaupel, D. A. Loy and K. J. Shea, *Chem. Mater.*, 2008, **20**, 1870–1876.
9. H. Nam, B. Boury and S. Y. Park, *Chem. Mater.*, 2006, **18**, 5716-5721.
10. Z. Ren, D. Sun, H. Li, Q. Fu, D. Ma, J. Zhang and S. Yan, *Chem. Eur. J.*, 2012, **18**, 4115-4123.

11. D. Sun, Q. Fu, Z. Ren, W. Li, H. Li, D. Ma and S. Yan, *J. Mater. Chem. C*, 2013, **1**, 5344-5350.
12. I. Imae, D. Tokita, Y. Ooyama, K. Komaguchi, J. Ohshita and Y. Harima, *J. Mater. Chem.*, 2012, **22**, 16407-16415.
13. J. M. Behrendt, A. B. Foster, M. C. McCairn, H. Willcock, R. K. O'Reilly and M. L. Turner, *J. Mater. Chem. C*, 2013, **1**, 3297–3304.
14. U. Asawapirom, R. Güntner, M. Forster and U. Scherf, *Thin Solid Films*, 2005, **477**, 48-52.
15. R. Guntner, U. Asawapirom, M. Forster, C. Schmit, B. Stiller, B. Tiersch, A. Falcou, N.-H. Nothofer and U. Scherf, *Thin Solid Films*, 2002, **417**, 1-6.
16. P. L. Rinaldi, in *NMR Spectroscopy of Polymers: Innovative Strategies for Complex Macromolecules*, Oxford University Press, Inc., 2011, p.37-63.
17. U. Koldemir, S. R. Puniredd, M. Wagner, S. Tongay, T. D. McCarley, G. D. Kamenov, K. Müllen, W. Pisula and J. R. Reynolds, *Macrolmolecules*, 2015, **48**, 6369−6377.
18. L. L. G. Justino, M. L. Ramos, P. E. Abreu, R. A. Carvalho, A. J. F. N. Sobral, U. Scherf and H. D. Burrows, *J. Phys. Chem. B*, 2009, **113**, 11808-11821.
19. L. D. Carlos, V. de Zea Bermudez, R. A. S. Ferreira, L. Marques and M. Assunção, *Chem. Mater.*, 1999, **11**, 581-588.
20. L. Fu, R. A. S. Ferreira, N. J. O. Silva, L. D. Carlos, V. de Zea Bermudez and J. Rocha, *Chem. Mater.*, 2004, **16**, 1507-1516.
21. P. P. Lima, R. A. S. Ferreira, S. A. Júnior, O. L. Malta and L. D. Carlos, *J. Photochem. Photobiol. A*, 2009, **201**, 214-221.
22. Scherrer equation: $L = 0.94\lambda/(A\cos\theta)$, where A (in radians) is the full-width-half-maximum of the Bragg peak. See A. Guinier, X-ray Diffraction in Crystals, Imperfect Crystals and Amorphous Bodies, Dover, New York 1994.
23. V. de Zea Bermudez, L. D. Carlos and L. Alcácer, *Chem. Mater.*, 1999, **11**, 569-580.
24. E. Da Como, E. Scheler, P. Strohriegl, J. M. Lupton and J. Feldmann, *Appl. Phys. A*, 2008, **95**, 61-66.
25. A. Monkman, C. Rothe, S. King and F. Dias, *Adv. Polym. Sci.*, 2008, **212**, 187-225.
26. U. Scherf and E. J. W. List, *Adv. Mater.*, 2002, **14**, 477-487.
27. R. C. Evans and P. C. Marr, *Chem. Commun.*, 2012, **48**, 3742-3744.
28. P. C. Marr, K. McBride and R. C. Evans, *Chem. Commun.*, 2013, **49**, 6155-6157.
29. M. Knaapila, H. L. Vaughan, T. P. A. Hase, R. C. Evans, R. Stepanyan, M. Torkkeli, H. D. Burrows, U. Scherf and A. P. Monkman, *Macromolecules*, 2010, **43**, 299-305.
30. M. Knaapila, V. M. Garamus, F. B. Dias, L. Almasy, F. Galbrecht, A. Charas, J. Morgado, H. D. Burrows, U. Scherf and A. P. Monkman, *Macromolecules*, 2006, **39**, 6505-6512.
31. J. Pina, J. S. S. de Melo, N. Koenen and U. Scherf, *J. Phys. Chem. B*, 2013, **117**, 7370-7380.
32. L. D. Carlos, R. A. S. Ferreira, V. de Zea Bermudez and R. S. J. L., *Adv. Funct. Mater.*, 2001, **11**, 111-115.
33. J. R. Lakowicz, *Principles of Fluorescence Spectroscopy*, Springer, 2006, p. 965-967.
34. C. Casanova, D. Giaume, T. Gacoin, J.-P. Biolot and A. Alexandrou, *J. Phys. Chem. B*, 2006, **110**, 19264-19270.
35. F. B. Dias, A. L. Macanita, J. S. de Melo, H. D. Burrows, R. Guntner, U. Scherf and A. P. Monkman, *J. Chem. Phys.*, 2003, **118**, 7119-7126.
36. M. Fernandes, V. de Zea Bermudez, R. A. S. Ferreira, L. D. Carlos and N. V. Martins, *J. Lumin.*, 2008, **128**, 205-212.
37. M. E. Mesquita, S. S. Nobre, M. Fernandes, R. A. S. Ferreira, S. C. G. Santos, M. O. Rodrigues, L. D. Carlos and V. d. Z. Bermudez, *J. Photochem. Photobiol. A*, 2009, **205**, 156-160.
38. D. E. Loy, B. E. Koene and M. Thompson, *Adv. Funct. Mater.*, 2002, **12**, 245-249.
39. I. T. Sachs-Quintana, T. Heumüller, W. R. Mateker, D. E. Orozco, R. Cheacharoen, S. Sweetnam, C. J. Brabec and M. D. McGehee, *Adv. Funct. Mater.*, 2014, **24**, 3978-3985.
40. K. L. Chan, M. Sims, S. I. Pascu, M. Ariu, A. B. Holmes and D. D. C. Bradley, *Adv. Funct. Mater.*, 2009, **19**, 2147–2154.
41. M. Kuik, G. A. H. Wetzelaer, J. G. Ladd´e, H. T. Nicolai, J. Wildeman, J. Sweelssen and P. W. M. Blom, *Adv. Funct. Mater.*, 2011, **21**, 4502–4509.

42. X. H. Yang, F. Jaiser, D. Neher, P. V. Lawson, J. Brédas, E. Zojer, R. Güntner, P. S. de Freitas, M. Forster and U. Scherf, *Adv. Funct. Mater.*, 2004, **14**, 1097–1104.
43. E. T. Hoke, I. T. Sachs-Quintana, M. T. Lloyd , I. Kauvar, W. R. Mateker, A. M. Nardes, C. H. Peters, N. Kopidakis and M. D. McGehee, *Adv. Energy Mater.*, 2012, **2**, 1351–1357.
44. H. Santos Silva, A. Tournebize, D. Bégué, H. Peisert, T. Chassé, J.-L. Gardette, S. Therias, A. Rivatonde and R. C. Hiorns, *RSC Adv.*, 2014, **4**, 54919–54923.
45. N. Mizoshita, T. Tani and S. Inagaki, *Adv. Funct. Mater.*, 2011, **21**, 3291-3296.
46. E. Dovgolevsky, S. Kirmayer, E. Lakin, Y. Yang, C. J. Brinkerb and G. L. Frey, *J. Mater. Chem.*, 2008, **18**, 423–436.

Chapter Eight

Conclusions and Outlook

This thesis explored the optical properties of a number of conjugated polymers and polyelectrolytes with a focus towards the development of optical sensors and light-emitting materials.

In **Chapter 3** an optical sensing platform was developed through mapping of the optical response of the diblock copolymer **PF2/6-*b*-P3TMAHT** as a function of increasing concentration of the biologically important anions **GTP**, **GDP**, **GMP**, **ATP** and **CTP**. The response in the UV/Vis absorbance and emission spectra indicated a specific interaction with the polythiophene block which is dependent on the charge and nature of the anion. The mechanism behind the quenching was subsequently investigated and found to be a complex interplay of different processes. The proposed mechanism involves electrostatic binding of the nucleotide to the PT block of **PF2/6-*b*-P3TMAHT** *via* the phosphate groups. Following this, a non-fluorescent species is formed through electron transfer from the nucleobase to the PT block which is mediated by a charge transfer state. The order of fluorescence quenching of the polythiophene block follows the oxidation potentials of the nucleobases for the triphosphate series, while the order of quenching for the guanosine series (**GTP**>**GDP**>**GMP**) is rationalised by the fact that an increased number of phosphate groups should lead to stronger interactions with the charged PT block, bringing the nucleotide and polymer into closer contact. These results highlight both the sensitivity and selectivity of the optical response of **PF2/6-*b*-P3TMAHT** to various nucleotides, characteristics which are vital for the development of any type of sensing platform.

Investigation of the fluorescence behaviour of this system has suggested that the observed response arises due to a micelle-like model in which quenching is brought about by analytes held in the Stern layer of the charged micelle. Future work on this project aims to use SANS to investigate the structure of **PF2/6-*b*-P3TMAHT** in solution in the presence of increasing concentration of each of the anions in an attempt to add to the knowledge of the structure-property relationship for this CPE. Furthermore, due to the fact that this interaction appears to be mediated through electrostatic interactions, it is possible that this sensing platform may be extended to other negatively-charged biological species, such as a number of amino acids and proteins. It is also possible that the larger dimensions of such protein species may induce a greater change in the CPE aggregate structure, affecting FRET between the two blocks, thus amplifying any observed response.

In **Chapter 4** the formation of poly-*pseudo*-rotaxanes by the threading of a number cucurbit[*n*]urils onto the backbone of a positively charged CP, **PPyV**, was successfully demonstrated. Threading of the **CB[n]**s onto the CP backbone caused an enhancement in the fluorescence intensity of the CP. A ‘Goldilocks-like’ situation was observed due to the increasing cavity size of the macrocycles. **CB[6]** is a little too small to easily thread the CP backbone and thus takes some time to thread it to a reasonable extent. **CB[8]** is a little too big, it threads easily but is

too large to effectively interact with the CP backbone and de-threads again, while **CB[7]** is just the right size to thread onto the **PPyV** backbone and to have sufficient dipole-dipole interactions with the positively charged backbone to be held in place. The size of the **CB[n]** cavity was further exploited to develop a sensing system for electron-rich analytes based on the principles of size exclusion. The presence of the electron-rich analyte indole brought about quenching of the fluorescence of **PPyV** in the order **CB[8]**>**CB[7]**>**CB[6]**, attributed to the ability of the **CB[n]** rings to incorporate both the analyte and the **PPyV** backbone. This sensing system may be transferred to the solid-state as the PL intensity of thin films of **CB[n]-PPyV** were also found to be quenched by the presence of indole vapour. This sensing system is a rare example of an electron deficient polymer developed for sensing of electron-rich analytes. Further work on this project will involve further optimisation of the stoppering mechanism to create fully fledged polyrotaxanes and of the method of thin film deposition to create a more robust sensing scheme. The future aims of this project are to investigate the possibility that the size of the **CB[n]** cavities offers the possibility of selective discrimination of electron-rich analytes from a complex mixture.

The second portion of this work focused on incorporation of CPs and CPEs into a di-ureasil host matrix in an effort to enhance the thermal and photochemical stability of the polymers and to exploit the resulting optical properties to develop light-emitting materials.

In **Chapter 5** CPEs were successfully incorporated into di-ureasils *via* two different methods; *Direct Insertion* and *Solvent Permeation*. Confocal microscopy showed that the *DI* method led to a homogeneous distribution of CPE domains throughout the entire di-ureasil host, while the *SP* method yields a confined layer of CPE at the di-ureasil surface. Through a combination of XRD, ss-NMR and FTIR, the incorporation of the CPEs was found to have no adverse effect on the structural properties of the di-ureasil. Examination of the photophysical characteristics of the CPE-di-ureasils indicates that both CPE and di-ureasil components contribute to the photoluminescence properties which gives rise to a dramatic enhancement of the PLQY. This is in part due to effective prevention of aggregation of CPE chains through weak physical interactions with the di-ureasil matrix, which are more favourable for **PBS-PFP** than **HTMA-PFP**. Steady-state PL and TCSPC measurements also indicated that cooperative electronic interactions between the two components are important.

In **Chapter 6** CP-di-ureasils were successfully prepared with two red-emitting CPs *via* the *Direct Insertion* method introduced during the previous chapter. These CPs were chosen in an attempt to extend the emission further across the spectrum from the blue emission of the di-ureasils. The samples displayed a tunable emission colour caused by incomplete energy transfer between the host and guest. Through a combination of XRD, ss-NMR and FTIR, the incorporation of the CPs was found to have no adverse effect on the structural properties of the di-ureasil, despite the larger molecular weight of **MEH-PPV**. Furthermore, P3T- and MEH-di-ureasils exhibited

significantly superior thermal and photostability in comparison to the parent conjugated polymers, providing a route to light-emitting materials with an extended shelf-life.

Investigation of the photophysical characteristics of the CP-di-ureasils indicates that both CP and di-ureasil components contribute to the photoluminescence properties. Although large spectral overlap integrals are calculated for the di-ureasil host with both **MEH-PPV** and **P3TMAHT**, incomplete energy transfer from the di-ureasil host to the CP dopant results in emission from both species on direct excitation of the di-ureasil matrix. The contribution from each of these species can be modulated through judicious selection of the CP concentration or excitation wavelength. Although both CPs absorb to some extent at the wavelengths used to directly excite the di-ureasil, TCSPC experiments indicated that energy transfer occurs from the di-ureasil to the CP. CIE chromaticity diagrams show that the subsequent emission colour is tunable from the blue to the yellow spectral region, along a trajectory that passes through white.

In **Chapter 7** the incorporation of a polyfluorene, **PF2/6-NH$_2$**, into a di-ureasil matrix was successfully prepared *via* two different methods; *Direct Insertion* and *Grafting*. The methods differ in whether the PF is covalently bound to the final di-ureasil network or not, with **PF2/6-NH$_2$** directly bound to the di-ureasil host matrix in the *Grafting* method. Through a combination of XRD, ss-NMR and FTIR, the incorporation of the CPs *via* either method was found to have no adverse effect on the bulk structural properties of the di-ureasil. Despite the different structures provided by the two methods, both sample series retain the structural and mechanical properties of the organic-inorganic hybrid host.

Investigation of the photophysical characteristics of the PF-di-ureasils indicated that the PF provides the major contribution to the optical properties, while increasing the **PF2/6-NH$_2$** concentration showed evidence of increasing self-absorbance. It is most likely that this masks any possible subtle differences between the two incorporation methods. Both sets of samples showed increased PLQY values and increased photostability when compared to a thin film of pure **PF2/6-NH$_2$**. Once encapsulated within the di-ureasil, the PF showed resistance to ketone defect formation and the concomitant green emission band which causes a degradation of colour purity in PF-based devices.

There is very little difference in the optical or bulk structural properties between the *DI* and *GF* methods, despite the fact that the organic-inorganic interface between the CP and the di-ureasil network differs between the two preparation methods. This would seem to suggest that there is limited advantage to using the more synthetically challenging *Grafting* method. However, recent reports in the literature have shown that covalently binding the optically active perylene bisimide species to a siloxane network shows an increase in the conductivity through the organic-inorganic hybrid material.[1] Furthermore, directing the placement of conjugated polymers within a

silica matrix through surfactant templating has been shown to control the emission and diode behaviour of the devices prepared.[2] Thus, it is possible that the **GF-PF-x** samples may yet show improved conductivity and LED performance. Further investigations into device preparation are currently underway.

The power of the approach presented in this section of the thesis lies in both its simplicity and versatility. Incorporation within a di-ureasil host has showed improved thermal and photostability for each of the CP/CPEs investigated when compared to in their pure thin film formats which are used currently in PLED devices. The doped di-ureasils discussed in **Chapters 5-7** can also be cast from solution as single layer thin films. The di-ureasil host may protect the incorporated CP from modification from the deposition of further layers in a multi-layered PLED device architecture, in a similar manner to the post-deposition cross-linking or 'hard-baking' methods currently suggested in the literature. The electronic coupling between the CPE and the di-ureasil observed in **Chapter 5** suggests that CPE-di-ureasils also offer a wealth of potential applications from composite photovoltaics, to luminescent solar concentrators and optical sensors. **Chapter 6** highlights the fact that through rational selection of the constituents, it is possible to tailor the optical properties (*e.g.* emission colour or energy transfer) for a targeted application, such as white-light emission. Furthermore, a wide variety of Jeffamine® precursors are commercially available, which makes tuning of the mechanical properties possible. While the confinement of the CPE within a specific region of an active layer offers the potential to reduce the complexity of multi-layer device architectures and may yield improved device performance. However, while a variety of applications are possible, the immediate future goal of this project is to capitalise on the stability and versatility of the above materials to investigate LED device preparation using each of the doped di-ureasil preparation methods discussed.

8.1 References

1. N. Mizoshita, T. Tani and S. Inagaki, *Adv. Funct. Mater.*, 2011, **21**, 3291-3296.
2. E. Dovgolevsky, S. Kirmayer, E. Lakin, Y. Yang, C. J. Brinkerb and G. L. Frey, *J. Mater. Chem.*, 2008, **18**, 423–436.

Appendix

Table of Contents

Chapter 3

Chapter 5

Chapter 6

Chapter 7

1.1 Chapter 3

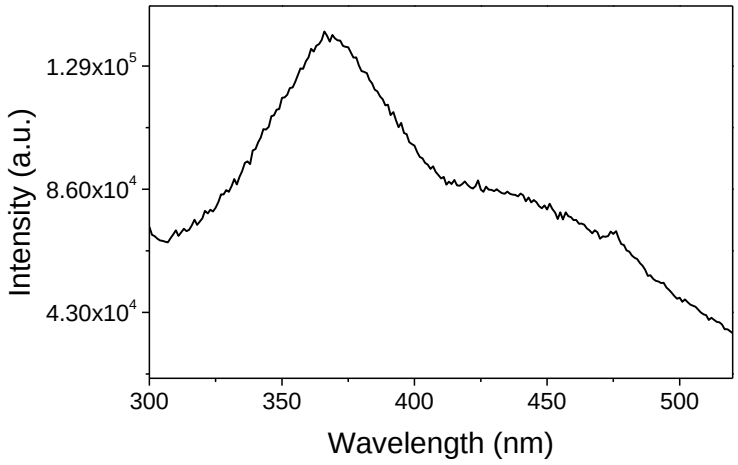

Figure A.3.1. PL excitation (λ_{em} = 570 nm) spectrum for **PF2/6-*b*-P3TMAHT** in aqueous solution (1.06×10^{-6} M).

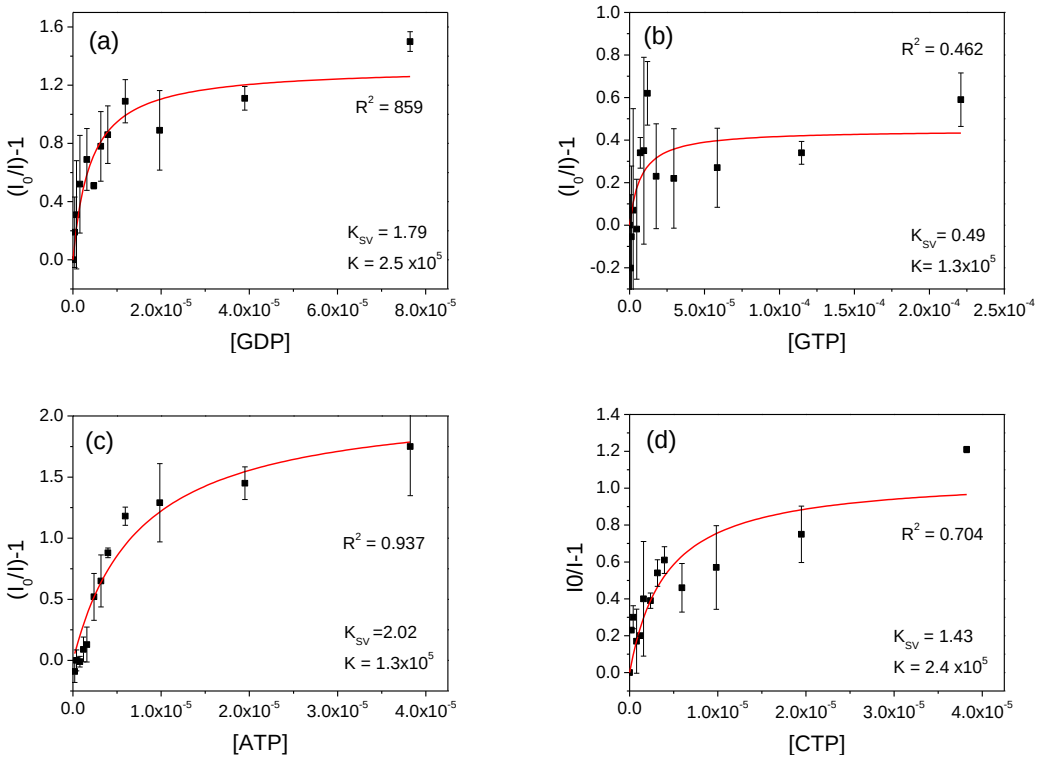

Figure A.3.2. Fit to a multi-equilibrium model (**Eqn. 3.20**) of modified Stern-Volmer plot for fluorescence quenching of **PF2/6-*b*-P3TMAHT** (λ_{ex} = 380 nm) by (**a**) **GDP** (**b**) **GMP** (**c**) **ATP** and (**d**) **CTP**.

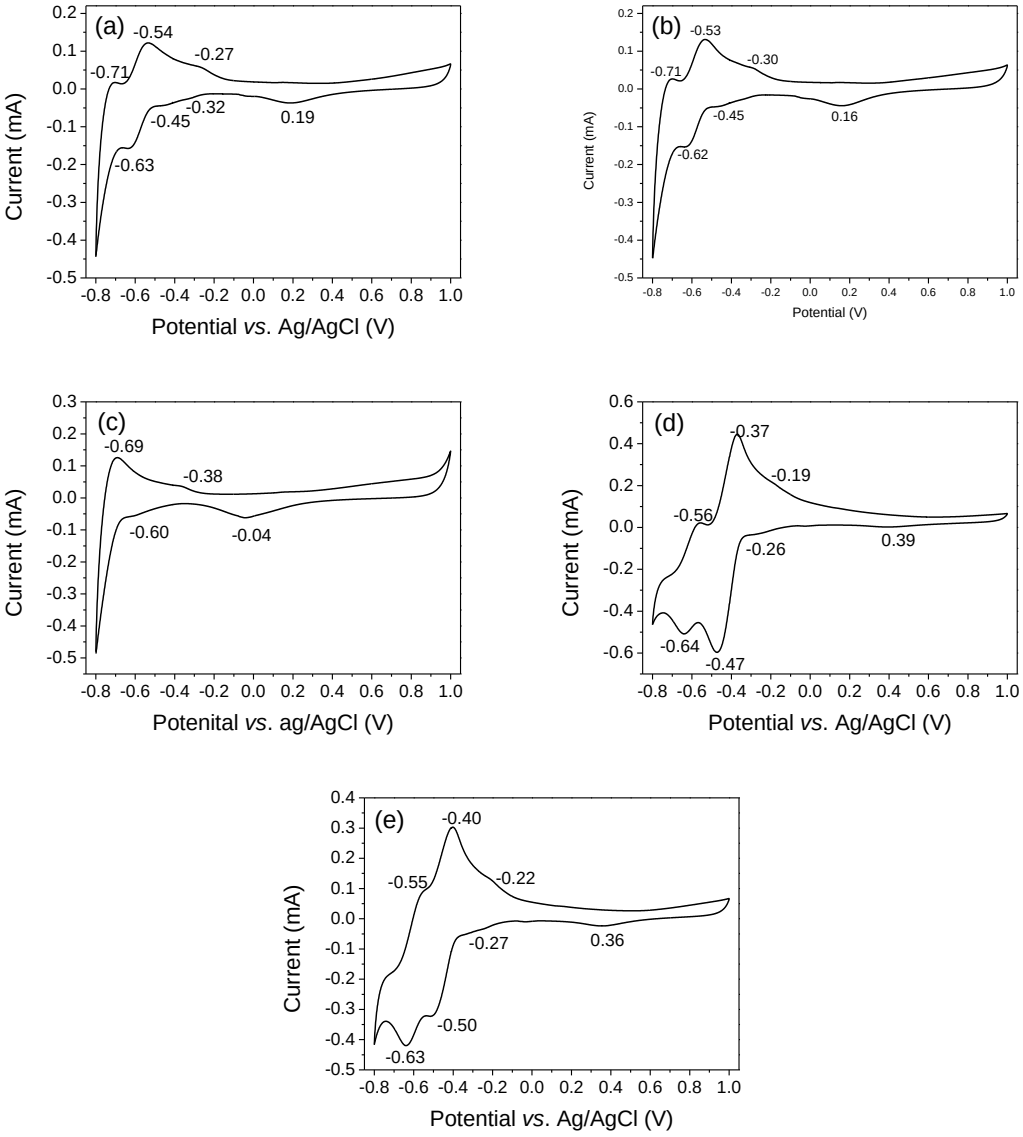

Figure A.3.3. Cyclic voltammogram in H_2O at 50 mV s^{-1} using Pt as the working and counter electrode, Ag/AgCl as reference electrode and KCl (0.1 M) as the supporting electrolyte for (**a**) **GTP**, (**b**) **GDP**, (**c**) **GMP**, (**d**) **ATP** and (**e**) **CTP**.

1.2 Chapter 5

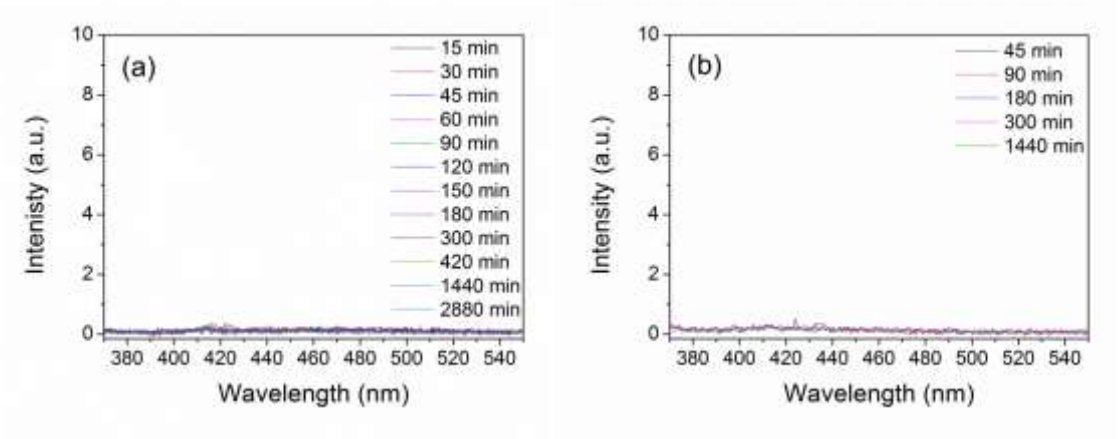

Figure A.5.1. Photoluminescence spectra of the immersion solutions following sample removal after different immersion times for (**a**) **DI-HTMA-4.0** in MeCN/H_2O (25:75% *v/v*) (λ_{ex} = 360 nm) (**b**) **SP-PBS-3.4** in 1,4-dioxane/H_2O (25:75% *v/v*) (λ_{ex} = 360 nm).

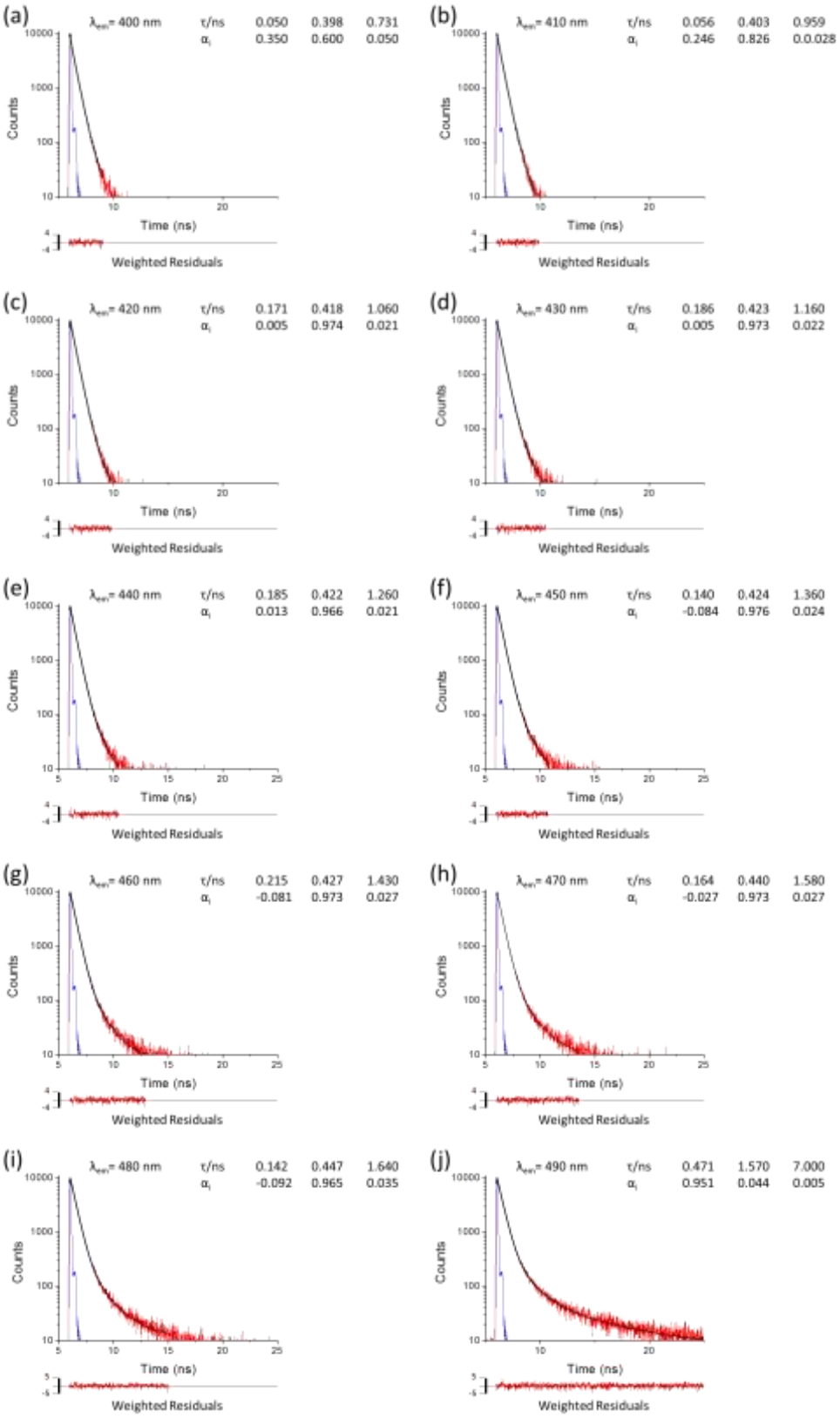

Figure A.5.2. PL emission decay curves (solid red lines) and fits (solid black lines) for **DI-PBS-1.0** as a function of emission wavelength (a) λ_{em}= 400 nm, (b) λ_{em}= 410 nm, (c) λ_{em}= 420 nm, (d) λ_{em}= 430 nm, (e) λ_{em}= 440 nm, (f) λ_{em}= 450 nm, (g) λ_{em}= 460 nm, (h) λ_{em}= 470 nm, (i) λ_{em}= 480 nm and (j) λ_{em}= 490 nm. The fitted decay times (τ_i), pre-exponentials (α_i), fits, weighted residuals and instrument response function (solid blue line) are also shown.

Table A.5.1. Decay times (τ_i), pre-exponential coefficients (α_i), fractional contribution (f_i) and chi squared (χ^2) values resulting from individual fits of the photoluminescence decays (λ_{ex}= 365 nm) of **PBS-DI-1.0** at different emission wavelengths (λ_{em} = 400 – 500 nm).

λ_{em} (nm)	τ_1 (ns)	τ_2 (ns)	τ_3 (ns)	τ_4 (ns)	α_1	α_2	α_3	α_4	f_1	f_2	f_3	f_4	χ^2
400	0.05 ±0.01	0.40 ±0.01	0.73 ±0.25		0.35 ±0.01	0.60 ±0.01	0.05 ±0.01		0.06 ±0.01	0.82 ±0.04	0.13 ±0.04		1.13
410	0.06 ±0.01	0.40 ±0.01	0.96 ±0.08		0.15 ±0.01	0.83 ±0.01	0.03 ±0.01		0.02 ±0.01	0.90 ±0.02	0.07 ±0.01		1.15
420	0.17 ±0.01	0.42 ±0.01	1.06 ±0.05		0.01 ±0.01	0.97 ±0.01	0.02 ±0.01		0.01 ±0.01	0.95 ±0.01	0.05 ±0.01		1.13
430	0.19 ±0.01	0.42 ±0.01	1.16 ±0.13		0.01 ±0.01	0.97 ±0.01	0.02 ±0.01		0.01 ±0.01	0.94 ±0.03	0.06 ±0.01		1.22
440	0.19 ±0.01	0.42 ±0.01	1.26 ±0.15		0.01 ±0.01	0.97 ±0.01	0.02 ±0.01		0.01 ±0.01	0.93 ±0.03	0.06 ±0.01		1.18
450	0.14 ±0.04	0.42 ±0.01	1.36 ±0.03		-0.08 ±0.01	0.98 ±0.01	0.02 ±0.01		-0.03 ±0.01	0.95 ±0.01	0.08 ±0.01		1.01
460	0.22 ±0.06	0.43 ±0.01	1.43 ±0.06		-0.08 ±0.01	0.97 ±0.01	0.03 ±0.01		-0.04 ±0.01	0.95 ±0.02	0.09 ±0.01		1.12
470	0.16 ±0.09	0.44 ±0.01	1.58 ±0.03		-0.03 ±0.01	0.97 ±0.01	0.03 ±0.01		-0.01 ±0.01	0.92 ±0.01	0.09 ±0.01		1.05
480	0.14 ±0.03	0.45 ±0.01	1.64 ±0.04		-0.09 ±0.01	0.97 ±0.01	0.04 ±0.01		-0.03 ±0.01	0.91 ±0.01	0.12 ±0.01		1.10
490		0.47 ±0.01	1.57 ±0.02	7.00 ±0.64		0.95 ±0.01	0.04 ±0.01	0.01 ±0.01		0.81 ±0.01	0.13 ±0.02	0.06 ±0.01	1.05
500		0.48 ±0.01	1.59 ±0.07	8.09 ±0.79		0.93 ±0.01	0.07 ±0.01	0.01 ±0.01		0.74 ±0.01	0.17 ±0.01	0.09 ±0.09	1.08

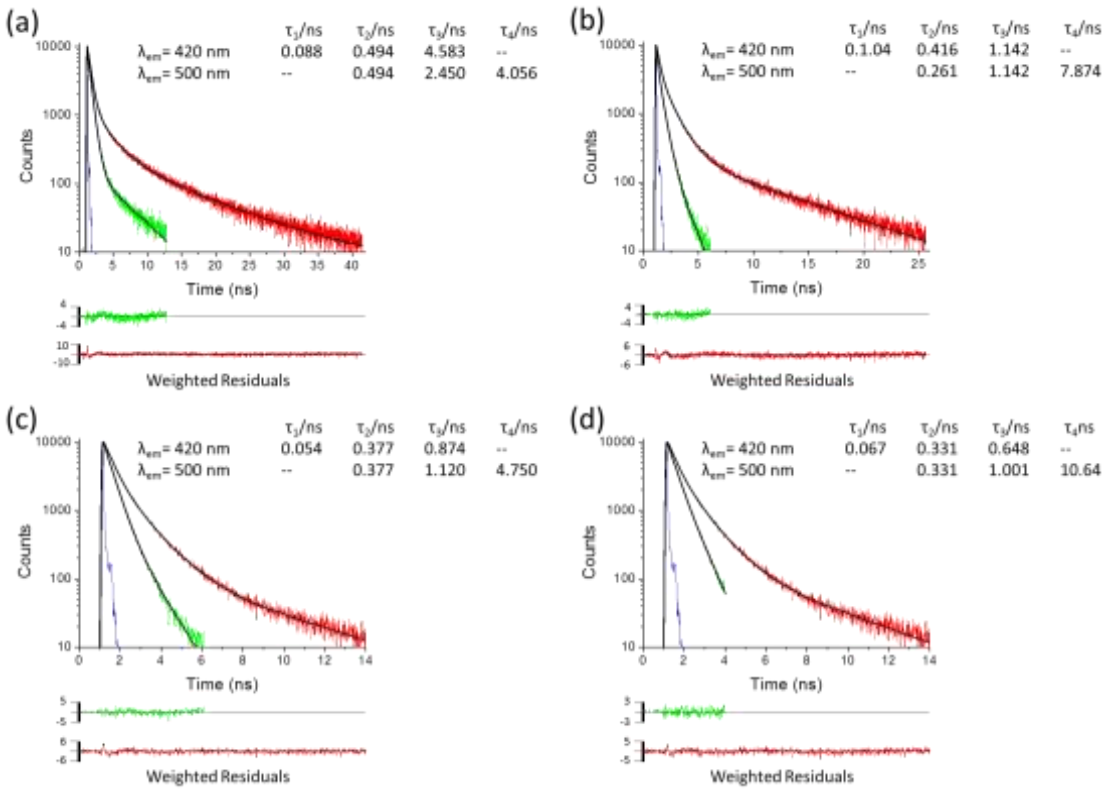

Figure A.5.3. PL emission decay curves (solid green lines - λ_{em}=420 nm, solid red lines - λ_{em}=500 nm) and fits (solid black lines) for (**a**) **DI-HTMA-1.0**, (**b**) **DI-HTMA-2.0**, (**c**) **DI-HTMA-4.0** and (**d**) **DI-HTMA-8.0**. The fitted decay times (τ_i), pre-exponential values (α_i), fits, weighted residuals and instrument response function (solid blue line) are also shown.

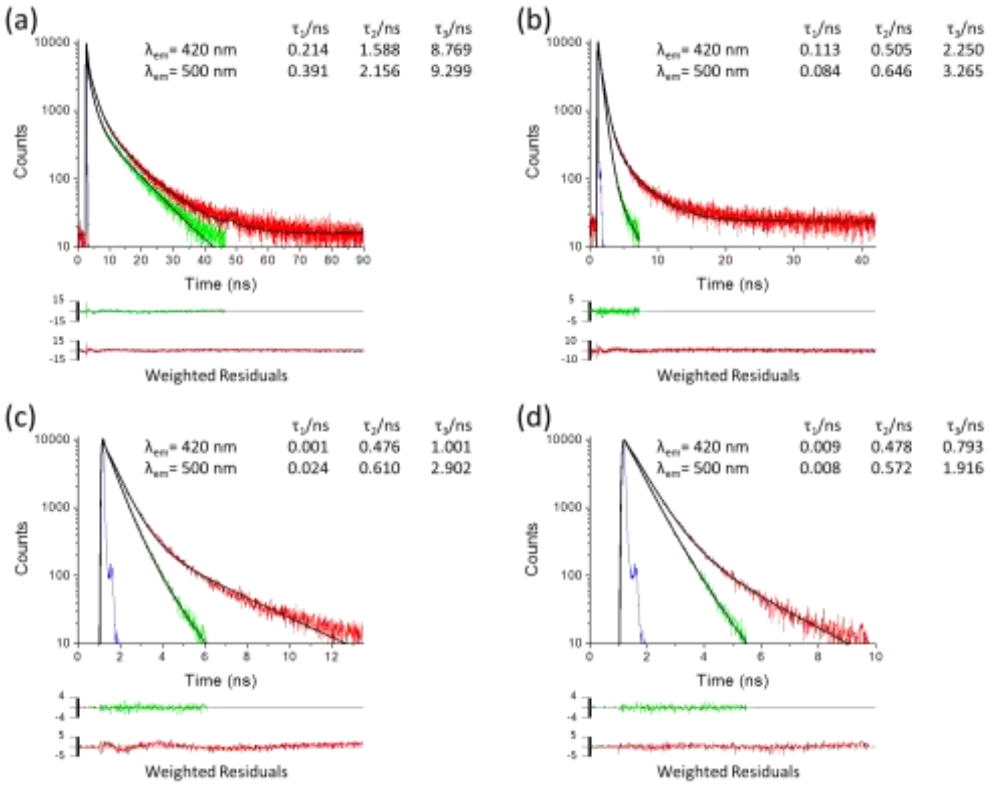

Figure A.5.4. PL emission decay curves (solid green lines - λ_{em}=420 nm, solid red lines - λ_{em}=500 nm) and fits (solid black lines) for (**a**) **SP-PBS-1.0**, (**b**) **SP-PBS-2.0**, (**c**) **SP-PBS-4.0** and (**d**) **SP-PBS-8.0**. The fitted decay times (τ_i), pre-exponential values (α_i), fits, weighted residuals and instrument response function (solid blue line) are also shown.

1.3 Chapter 6

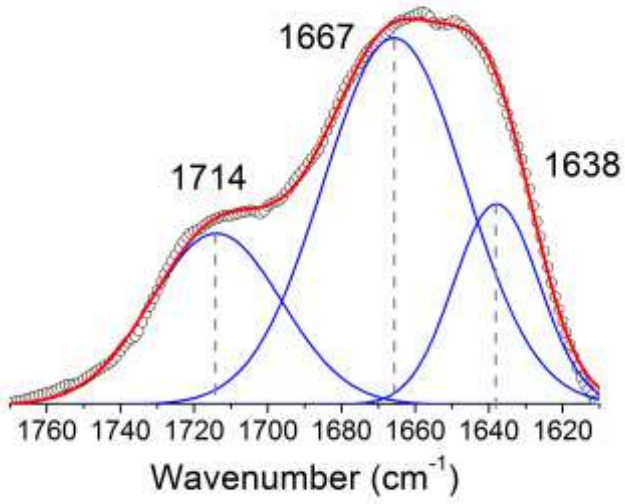

Figure A.6.1. Results of curve-fitting performed in the 'amide I' region of the sample **P3T-1.8**. The frequencies given are those of the dashed lines and serve solely to guide the eye.

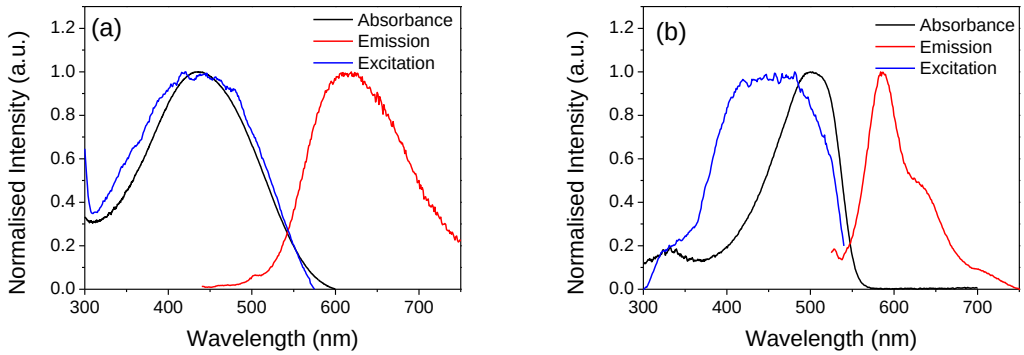

Figure A.6.2. UV/vis absorption (black line), PL (red line) and PL excitation (blue line) for (**a**) **P3TMAHT** in aqueous solution (16 µM, λ_{ex} = 420 nm and λ_{em} = 630 nm) and (**b**) **MEH-PPV** in THF (5 µM, λ_{ex} = 420 nm and λ_{em} = 630 nm)

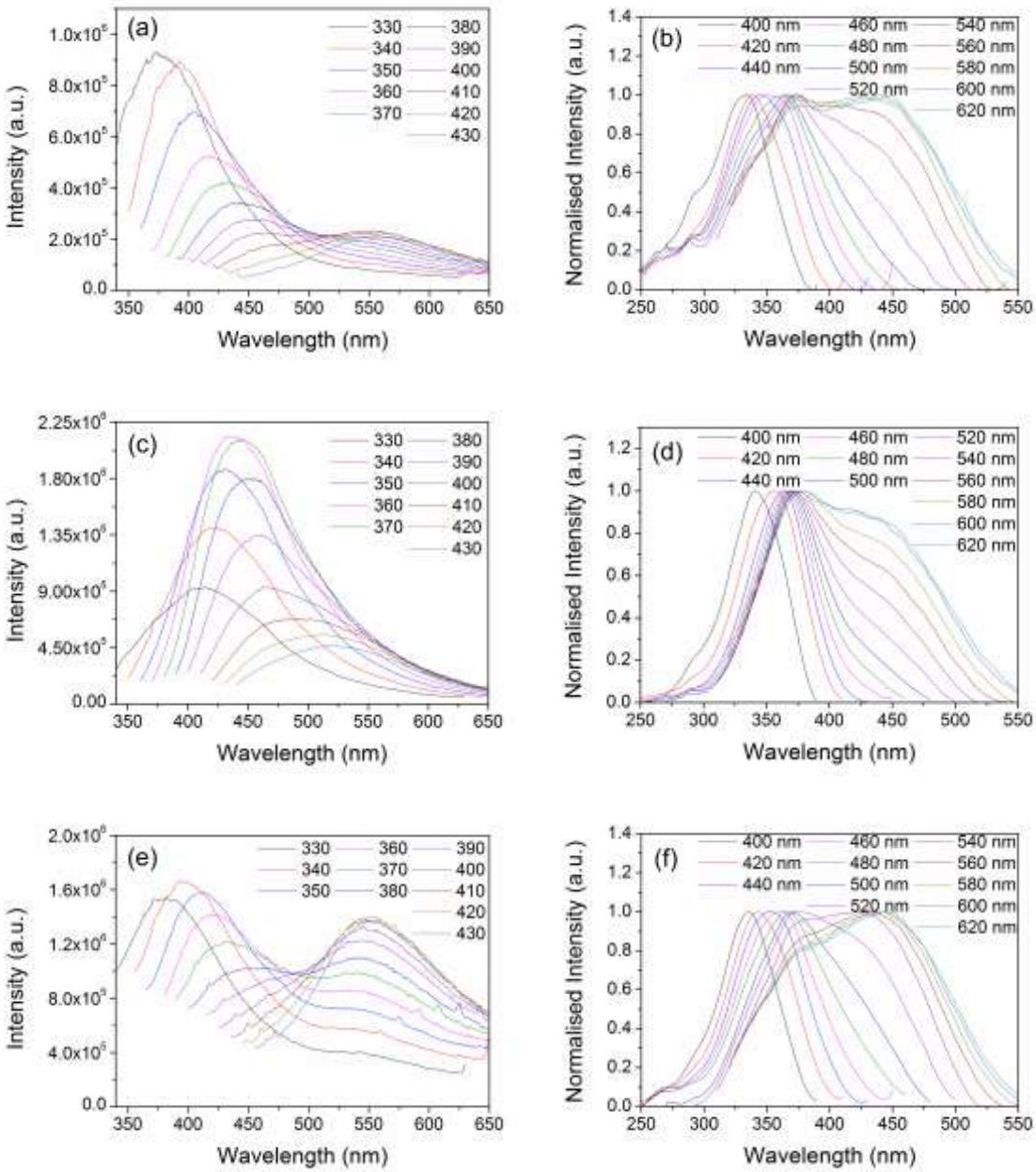

Figure A.6.3. (**a**) PL and (**b**) PL excitation spectra of **P3T-0.6**. (**c**) PL and (**d**) PL excitation spectra of **P3T-1.2**. (**e**) PL and (**f**) PL excitation spectra of **P3T-2.4**. For all PL spectra (λ_{ex} = 330, 340, 350, 360, 370, 380, 390, 400, 410, 420 and 430 nm) and for all PL excitation spectra (λ_{em} = 400, 420, 440, 460, 480, 500, 520, 540, 560, 580, 600 and 620 nm).

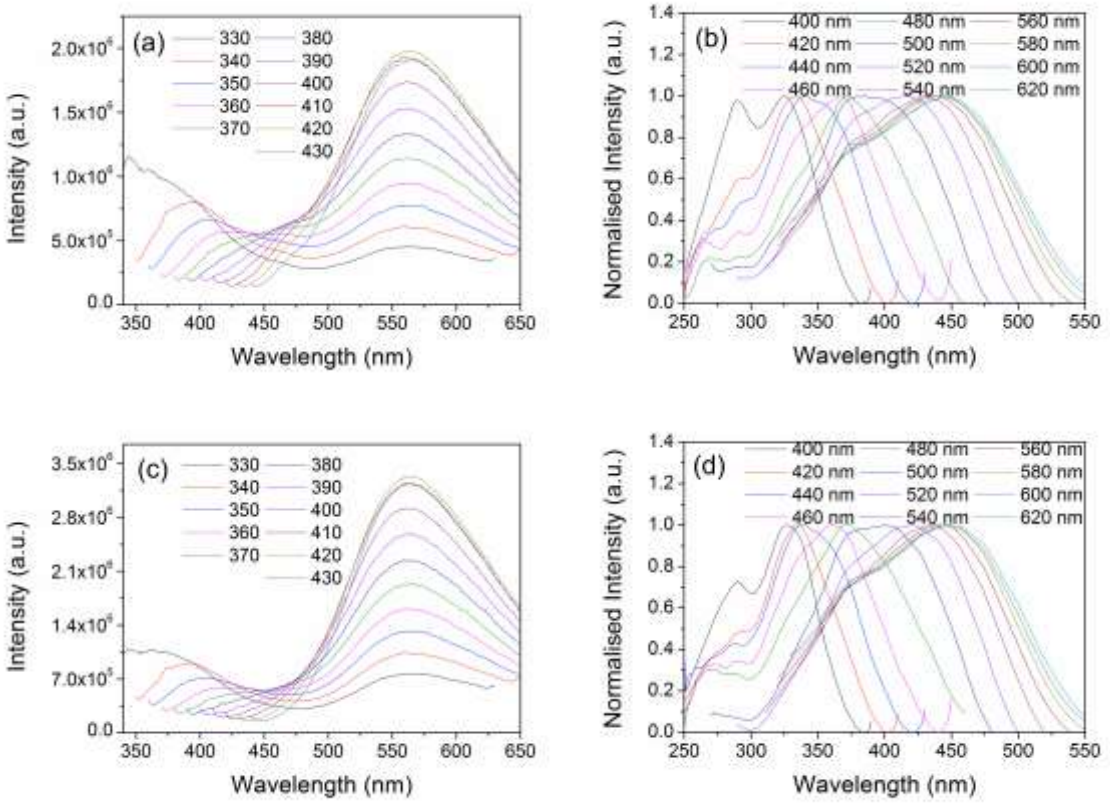

Figure A.6.4. (**a**) PL and (**b**) PL excitation spectra of **P3T-3.3**. (**c**) PL and (**d**) PL excitation spectra of **P3T-6.6**. For all PL spectra (λ_{ex} = 330, 340, 350, 360, 370, 380, 390, 400, 410, 420 and 430 nm) and for all PL excitation spectra (λ_{em} = 400, 420, 440, 460, 480, 500, 520, 540, 560, 580, 600 and 620 nm).

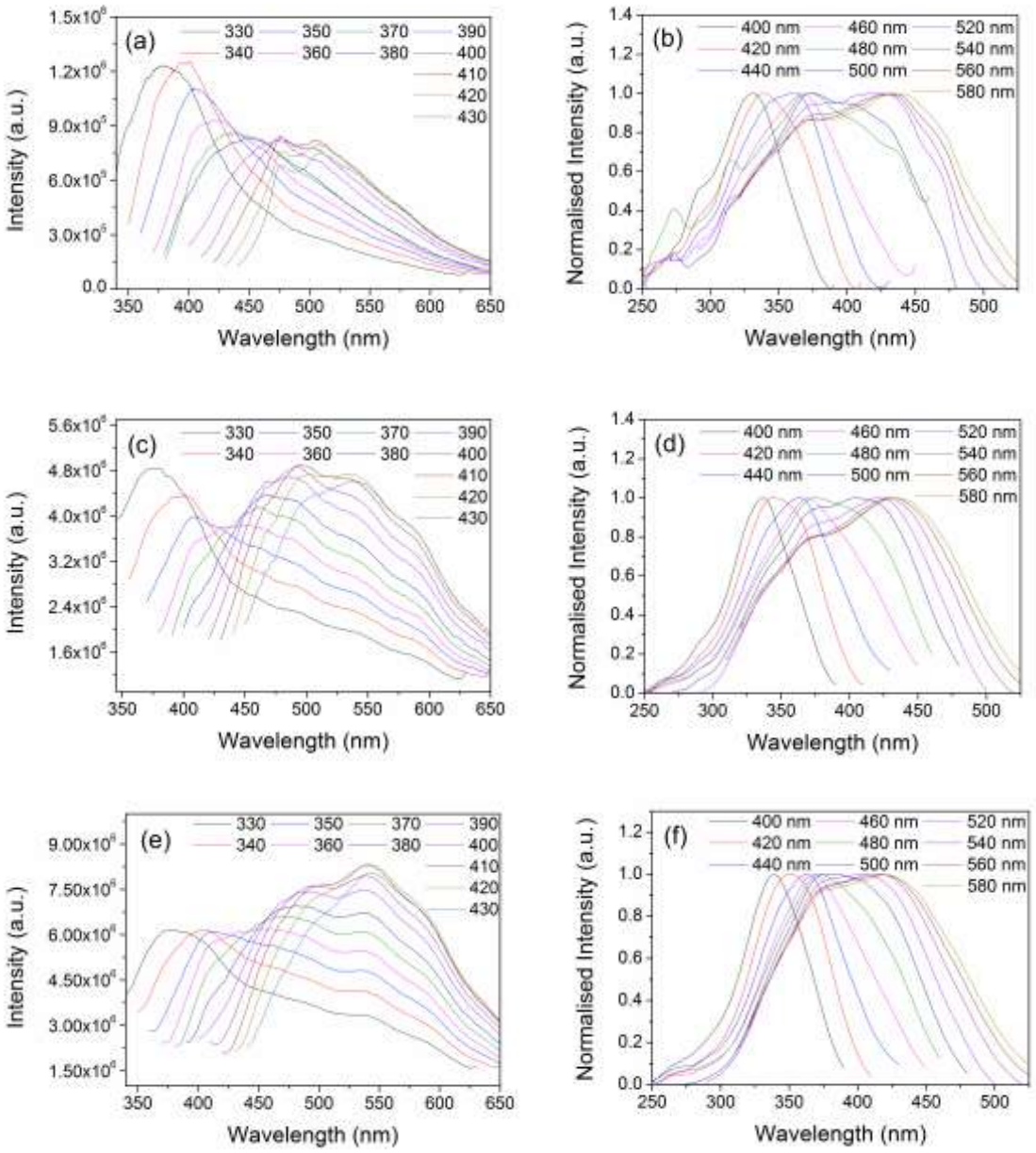

Figure A.6.5. (**a**) PL and (**b**) PL excitation spectra of **MEH-0.2**. (**c**) PL and (b) PL excitation spectra of **MEH-0.7**. (**e**) PL and (**f**) PL excitation spectra of **MEH-1.0**. For all PL spectra (λ_{ex} = 330, 340, 350, 360, 370, 380, 390, 400, 410, 420 and 430 nm) and for all PL excitation spectra (λ_{em} = 400, 420, 440, 460, 480, 500, 520, 540, 560 and 580 nm).

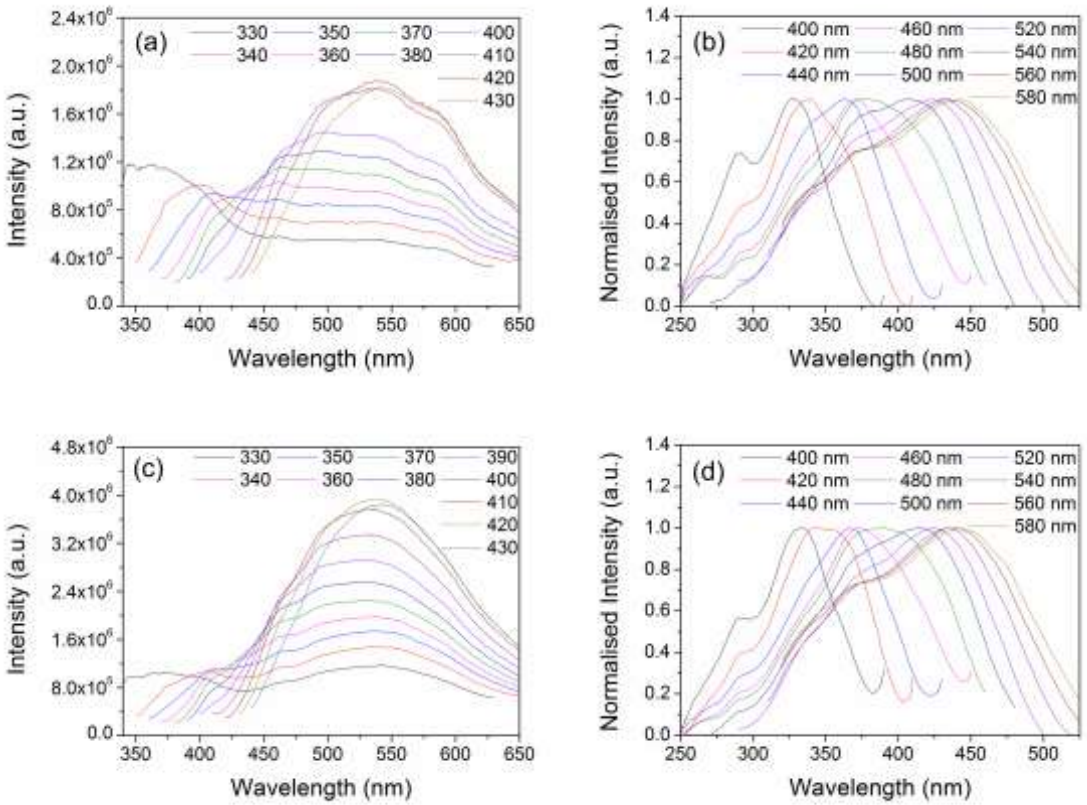

Figure A.6.6. (**a**) PL and (**b**) PL excitation spectra of **MEH-1.3**. (**c**) PL and (**d**) PL excitation spectra of **MEH-2.7**. For all PL spectra (λ_{ex} = 330, 340, 350, 360, 370, 380, 390, 400, 410, 420 and 430 nm) and for all PL excitation spectra (λ_{em} = 400, 420, 440, 460, 480, 500, 520, 540, 560 and 580 nm).

1.4 Chapter 7

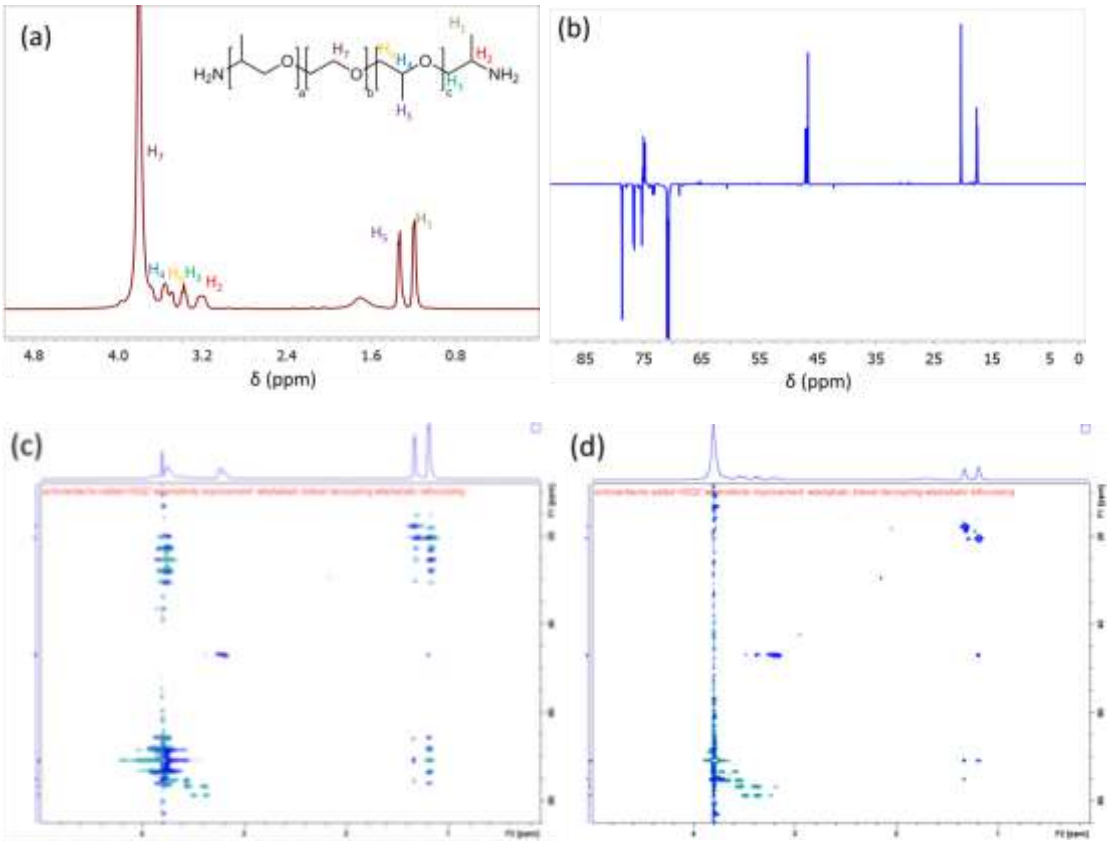

Figure A.7.1. (**a**) ^{1}H spectrum, (**b**) DEPT 13 spectrum, (**c**) CH COSY and (**d**) long range CH COSY for ED-600 in the absence of solvent at 298 K.

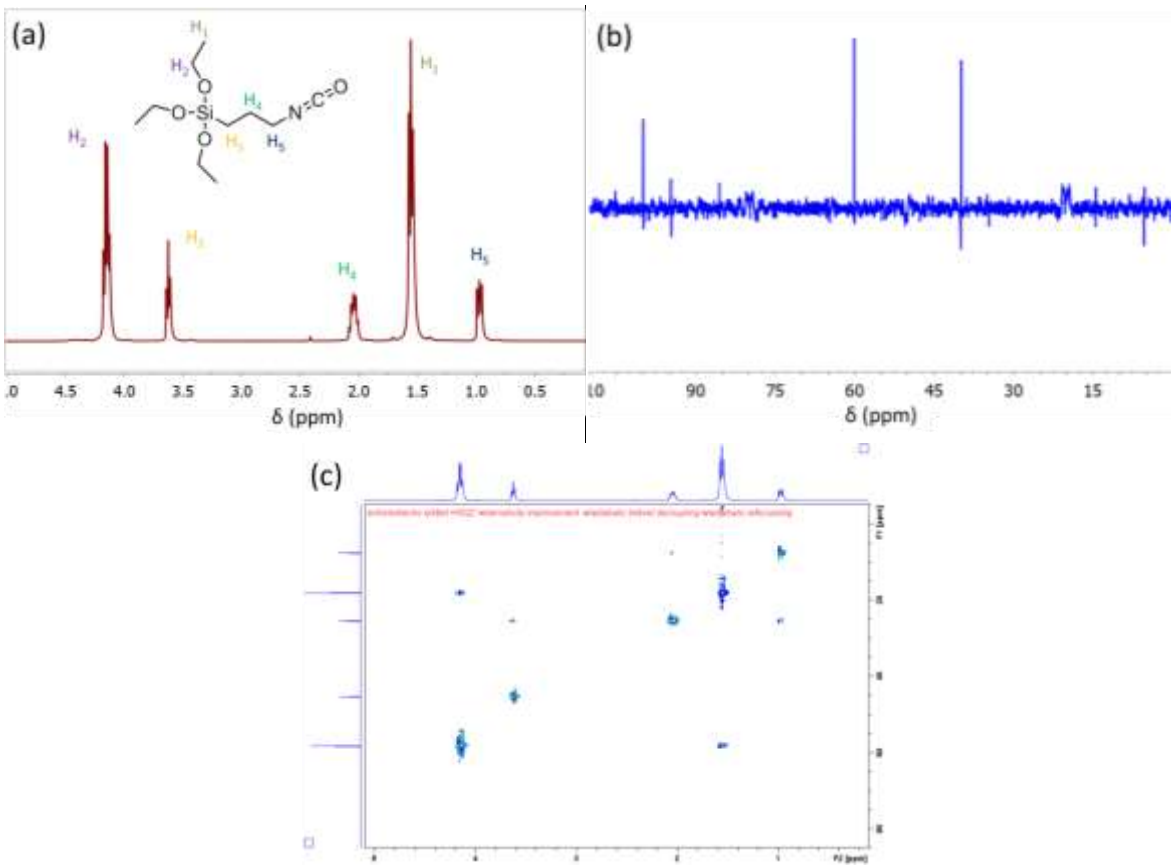

Figure A.7.2. (**a**) ^{1}H spectrum, (**b**) DEPT 13 spectrum and (**c**) CH COSY for ICPTES in the absence of solvent at 298 K.

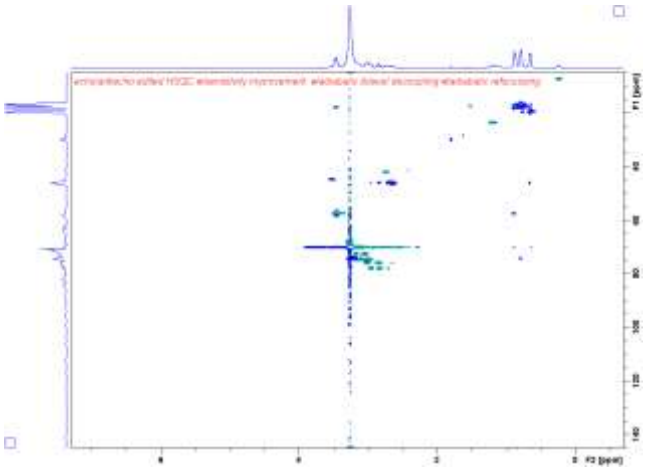

Figure A.7.3. CH COSY for d-UPTES in the absence of solvent at 298 K.